

# THE STUDY OF PROPERTIES OF SUNSPOTS

A THESIS

submitted for the Award of Ph.D. degree of

**MOHANLAL SUKHADIA UNIVERSITY**

in the

Faculty of Science

By

**Suruchi Goel**



Under the supervision of

**Prof. Shibu K. Mathew**  
PROFESSOR

**UDAIPUR SOLAR OBSERVATORY  
PHYSICAL RESEARCH LABORATORY**

YEAR OF SUBMISSION: 2015

## DECLARATION

I hereby declare that the work incorporated in the present thesis entitled **“The study of properties of sunspots”** is my own work and is original. This work, in part or in full, has not been submitted to any University for the award of a Degree or a Diploma. I have properly acknowledged the material collected from secondary sources wherever required.

Date:

**Suruchi Goel**  
**(Author)**  
Udaipur Solar Observatory  
Physical Research Laboratory  
P.B. No. 198, Dewali, Badi Road  
Udaipur-313 001  
Rajasthan, India.

## CERTIFICATE

I feel great pleasure in certifying that the thesis entitled “**The study of properties of sunspots**” embodies a record of the results of investigation carried out by **Ms Suruchi Goel** under my guidance. I am satisfied with the analysis of data, interpretation of results and conclusions drawn.

She has completed the residential requirement as per the rules.

I recommend the submission of this thesis.

Date:

**Prof. Shibu K. Mathew**  
**(Thesis Supervisor)**  
Udaipur Solar Observatory  
Physical Research Laboratory  
P.B. No. 198, Dewali, Badi Road  
Udaipur-313 001  
Rajasthan, India.

Dedicated to

My First Guru

**MY MOTHER**

# Contents

<b>List of Figures</b>	<b>iv</b>
<b>List of Tables</b>	<b>vii</b>
<b>Acknowledgments</b>	<b>ix</b>
<b>Abstract</b>	<b>x</b>
<b>1 Introduction</b>	<b>1</b>
1.1 Introduction . . . . .	1
1.2 Observations of flows of convection zone . . . . .	2
1.2.1 Solar surface velocity fields . . . . .	2
1.2.2 Solar differential rotation . . . . .	3
1.2.3 Meridional circulation . . . . .	3
1.3 Observations of magnetic activity on solar surface . . . . .	4
1.3.1 Solar surface magnetic regions . . . . .	4
1.3.1.1 Spatial-temporal distribution of active regions	5
1.3.1.2 Magnetic polarity distribution of active regions	5
1.4 Solar global dynamo . . . . .	7
1.5 Motivation and objectives of the thesis . . . . .	10
1.6 Outline of the thesis . . . . .	12
<b>2 Materials and Methods</b>	<b>14</b>
2.1 Introduction . . . . .	14
2.2 SoHO/MDI instrument and observables . . . . .	15
2.3 Pre-processing of SoHO/MDI continuum images . . . . .	19
2.3.1 Stray-light and limb-darkening removal . . . . .	20
2.3.2 Flat-fielding . . . . .	25
2.4 Automated sunspot detection and cataloging . . . . .	27
2.4.1 Review of sunspot detection methods . . . . .	28
2.4.2 Active contours and level set methods . . . . .	30
2.4.3 Identification of sunspots . . . . .	32
2.4.4 Characterization of sunspots . . . . .	35
2.4.5 Sunspots catalog . . . . .	38

---

2.5	Automated sunspot tracking . . . . .	40
2.6	Sunspot bipoles identification . . . . .	43
2.7	Summary . . . . .	44
<b>3</b>	<b>Statistical Properties of Sunspots</b>	<b>46</b>
3.1	Introduction . . . . .	46
3.1.1	Sunspot features . . . . .	46
3.1.2	Magneto-convection and sunspot models . . . . .	47
3.1.3	Sunspot's magnetic field, darkness, size, and solar-cycle	49
3.1.3.1	Sunspot size dependence . . . . .	50
3.1.3.2	Solar cycle dependence . . . . .	51
3.1.3.3	Limb variation . . . . .	52
3.1.4	Sunspot's penumbra-umbra area ratio . . . . .	53
3.1.5	Objectives of the present study . . . . .	54
3.2	Sunspots data and parameters . . . . .	55
3.3	Results . . . . .	57
3.3.1	Umbral core intensity and sunspot area . . . . .	57
3.3.2	Umbral core intensity and circularity index . . . . .	63
3.3.3	Umbral mean intensity and sunspot area . . . . .	66
3.3.4	Penumbral mean intensity and sunspot area . . . . .	68
3.3.5	Penumbra-umbra area ratio . . . . .	69
3.3.6	Sunspot-umbra area ratio . . . . .	71
3.3.7	Leading and following sunspots . . . . .	71
3.3.8	Verification of results via thresholding method . . . . .	75
3.3.9	Temporal and center-to-limb variation . . . . .	76
3.3.9.1	Umbral-core intensity . . . . .	78
3.3.9.2	Penumbra-umbra area ratio . . . . .	86
3.4	Summary and Discussion . . . . .	89
3.4.1	Sunspot brightness and size . . . . .	89
3.4.2	Solar-cycle and limb variation of sunspot brightness . . . . .	93
3.4.3	Penumbra-umbra and sunspot-umbra area ratio . . . . .	94
3.5	Conclusion . . . . .	95
<b>4</b>	<b>Study of Differential Rotation of Sun</b>	<b>97</b>
4.1	Introduction . . . . .	97
4.1.1	Helioseismic records of solar rotation . . . . .	99
4.1.2	Rotation rate and sunspot parameters . . . . .	101
4.1.3	Temporal variation of rotation . . . . .	102
4.1.4	North-South asymmetry of solar rotation . . . . .	104
4.2	Objectives of the present study . . . . .	105
4.3	Observables and data analysis . . . . .	106
4.4	Results and discussion . . . . .	108
4.4.1	Solar differential rotation using sunspots as tracers . . . . .	108

---

4.4.2	Rotation dependence on sunspot size, age and life-span	111
4.4.2.1	Rotation variation with sunspot area . . . . .	112
4.4.2.2	Initial rotation rate and life span . . . . .	118
4.4.2.3	Rotation variation with age . . . . .	119
4.4.3	Solar-cycle phase variation of rotation parameters . . .	121
4.4.4	North-south asymmetry of rotation for cycle 23 . . . .	126
4.5	Conclusion . . . . .	140
<b>5</b>	<b>Study of Bipolar Tilt angles</b>	<b>144</b>
5.1	Introduction . . . . .	144
5.2	Data and observables . . . . .	147
5.3	Results and discussion . . . . .	148
5.3.1	Latitudinal distribution of bipoles and joy's law . . . .	148
5.3.2	Bipoles separation distance distribution . . . . .	152
5.3.3	North-South asymmetry in distribution of bipoles . . .	154
5.3.4	Tilt-angle and polarity separation distance dependence on sunspot bipoles area . . . . .	158
5.3.5	Solar cycle phase variation of bipoles properties . . . .	161
5.4	Conclusions . . . . .	168
<b>6</b>	<b>Summary, Conclusions and Future prospects</b>	<b>170</b>
6.1	Modules for processing solar images . . . . .	170
6.2	Statistical studies of sunspot properties . . . . .	170
6.3	Study of solar differential rotation . . . . .	172
6.4	Study of sunspot-groups tilt-angles . . . . .	174
	<b>Bibliography</b>	<b>176</b>
	<b>List of Publications</b>	<b>200</b>
	<b>Solar Physics 2014 Paper</b>	<b>201</b>

# List of Figures

1.1	Sunspot-butterfly and sunspot-area activity cycle . . . . .	6
1.2	Magnetic-synoptic map . . . . .	6
2.1	Optical layout of SoHO/MDI . . . . .	17
2.2	Ni I 6768 Å line profile and MDI Filtergrams . . . . .	18
2.3	Corrected continuum images and corresponding radial intensity profiles . . . . .	22
2.4	Flat-field frames of MDI continuum images . . . . .	26
2.5	Detected sunspots from SoHO/MDI continuum image . . . . .	34
2.6	Passage of a sunspot from East-to-West Limb . . . . .	41
2.7	Longitude vs Day of traced sunspot . . . . .	41
3.1	Umbral-core intensity vs Sunspot area (MSH) . . . . .	58
3.2	Umbral-core intensity vs sunspot area (MSH) for distinct sunspots . . . . .	59
3.3	Umbral-core intensity vs umbral effective radius (Mm) . . . . .	60
3.4	Histogram of umbral-circularity measure . . . . .	63
3.5	Umbral-core intensity vs sunspot area (MSH) for different range of umbral-circularity measures . . . . .	64
3.6	Residual core intensity vs umbral-circularity measure . . . . .	65
3.7	Umbral-mean intensity vs sunspot area . . . . .	66
3.8	Umbral-mean intensity vs umbral effective radius . . . . .	67
3.9	Penumbral-mean intensity vs sunspot area . . . . .	69
3.10	Penumbra-umbra area ratio histogram. . . . .	70
3.11	Penumbra to umbra area ratio vs sunspot area. . . . .	71
3.12	Sunspot-umbra area ratio histogram. . . . .	72
3.13	Sunspot to umbra area ratio vs sunspot area. . . . .	73
3.14	Umbral-core intensity vs sunspot area for leading and following sunspots . . . . .	73
3.15	PU ratio vs sunspot area for leading and following sunspots . . . . .	74
3.16	Variation of umbral-core and umbral-mean intensity with sunspot area for sunspots identified using thresholding method. . . . .	76
3.17	Variation of penumbral-mean intensity with sunspot area for sunspots identified using thresholding method. . . . .	77

3.18	Variation of PU ratio and TU ratio with sunspot area for sunspots identified using thresholding method. . . . .	77
3.19	Temporal variation of umbral-core intensity for small, intermediate, and large size sunspots. . . . .	79
3.20	Center-to-limb variation of umbral-core intensity for small, intermediate, and large size sunspots. . . . .	80
3.21	Center to limb variation of residual umbral-core intensity using residual method. . . . .	81
3.22	Variation of residual umbral-core intensity with heliocentric positions by multivariate analysis. . . . .	84
3.23	Variation of umbral-core intensity with sunspot area derived by multivariate analysis. . . . .	85
3.24	Variation of umbral-core intensity ( $\Delta I_3$ ) with umbral-circularity measure derived by multivariate analysis. . . . .	86
3.25	Temporal variation of penumbra-umbra area ratio for small, intermediate, and large size sunspots. . . . .	87
3.26	Center-to-limb variation of penumbra-umbra area ratio for small, intermediate, and large size sunspots. . . . .	88
4.1	Inferred radial profile of solar rotation . . . . .	100
4.2	Latitudinal distribution of solar rotation velocities . . . . .	109
4.3	Latitudinal profile of solar differential rotation . . . . .	110
4.4	Mean Rotation rate variations with sunspot area (in MSH) . . . . .	112
4.5	Mean Rotation rate variations with sunspot area (in MSH) . . . . .	113
4.6	Latitudinal profile of solar rotation for different ranges of sunspot area (in MSH) . . . . .	114
4.7	Equatorial rotation rate, A variations with sunspot area (in MSH)	115
4.8	Latitudinal gradient of rotation rate, B variations with sunspot area (in MSH) . . . . .	116
4.9	Initial rotation rate for sunspot having different life-span for different latitude bands . . . . .	118
4.10	Mean Rotation rate variations with sunspot age for different latitude bands . . . . .	120
4.11	Annual latitudinal profile of sunspot rotation rates during cycle 23 . . . . .	122
4.12	Yearly differential rotation profile of cycle 23 . . . . .	123
4.13	Annual variation of Mean rotation rate in solar cycle 23 . . . . .	124
4.14	Annual variation of Equatorial-rotation rate and Differential-rotation coefficient in Solar cycle 23. . . . .	125
4.15	North-South asymmetry in latitudinal profile of solar differential rotation . . . . .	127
4.16	North and South hemispheres solar differential rotation at different phase of solar cycle . . . . .	130

---

4.17	A and B coefficients and sunspot area coverage for North and South hemispheres at different cycle phases . . . . .	131
4.18	Variation of A and B coefficients with difference of mean of sunspot-area . . . . .	133
4.19	Variation of NS-asymmetry index of Sunspot area coverage with the cycle phase . . . . .	136
4.20	Variation of A and B coefficients with sunspot-area coverage percentage . . . . .	138
5.1	Sunspot-bipoles tilt angle distribution in solar cycle 23 . . . . .	150
5.2	Latitudinal distribution of sunspot-bipole tilt-angles . . . . .	151
5.3	Distribution of sunspot-bipoles polarity separation distance in solar cycle 23 . . . . .	153
5.4	Latitudinal variation of Polarity separation distance . . . . .	154
5.5	Sunspot-bipoles tilt-angle distribution for northern and southern hemispheres . . . . .	155
5.6	Latitudinal distribution of sunspot-bipole tilt-angles for North-South hemispheres . . . . .	156
5.7	Sunspot-bipoles separation distance distribution for northern and southern hemispheres . . . . .	157
5.8	Latitudinal distribution of sunspot-bipole separation distance for North-South hemispheres . . . . .	157
5.9	Tilt-angle and sunspot-group area dependence . . . . .	160
5.10	Polarity separation distance and sunspot-group area dependence	160
5.11	Solar-cycle variation of median tilt-angle . . . . .	162
5.12	Variation of mean tilt-angle with cycle phase. . . . .	164
5.13	Solar-cycle variation of median polarity separation distance . .	165
5.14	Variation of mean polarity-separation distance with cycle phase.	166

# List of Tables

2.1	PSF parameters of MDI full-disk continuum images . . . . .	24
2.2	CLV coefficients of MDI full-disk continuum images. . . . .	24
2.3	Sunspot parameters list . . . . .	39
3.1	Fit parameters of umbral-core intensity vs sunspot area (MSH) for Figure 3.1 . . . . .	58
3.2	Fit parameters of umbral-core intensity vs Sunspot area (MSH) for distinct sunspots (Figure 3.2) . . . . .	59
3.3	Fit parameters of umbral-core intensity vs umbral radius (Mm) for Figure 3.3 . . . . .	60
3.4	Fit parameters of umbral-core intensity vs sunspot area for dif- ferent circularity measures (Figure 3.5) . . . . .	64
3.5	Fit parameters of umbral-core intensity vs circularity measure for Figure 3.6 . . . . .	65
3.6	Fit parameters of umbral-mean intensity vs sunspot area (MSH) for Figure 3.7 . . . . .	67
3.7	Fit parameters of umbral-mean intensity vs umbral effective radius (Mm) for Figure 3.8 . . . . .	68
3.8	Fit parameters of penumbral-mean intensity vs sunspot area for Figure 3.9 . . . . .	68
3.9	Fit parameters of penumbra-umbra area ratio vs sunspot area for Figure 3.11 . . . . .	70
3.10	Fit parameters of sunspot-umbra area ratio vs sunspot area for Figure 3.13 . . . . .	72
3.11	Fit parameters of umbral-core intensity and PU ratio vs sunspot area (in MSH) for leading sunspots . . . . .	74
3.12	Fit parameters of umbral-core intensity and PU ratio vs sunspot area (in MSH) for following sunspots . . . . .	75
3.13	Fit parameters of umbral-core intensity vs sunspot area (MSH) for Figure 3.1 . . . . .	75
3.14	Fit parameters of umbral-core intensity vs solar-cycle phase for Figure 3.19 . . . . .	78

---

3.15	Fit parameters of umbral-core intensity vs heliocentric positions for Figure 3.20 . . . . .	78
3.16	Fit parameters of residual umbral-core intensity vs heliocentric positions for Figure 3.21 . . . . .	82
3.17	Fit parameters of multivariate analysis of umbral-core intensity. . . . .	83
3.18	Fit parameters of penumbra-umbra area ratio vs solar-cycle phase for Figure 3.25 . . . . .	86
3.19	Fit parameters of penumbra-umbra area ratio vs heliocentric positions for Figure 3.26 . . . . .	89
4.1	Mean sunspot rotation rates for cycle 23 . . . . .	109
4.2	Rotation parameters variation with sunspot area . . . . .	115
4.3	North and South Hemispheres rotation rates . . . . .	129
4.4	Mean sunspot latitude and population of sunspots in higher latitudes at different cycle phase for Northern and Southern hemisphere . . . . .	132
4.5	Correlation-coefficients of A and B with the percentage of sunspot area-coverage . . . . .	137
5.1	Slope of tilt-angle vs latitude . . . . .	150
5.2	Fit-parameters for tilt-angle and polarity-separation distance variation with sunspot-group area . . . . .	159
5.3	Fit-parameters for tilt-angle and polarity-separation distance variation with solar cycle phase . . . . .	163

## Acknowledgments

I am thankful to all PRLites, family members and friends who had extended their support towards the completion of my PhD research work.

In particular, I extend my gratitude to some of the associates who have played significant roles to shape the thesis and to ingrain some qualities in me as a scientist. I started my scientific research from Noble Gas Mass-spectrometer Lab at PRL, Ahmedabad, under the supervision of Prof. Murty and I will always treasure the scientific-learning experiences I had during my tenure there. I will always be obliged towards him, since regular weekly Lab-seminars conducted by him propelled me to develop presentation skill and confidence to express own scientific views to audiences. I extend my gratitude to thesis supervisor Prof. Shibu K. Mathew for extending his support, and his inner strength is commendable. The interactions and discussions with Prof. Solanki, MPS, has gave me confidence to present results in appropriate format and with better clarity and critical assessment. The most appealing quality of Prof. Solanki is the enthusiasm he has for science, that indeed is motivational for young researchers. I am thankful to him and also to Prof. Krivova for providing their valuable time at MPS. Prof. Javaraiah from IIA, Bangalore, provided his able guidance to shape the study of solar differential rotation, small-span of interaction with him at Bangalore turned fruitful and valuable for the thesis. Lastly, I express my gratitude to Prof. Venkat, who kindly took time and interest to discuss all the thesis results and provided valuable inputs for further improvements.

# Abstract

Sunspots are the most prominent manifestations of large-scale magnetic field observed on solar surface. They are the unique test-bed for the understanding of feedback mechanism between the convective flows, magnetic-fields, and large scale flows such as, differential rotation and meridional flow, which are the key ingredients of solar global dynamo.

In the thesis, we studied various properties of sunspots, which were extracted from the stray-light-corrected SoHO/MDI full-disk continuum images for the period of solar cycle 23. To understand the magnetoconvection within sunspots and its modulation with the activity phase, we studied the inter-dependency of various global properties of sunspots. We found that the minimum and also the mean of umbral intensity statistically decreases nearly exponentially with the sunspot size, though there is large intrinsic scatter in all size ranges; for sunspots having area greater than 600 MSH have nearly constant intensity. The circular umbrae were found to be darker than the elongated ones. The penumbral mean intensity for sunspots  $> 100MSH$  decreases with the sunspot size. The sunspot intensity does not show any variation with the cycle phase, in contrast to the secular increase observed by Penn *et al* (2006). We found that the minimum umbral intensity increases towards the limb. The ratio of penumbra-umbra area is found to be not a constant value, instead it decreases with the sunspot area; the mean value of penumbra-umbra area ratio for sunspots sampled from cycle 23, is close to 4, which is the value utilize for past irradiance reconstruction.

In most of the previous studies, the differential rotation rates had been derived using sunspot-groups which usually have amalgamation of varied range of size of sunspots. We have calculated the differential rotation rate for cycle 23 using individual sunspots as tracers. The larger sunspots have slower equatorial rotation rate than the smaller sunspots. In our study, we found that in the cycle 23, Northern hemisphere has higher differential rotation rate than the southern hemisphere. The hemispheric rotation was found

to be anti-correlated with the North-South asymmetry in the hemispheric fraction of total sunspot area. That is, for a given phase of cycle, when a hemisphere has larger activity (larger fraction of total sunspot area), then that hemisphere has relatively slower and rigid rotation. This suggests that the magnetic-field distribution modulates the solar differential rotation and that too asymmetrically across the equator. The solar activity index defined as fraction of total sunspot area was found to have changed radically across hemispheres during the sunspot maximum, which needs further justification from further investigations.

Sunspots are part of bipolar active regions, and properties of bipolar tilt angles can provide insights about poloidal field generation, and flux emergence process. From our study of sunspot bipoles obtained from MDI continuum images, we found the slope of Joy's law of  $0.38^\circ$  per degree of latitude. The most probable value of tilt-angle was found to be a positive value (*i.e.*, with the equatorward leading polarity) of  $6.5^\circ$ . The tilt angle and polarity separation distance decreases with sunspot-group size, which supports the Coriolis force theory of the origin of observed bipoles inclination with respect to the equator. For our sample of sunspot bipoles from solar cycle 23, the northern hemisphere has larger slope of Joy's law than the Southern hemisphere. We found that the mean tilt angle decreases with the solar cycle phase, this rate of decrease of tilt angles can not be explained by decreasing median latitude of active regions in during the solar cycle, while this decrease in tilt angle is in anti-correlation with the average of sunspot-bipole area in each phase. Also decrements in tilt angle with cycle phase is relatively higher in Northern hemisphere than Southern hemisphere. These observations possibly indicates that the Joy's law depends on solar activity parameters and thus needs further detailed studies using long-term series of sunspot-bipoles data. This also suggests existence of North-South asymmetry in tilt-angle distribution during the solar cycle.

# Chapter 1

## Introduction

### 1.1 Introduction

The Sun exhibits activity cycle of about 11 years, which includes changes in levels of solar radiation and mass ejection and, its appearance, with the variation in photospheric magnetic flux concentrations to the changing coronal structure. The underlying cause of activity cycle is the variation in spatio-temporal distribution of solar magnetic-fields from local to global-scales, which is supposed to be driven by hydromagnetic dynamo. Sunspots are the strong seats of magnetic flux observed on solar photosphere, and their formation, latitudinal distribution, systematic polarity alignment, latitudinal and longitudinal drifts have been the key ingredients for the development of dynamo, and the understanding of solar activity phenomena. The solar global dynamo is essentially the interaction between convection, magnetic field, and large-scale flows such as differential rotation and meridional flows. In the following Section [1.2], we will discuss about the small and large-scale flows observed in the solar convective zone. Observational features of solar surface magnetic fields and inferences drawn from these observations are discussed in the Section [1.3]. In Section [1.4], we discussed about the development of the solar dynamo models on the basis of observed properties of sunspots. The objectives and motivation of the thesis are presented in Section [1.5], followed by

the outline of the thesis in Section [1.6].

## 1.2 Observations of flows of convection zone

Convection is the transport of energy by bulk mass motions. Solar outer layer, which is 30% by radius and 2% by mass, with strong density stratification, is called the convection zone, since in this layer solar luminosity is mostly transported by fluid motions driven by thermal buoyancy. At the upper boundary of the convection zone, the solar surface is a radiating surface, *i.e.* energy is carried by photons. The flow of conducting fluid is the driver of magnetic activity. In the solar convection zone, the plasma motion fields range from typical horizontal scale of 1 Mm corresponding to granulation, upto the scale of global differential rotation. Here, we briefly note the observed small and large-scale fluid motions within the convection zone.

### 1.2.1 Solar surface velocity fields

The solar surface shows pattern in velocity-fields that are structures in a hierarchical order (Nordlund, Stein, and Asplund, 2009; Rast, 2003). The smallest pattern is called the solar granulation. It constitutes of hot plume of plasma rising to the surface, that cools off, and descends down to the surrounding inter-granular lanes. They have typical vertical velocity of  $1\text{Kms}^{-1}$ . They have been observed from size range of less than an arc-sec to few arc-sec (Hirzberger *et al.*, 1997). They have a mean lifetime of about 6-10 minutes (Hirzberger *et al.*, 1999).

The next larger flow field is mesogranulation. The vertical velocities of mesogranule upflows are  $\approx 60\text{ms}^{-1}$  and have a spatial scale of 5-10 Mm with mean lifetime of 5-6 hours (Hirzberger *et al.*, 1997; November *et al.*, 1981).

The supergranulation refers to a physical pattern that covers the surface of the quiet Sun with a typical horizontal scale of approximately 20-50 Mm and have a lifetime of around 1.8 day. It has a fluctuating velocity field of

$360 \text{ ms}^{-1}$  rms whose components are mostly horizontal (Leighton, Noyes, and Simon, 1962).

Giant cells as the name suggests comprise a large fraction of solar surface area, typically  $40^\circ - 50^\circ$  of longitude and  $\sim 10^\circ$  of latitude (about 100 Mm or larger) and lifetime of  $\approx 120$  days (Beck, Duvall, and Scherrer, 1998).

### 1.2.2 Solar differential rotation

The well-established global circulation is the solar differential rotation. The solar rotation has been observed to be differential; *i.e.*, the rotation rate is dependent on both the heliocentric latitude and also on the radial distance to the solar center and may be vary in time (Beck, 2000; Howe, 2009). The latitudinal variation refers to monotonic decrease of angular velocity from equator to the poles, which persist almost throughout the convection zone. The radial shear is largely confined to the upper and lower boundary of layers of convection zone. The lower boundary layer called as the tachocline, is the transition region between the differentially rotating convection zone and the almost rigidly rotating region below. At the top of the convection zone at about  $0.95R_\odot$  is the near-surface shear layer, where the rotation rate increases inward by about 2 – 3% from the photosphere. The detailed observations of differential rotation from tracers and also from helioseismological inversions are presented in Chapter 4.

### 1.2.3 Meridional circulation

The meridional circulation refers to flows of material along meridian lines (poloidal), either from the equator towards the poles or vice-versa. At the solar surface, the meridional flow is observed to be poleward flow with amplitude around  $15 - 20 \text{ ms}^{-1}$  (Hathaway, 2011, and references therein). Recently, Zhao *et al.* (2013) from helioseismic observations of SDO/HMI data found evidence for double-cell meridional circulation, with poleward flows from the surface to  $0.91R_\odot$  (flow speed of  $15 \text{ ms}^{-1}$ ) and from  $0.82R_\odot$  to about  $0.75R_\odot$ ;

and an equatorward flow located between these in a layer of about  $0.09R_{\odot}$  (flow speed of  $10 \text{ ms}^{-1}$ ).

## 1.3 Observations of magnetic activity on solar surface

### 1.3.1 Solar surface magnetic regions

The magnetic structures threading through the photosphere and regions above it, have been the main source of information about the process of generation and transport of solar magnetic fields in the convection zone and related solar-activity dynamics. These magnetic features appear in the form of bipolar regions and embrace wide-range of size and magnetic flux (Harvey and Zwaan, 1993; Schrijver and Zwaan, 2008; Solanki, Inhester, and Schüssler, 2006). The larger of these are the active regions and the smallest are called ephemeral regions. The largest active regions reach fluxes of nearly  $10^{23}$  Mx and lifetimes of months, and smallest ephemeral regions contain less than  $10^{19}$  Mx and have lifetime of less than a day. Larger bipole regions constitutes groups of sunspots (size of  $\sim 10^{14} - 2 \times 10^{19} \text{cm}^2$ ) and faculae. Sunspots being seats of strong magnetic flux have reduced convection and hence lowered brightness relative to the surrounding photosphere (more discussion on this in Chapter 3); while faculae are arranged in plages, *i.e.*, as irregular network, and visible as brighter specks close to the limb. Sunspots also exhibits magnetic structure within; the central-darker core called umbra consists of primarily vertical fields, while relatively more brighter surrounding region called as penumbra have inclined magnetic fields.

Apart from the bipolar active regions having highly concentrated magnetic flux, the network of small magnetic flux ( $\sim 10^{17}$  and below) carpet the solar surface, these are essentially organized in network structures defined by convective patterns, which becomes globally redistributed by large-scale flows (Meunier, 2003; Parnell *et al.*, 2009; Sánchez Almeida and Martínez González, 2011, and reference therein). The main observed properties of small-scale

magnetic structures are; strong fields tend to be vertical and weaker fields horizontal (de Wijn *et al.*, 2009).

Bipolar active regions exhibits a number of systematic properties during the course of the solar activity cycle. Here, we will note some of the solar magnetic-activity characteristics observed on solar surface which should be the stepping stones for the solar dynamo modeling.

### 1.3.1.1 Spatial-temporal distribution of active regions

Sunspots visible as dark spots in the white-light images have been the most widely studied surface magnetic feature. The solar activity period of 11 years is defined in terms of waxing and waning counts (or area) of sunspots visible on photosphere (as shown in lower panel of Figure 1.1). The sunspots and active regions are restricted to heliographic latitudes of  $\leq 40^\circ$ . At the start of each cycle the spots appear at higher latitudes  $30^\circ - 35^\circ$ , and as the cycle progresses the latitude band coverage broadens and the median latitude slowly converges towards the equator. This behaviour is referred to as “Spörer’s Law of Zones” by Maunder (1903). As the cycle advances, the zones of sunspot occurrence migrate towards lower latitude, and the last spots of a cycle are within  $\pm 10^\circ$  of the equator. The latitude distribution of sunspots are described as the wings of butterfly, hence the name butterfly diagram for latitudinal distribution of sunspots (as shown in the top panel of Figure 1.1). Also, an important feature observed from the butterfly diagram is that the sunspots of the next cycle appear at high latitude zones, even when the on-going cycle’s sunspots are present at the lower latitude zones. Hence there is an overlap of two consecutive cycles of about 2-3 years (see review by Hathaway, 2010).

### 1.3.1.2 Magnetic polarity distribution of active regions

In a bipolar sunspot group, the leading spot (in the direction of solar rotation) and the following spot(s) are of opposite polarity. In general the

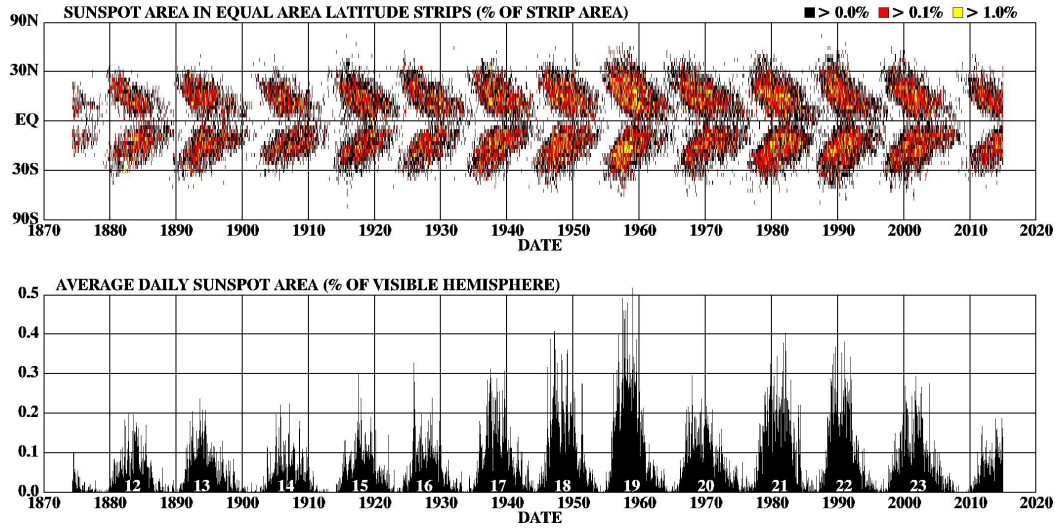


**Figure 1.1:** *Top:* Time-latitude distribution of sunspot area; *Bottom:* The average daily sunspot area for each solar rotation cycle since May 1874. (courtesy D. Hathaway, NASA).

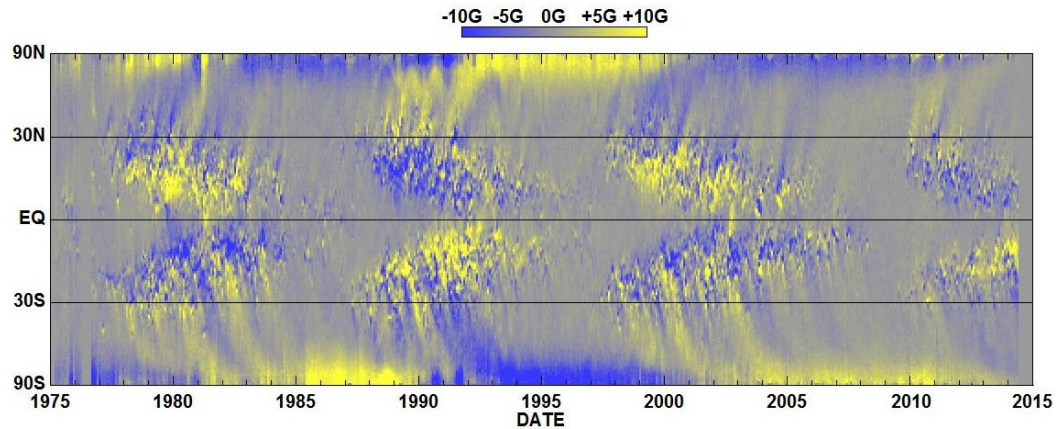


**Figure 1.2:** Time-latitude diagram of longitudinally averaged magnetic field in the solar photosphere for the last three activity cycles. (courtesy D. Hathaway, NASA).

leading sunspots tend to have more compact morphology as compared to the following spot (Fan, Fisher, and Deluca, 1993). The magnetic orientation of the leader and follower spots in bipolar groups remains the same in each hemisphere over each solar cycle. While, the bipolar groups in two hemispheres have opposite magnetic orientation. Furthermore, from one cycle to the next, the magnetic orientation of bipolar groups reverses in each hemisphere. This phenomenon is known as “Hale’s Polarity Law” (Hale *et al.*, 1919). Since, the

sunspots resumes the initial polarity after two consecutive 11-years cycles, the magnetic cycle is of period  $\sim 22$  year.

In a bipolar group, the leader spots generally appear near to the equator in comparison to the follower spots. Hence, there is an inclination angle between the leader and follower spot with respect to the east-west direction. Statistically, the magnitude of the tilt increases with increasing heliocentric latitude. This phenomenon is known as “Joy’s Law” (Hale *et al.*, 1919). The synoptic (time-latitude) diagram of the longitudinally-averaged photospheric radial magnetic field component, covering three sunspot cycles, constructed by averaging magnetograms over longitude for each solar rotation is shown in Figure [1.2]. At high heliocentric latitudes, the synoptic magnetogram shows the clear pattern of polarity reversal near the sunspot maximum. At mid-latitudes the most prominent feature is a fairly regular poleward drift of magnetic fields originating in sunspot latitudes. This “Magnetic Butterfly Diagram” (Figure 1.2) exhibits Hale’s Polarity Laws and the polar field reversals as well as Joy’s Law.

## 1.4 Solar global dynamo

The above discussed observed magnetic activity cycle, in conjunction with systematic distribution of magnetic polarities in latitude bands or across hemispheres, has provided following clues of the solar magnetic-field dynamics (Charbonneau, 2010):

- (a) **Bipolar nature:** This can be interpreted as that the sunspots are surface manifestation of large-scale toroidal (azimuthal) field that emerged on the photosphere in the form of  $\Omega$ -loop, hence the loop intersection on the photosphere produce sunspot pairs of opposite polarities. This picture then demands for the generation of toroidal flux and its magnitude being modulated in a period of 11 year cycle. Joy’s law suggests that the emerging  $\Omega$ -loops have slight tilt with respect to the east-west

direction

- (b) **Butterfly effect:** The toroidal field to be concentrated at latitudes  $\sim 45^\circ$  at the start of the new cycle and migrate equatorward in the course of the cycle.
- (c) **Hale polarity law and polar field reversal:** The opposite polarity distribution across hemisphere, suggests that the solar toroidal field is antisymmetric about the equator, and also reverses polarity from one cycle to the next with  $\sim 20$  year oscillation period. Observed polar-field reversal requires generation of large-scale surface poloidal (meridional) field, which migrate poleward during the course of the cycle, and reverses the polarity during sunspot maximum, which is in out-of-phase of toroidal field cycle.
- (d) The magnitude of the Scwhabe cycle varies greatly on the centennial time scale (Steinhilber *et al.*, 2012). It includes the Maunder minimum in 1645-1715, when no sunspots were present, and the Dalton minimum at the turn of the 18<sup>th</sup> to 19<sup>th</sup> centuries. The secular variations in solar activity has been the subject of intense studies for a long-time (Hathaway, 2010), but the causes of this phenomena is not yet understood in the present realm of solar dynamo models (Charbonneau, 2010).

The cyclic generation of large-scale magnetic field is likely operated by a dynamo, *i.e.*, the generation of magnetic field through the motion of conducting fluid. Following is the brief discussion of evolving theoretical understanding of solar dynamo mechanism (see the reviews by Charbonneau, 2010; Jones, Thompson, and Tobias, 2010; Miesch *et al.*, 2012; Ossendrijver, 2003, and references therein):

- (a) The magnetic field is described in terms of its poloidal and toroidal components, and the dynamo should be capable to regenerate these components from one another. The differentially rotating highly conducting

plasma can stretch the initial poloidal field to provide the toroidal component. This effect is known as  $\omega$ -effect.

- (b) Parker (1955) suggested that the small-scale helical motions, resulting from the convection in a rotating body could twist the toroidal fields into loops of field in the meridional plane, and the net-effect of these small-scale events would build a large-scale poloidal field. This effect was theoretically developed in the context of “Mean-field dynamo” by (Steenbeck, Krause, and Rädler, 1966), and this mechanism of poloidal field generation is known as  $\alpha$ -effect owing to its mathematical formulation.
- (c) To circumvent the problem of storage and amplification of toroidal field sufficient for cyclic regeneration in the realm of turbulent convection, (Parker, 1993) formulated a new model known as “Interface Dynamo”, in which the  $\alpha$ -effect operates in the turbulently convective layer, while the  $\omega$ -effect operates in the shear layer at the base of convection zone, *i.e.*, the tachocline (existence of such a shear layer is supported by helioseismological results). Diverging convective upflows and magnetic buoyancy carry magnetic flux towards the surface. In this model, the convection zone acts a filter to buoyantly rising toroidal field; allowing only strongest field to rise to the surface and appear as active regions, while weaker fields get dispersed by the convection, and is recycled and transported back to the tachocline by turbulent pumping, and the cycle repeats (Dikpati *et al.*, 2004).
- (d) The interface model has been reformulated as “flux transport dynamo” model (Dikpati and Charbonneau, 1999; Dikpati and Gilman, 2009; Nandy and Choudhuri, 2002; Nandy, Muñoz-Jaramillo, and Martens, 2011), in which the  $\omega$ -effect operates at the tachocline; while the  $\alpha$ -effect operates at the solar surface, via the decay of tilted bipolar active regions as was suggested in the Babcock-Leighton dynamo model (Babcock, 1961; Leighton, 1969). Moreover, the flux transport dynamo in-

vokes the meridional circulation for cyclic regeneration of two magnetic components. This model has been able to explain some of the main features of solar cycle such as, periodicity, North-South asymmetry of polarities, equatorward migration of sunspots, and the phase difference between the toroidal and dipolar magnetic fields.

Thus, the solar-magnetic activity is the result of interaction of turbulent convection with the rotational shear and global circulation and also with the magnetic-fields. However, there are no clear consensus about the mechanism for the poloidal-field generation which accounts for the observed polar-field reversal at sunspot maximum. Different models discussed above have their own sets of assumptions and restrictions, and the preferred dynamo model should account for all the multi-faceted characteristics of solar magnetic activity from small-scale to large scale, including the activity modulation.

In recent developments of solar dynamo models, in order to circumvent some of the crucial restrictions and flaws of existing models, and also to be able to explain activity modulations and also torsional oscillations, the feedback mechanism of magnetic fields on the differential rotation and global circulations has also been incorporated (Bushby, 2006; Passos, Charbonneau, and Beaudoin, 2012; Rempel, 2006).

## 1.5 Motivation and objectives of the thesis

Further detailed observational investigations are needed to develop the understanding of interplay of convection and magnetic fields; the feedback mechanism between magnetic field, solar rotation and global circulations; and how this feedback-loop modulates the strength of solar activity. In this thesis, we undertook three different kinds of investigations of properties of sunspots as described below:

- (a) **Study of global properties of sunspots:** Sunspots are unique proxy to understand the interaction between magnetic fields and convection.

As discussed above, sunspots are the surface manifestation of buoyantly rising magnetic flux within the convection zone. Thus, the sunspot structures are defined by the interaction between its rising magnetic flux tube and convective flows. Also observations (as well as simulations) of sunspots, suggests that the emerging magnetic flux alters the convective properties, producing larger and darker granules (Cheung, Schüssler, and Moreno-Insertis, 2007; Rempel *et al.*, 2009). Magnetic fields influence convection via the Lorentz force, which inhibits the convective motions across the field, which results in suppressed overturning motions within sunspots (see review by Stein, 2012). Hence, apart from the global dynamo models for the generation of large-scale magnetic fields within convection zone, magneto-convective simulations have been developed to generate realistic sunspot structures (Rempel and Schlichenmaier, 2011).

In pursuit of understanding of magnetoconvection at play during sunspot formation and evolution, we undertook the study of interdependence of sunspot properties such as sunspot area (equivalent to sunspot's magnetic flux) with the minimum brightness, the relative size of umbra and penumbra, and the variation of these properties over the course of solar cycle.

- (b) **Study of differential rotation using sunspots as tracers:** Differential rotation rates derived from magnetic tracers such as, sunspots are higher than that obtained for surface plasma (Beck, 2000). Further, various studies suggested that the differential rotation rate varies with the sunspot-activity, during lower activity period the rotation is more differential (Javaraiah, 2013). These observations suggest towards the possible back-reaction of magnetic-fields on solar rotation. Thus, it is important to study the difference in differential rotation rate from sunspot minimum to sunspot maximum, and possible dependence of rotation rate on the amount of magnetic flux and magnetic-field strength.

- (c) **Study of sunspot-group tilt-angles:** There are no clear consensus about the origin of bipolar inclinations, and the evolution of bipole polarities such as to regenerate poloidal field. Due to difficulty in estimation of bipolar tilt-angles owing to large amount of data-set involved, there have been less coherent investigations on bipolar tilt-angles. Only recently, few scientific groups undertook the study of bipolar active regions using high computational methods. To understand the origin of bipolar tilt-angles and to distinguish the valid mechanism of their origin among existing theories, it is necessary to study the relation of tilt-angle with other bipole properties such as bipole-size, their separation distance, and also with the phase of activity cycle.
- (d) **Extraction of sunspots parameters from solar images:** In order to undertake all the above mentioned investigations, we developed various programming modules to process solar images and derived required sunspot parameters. For this study we used the continuum images from MDI instrument on-board SoHO spacecraft (Scherrer *et al.*, 1995), since it provided continuous observations of Sun, for the complete solar cycle 23, and also it was not contaminated by atmospheric seeing.

## 1.6 Outline of the thesis

- (a) The Chapter 2 provides the description of MDI instrument and its data-products; we further provided the details of: procedure for the center-to-limb and stray-light correction of MDI Level-1.8 full-disk continuum images; automated methods developed for identification, characterization and tracking of sunspots from continuum images (Goel and Mathew, 2012, 2014); procedure for sunspot-group identification and bipole tilt-angle measurements.
- (b) The Chapter 3 discusses the observed properties of sunspots and the present understanding of sunspot structure. We presented the results of

sunspot intensity dependence on sunspot size, umbral shape, solar-cycle phase and the heliocentric position. We also investigated the penumbra-to-umbra area ratio dependence on various parameters.

- (c) The Chapter 4 provides details of observed differential rotation profile in the convective envelope from helioseismological methods. We discussed the obtained results on differential rotation rate of cycle 23 using sunspots as tracers which includes; dependence of rotation rate on sunspot size; the north-south asymmetry of rotation and its relation to the activity.
- (d) In Chapter 5, we looked for the validity of Joy's law from sunspot-group's tilt-angle data extracted from MDI continuum images. In pursuit of distinguishing the mechanism of origin of bipolar tilt-angles and its latitude dependence, we studied the bipolar tilt-angle and polarity separation distance dependence on size and the solar cycle phase, as well as the their north-south asymmetries.

# Chapter 2

## Materials and Methods

### 2.1 Introduction

For investigations of sunspot properties and related solar activity cycle studies as discussed in Section [1.5], we have used the continuum images and magnetograms provided by the *Michelson Doppler Imager* (MDI; Scherrer *et al.*, 1995) instrument on-board the SoHO space-craft, covering the period from May 1996 to April 2011. The large time series of data covering the entire solar cycle 23 and the rising phase of solar cycle 24, enables us to investigate the long-term variations of sunspots properties and differential rotation using sunspots as tracers. The advantage of this data is that it provided the uninterrupted view of sun during its operation for about 14 years (except for few months of data-loss during rising phase of cycle due to technical failure) and also it is free from effects of seeing caused by earth's atmosphere, hence a better spatial resolution than other ground-based counter telescopes.

To carry out the investigations for various scientific objectives outlined for this thesis, we developed four programming modules. The first module consist of procedures for the pre-processing and stray-light correction of MDI continuum images. In order to have consistent sunspots parameters like their area, intensity and coordinates observed for the whole cycle, we developed a

module for automated identification of sunspots from the continuum images and which also includes the procedures for characterization and cataloging of identified sunspots. Further to derive differential rotation rates using sunspots as tracers, we developed a procedure for the generation of tracking records of sunspots. For the study of tilt angles of sunspot groups, a programming module to identify sunspot bipoles from intensity images and to calculate the leading and following coordinates was developed.

The details of SoHO/MDI operation and its observables are discussed in Section [2.2]. The Pre-processing methods of MDI level-1.8 continuum images which includes the corrections for center-to-limb variation and stray-light and, the flat-fielding are described in Section [2.3]. The automated sunspot detection method and the description of generated sunspot catalog is in Section [2.4]. In Section [2.5], the procedure for automated tracking of sunspots is presented. The procedures for unsupervised grouping of sunspots and derivation of group parameters are described in Section [2.6].

## **2.2 SoHO/MDI instrument and observables**

The Solar and Heliospheric Observatory (SOHO) (Domingo, Fleck, and Poland, 1995) is a cooperative mission between European Space Agency (ESA) and National Aeronautics and Space Administration (NASA) to observe the Sun's internal stratification, dynamical parameters of corona and particle composition and energy of the solar wind. It was launched on 02 December 1995, however regular operations by SoHO only began from May 1996. It was placed in a halo orbit around the Sun-Earth L1 Lagrangian point and continuously pointing to the sun center. Three helioseismology instruments (GOLF VIRGO, MDI) have been providing data for the study of the structure and dynamics of the solar interior, from the very deep core to the outermost layers of the convection zone. The details of the scientific objectives and payloads of SoHO can be found in Fleck, Domingo, and Poland (2011).

The Michelson Doppler Imager (MDI) instrument was designed to probe

the solar interior by measuring the photospheric manifestations of solar oscillations (Scherrer *et al.*, 1995). The MDI instrument images the Sun on a  $1024 \times 1024$  CCD camera through a series of increasingly narrow spectral filters sampling around magnetically sensitive Ni I 6768 Å mid-photospheric absorption line with  $g = 1.426$ . MDI made high-resolution and full-disk observations (with a resolution of 1.25 arc-sec per pixel and 4 arc-sec per pixel, respectively. The theoretical diffraction-limited resolution of the telescope is 1.25 arc-sec per pixel.) of line-of-sight velocity (Dopplergrams), line-of-sight magnetic field (magnetograms), line intensity, continuum intensity, and high resolution transverse velocity. Following is the description of the MDI instrument and the derived observables<sup>1</sup>.

MDI uses a refracting telescope, cascade of filters and a CCD camera. The instrument consists of two physical enclosures: the optics package (OP) and the electronics package (EP). The OP contains all the optical components: the telescope, the image stabilizers, the shutter, the beam distribution systems, spectral and polarizing filters and the CCD camera. The Figure [2.1] shows the optical layout of the MDI. The EP consists of the circuit boards for instrument control and communications, the image processor and the power supply.

The filter system consists of the front window, the blocker, the Lyot filter and two tunable Michelson interferometers. The blocking filter is 8 Å wide and the Lyot FWHM is 465 mÅ. Two Michelsons (FWHM of 188 mÅ and 94 mÅ) are tuned with rotating waveplates. MDI provides five narrow-band filtergrams of passband 94 mÅ FWHM, equally spaced by 75 mÅ spanning the 377 mÅ tuning range around the Ni I 6768 Å mid-photospheric absorption line. They are labeled as F<sub>0</sub>-F<sub>4</sub>, where F<sub>0</sub> is divided over two bands taken near the continuum, on either side of the line, F<sub>1</sub> and F<sub>4</sub> are centered on the wings and F<sub>2</sub> and F<sub>3</sub> centered about the core of the center-of-disk Ni line. The Figure [2.2] shows the Ni I 6768 Å profile and the five representative MDI

---

<sup>1</sup>[http://soi.stanford.edu/science/obs\\_prog.html](http://soi.stanford.edu/science/obs_prog.html)

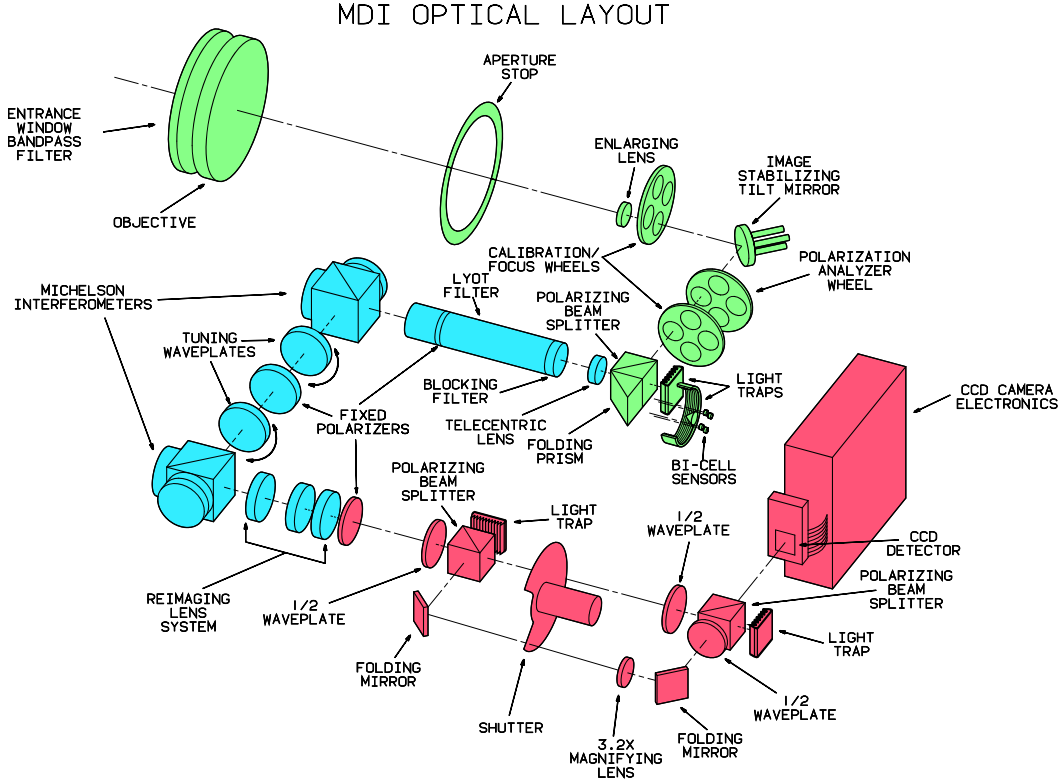


**Figure 2.1:** The optical layout of MDI instrument on-board SoHO spacecraft.

filter transmission profiles. Hence, different part of the line spectra and with different polarization that are used for the reconstruction of both white-light images and magnetograms. Due to insufficient telemetry, the observables were computed from these filtergrams on-board.

The instrument does not sample the true continuum at  $F_0$ . Instead, a proxy continuum intensity is computed by combining the five filtergrams in the following way:

$$I_c = 2F_0 + I_{\text{depth}}/2 + I_{\text{ave}}, \quad (2.1)$$

where  $I_{\text{ave}}$  is the average of the four filtergrams,  $F_{1-4}$  and  $I_{\text{depth}}$  is the line depth (continuum intensity minus the line-center intensity) is estimated from the four filtergrams by:

$$I_{\text{depth}} = \sqrt{2 \left( (F_1 - F_3)^2 + (F_2 - F_4)^2 \right)} \quad (2.2)$$

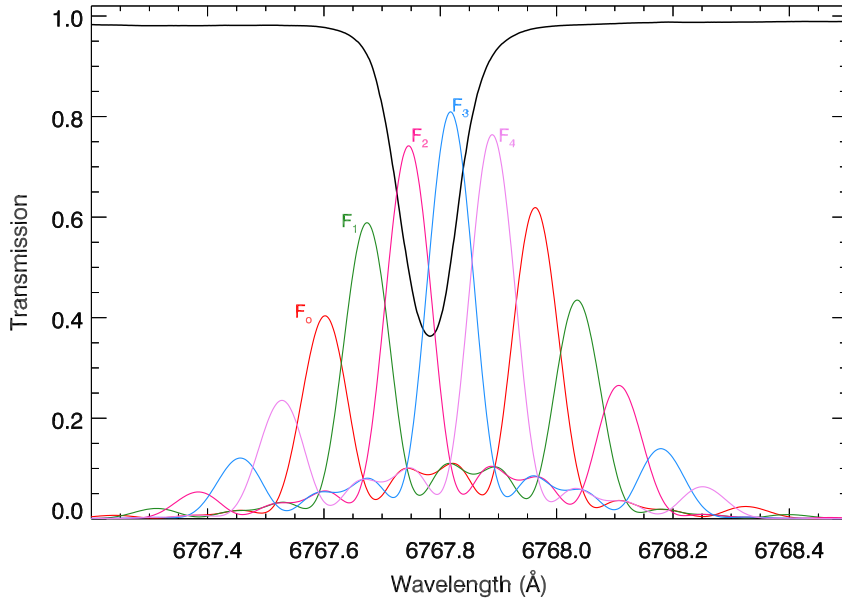


**Figure 2.2:** The representation of Ni I 6768 Å line profile (black) and the five filtergrams ( $F_0$ - $F_4$ ) of MDI around the line.

The Doppler velocity is estimated from the index  $\alpha$ , which is the ratio of differences of filtergrams  $F_1$  through  $F_4$  using a calibrated lookup table.

$$\begin{aligned} \alpha &= (F_1 + F_2 - F_3 - F_4) / (F_1 - F_3), \text{ if numerator } > 0 \\ &= (F_1 + F_2 - F_3 + F_4) / (F_4 - F_2), \text{ if numerator } \leq 0 \end{aligned} \quad (2.3)$$

A longitudinal magnetogram was constructed by measuring the Doppler-shifts calculated from the filtergram components taken separately in right-hand (RCP) and left-hand circularly polarized (LCP) light. The difference between LCP and RCP doppler shifts is a measure of the Zeeman splitting and is roughly proportional to the magnetic flux density, the line-of-sight component of magnetic field averaged over the resolution element.

We used the full-disk continuum images (cadence of 60s) from the hourly data sets of Level-1.8 having calibrated physical observables. In the later years of operation of MDI usually there was one continuum image per hour but not in every hours. The full-disk image of the Sun has a plate scale of 2 arcsec per

pixel and a spatial resolution of 4 arcsec. The full-disk magnetograms were recorded every 90 minutes *i.e.*, 16 images per day during the MDI observations period.

### 2.3 Pre-processing of SoHO/MDI continuum images

To attain precise sunspot physical parameters it is necessary to do some pre-processing to the Level-1.8 MDI white-light continuum images, which includes corrections for stray-light and center-to-limb variation, and flat-fielding.

Solar images in the visible wavelength range show that the photospheric intensity falls off significantly towards the limb due to increasing radiation optical depths towards the limb. This phenomenon is known as the limb-darkening or as center-to-limb variation (CLV) (Foukal, 2004). Before quantitative analysis, solar images require intensity re-normalization to compensate for the effect of radial limb-darkening. This re-normalization is achieved by fitting a quiet-photospheric radial intensity profile. This radial profile is obtained by calculating median radial intensities at radial sample points (Section [2.3.1]).

All telescopes, including space-based SoHO/MDI instruments images suffer some degradation due to optical scattering. The principal scattering mechanisms in a space-based telescope include diffraction through the aperture or any obscuration in the beam path, dust or irregularities on the mirror, and reflection or scattering in the detector at the focal plane (DeForest, Martens, and Wills-Davey, 2009). All these effects cause contamination of solar images with a halo of stray-light, significant fraction of Sun's brightness is scattered across the entire imaging plane. Hence, stray-light reduces the contrast of the image, making bright regions appear dimmer and faint regions brighter than the factual intensity. Accounting for the effects of stray-light on solar images is necessary for their proper quantitative analysis and interpretations, since contrast of magnetic feature is an important diagnostic to their thermal structure.

Point-Spread Function (PSF) is the normalized intensity distribution of the image produced by an instrument when viewing an ideal point source of light. Such stray-light contribute to forming broad, shallow wings on the PSF of the instrument. The clean image can be restored by deconvolving the PSF (that account for non-ideal contributions due to instrumental stray-light and imperfections) from the contaminated image (Starck, Pantin, and Murtagh, 2002). For spaceborne instruments stray-light can be characterized and removed by estimating the instruments PSF using information from the images themselves. Specifically, the PSF is estimated from the distribution of intensity about the boundary for example, at the solar limb, across the occulting bodies like the Moon or Venus or Mercury over the Solar disk during their respective transits (DeForest, Martens, and Wills-Davey, 2009; Mathew, Zakharov, and Solanki, 2009; Mathew *et al.*, 2007; Poduval *et al.*, 2013; Wedemeyer-Böhm, 2008; Wedemeyer-Böhm and Rouppe van der Voort, 2009; Yeo *et al.*, 2014).

Further, to derive meaningful sunspot intensity parameters, the flat-fielding is required to remove inhomogeneities in the field illumination which is due to anomalies in the optical path, such as specs of dust on the optical surfaces, sensitivity variances between pixels in the CCD, and illumination variations within the optical system (vignetting) (Berry and Burnell, 2005). ‘Flat-field frames’ are used to correct for the combined optical-system and CCD throughput at each pixel so that each pixel on the CCD would respond equally to a source with the same photon flux.

The details of pre-processing methods adopted for each correction is described in the following sections.

### **2.3.1 Stray-light and limb-darkening removal**

To remove stray light, we assume that each observed image is the convolution of a point spread function with an unknown true image. To correct the MDI continuum images for the stray light, we estimated the point spread

function (PSF) of the instrument by making use of the residual intensity outside the solar limb called as aureole, the details of this method are available in Martínez Pillet (1992); Mathew *et al.* (2007).

For MDI continuum images Mathew *et al.* (2007) found that the stray-light contamination can be best represented by the PSF function consisting of three Gaussians and one Lorentzian component. The PSF ( $\psi$ ) kernel is represented as:

$$\psi(r) = \sum_{i=1}^3 m_i a_i \exp\left(-\frac{r^2}{b_i^2}\right) + M \frac{A}{B^2 + r^2}, \quad (2.4a)$$

$$a_i = \frac{2}{\sin^2 R b_i^2}, \quad (2.4b)$$

$$A = \frac{2}{\log \frac{4}{kk} \sin^2 R}, \quad kk = B^2 \sin^2 R. (0.0047)^2, \quad (2.4c)$$

$$M + \sum_{i=1}^3 m_i = 1.0, \quad (2.4d)$$

where,  $r$  is the radial distance from the solar disk center,  $R$  is the solar disk radius in radians,  $m_i$  and  $M$  are the weights of the Gaussian and Lorentzian components respectively;  $b_i$  are Gaussian width parameters,  $B$  is the Lorentzian width parameter;  $A$  is the normalization constant for the Lorentzian part of the spread function, and  $a_i$  are normalization constants for Gaussian components. The PSF parameters are obtained in units of solar radii (Martínez Pillet, 1992).

Thus, estimation of PSF parameters consists of estimation of weights and widths of three Gaussian components, and weight parameter of Lorentzian function (a fixed width of 40 arcsec is considered here for Lorentzian). The CLV is best represented by a fifth order polynomial of  $\cos \theta$  ( $\theta$  is the angular distance from the Sun center) (Neckel and Labs, 1994).

$$\frac{I(\mu)}{I_0} = \sum_{i=0}^5 c_i \mu^i, \quad \sum_{i=0}^5 c_i = 1.0, \quad (2.5)$$

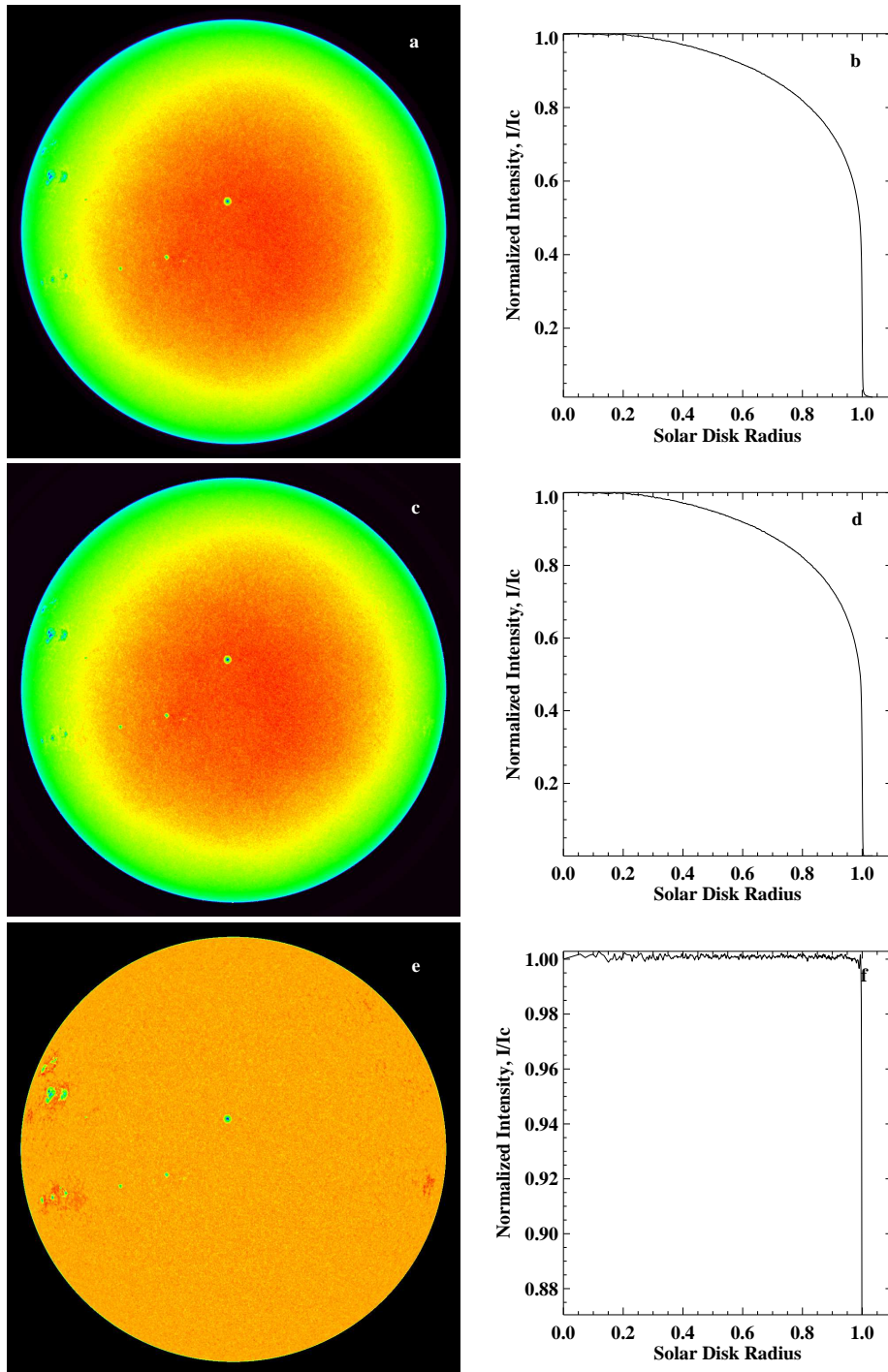


**Figure 2.3:** The continuum image and corresponding intensity radial profiles: for original MDI Level-1.8 continuum image (a-b); after correction for stray-light (c-d) and; after stray-light and center-to-limb variation correction (e-f). Here, the intensity profiles are normalized to the median intensity around the solar-disk center.

where,  $\mu = \cos \theta$ . The initial coefficients for the fitting were taken from Pierce and Slaughter (1977) *i.e.*,  $c_{0-5} = [0.353, 1.39, -2.148, 2.951, -2.206, 0.660]$ .

From full-disk continuum images, the radial profiles (azimuthally averaged) were generated by taking the median intensity in each annular ring from disk-center to regions beyond solar limb. The PSF parameters and the CLV coefficients were estimated by iteratively fitting this observed radial profile on the interval  $r \in [0.0, 2.0]$  (normalized to solar-disk radius,  $R$ ) with the computed profile. The intensity values of computed profile were calculated by the convolution of the guess PSF kernel and the CLV profile.

For MDI instrument, the instrumental scattered light contamination has increased with the aging (Mathew *et al.*, 2007), hence we estimated PSF for each observation year. Around June month of each year, MDI continuum intensity images the solar-disk occupies less CCD image plane and we get better coverage of outside-limb intensity. Hence, few images from June month from each observation year were selected and their intensity radial profiles were computed. The CLV and PSF parameters were obtained by fitting these radial profiles using the above functional forms (Eqns. [2.4a] & [2.5]). For each year, using the fitted parameters from number of June images, we calculated the average CLV and PSF parameters for that year. A given MDI continuum image can then be restored by deconvolution with the model PSF, where the PSF parameters for respective image was obtained by interpolating the derived yearly PSF parameters at the time of its observation. In this manner, all the images from May 1996 to April 2011 were corrected for stray-light. These restored images were then corrected for center-to-limb variation using the average CLV coefficients derived for each year. Tables 2.1 & 2.2 lists all the yearly values of obtained PSF parameters and CLV coefficients respectively.

Figure [2.3] shows the original MDI Level-1.8 full-disk continuum intensity image and its radial intensity profile (Fig [2.3](a-b)). The Figure [2.3](c-d) shows the stray-light-corrected continuum image and the corresponding radial profile (normalized to disk-center intensity) having flat off-limb intensity at

Year	julian day	$R_s$	$m_1$	$b_1$	$m_2$	$b_2$	$m_3$	$b_3$	M	B
1996	2450276.8	953.8004	0.7856	0.0021	0.0866	0.0062	0.0230	0.0228	0.1048	0.0414
1997	2450649.4	953.8724	0.7879	0.0022	0.0807	0.0067	0.0242	0.0225	0.1072	0.0412
1998	2450983.9	954.3825	0.7621	0.0020	0.0997	0.0064	0.0255	0.0226	0.1127	0.0392
1999	2451375.2	952.4837	0.7079	0.0015	0.1392	0.0052	0.0293	0.0199	0.1236	0.0417
2000	2451734.8	952.1870	0.7135	0.0020	0.1259	0.0059	0.0270	0.0204	0.1336	0.0418
2001	2452111.4	952.4825	0.6770	0.0016	0.1354	0.0050	0.0330	0.0166	0.1546	0.0411
2002	2452459.8	952.6902	0.6877	0.0017	0.1274	0.0056	0.0287	0.0178	0.1562	0.0396
2003	2452826.6	952.1467	0.6797	0.0019	0.1175	0.0055	0.0324	0.0163	0.1704	0.0418
2004	2453197.8	952.0581	0.6311	0.0017	0.1463	0.0051	0.0340	0.0167	0.1887	0.0417
2005	2453553.9	952.0089	0.6450	0.0021	0.1190	0.0058	0.0278	0.0168	0.2083	0.0419
2006	2453912.9	952.2361	0.6215	0.0019	0.1227	0.0055	0.0278	0.0145	0.2280	0.0410
2007	2454284.4	952.6815	0.6207	0.0021	0.1023	0.0063	0.0260	0.0134	0.2510	0.0416
2008	2454647.9	952.8777	0.6070	0.0021	0.0739	0.0060	0.0437	0.0116	0.2754	0.0416
2009	2455006.4	953.7741	0.5354	0.0015	0.1158	0.0045	0.0408	0.0123	0.3080	0.0414
2010	2455364.0	953.9404	0.5142	0.0016	0.0983	0.0044	0.0437	0.0096	0.3437	0.0400

**Table 2.1:** Yearly values of obtained PSF parameters,  $R_s$  is solar disk radius in arc-sec,  $m_{1-3}$  and  $b_{1-3}$  are respectively the weights and widths of three Gaussian functions and  $M$  and  $B$  are the weights and widths of Lorentzian function respectively. The width parameters are normalized to solar disk radius,  $R_s$ .

Year	$c_0$	$c_1$	$c_2$	$c_3$	$c_4$	$c_5$
1996	0.3439	1.2941	-1.6870	2.0028	-1.2379	0.2844
1997	0.3289	1.4693	-2.3483	3.1383	-2.1806	0.5922
1998	0.3554	1.1905	-1.2409	1.0954	-0.3952	-0.0051
1999	0.2379	2.4915	-6.3807	10.1934	-7.7618	2.2196
2000	0.3707	0.9837	-0.0032	-1.8986	2.8049	-1.2573
2001	0.2515	2.4861	-6.2190	9.7737	-7.3853	2.0930
2002	0.3206	1.6769	-2.8036	3.2677	-1.6868	0.2252
2003	0.3566	1.3290	-1.6544	1.5751	-0.6077	0.0018
2004	0.2678	2.3216	-5.6067	8.7549	-6.7049	1.9673
2005	0.3597	1.2534	-1.4351	1.2909	-0.4697	0.0013
2006	0.3449	1.4381	-2.2332	2.9903	-2.1427	0.6028
2007	0.3700	1.2540	-1.6689	2.2620	-1.8132	0.5964
2008	0.3772	1.3026	-1.8934	2.7753	-2.3192	0.7577
2009	0.2206	3.1814	-9.6132	17.1129	-14.6412	4.7395
2010	0.2647	2.6898	-7.6008	13.3972	-11.4977	3.7466

**Table 2.2:** Yearly values of obtained CLV coefficients,  $c_{0-5}$

zero value. Further after applying the correction for center-to-limb variation to the stray-light-corrected continuum image, the intensity radial profile is flat at nearly the value of 1 (Fig [2.3](f)). After stray-light and limb-darkening

removal from the continuum image, in Figure [2.3](e) the sunspots and pores have better contrast.

To generate the radial intensity profile, the prior knowledge of solar-disk radius (in pixel) is required. But, this information was erroneous in the MDI FITS image headers for years 2007 onward. Hence, we first identified the solar-limb for all available images by using second-derivative method.

### 2.3.2 Flat-fielding

Over the period of MDI operations, the non-uniformity in detector sensitivity due to the degradation of the instrument has increased considerably in the continuum images (Goel and Mathew, 2014; Potts and Diver, 2008). In the flat-field-correction procedure, we have utilized all available stray-light and CLV-corrected continuum images to produce flat-field frames. For each Carrington rotations over the 14 years of MDI operation, we generated a master-flat-field image by median-combining the corrected images of that period. These master-flat-field frames contains the variations in illumination due to variations within the optical system. Dividing the continuum image by the normalized flat-filed frame will correct the image for these variations. We developed the following procedure for obtaining the master-flat-field frame and correcting the continuum images using these flat-images:

- (a) **Masking the active regions:** To generate the flat-frames, it is necessary to avoid the contribution of the high contrast solar features, such as sunspots and facular regions, which are darker and brighter regions than quiet-photosphere respectively. Hence, for each continuum image we statistically calculated two threshold intensities from their histogram, one lower threshold to mask regions having intensity below the maximum of penumbral intensity and other higher threshold to mask facular regions. But as the instrument aged, the non-uniformity in the image increased, which resulted in reduction in intensity at some locations on the CCD plane to almost the normal penumbral intensity values (Figure 2.4(c)).

Hence, to avoid removal of large portions of images during masking via thresholding, we chose a bit lower value of the first threshold for masking sunspots. Further, we dilated the masked regions in order to mask the left-out penumbral regions completely. The masked regions and the off-limb regions were set at the value of zero.

- (b) **Median-combined-master-flat frame:** For each Carrington rotation (CR), we generated the master-flat frame by median combining the corresponding set of masked continuum images, *i.e.* each pixel of the master-flats image contains the median value of the intensity at that pixel of the set of masked continuum images. During the median combine, the pixels having the zero value were not counted. Further, each master-flat frame was median filtered to remove small scale structures and normalized with its global median intensity value.
- (c) **Flat-fielding:** All the MDI continuum images according to their Carrington rotation number, were then normalized with their respective master-flat image. Further, the quiet-Sun intensity value was established from the image histogram as an intensity with the highest pixel count, which was used to normalize the corrected continuum images (Steinegger *et al.*, 1996; Zharkov, Zharkova, and Ipson, 2005).

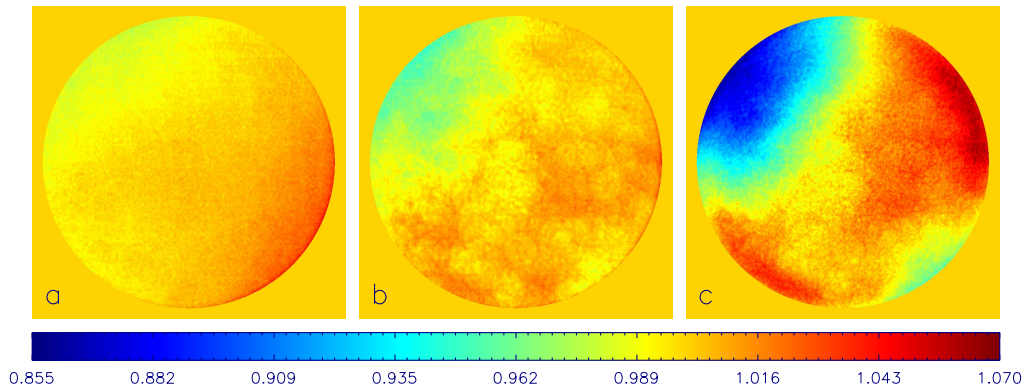


**Figure 2.4:** Flat field images for Carrington rotation No. (a) 1910 (year 1996), (b) 2004 (year 2003) and (c) 2080 (year 2009). The change in uniformity due to the instrument is clearly visible in these images.

Figure [2.4] shows the master flat-field images for three different Carrington rotations during the operation period of the SoHO/MDI. At the start of operation in 1996 the flat-field was nearly uniform, but it started developing small scale structures over the period. By the year 2008, some portions of the image have the intensity values similar to penumbral region intensities (Figure 2.4(c)).

## 2.4 Automated sunspot detection and cataloging

In recent years, due to increasing amount of available solar data volumes, there are advances in the application of image processing techniques to the automated detection of various solar features for example, active regions, coronal holes, filaments, CMEs, and coronal dimmings. The consistent and faster computation of solar features parameters facilitates in the quantitative analysis, interpretation, and also in space weather monitoring and prediction. Aschwanden (2010) provides a comprehensive review of techniques used to detect a multitude of solar features. The various automated feature-recognition modules adopted for the Solar Dynamics Observatory (SDO) science products are discussed in (Martens, Attrill, and *et al*, 2012).

Sunspots were the first solar feature to be cataloged and have been routinely measured by multiple observatories over the last four centuries. The sunspots are visible on the solar surface as dark features with a dark core called the umbra and surrounded by a lighter region called the penumbra. Image segmentation is defined as partitioning an image into non-overlapping regions based on the intensity or texture. In case of identification of sunspots from white-light images, the essential image segmentation problem is to identify dark sunspot regions from brighter background (photosphere).

There are several methods available in literature for sunspot detection from solar images (Aschwanden, 2010; Verbeeck, Higgins, and *et al*, 2013). These methods involve different image processing techniques, for example, intensity threshold, edge detection, morphological operations, region growing

and merging, fuzzy clustering, neural networking, wavelet, phase congruency *etc* (Beck and Chapman, 1993; Colak and Qahwaji, 2008; Curto, Blanca, and Martínez, 2008; Djafer, Irbah, and Meftah, 2012; Feng *et al.*, 2014; Fonte and Fernandes, 2009; Zharkov *et al.*, 2005). A brief discussion on some of these methods are available in Section [2.4.1].

The robust automated detection and characterization procedure of sunspots is a necessary tool to process large archives of full-disk SoHO/MDI continuum images, approximately covering 5 images per day for about 14 years. To achieve this we developed programming modules which consists of 1) identification of the umbra-penumbra and penumbra-photosphere boundaries from continuum images using a level-set method and storing the identified sunspot regions as image objects (Section [2.4.3]), 2) characterization algorithm to derive the important sunspot physical parameters of extracted sunspots (Section [2.4.4]), and 3) making of catalog of identified sunspots of solar cycle 23 (Section [2.4.5]). The further details of the detection and cataloging of SoHO/MDI sunspots is available in the published article Goel and Mathew (2014). The catalogs from two sources; Solar Feature Catalogues (SFC<sup>2</sup>; Zharkov, Zharkova, and Ipson (2005); Zharkova, Aboudarham, and *et al* (2005)) and STARA<sup>3</sup> (Watson, Fletcher, and Marshall, 2011), were also generated from the MDI data using the automated detection techniques. But, these catalogs did not used stray-light-corrected images for sunspot identification.

### 2.4.1 Review of sunspot detection methods

The simplest approach for sunspot detection is to set threshold intensities for umbra-penumbra and penumbra-photosphere boundaries. Various groups adopted different techniques to derive these threshold intensities. Brandt, Schmidt, and Steinegger (1990); Grossmann-Doerth and Schmidt

---

<sup>2</sup><ftp://ftpbass2000.obspm.fr/pub/helio/mdiss/>

<sup>3</sup><http://www.nso.edu/staff/fwatson/STARA>

(1981); Steinegger *et al.* (1990) estimated the thresholds from the brightness distribution of several sample of sunspot regions. Beck and Chapman (1993) obtain intensity profiles of sunspots from continuum images and chosen the intensities at the point of maximum slope as thresholds for sunspot boundaries. Mathew *et al.* (2007); Pettauer and Brandt (1997); Steinegger *et al.* (1996) generated the cumulative histogram of number of sunspots and the threshold intensity is derived from intersections of linear fits to the curves in the histograms. However, it is not true that in a given image, all sunspots will have the same intensity value at boundaries, which can then affect the calculated sunspot area values and hence inferences drawn from them (Jones *et al.*, 2008).

Another approach for segmentation is to use the gradient information at the sunspot boundaries, which is termed as edge-detection (Gonzalez and Woods, 2008). From the use of edge-operators on white-light images, the resultant gradient map does not clearly identifies the sunspots boundaries. This is due to the fact that sunspot do not have uniform and sharp gradient at its boundaries and hence the map does not provide the connected edges/boundaries. Moreover, the gradient map often consists of spurious edges due to noise. Preminger, Walton, and Chapman (2001) use the gradient information along with the threshold intensity. But, even setting a threshold to the gradient/edge map will may remove false contributions but this does not give connected boundaries and further computational techniques are required to properly segment the sunspot regions (Győri, 1998; Zharkov *et al.*, 2005). For example, in Zharkov, Zharkova, and Ipson (2005), the initial segmentation is obtained using a Sobel edge-detection technique on the photospheric images. A global threshold segments the edges and the existing gaps are filled with morphological operators, followed by dynamic thresholding to extract the sunspot umbra and penumbra.

Segmentation based on morphological tools are also used to extract sunspots from white-light images (Curto, Blanca, and Martínez, 2008; Watson

*et al.*, 2009). Curto, Blanca, and Martínez (2008) generates various sunspot candidate maps using a top-hat transformation of different size of structure elements (SE) followed by thresholding. Then, a region-growing procedure is applied to group the candidate sunspot regions. Watson *et al.* (2009) use the erosion and dilation morphological operations to identify the sunspot candidates regions. Advantage of this particular method is that this can be applied to continuum images without CLV correction. However, the above two methods are only capable of extracting whole sunspot regions without distinguishing the umbral and penumbral regions.

Other computationally extensive methods are also available. A Bayesian technique for active region and sunspot detection and labeling was developed by Turmon, Pap, and Mukhtar (2002). Colak and Qahwaji (2008) applies intensity threshold and region growing technique for sunspot region detection and artificial neural network for their classification according to the McIntosh classification system (McIntosh, 1990). Fonte and Fernandes (2009) applied fuzzy set theory for determination of umbra and penumbra boundaries.

## 2.4.2 Active contours and level set methods

Active contour models (ACM) is one of the most widely used image segmentation technique (Blake and Isard, 1998). Its classical version based on dynamic curves called as “*snakes*” was first introduced by Kass, Witkin, and Terzopoulos (1988), which has been further developed by various innovative approaches. The basic idea of ACM is to iteratively deform (or evolve) a closed curve defined in the image plane according to some mathematically defined constraints from the given image, to detect the feature of interest in the image. These constraints are basically some defined energy functionals based on some of the properties of image or its features, and also that of the curve itself. It is designed such that the minimization of this energy balance through curve deformation, leads the curve to approach and take the shape of boundary of the feature of interest in the given image.

ACM can use diverse image properties like gradient, texture, color, grey-level, region statistics *etc.* in accordance to the requirement and suitability with the given image. ACM models are broadly categorized into two types according to the nature of the image-driven force chosen to evolve the curve: edge-based models and region-based models. Edge-based segmentation partitions the image utilizing the discontinuity of desired property between different sub-regions of the image. While region-based segmentation looks for uniformity within sub-regions, based on desired property *e.g.*, intensity, texture, color, *etc.* A benefit of dynamic contours as image segmentation method is that they divide an image into sub-regions with continuous boundaries, while edge-detectors often results in dis-connected boundaries.

The level-set formulation of active contours extends the task of moving curves to that of moving surfaces, which adds certain advantages to the traditional active contours (Osher and Fedkiw, 2003; Osher and Sethian, 1988; Sethian, 1999). The basic idea is to represent propagating contours as the interface of an implicit function defined in a higher dimension and to evolve this function according to a partial differential equation (PDE). Here, the curve,  $C$ , are represented by the zero-level-set of a two-dimensional function  $\phi(t, x, y)$  called as level-set function (LSF) defined in an image plane with coordinates  $(x, y)$  and  $t$  is an artificial time such that:

$$\begin{aligned} C(t) &= \{\phi(x, y) | \phi(t, x, y) = 0\} , \\ \text{Inside}(C(t)) &= \{\phi(t, x, y) < 0\} , \\ \text{Outside}(C(t)) &= \{\phi(t, x, y) > 0\} . \end{aligned} \tag{2.6}$$

The LSF is evolved using the speed function  $F$  in the following way:

$$\frac{\partial \phi}{\partial t} + F |\nabla \phi| = 0 . \tag{2.7}$$

For image segmentation, the function  $F$  depends on the image data and the  $\phi$  (Osher and Fedkiw, 2001).

### 2.4.3 Identification of sunspots

In our automated sunspot detection module, we implemented a level-set method proposed by Zhang *et al.* (2010) namely the *selective binary and gaussian filtering regularized level set* (SBGFRLS) method. In this method we construct a region-based signed-pressure force function (SPF) to evolve the level-set function. For a given image,  $I$ , we construct the SPF function as follows:

$$\text{SPF}(I(x)) = \frac{I(x) - \frac{c_1+c_2}{2}}{\text{Max}\left(\left|I(x) - \frac{c_1+c_2}{2}\right|\right)} \quad (2.8)$$

where,  $c_1$  and  $c_2$  are the average intensities inside and outside the contour, respectively. Thus, SPF utilize the statistical information inside and outside the contour, such that it has opposite signs around the object boundary. The level-set formulation for this method is:

$$\frac{\partial \phi}{\partial t} + \text{SPF}(I(x)) \cdot \alpha |\nabla \phi| = 0 \quad (2.9)$$

where,  $\alpha$  is a constant velocity term to increase the propagation speed and,  $\nabla \phi$  is the gradient of  $\phi$ . Since, the SPF has opposite signs around the object boundary, it directs the direction of propagation of the zero-level-set, while the speed is controlled by the gradient. Thus this method has the ability to detect both the exterior and interior boundaries irrespective of the position of the initial contour in the image. This property makes it a suitable method for the umbra-penumbra detection.

We have developed this SBGFRLS method for the detection of umbra-penumbra and penumbra-photosphere boundaries from the SoHO/MDI full-disk continuum images. For the extraction of sunspots we have used stray-light-corrected, center-to-limb-variation-corrected and flat-fielded continuum images (Section [2.3]). In the first step, we first identified the umbra-penumbra boundaries using the protocol as listed below. Once, the umbral regions (and pores) are extracted and saved as binary object, we first replaced the umbral

pixels with the value of 1, and then used the same protocol for identification of penumbra-photosphere boundary from this modified continuum image. The basic protocol for sunspot (umbra or penumbra) region identification is as follows.

- (a) Using the given image,  $I(x, y)$ , define a level-set function;

$$\phi(x, y) = I(x, y) - T . \quad (2.10)$$

where,  $T$  is a statistically chosen threshold intensity such that the region of interest attains negative values in the  $\phi$ .

- (b) Compute the  $c_1$  &  $c_2$ , where,

$$\begin{aligned} c_1 &= \text{Average}(\phi(x, y) < 0), \\ c_2 &= \text{Average}(\phi(x, y) > 0) . \end{aligned} \quad (2.11)$$

- (c) Compute Signed-pressure function (SPF) as given in Eqn [2.8].  
 (d) Calculate the gradient of LSF, *i.e.*,  $\nabla\phi$ .  
 (e) Obtain the new LSF (based on Eqn[2.9]:

$$\phi_1(x, y) = \phi(x, y) + (\alpha * SPF(x, y) * \nabla\phi(x, y)) . \quad (2.12)$$

- (f) Regularize the new LSF by convolving with a Gaussian function:

$$\phi_1(x, y)^* = \phi_1(x, y) * G_\sigma . \quad (2.13)$$

- (g) Check whether the evolution of the LSF has converged using the length of the zero-level-set curve. If not, then continue with the first step using the  $\phi_1(x, y)^*$ .

The first-level detection for the umbra results in contour around the umbral regions as well as the pores, since pores by definition are naked umbra

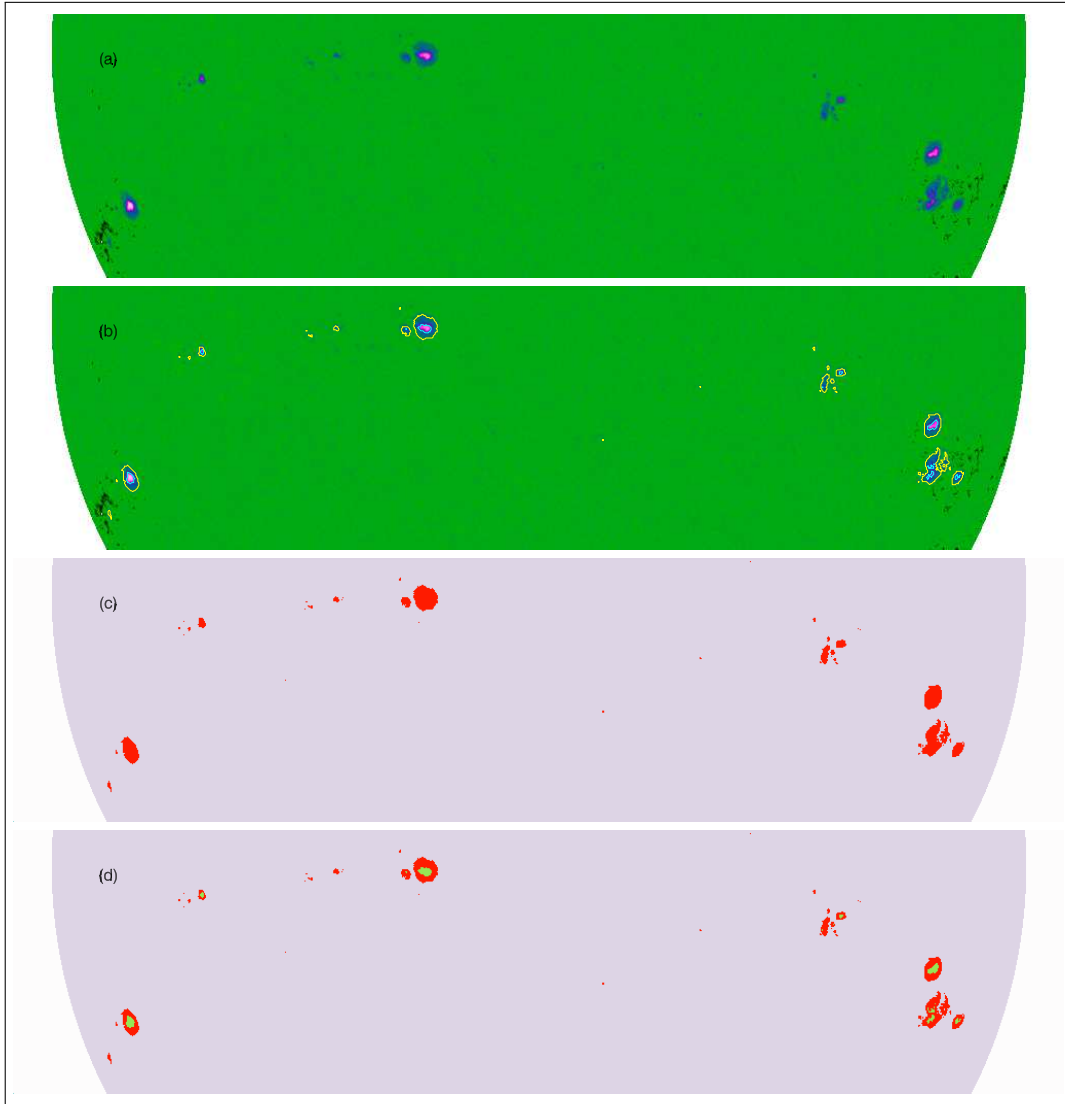


**Figure 2.5:** (a) Fragment of SoHO/MDI full-disk continuum image of 11<sup>th</sup> May, 2002. (b) Detected sunspots and pores boundaries in yellow contours and, umbrae contours in cyan color. (c) extracted sunspot and pore regions are shown in red color and, (d) Overlapped the umbral regions in green color.

without surrounding penumbra. These extracted regions pixels were replaced by maximum value of the image, and the detection code was run again in order to find the contours at penumbral boundaries. Since, this detection method can locate both interior and exterior boundaries, the second-level detection for penumbra resulted in boundaries at both penumbra-photosphere and umbra-photosphere boundaries. Hence, before using the extracted regions for their

characterization (Section[2.4.4]) we first did some filtering of extracted regions from each image for 1) separate the pores from umbral regions, 2) assign the umbra(s) to their respective penumbra region, and 3) remove the regions close to the limb.

To achieve this, the basic idea we incorporated was to look for the criteria of containment. First, in second-level detection results, apart from the sunspot regions, we get two spurious regions, first, the umbral regions, second the regions with quiet-photospheric intensity region within the sunspot. So we identified these regions by checking their containment within sunspots region. After containment check, the identified umbral regions were removed, while second type of regions were kept to be incorporated during the characterization of their respective sunspot. Then on second-stage, we applied the containment check on combined results of the first-level detection with the filtered sunspot regions of second-level. In this stage, we filtered pores from the umbral regions and assigned the umbral regions with their respective sunspot regions. Lastly, we removed those sunspots and their respective umbra (if any) and pores that consists of pixels in the range of about ten-pixels inwards from the solar-limb. Using a naming convention with separate labels for umbra, sunspot and pores we saved these extracted regions for deriving the physical parameters as discussed in the next section. Figure [2.5] shows an example of the sunspot identification results from a MDI continuum image. Figure [2.5(b)] shows the contours of umbrae-penumbra and penumbra(pores)-photosphere boundaries separately. The extracted sunspot and pore regions are shown in red-filled color in Figure [2.5(c)] with overlapped umbral regions in green color in Figure [2.5(d)].

#### **2.4.4 Characterization of sunspots**

To facilitate the study of sunspot properties and other solar activity related studies of this thesis, we derived various important physical parameters of identified sunspots. These parameters include, intensity, area, position

coordinates *etc.* For their calculations we used some of the image parameters available in their respective FITS header file, such as, solar-disk center position in image:  $x_c$ ,  $y_c$ ; disk radius in pixel:  $R_p$ ; semi-diameter in radians:  $R_r$ ; plate-scale:  $ps$ ; heliographic latitude and longitude at the solar-disk center:  $B_0$ ,  $L_0$ ; the position angle between the geocentric north pole and the solar rotational north pole measured eastward from geocentric north:  $P_0$ ; date and time of observation, and carrington rotation number ; CR. From the level-set automated procedure described in previous Section [2.4.3], we got the full-sunspot regions, umbral regions and the pore regions as a result. From each sunspot region, we first separated the pixel information of penumbral region using the full-sunspot and umbral region's pixel informations. We derived parameters for each type of region that is for umbra, penumbra and pores separately. Following is the description of some of the parameters derived from the sunspots extracted:

- (a) **Geometrical area:** Geometric area ( $gar$ ) is the sum total of the fraction of each pixel covered in the region. That is for a region with  $n$  pixels:

$$gar = \sum_{i=1}^n FRA_i \quad (2.14)$$

where, FRA is the array having information of fraction value of each pixel within the region. That is, if a pixel is completely within the identified region its corresponding FRA will be equal to 1.

- (b) **Centroid:** For each umbrae, penumbra, and pore region we derived its inverse-intensity-weighted centroid coordinates. To compute the centroid, we first identified the pixels which contributes more than 20%, that is having  $FRA \geq 0.2$ . The centroid image-coordinates of a given region were then calculated using the inverse-intensity weights of those selected pixels. Further, using the heliographic coordinates computation methods described in (Smart and Green, 1977; Thompson, 2006) we calculated Carrington and Stonyhurst heliographic coordinates of the

centroid.

- (c) **Intensity:** For each region (umbra, penumbra, and pores separately) we calculated the minimum, maximum and the average intensity. Only the pixels having their FRA  $\geq 0.2$  contributed to the maximum and average intensity calculations.
- (d) **Projection-corrected area:** The plate scale of the MDI full-disk continuum images is approximately 2 arc-sec. Hence, the area of the region is basically the number of pixels times the square of plate-scale. Since solar images are projection of spherical object on an image plane, the plate-scale is not a constant value, it depends on its distance from the image-center. To derive the projection-corrected area of each region type, we generated a map called *amap* for each image, which is the function of the heliocentric-position of each pixel.

$$\text{amap}(i, j) = \frac{\left(\frac{R_0}{R_p}\right)^2}{\sqrt{1 - \left(\frac{r_{ij}}{R_p}\right)^2}} \quad (2.15)$$

where,  $R_0$  is the solar-disk radius in arc-sec,  $R_p$  is the radii in pixel,  $r_{ij}$  is the distance of  $(i, j)^{\text{th}}$  pixel from the solar-disk center  $(x_c, y_c)$ . The numerator of  $\text{amap}(i, j)$  is the area of the pixel in arc-sec (uncorrected) and denominator is the cosine of the heliocentric angle of that pixel. The projection-corrected area, *car* in Millionth of Solar Hemisphere (MSH) unit is calculated in the following way:

$$\text{car} = \sum_{i=1}^n (\text{FRA}_i * \text{amap}_i) * \left(\frac{10^6}{2 * \pi * R_0^2}\right) \quad (2.16)$$

where,  $n$  is the number of pixels in the region.

- (e) **Region coordinates range:** For each region type, its x-y range in image, as well as latitude and longitude coordinates ranges were computed using its pixel information. These parameters are of benefit for the

grouping of sunspot groups to find the neighboring spots as discussed in Section [2.6].

### 2.4.5 Sunspots catalog

As discussed in Section [2.4], we identified the penumbra, umbra, and pores from each pre-processed SoHO/MDI continuum images, covering the period from May, 1996 to April, 2011. The computation of intensity, area, and position parameters for each region type is described in Section [2.4.4]. In the next step, we identified the bad pixels from the continuum images, which increased in number over the course of MDI operation. Using the bad pixel information we then rejected the sunspots which consists of these bad pixels in order to avoid contribution of false sunspots. After rejection of false detection, the sunspots of individual images were cataloged with all the derived parameters. In the Table [2.3] is listed the parameters obtained for an image.

The Column 1 gives the serial number of the detected region. Columns 2 and 3 are the labels and sub-labels for each object. The sub-label ‘0’ corresponds to a pore while ‘-1’ corresponds to a full sunspot while the objects with a positive value represent umbra. For a given sunspot, the related sunspot and umbral region(s) can be identified with the same value in the Column 2, *i.e.*, ‘label’ value. In Table [2.3], the given image has total of 39 identified objects, with consists of 7 sunspots (sub-label = -1), 15 umbral regions (sub-label > 0) and 17 pores (sub-label = 0). In case of sunspots with multiple umbrae, the sub-label has the increasing count number of these regions. For example, the sunspot with ‘lbl’ = 1 has 5 umbrae with the same ‘lbl’ value of 1, but an increasing numbering for sub-label (‘slb’) from 1 to 5.

For each detected sunspot, pore, and umbral region, the other important parameters which are listed in the table are: geometric area (effective number of pixels covered) (column 4); center of gravity (CG) position in the heliographic latitude and longitude (both carrington and stonyhurst) in de-

No.	lb	slb	gar	CGB	CGeL	CGsL	CGeL	CGX	CGY	AvI	MnI	MxI	Area	$\mu$	X1	X2	Y1	Y2	B1	B2	sL1	sL2
1	1	-1	830.06	-14.33	82.30	12.44	614.48	355.59	0.7080	0.0767	0.9572	589.37	0.93	587	637	339	371	-16.33	-12.50	9.18	15.10	
2	2	-1	539.39	-17.06	71.74	1.88	526.86	332.64	0.7276	0.2202	0.9725	381.10	0.93	511	545	314	348	-19.40	-15.17	-0.04	4.05	
3	3	-1	183.39	7.62	25.95	-43.91	172.03	551.04	0.7489	0.4539	0.9544	169.56	0.72	161	182	543	559	6.60	8.62	-45.61	-42.44	
4	4	-1	50.39	-15.44	46.90	-22.96	325.64	348.47	0.7130	0.3029	0.9404	38.31	0.86	321	329	343	353	-16.14	-14.87	-23.65	-22.46	
5	5	-1	49.39	9.01	27.76	-42.10	184.49	562.21	0.7314	0.3893	0.9208	43.91	0.74	179	188	557	566	8.36	9.47	-42.88	-41.61	
6	6	0	41.89	13.24	143.80	73.94	613.96	613.96	0.5382	0.9242	0.9242	52.53	0.29	945	965	607	620	12.53	13.83	72.10	75.81	
7	7	-1	32.39	13.82	135.96	66.10	948.93	614.50	0.7511	0.4311	0.9462	58.23	0.41	949	952	610	618	13.37	14.16	64.72	67.24	
8	8	0	28.06	-17.74	73.55	3.69	541.63	327.24	0.7967	0.5474	0.9351	19.93	0.93	537	545	322	331	-18.40	-17.28	3.14	4.09	
9	9	0	26.72	8.94	23.85	-46.01	160.57	563.25	0.7712	0.5806	0.9057	25.36	0.69	156	163	559	566	8.41	9.28	-46.71	-45.66	
10	10	-1	20.89	12.31	136.05	66.19	951.93	601.89	0.7386	0.4644	0.9578	33.98	0.41	949	954	598	605	11.92	12.63	65.15	66.99	
11	11	0	16.72	12.05	142.42	72.56	970.99	603.20	0.8040	0.6190	0.9160	36.37	0.31	968	973	599	606	11.65	12.32	71.14	73.58	
12	12	0	14.56	-12.30	44.66	-25.20	305.88	374.85	0.7422	0.5621	0.9194	11.06	0.86	303	308	372	377	-12.65	-12.03	-25.62	-24.89	
13	13	0	9.06	-14.44	74.43	4.57	549.49	354.02	0.8257	0.6811	0.9315	6.31	0.94	547	551	351	356	-14.81	-14.20	4.28	4.75	
14	14	0	9.06	-16.35	70.05	0.19	512.90	338.39	0.8466	0.7582	0.9227	6.36	0.94	510	515	336	340	-16.64	-16.15	-0.16	0.44	
15	15	0	6.89	11.83	140.02	70.16	964.98	600.00	0.8274	0.7403	0.9227	13.22	0.34	963	966	597	602	11.53	12.04	69.30	70.64	
16	16	0	6.89	10.63	24.30	-45.56	165.01	577.49	0.7685	0.7807	0.8195	6.50	0.70	163	166	575	579	10.32	10.81	-45.84	-45.43	
17	17	0	6.89	-15.79	74.47	4.61	549.55	342.99	0.7569	0.6896	0.8629	4.84	0.94	547	551	341	344	-16.04	-15.67	4.30	4.78	
18	18	0	6.72	-13.58	79.95	10.09	595.49	361.50	0.8629	0.8183	0.9209	4.72	0.94	593	597	359	363	-13.88	-13.40	9.80	10.26	
19	19	0	6.72	-17.05	81.85	11.99	609.48	333.51	0.8373	0.6894	0.9193	4.85	0.91	607	611	331	335	-17.35	-16.86	11.70	12.17	
20	20	0	5.72	-15.24	74.99	5.13	553.98	347.47	0.8336	0.7681	0.9147	4.01	0.94	552	555	345	349	-15.55	-15.06	4.90	5.25	
21	21	0	4.56	-14.27	75.93	6.07	561.97	355.51	0.8484	0.7077	0.9458	3.18	0.94	560	563	353	357	-14.57	-14.08	5.84	6.19	
22	22	0	3.39	-16.66	74.30	4.44	548.01	335.99	0.8543	0.8308	0.9008	2.39	0.93	546	549	334	337	-16.90	-16.53	4.20	4.56	
23	23	0	3.39	-17.28	74.80	4.94	552.02	330.99	0.8362	0.7829	0.8687	2.40	0.93	550	553	329	332	-17.53	-17.16	4.70	5.06	
24	24	0	2.22	-14.14	75.09	5.23	555.02	356.50	0.8086	0.7810	0.8362	1.55	0.95	553	556	355	357	-14.32	-14.08	4.99	5.34	
25	1	2	80.50	-14.04	83.37	13.52	623.98	358.12	0.3311	0.0767	0.5550	57.35	0.92	616	627	354	363	-14.53	-13.45	12.64	13.93	
26	1	2	27.50	-15.09	81.53	11.67	607.83	349.31	0.3389	0.1461	0.5482	19.58	0.92	604	610	346	351	-15.49	-14.89	11.22	11.92	
27	1	3	10.50	-14.92	80.71	10.85	601.26	350.57	0.3817	0.2394	0.5369	7.44	0.93	599	602	349	351	-15.11	-14.87	10.59	10.94	
28	1	4	9.50	-14.29	81.11	11.25	604.80	355.79	0.4283	0.2902	0.5464	6.72	0.93	603	606	354	357	-14.51	-14.14	11.04	11.39	
29	1	5	3.50	-14.09	81.74	11.88	610.02	357.52	0.5172	0.4877	0.5358	2.48	0.93	609	610	356	358	-14.27	-14.03	11.77	11.87	
30	2	1	34.50	-16.56	71.71	1.85	526.63	336.72	0.3621	0.2202	0.5571	24.28	0.93	522	531	334	338	-16.89	-16.40	1.29	2.37	
31	2	2	20.50	-15.96	72.78	2.92	535.58	341.60	0.4851	0.3294	0.5501	14.38	0.94	532	538	338	343	-16.40	-15.78	2.50	3.21	
32	2	3	19.50	-18.28	71.26	1.40	522.85	322.90	0.4560	0.2952	0.6264	13.88	0.92	521	524	319	326	-18.77	-17.89	1.18	1.54	
33	2	4	3.50	-17.52	70.79	0.93	519.03	329.00	0.5132	0.4769	0.5498	2.48	0.93	518	519	328	329	-17.64	-17.52	0.81	0.93	
34	3	1	10.50	7.74	26.44	-43.42	175.15	551.86	0.5028	0.4539	0.5517	9.52	0.72	173	176	550	553	7.50	7.88	-43.74	-43.30	
35	3	2	4.50	7.50	25.45	-44.41	168.90	550.25	0.4922	0.4570	0.5535	4.15	0.71	168	169	549	551	7.35	7.59	-44.54	-44.41	
36	4	1	10.50	-15.48	46.89	-22.97	325.61	348.15	0.4072	0.3029	0.5238	7.99	0.86	324	326	346	349	-15.75	-15.38	-23.21	-22.90	
37	5	1	6.50	9.00	27.97	-41.89	185.82	562.06	0.4418	0.3893	0.4894	5.76	0.74	184	186	560	563	8.75	9.11	-42.14	-41.87	
38	7	1	3.50	13.88	136.00	66.14	948.96	615.00	0.4791	0.4311	0.5280	5.69	0.41	948	949	614	615	13.78	13.87	65.80	66.15	
39	10	1	3.50	12.31	136.00	66.14	951.75	601.79	0.5126	0.4644	0.5472	5.67	0.41	951	952	600	602	12.11	12.33	65.82	66.22	

**Table 2.3: The list of properties of detected sunspots and pores of the image dated 3 Nov 2004, 03:11:32 UT.** ‘lb’: Label; ‘slb’: Sub-label; ‘gar’: Geometric area; ‘CGB’, ‘CGeL’, ‘CGsL’, ‘CGX’, and ‘CGY’: Center of gravity (CG) position in heliographic latitude (deg), heliographic carrington and stonyhurst longitude and stonyhurst longitude (deg), image X position, and Y position respectively; ‘AvI’, ‘MnI’, and ‘MxI’: Average, Minimum, and Maximum intensity of the region (full sunspot, umbral, pore); ‘Area’: Projection-corrected area (millionth of solar hemisphere, MSH); ‘ $\mu$ ’: Heliocentric position of region; ‘X1’, ‘X2’, ‘Y1’, and ‘Y2’: The region’s bounding box image coordinates (top left and bottom right), and the corresponding heliographic latitude and stonyhurst longitudes given by ‘B1’, ‘B2’, ‘sL1’, ‘sL2’.

degrees (columns 5, 6, and 7), pixel position of CG (columns 8 and 9); average, minimum, and maximum intensity (columns 10, 11 and 12); projection-corrected area in millionths of solar hemisphere (column 13); heliocentric position (columns 14); image coordinates of region's bounding box (columns 15–18); heliographic coordinates of region's bounding box (columns 19–22).

We generated a sunspot catalog for the complete solar cycle 23 and termed it as ‘feature detection, characterization, and tracking’ (FDCT) catalog. The comparison of the FDCT catalog with other available sunspot catalogs for the same period has been reported in the published paper of Goel and Mathew (2014).

## 2.5 Automated sunspot tracking

After detecting and cataloging the sunspots from the MDI images, we developed a tracking algorithm to associate these regions over different time intervals. In this algorithm we used the sunspot centroid coordinates available in the sunspot ‘FDCT’ catalog. In Goel and Mathew (2014); Higgins, Gallagher, and *et al* (2011), sunspots coordinates in one image is compared with the features over consecutive images positioned at similar latitudinal zone. For this comparison with features observed at different time, the coordinates of feature in first image is differentially rotated, using the latitudinal dependence derived in Howard, Harvey, and Forgach (1990), to the time of observation of next available image. In the present algorithm, we have tweaked this approach. Instead of differentially rotating the coordinates to different time stamps, we looked for the linearity of the motion of features over the consecutive images.

This algorithm takes four consecutive images at a time, and pick one-by-one the sunspot from the first selected image. It then makes different permutations of sunspots from the rest of the three images. Only those sunspots were considered for permutation which are within the  $2^\circ$  range of latitude from that of the picked sunspot from the first image. That is, if the latitude

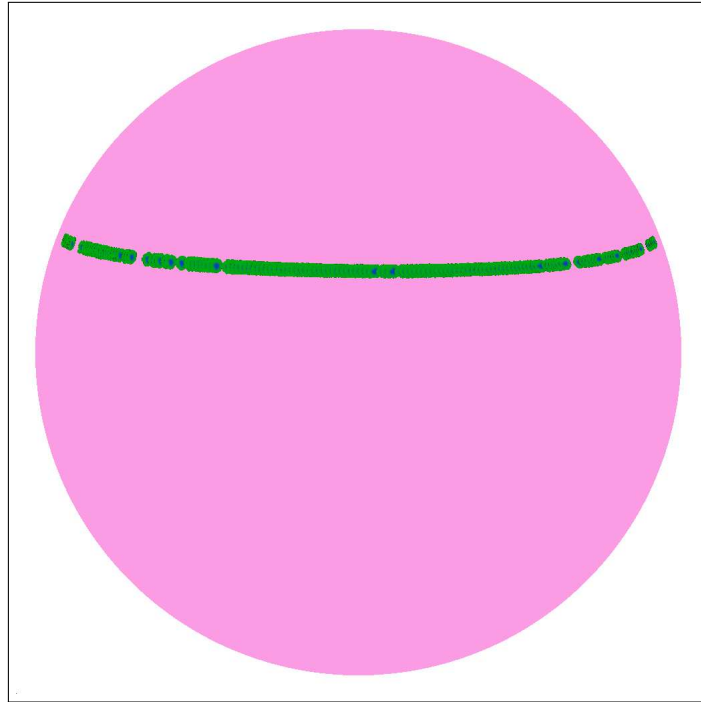


**Figure 2.6:** A sunspot followed over 150 images is overplotted on the solar-disk, starting from an image dated 25 Aug 2001, 23:59:32 UT to image dated 7 Sep, 2001, 01:35:32 UT.

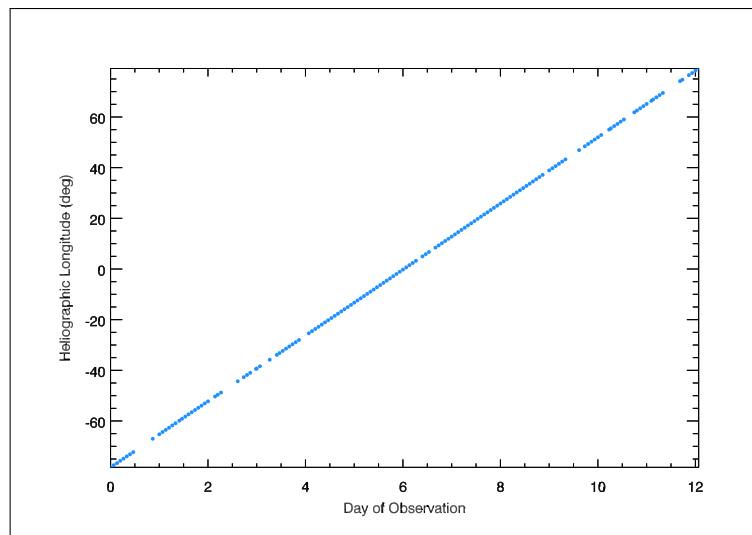


**Figure 2.7:** The heliographic longitude vs day of observation of sunspot followed over 150 images, starting from an image dated 25 Aug 2001, 23:59:32 UT to image dated 7 Sep, 2001, 01:35:32 UT.

of first sunspot is  $B$  degree, then from the consecutive images, the sunspots in the range of  $B - 2^\circ$  and  $B + 2^\circ$  will be considered. In addition, since this

tracking records are of importance for differential study, the sunspots which were more than 4 degree per day apart in the carrington heliographic longitudes from that of initial sunspot were rejected. This last criteria was to mitigate the contribution from the sunspots with anomalous rotation. Now, this algorithm checks for the linearity of longitude versus time data of each combination of four sunspots. The combination which satisfied the linearity criteria was considered as associated sunspots at four different times and a unique identification number was assigned to such first time observed associated regions and this number was stored in an array to keep their tracking record. This procedure was repeated for all the sunspots from the first image, and each time from the next consecutive images, different permutations of sunspots with the latitudinal criteria was generated. If from the three images, there is a missing sunspot within a given latitude band, then that sunspot from the first image was dropped. In the next step, the other four consecutive images will be taken, where the first image will be the second image from the earlier step. This allows the associated sunspots from previous images to be continued in next available images with same identification numbering. This whole process of taking four consecutive images at a time and checking the linearity of longitude shift with time for different combinations of sunspots was repeated till we reached the last available image. At each step of taking four consecutive images, the tracking array was updated.

Figure [2.6] shows the tracking result of a sunspot. The sunspot was first observed in an image dated 25 Aug 2001, 23:59:32 UT, near the East-limb. It has been traced over 150 images till it reaches the West-limb of image dated 7 Sep, 2001, 01:35:32 UT. The tracking array stores the identification information of each traced sunspot, using which the saved sunspot regions from the detection results can be extracted. In the Figure [2.6], the traced sunspot regions have been over-plotted on the solar-disk. The corresponding centroid longitude of the traced sunspot is plotted with the day of observation (starting from the first image) in Figure [2.7].

## 2.6 Sunspot bipoles identification

We developed an algorithm to identify the bipolar sunspots from the continuum images in an unsupervised manner. For grouping of sunspots based on their polarity, we first derived the polarities and maximum field strength of sunspots (listed in the FDCT catalog) using the MDI magnetogram images. For each continuum image we first grouped sunspots of same polarity using two criteria, first, the maximum field strength of two sunspots of same polarity should be within 50% value of each other, and they should be in close proximity to each other. For a given sunspot in an image, the search was performed in a rectangular box around this sunspot such that, the box's boundaries are 2 deg for latitude and 3 deg for longitude away from the sunspot's bounding box (Table [2.3]). If another sunspot of similar polarity with that of first sunspot was found within the rectangular boundaries, then it was grouped with the first sunspot. For next search, a new rectangular box coordinates were generated using the new lower and upper bounds of recent grouped sunspots. The area-weighted centroid coordinates, area and polarity information of grouped sunspots was stored for each images. This search was performed iteratively for all the ungrouped sunspots in an image for both the polarity types.

The next step was to assign negative and positive polarity groups to a bipole in each image. In an image with identified polarity regions, for each negative polarity region we computed the separation distance and angle with all the un-grouped opposite polarity regions of the image. In this computation only combination with a maximum separation distance of  $15^\circ$  was allowed. The negative-positive polarity pair having the minimum separation angle between their geometrical centers were chosen as bipole pairs. Once the bipoles were identified their area-weighted centroid coordinates, total area, leader and following polarity coordinates, tilt angles and separation distance were calculated (the details of parameter calculations are given in Section [5.2])

of Chapter 5).

## 2.7 Summary

Towards the objectives of the thesis, consisting of various studies pertaining to statistical properties of sunspots and sunspot-groups using SoHO/MDI continuum images for period of 15 years (1996-2011), we developed various programming modules. Here are the brief summary of each programming module:

- (a) **Pre-processing module:** We developed programming modules which supports; identification of solar-limb in an image and estimates solar radius in pixels; the estimation of yearly point-spread-function (PSF) of MDI continuum images based on the method of aureole intensity measurement; to estimate the limb-darkening function in the form of five-degree polynomial; deconvolution of images with the modeled PSF; and, generating master-flat for every carrington-rotation period (between years 1996-2011) by median combining stray-light-corrected images (masked for active regions) and use them for flat-fielding. Approximately, 50K MDI Level-1.8 full-disk continuum images were corrected for center-to-limb-variation and stray-light. Further, these stray-light-corrected images were flat-fielded.
- (b) **Sunspot-extraction module:** Based on a novel level-set formulation of active contours method, we developed an automated umbra-penumbra identification module. Using this module we identified pores, umbral and penumbral regions from stray-light-corrected full-disk MDI continuum images. Further, we removed false-identified-objects, and also related to bad-pixels.
- (c) **Sunspot-cataloging module:** This module calculated various parameters such as, mean/min/max intensity, foreshortening-corrected area, perimeter, latitude-longitude coordinates, *etc.*, of each identified regions

of pores, umbra-penumbra. All characterized pores and sunspots were cataloged with proper identifier names and information of their referring image and position on the solar-disk.

- (d) **Sunspot-tracking module:** We developed a method for tracing sunspots during its motion from east-to-west limb of solar-disk. Using this method, we made tracking reports of more than 2K individual sunspots observed during cycle 23.
- (e) **Sunspot-group identification and characterization module:** We made a module for extraction of sunspot-groups, constituting of; identification of polarity of sunspots using magnetograms; grouping same polarity regions (pores and sunspots) in each image on the basis of proximity and calculating their area-weighted centroid position, maximum field strength *etc.*; pairing of identified opposite polarity-groups in each image on the basis of proximity and analogous magnetic-field strength; calculation of bipole parameters such as, bipole-area (corrected for foreshortening), area-weighted centroid, tilt-angle, separation-distance between centroids of two polarity regions, *etc.*.

# Chapter 3

## Statistical Properties of Sunspots

### 3.1 Introduction

Sunspots are most prominent manifestation of solar magnetic activity observed on solar surface. They are one of the best proxies to infer about the cyclic regeneration and emergence of large-scale solar magnetic fields (Chapter 1). Understanding their sub-surface structure, processes of their formation, dynamic evolution, and decay impose constraints on theoretical dynamo models (Borrero and Ichimoto, 2011; Charbonneau, 2010; Fan, 2009; Hathaway, 2010; Ossendrijver, 2003; Rempel and Schlichenmaier, 2011; Solanki, 2003; Thomas and Weiss, 2008). Moreover, sunspots are unique test-bed to understand the inter-play of magnetic fields and convective plasma (Jahn, 1992; Rempel and Schlichenmaier, 2011, and references therein).

#### 3.1.1 Sunspot features

Sunspots are largest compact magnetic concentrations observed on solar surface, with fluxes in the range  $5 \times 10^{20}$  to  $3 \times 10^{22}$  Mx. Sunspots appear darker than the surrounding granules on the solar photosphere. They all

are composed of an inner, darker region called umbra, which radiates only 20-30% of the flux (integrated over wavelength) of quiet Sun, and an outer, less dark region called penumbra radiates 75-85% of quiet Sun's flux. The lowered brightness implies that umbra are roughly 1000 – 1900 K cooler, and penumbra are 250 – 400K cooler than the quiet Sun. The magnetic field strength varies gradually from a value of 1800 – 3600 G in the darkest part of umbra to 700 – 1000 G at the outer periphery of penumbra. The strongest field within a sunspot is usually associated with the darkest part of its umbra (dark nucleus) and is generally close to vertical, while at the visible sunspot (penumbral) boundary it is inclined by  $70^\circ - 80^\circ$  to the vertical (Mathew *et al.*, 2003; Solanki, 2003).

Both umbra and penumbra show fine structures at the photospheric level (Scharmer *et al.*, 2002; Sobotka, 1997; Solanki, 2003). Umbras show a pattern of fine ( $\lesssim 1''$ ) umbral-dots that are brighter than the umbral background (Bray and Loughhead, 1979; Danielson, 1964). In addition, many umbrae contain extended bright features, such as light bridges (Muller, 1992). While in penumbras, the fine structure is commonly referred to as penumbral-grains and penumbral-filaments.

### 3.1.2 Magneto-convection and sunspot models

In the presence of magnetic field, certain thermodynamic quantities that control the efficiency of convective transfer are altered (Chandrasekhar, 1952; Chandrasekhar, 1981; Danielson, 1961; Gough and Tayler, 1966; Lydon and Sofia, 1995; Thompson, 1951; Weiss, 1964). Biermann (1941) and Cowling (1953) suggested that in sunspots, the strong magnetic field lines inhibit convection cells, thus regions with strong magnetic flux are cooler and appears dark. But brightness of sunspots are too high to be explained by radiative energy transport alone, and some form of convection is required to explain the observed sunspot's intensity (Deinzer, 1965). Hoyle (1949) argued that convective motions in sunspots are channeled by magnetic field, while heat ex-

change across the field is inefficient (also see Chitre, 1963; Chitre and Shaviv, 1967). According to this concept, a sunspot is like a magnetic plug, thermally isolated from its surrounding photosphere.

To understand the structure and dynamics of magnetic and thermodynamic properties of sunspots, diverse sunspot-modeling approach had been considered and this has evolved in recent years due to advancement in resolution and quality of sunspot-data and computational capability. Semi-empirical models of umbral or penumbral atmospheres give the variation of thermodynamic variables and magnetic field vector with optical depth based on empirical data and theoretical considerations of magneto-hydrostatic (MHS) equilibrium and radiative transfer (Solanki, 1997; Solanki *et al.*, 1999; Spruit, 1981b). Magneto-hydrostatic equilibrium describes the balance of magnetic-field and thermal pressures across individual sunspots (Alfvén, 1943). These models generally consider an axially symmetric vertical flux-tube in approximate MHS equilibrium such that all fluctuations related to convective and Evershed motions are ignored (Jahn, 1992). A static axisymmetric model is given by Jahn (1997); Jahn and Schmidt (1994). The detailed and realistic modeling of sunspots with consideration of magneto-convection in strong magnetic-fields is based on numerical magnetohydrodynamic (MHD) models, which have advanced to the degree that simulations of entire sunspot with sufficient resolution to resolve its fine structure are now feasible (Heinemann *et al.*, 2007; Rempel, 2010; Rempel and Schlichenmaier, 2011; Rempel, Schüssler, and Knölker, 2009; Rempel *et al.*, 2009; Schüssler and Vögler, 2006).

There are two hypotheses for possible subsurface magnetic configuration of sunspots: 1) Cowling (1946), Cowling and Lindsay (1957) and Cowling (1976) suggested a single, coherent, monolithic tube of magnetic flux both above and below the solar surface; and 2) the cluster model (also known as jellyfish or spaghetti model), where the field split into many independent flux tubes which spread out like the tentacles of a jellyfish immediately below the photosphere and are surrounded by field-free plasma (Choudhuri,

1992; Parker, 1975, 1979b; Spruit, 1981a; Zwaan and Brants, 1981). The detailed comprehensive review of thermal and magnetic structure of sunspots, the recent understanding of sub-surface structure obtained from helioseismic inversion techniques, and the development in numerical MHD modeling are available in Borrero and Ichimoto (2011); Moradi, Baldner, and *et al* (2010); Rempel and Schlichenmaier (2011); Solanki (2003); Stein (2012); Thomas and Weiss (2008), and references therein.

All conventional models which assumes a continuous distribution of magnetic field in a sunspot (monolithic-model) requires some heat transport by magnetoconvection below the photosphere-level of umbra. For example, in the Jahn and Schmidt (1994) sunspot model, the cross-sectional area of the flux tube increases with height, which dilutes the heat-flux and hence reduces the temperature of the spot at the surface. While in case of cluster models, inside the tubes, the energy is carried by radiation only, and most (or all) of the heat flux emitted in the umbra can be explained by field-free columns of hot gas penetrating the spot immediately below the photosphere (Parker, 1979a,b; Spruit, 1981a).

### **3.1.3 Sunspot's magnetic field, darkness, size, and solar-cycle**

The interaction between convective flows and magnetic fields during flux expulsion, modification or suppression of convective energy transport by strong fields and also their interaction with radiation, all determine the observed magnetic-field strength, brightness, and size of sunspots. In order to understand the intricate magneto-convection at play and to have a consistent sunspot model, it is important to have better understanding of interdependency of various sunspot parameters such as intensity, magnetic field strength and inclination, temperature, geometrical depth and size, as well as the variation of these parameters as sunspots evolve and at different phases of solar activity.

A number of observations have shown that thermal stratification of sunspots depends sensitively on its magnetic-field strength, sunspot size, and (possibly) on solar-cycle phase as well. Martínez Pillet and Vázquez (1993) studied the distribution of continuum intensity and magnetic field in eight umbrae and demonstrated that the minimum intensity of umbra (umbral-core intensity) generally corresponded to their maximum field strength, this was further supported by Norton and Gilman (2004), Schad and Penn (2010), and Rezaei, Beck, and Schmidt (2012). However, the mechanism responsible for an inverse relationship between magnetic fields strength and temperature remains unclear, since umbrae host a wide range of thermal and magnetic–field distributions (Leonard and Choudhary, 2008; Martínez Pillet and Vázquez, 1993).

### 3.1.3.1 Sunspot size dependence

Ringnes (1961), Brants and Zwaan (1982), Kopp and Rabin (1992), Collados *et al.* (1994), Solanki (1997), Livingston (2002), Norton and Gilman (2004), Schad and Penn (2010), Rezaei, Beck, and Schmidt (2012) and Pevtsov *et al.* (2014) observed that the maximum magnetic-field strength within a sunspot increases with sunspot diameter. This is also coupled with a question whether sunspot brightness (temperature) depends on its size. Bray and Loughhead (1979) observed that larger sunspots are darker as compared to small sunspots. In contrast, Albregtsen and Maltby (1981); Rossbach and Schröter (1970) indicated no dependence of umbral intensity on umbral size for umbral diameters greater than about 8". Zwaan (1965) suggested that small sunspots appear brighter because of contamination by stray-light. However, other recent observations (some of which are free from stray-light or have been corrected for it, including space-based observations) showed that umbral-core intensity correlates with sunspot or umbral size. The observations of Kopp and Rabin (1992), Martínez Pillet and Vázquez (1993), Collados *et al.* (1994) and Rezaei, Beck, and Schmidt (2012) showed a nearly linear decrease in um-

bral brightness with size of umbrae. While, Mathew *et al.* (2007), Wesolowski, Walton, and Chapman (2008) and Schad and Penn (2010) obtained different non-linear relationships between umbral-core intensity and umbral area, represented by logarithmic or power-law or quadratic functions.

### 3.1.3.2 Solar cycle dependence

The strength of a cycle is determined by number and area of sunspots, their darkness, and magnetic-field strength. The cyclic variation of umbral intensity and magnetic-field strength has been the subject of several investigations, particularly after intriguing results obtained by Penn and Livingston (2006) and Penn and Livingston (2011) and Livingston, Penn, and Svalgaard (2012). Their studies reported that the magnetic-field strength and continuum brightness within the darkest portion of the sunspot umbrae exhibit on average a long-term decline in field strength at a rate of  $52 \text{ G yr}^{-1}$  and a corresponding long-term increase in brightness ( $1.9 \% \text{ yr}^{-1}$ ) over the declining phase of solar cycle 23 and the rising phase of cycle 24 (between 1998-2011). On the basis of these observations they speculated that the number of sunspots in cycle 24 would be reduced by roughly half, and there would be very few sunspots visible on the disk during cycle 25, which seems to be partially valid in the light of the observed extended minimum of solar cycle 23. This is in agreement with the early work of Albregtsen, Joras, and Maltby (1984) which had also observed an increase in umbral-core intensity;  $1.2 \% \text{ yr}^{-1}$  for cycle 20 and  $1.9 \% \text{ yr}^{-1}$  for cycle 21; and similarly Rezaei, Beck, and Schmidt (2012) found an increase of  $1.3 \% \text{ yr}^{-1}$  for solar cycle 23. Nagovitsyn, Pevtsov, and Livingston (2012) suggested that the gradual decline in average sunspot field strength as observed by Penn and Livingston (2006) can be explained by change in fraction of small and large sunspots. de Toma *et al.* (2013) also reported that the long-term increase in umbral brightness found by Livingston, Penn, and Svalgaard (2012) can be explained by biased selection because of exclusion of small spots and pores in early observations. This caused lack of

weak magnetic-field and faint spots between 1998-2002 data and biased their data-set towards strong fields (and darker umbrae) during rise and maximum phase of cycle 23. And because of low activity at the end of cycle 23 and the beginning of cycle 24, there was pronounced observation of declination of magnetic-field strength over the cycle period.

In contrast, Watson, Fletcher, and Marshall (2011) observed solar-cycle-like variation and only a minor long-term decrease in vertical magnetic flux of active regions ( $23 \text{ G yr}^{-1}$ ) (also see Schad and Penn, 2010). Penn and MacDonald (2007) observed 3931 umbral measurements between 1992-2003 and reported a solar cycle variation in umbral intensity, with umbrae appearing brighter on average at cycle minimum and darker at cycle maximum and suggested that the umbral magnetic field also oscillates in strength during the solar cycle. Norton and Gilman (2004) found a decrease in the umbral intensity from early-to-mid-phase of cycle 23 and an increase after the maximum of the cycle. In contrast, Mathew *et al.* (2007) reported a constant umbral intensity for most part of the cycle 23. Pevtsov *et al.* (2011) observed that the maximum magnetic-field strengths vary strongly with the solar cycle, however, no long-term decline was noted for observations of solar-cycles 19-23. Pevtsov *et al.* (2014) extended the search for secular trend in magnetic fields to cycles 15-19 and found no long-trend.

### 3.1.3.3 Limb variation

To understand the temperature stratification of umbra, it is important to derive the limb-darkening behavior of umbral intensity. Semi-empirical umbral models predict a decrease in umbral intensity (normalized to quiet Sun's intensity) towards the limb, particularly for the infrared wavelength region (Maltby *et al.*, 1986). However, it is not clear that there is a consistent center-to-limb variation of umbral brightness. Norton and Gilman (2004) and Albregtsen and Maltby (1981) showed that the umbral brightness increases towards the limb, in contrast, some studies reported decrements in intensity, for

example Albregtsen, Joras, and Maltby (1984); Penn and MacDonald (2007).

### 3.1.4 Sunspot's penumbra-umbra area ratio

When the flux emerges, it is often in the form of a pore having dark core (umbra). If the magnetic flux reaches sufficient value and/or the inclination exceed a critical value (Leka and Skumanich, 1998; Martínez Pillet, 1997), the penumbra forms at the spot periphery. Danielson (1961) considered the penumbral filaments as elongated convective rolls oriented parallel to the horizontal fields (Heinemann *et al.*, 2007, also see), formed due to interaction between inclined magnetic field and convection (Chandrasekhar, 1981). Penumbra to Umbra area ratio (here termed as PU ratio) might provide some important information towards the sunspot structure and evolution, and magneto-convection (Hoyt and Schatten, 1997; Vaquero *et al.*, 2005).

The PU ratio is one of the important parameters in reconstruction of solar irradiance of past (Foukal and Lean, 1990). Modern images employed in irradiance models allows both umbra and penumbra to be identified, whereas only entire sunspot can be traced in older images (Wenzler *et al.*, 2006). Irradiance reconstruction on centennial time scales rely on sunspot numbers which does not distinguish between umbra and penumbra (Krivova, Balmaceda, and Solanki, 2007). Thus, irradiance reconstructions considered a fixed umbral to total area ratio of 0.2 (that is PU ratio of 4), irrespective of the sunspot size (Wenzler, Solanki, and Krivova, 2005).

In contrast, different studies suggested that PU ratio changes with sunspot size. These studies were of two kinds, first in which the PU ratio was derived for the whole sunspot group (using total area of identified penumbral region and that of umbral region within the group) and in other studies this ratio was obtained for individual sunspots only. From the study of isolated sunspots, Waldmeier (1939), Jensen, Nordø, and Ringnes (1955), Jensen, Nordø, and Ringnes (1956) and Brandt, Schmidt, and Steinegger (1990) found a slow decrease in PU ratio with the increase in sunspot size.

While Tandberg-Hanssen (1956), Antalová (1971) and Hathaway (2013) presented a slow increase in PU ratio with the area of sunspot group. Separate measurement and parameterization of umbral and penumbral contrast and their dependence on sunspot size will greatly benefit the total irradiance modeling.

Using Greenwich photoheliographic results, Jensen, Nordø, and Ringnes (1955), Tandberg-Hanssen (1956) and Ringnes (1964) reported a weak tendency for the average PU ratio to change in phase with the solar cycle. In contrast, the recent study by Hathaway (2013) of Greenwich records between 1874 to 1976 found no variation in PU ratio with the sunspot group latitude or the phase of the sunspot cycle.

### 3.1.5 Objectives of the present study

The SoHO/MDI provided continuous full-disk continuum observations of complete solar-cycle 23 and the rising phase of cycle 24 (between 1996-2011). Using these stray-light-corrected images, we had generated a thorough sunspot catalog having reliable and consistent sunspot parameters (Sections [2.3] & [2.4.5]). The obtained sunspot parameters of a complete solar cycle are best sample to re-investigate sunspot's brightness and PU ratio dependence on sunspot size and variation of these parameters with phase of solar-cycle and center-to-limb position. We also further extended these investigations; we studied the differences in sunspot properties between following and leading sunspots of bipolar groups and for umbral regions of varying shapes. The following Section [3.2] provides the details of sunspot data-set and parameters used for statistical studies of sunspots. Section [3.3] presents the results obtained, followed by discussions and conclusion in Sections [3.4] & [3.5].

## 3.2 Sunspots data and parameters

In the present study we exploited the parameters of sunspots identified from all the stray-light-corrected SoHO/MDI full-disk continuum images (on average five images per day) which were listed in the FDCT catalog (see Section [2.4.4]). However, we restricted our analysis to sunspots identified with single umbra only and having well-defined surrounding penumbral regions, this is in order to mitigate contribution to this study from pores and spots having rudimentary penumbral regions and complex configurations. Following are the selection criteria applied to all identified sunspots from all the available images. First, only sunspots having one umbra were selected and having atleast one complete pixel (*i.e.*, with FRA = 1.) within the umbral boundary. Second, the total number of pixels occupied by the umbra should at least be 20% of that of the respective penumbral region. The total pixel count is always larger than the geometric area, and some pixels will be common between umbra and penumbra regions. This criterion was set to deject the contribution from remnants of active regions, which have regions with penumbral intensities and insignificantly small umbral cores. Third criterion was that, the umbral boundary should be within the penumbral boundary. This last criterion deselected sunspots having rudimentary penumbra. Further, only sunspots having heliocentric position,  $\mu \geq 0.3$  (where  $\mu$  is cosine of the heliocentric angle) were included, since for sunspots observed close to the limb the intensity and area measurements become erroneous. We listed the parameters of these selected regular sunspots from the FDCT catalog and will call this data-set as SI.

Although MDI continuum images were corrected for center-to-limb-variation, but Doppler-shifts to the Ni I 6768 Å line introduced by the solar rotation could introduce differences in intensity measurements along the East-to-West longitude. Hence, we further generated another refined sunspot data-set called as SII from the SI data-set, limited to sunspots close to solar

disk-center *i.e.*,  $\mu \geq 0.94$  (where  $\mu$  is cosine of the heliocentric angle). However, in order to avoid multiple counts of same sunspot observed over a long period, we first tracked all these sunspots from the data-set SII and then each distinct sunspot was incorporated into another data-set SIII at different times during its passage across the disk, such that we sample the same sunspot at few discrete  $\mu$  values. The data-set SIII consists of total of 4482 sunspot regions within the  $\mu \geq 0.94$  range. An another refined data-set SIV was generated from the SIII by picking the total of 1194 distinct sunspots while they have the minimum value of umbral-minimum-intensity during their respective passage across the disk.

In summary, in the present analysis, we have used four kinds of data-sets with the following properties:

- (a) **Data-set SI:** Regular sunspots with single umbra (with  $\mu \geq 0.3$ ).
- (b) **Data set SII:** Regular sunspots with single umbra and restricted to  $\mu \geq 0.94$  range.
- (c) **Data set SIII:** Data set with reduced multiple counts of distinct sunspots obtained from SII.
- (d) **Data set SIV:** Distinct sunspots of Data set SIII.

In this chapter most of the analysis of sunspot properties is using data set SIII. The sunspot parameters such as, time of observation; heliocentric position ( $\mu$ ); projection-corrected sunspot total area and umbral area; umbral minimum/mean intensity; penumbral mean intensity were utilized in this study. The intensity values of sunspots are normalized to the quiet-sun photospheric intensity which is taken to be the peak intensity of the respective full-disk image histogram (Steinegger *et al.*, 1996; Zharkov, Zharkova, and Ipson, 2005). We had also incorporated the correction in intensity due to the line-shape variation introduced by the Zeeman-splitting in strong magnetic-field regions (Criscuoli *et al.*, 2013; Mathew *et al.*, 2007). This continuum

intensity correction was applied using the look-up table of corrected vs observed intensity in the Mathew *et al.* (2007).

For the present study, a new parameter called as Umbral-circularity index was also calculated for selected sunspots data set. The circularity index,  $U_c$ , which measures the degree to which a shape is compact, is given by;

$$U_c = 4 * \pi * \left( \frac{A_u}{P_u^2} \right) \quad (3.1)$$

where,  $A_u$  is the umbral area in degrees and  $P_u$  is the perimeter of the umbral region in degrees. To calculate the perimeter without much affect from the fore-shortening, we first identified the latitude and longitude coordinates of the vertices of the umbral-region boundary (which was saved during the sunspot identification, see Section 2.4.3). Perimeter is now simply the sum of the distance between vertices along a complete round of the boundary. That is, if there are  $n$  vertices in a given boundary, the perimeter  $P_u$  is calculated as;

$$P_u = \sum_{i=1}^{n-1} (d(i, i+1)) + d(n, 1) \quad (3.2)$$

where,  $d(i, i+1)$  is the distance between the  $i^{th}$  and  $(i+1)^{th}$  vertices.

### 3.3 Results

#### 3.3.1 Umbral core intensity and sunspot area

The Figure [3.1(a)] shows the scatter plot of umbral-core intensity and sunspot area (in Millionth of Solar Hemisphere (MSH); corrected for foreshortening) for the selected regular sunspots close to solar disk-center ( $\mu \geq 0.94$ ) from data set SII. This data set covers the solar cycle 23 as well as rising phase of cycle 24.

Clearly, the umbral-core intensity decreases with increasing sunspot area, and reaches a nearly asymptotic value for sunspots larger than 600

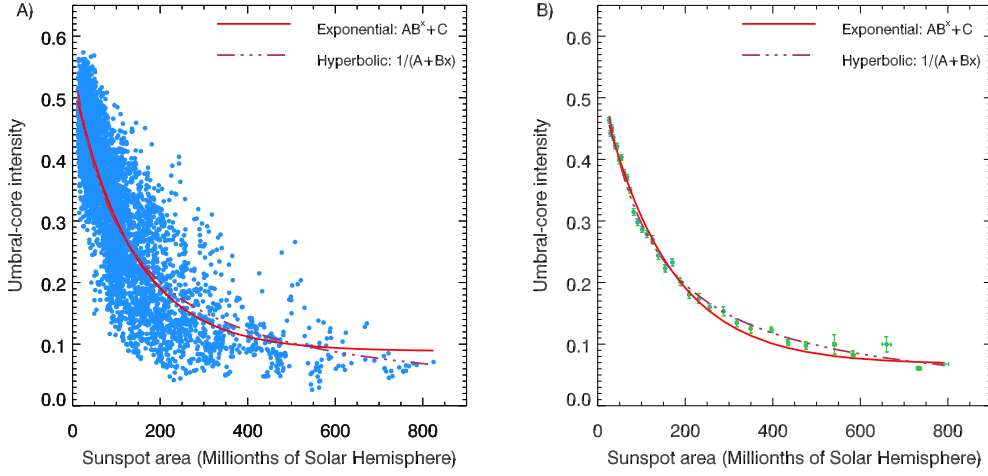


**Figure 3.1:** The variation of umbral-core intensity with sunspot area (in MSH; corrected for projection-effect) using the data set SIII. **A** the scatter plot, each point (blue) represent individual data points from Set SIII; and **B** the binned data, with area binned into equally-spaced 35 bins in log-scale starting from 5 MSH to 850 MSH; each blue dot represents the average intensity and corresponding average area in each bin. The x & y error-bars (green) are standard errors in each bin. The exponential (solid-line) and hyperbolic (dashed-triple-dot) fit functions are also shown in both plots. The fit parameters for both the plots are listed in Table 3.1.

MSH. The best non-linear fits to the umbral-core intensity versus sunspot area are exponential and rectangular hyperbolic functions, over-plotted with the scatter data in Figure [3.1(a)]. The fitting coefficients (with their one-sigma values) of both the functions and the respective chi-square values are listed in the Table [3.1].

Fit function	A	B	C	$\chi^2$
<b>For individual points (SIII)</b>				
Exponential	0.442(0.064)	0.993(0.003)	0.089(0.072)	0.0047
Hyperbolic	1.769(0.175)	0.016(0.003)	-	0.0047
<b>For binned-data (SIII)</b>				
Exponential	0.462(0.030)	0.993(0.0001)	0.067(0.001)	4.9201
Hyperbolic	1.676(0.013)	0.017(0.0002)	-	3.3464

**Table 3.1:** Fit-parameters and one-sigma errors (in brackets), and chi-square values for the Exponential ( $AB^x + C$ ) and Hyperbolic ( $1/(A + Bx)$ ) fits for umbral-core intensity vs sunspot area (MSH) (Figure [3.1]). The data set used for this plot was SIII (see Section [3.2]).

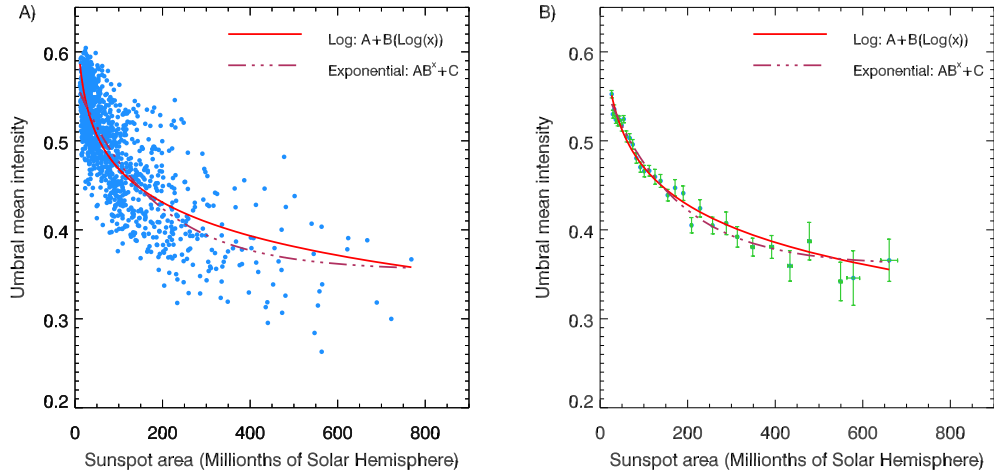


**Figure 3.2:** The variation of umbral-core intensity with sunspot area (in MSH; corrected for projection effect) using the data set SIV of distinct sunspots. **A** the scatter plot; and **B** the binned data, with area binned into equally-spaced 35 bins in log-scale starting from 5 MSH to 850 MSH. The x & y error-bars (green) are standard errors in each bin. The exponential (solid-line) and hyperbolic (dashed-triple-dot) fit functions are also shown in both plots. The fit parameters for both the plots are listed in Table [3.2].

Fit function	A	B	C	$\chi^2$
<b>For individual points (SIV)</b>				
Exponential	0.431(0.137)	0.993(0.007)	0.086(0.157)	0.0048
Hyperbolic	1.830(0.331)	0.017(0.007)	-	0.0048
<b>For binned-data (SIV)</b>				
Exponential	0.437(0.008)	0.993(0.0004)	0.082(0.007)	1.6052
Hyperbolic	1.7091(0.031)	0.018(0.0006)	-	1.6593

**Table 3.2:** Fit-parameters and one-sigma errors (in brackets), and chi-square values for the Exponential ( $AB^x + C$ ) and Hyperbolic ( $1/(A + Bx)$ ) fits for umbral-core intensity vs Sunspot area (MSH) for distinct sunspots (Figure [3.2]). The data set used for this plot was SIV (see Section [3.2]).

In Figure [3.1(b)], the scatter in umbra-core intensity is eliminated upon binning and the relationship between core intensity and sunspot area is more easily examined. Data were binned according to the sunspot area. We generated 35 equally spaced bins in logarithmic space<sup>1</sup> between the values 5 MSH and 850 MSH. In the binned data plot, each dot represents the average value of intensity and area in each bin. The x and y error-bars in the binned plot represents the standard-error (SE), *i.e.*,  $SE = \sigma/\sqrt{n}$ , where  $\sigma$  is the standard

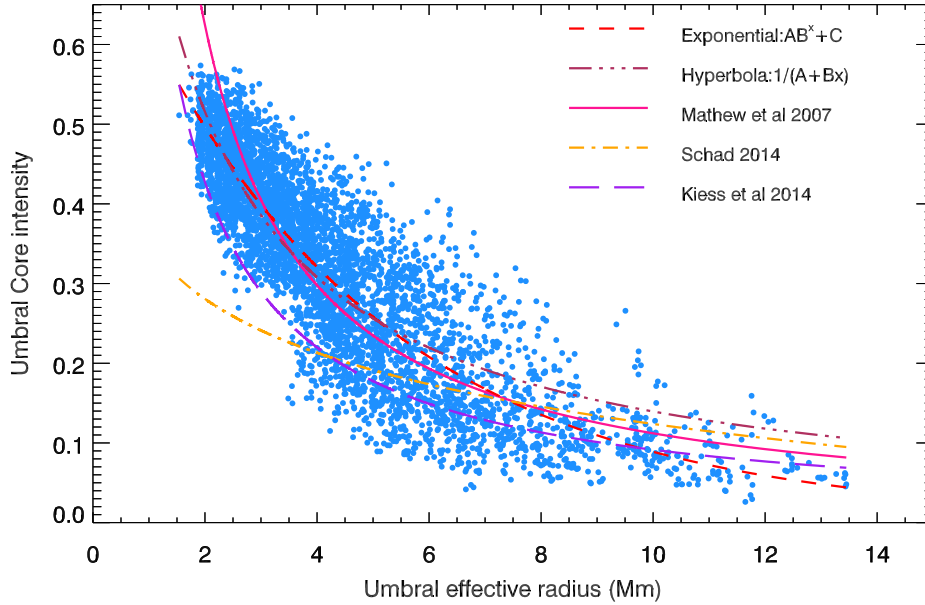


**Figure 3.3:** The variation of umbral-core intensity with umbral effective radius (in Mm) using the data set SIII. The exponential (small-dashed) and hyperbolic (dashed-triple-dot) fit functions as well as the functions obtained in Mathew *et al.* (2007) (solid-line), Schad (2014) (dashed-dot), and Kiess, Rezaei, and Schmidt (2014) (long-dashed) are plotted. The fit parameters for all these functions are listed in Table [3.3].

Data set	Fit function	A	B	C	$\chi^2$
SIII (binned)	exponential ( $AB^x + C$ )	0.765(0.096)	0.802(0.096)	0.005(0.146)	0.0037
	Hyperbola ( $1/(A + Bx)$ )	0.633(0.324)	0.654(0.112)	-	0.0041
Mathew <i>et al.</i> (2007)	power-Law ( $Ax^B$ )	1.859	-1.068(0.063)	-	0.0035
Kiess, Rezaei, and Schmidt (2014)	power-Law ( $Ax^B$ )	0.830(0.054)	-0.958(0.035)	-	-
Schad (2014)	log ( $A + B \log x$ )	0.348	-0.098	-	-

**Table 3.3:** Fit-parameters and one-sigma errors (in brackets), and chi-square values for the Exponential and Hyperbolic functions for umbral-core intensity vs umbral radius (Mm) (Figure [3.3]). The data set used for this plot was SIII (see Section[3.2]). Also shown the fit-parameters for the functions obtained in Mathew *et al.* (2007), Schad (2014), and Kiess, Rezaei, and Schmidt (2014).

deviation and  $n$  is the number of data-points in a bin. Here, the exponential and hyperbolic functions are more easily distinguishable, the exponential function appears to have better fit and have lower chi-square ( $\chi^2$ ) value as shown in the Table [3.1]. The flattening behavior for larger sunspots is still preserved in the binned plot.

<sup>1</sup>[http://www.idlcoyote.com/code\\_tips/evenlog.php](http://www.idlcoyote.com/code_tips/evenlog.php)

In the Figure [3.1(a)], considerable scatter is present in intensity values for each size range of sunspot area. This scatter has a variety of possible sources: 1) differences between umbrae with different shapes (*e.g.* elongated vs. round, see Section [3.3.2]); 2) sampling sunspots during different phases of their evolution (Leonard and Choudhary, 2008); 3) remaining intrinsic variations from one spot to another (*e.g.* due to the spatial distribution of umbral dots) (Collados *et al.*, 1994); 4) noise and errors in the measurement of intensity (*e.g.* introduced by different field strengths, flow velocities, possible hidden molecular blends, *etc.*); 5) possible errors in the determination of the sunspot boundary. There are also further sources of scatter. For example, we consider the area of the sunspot as a whole, but the minimum brightness in an umbra may be more closely related to the umbral area and there is a scatter in the area ratios of umbral to total area of a sunspot. We will study this last point in Sections [3.3.5] & [3.3.6].

We further check if there is any difference in the above obtained results if we only consider distinct sunspots that is, if we limit the contribution from a same sunspot to only once when it has minimum value of umbral-core intensity during its evolution. In Figure [3.2(a)], we again plotted core-intensity and sunspot area now using the data set SIV, having 1194 distinct regular sunspots (see Section [3.2]). This plot has similar scatter as it was for sunspots with multiple counts (Figure [3.1(a)]). The binned data and corresponding exponential and hyperbolic fit functions are also plotted in Figure [3.2(b)]. All the fit-parameters with one-sigma values are listed in the Table [3.2]. From the binned-plot of distinct sunspots, again the exponential fit function has lower chi-square value. The fit-parameters obtained for both the data sets SIII & SIV are almost same.

In Figure [3.3], we have plotted the core-intensity with the umbral effective radii in Mega-meter (Mm)<sup>2</sup>, where umbral radii was calculated from the umbral area considering it to be a circular region. This plot is to com-

---

<sup>2</sup>1MSH = 3.044 × 10<sup>6</sup>km<sup>2</sup>.

pare our present results with some of the recent studies which have looked for dependence of core-intensity with the umbral area (or radius) instead of whole sunspot area. This is also well described by exponential and hyperbolic fit functions. The fit parameters for exponential and hyperbolic functions are listed in the Table [3.3].

Mathew *et al.* (2007) obtained a power-law function for the dependence of umbral-core intensity with the umbral effective radii using 160 regular sunspots from SoHO/MDI continuum images (stray-light corrected) for the period between 1998 March to 2004 March. Kiess, Rezaei, and Schmidt (2014) used 205 umbral data obtained from HMI continuum images at neutral iron line at 617.33 nm (not corrected for stray-light) and they also obtained a power-law relation. While, Schad (2014) studied 7530 sunspot umbrae and pores measured by the Hinode Spectropolarimeter (SP) between November 2006 and November 2012 and obtained a log-function relation between core-intensity and umbral radius. The coefficients of obtained functions for all these studies are also listed in the Table [3.3]. The exponent value of power law functions from the present study and also from Mathew *et al.* (2007) and Kiess, Rezaei, and Schmidt (2014) is around  $-1$ , which is in approximation to a hyperbolic function.

However, it is not straightforward to compare results from various data sets obtained at different wavelengths, since continuum contrast changes with the wavelength used. In Figure [3.3], the fits by Schad (2014) and Kiess, Rezaei, and Schmidt (2014) follows closely with the presented data set for large sunspots, but small sunspots are significantly cooler as compared to our sampled sunspots from SoHO/MDI. One possible reason for this difference in intensity for small and intermediate sunspots may be because of observing the cooler core region within umbrae owing to higher resolution of the Hinode and HMI data set in comparison to MDI.

### 3.3.2 Umbral core intensity and circularity index

We investigated whether the umbral-core intensity and sunspot area relation is affected by the shape of the umbra. For this we derived the compactness or circularity measure of the umbral region of a sunspot. This measure is the ratio of the area of the shape to the area of a circle (the most compact shape) having the same perimeter as given in the equation [3.1]. Figure [3.4] shows the histogram of the umbral-circularity measure of the 4482 sunspots of data set SIII which are close to solar disk-center.

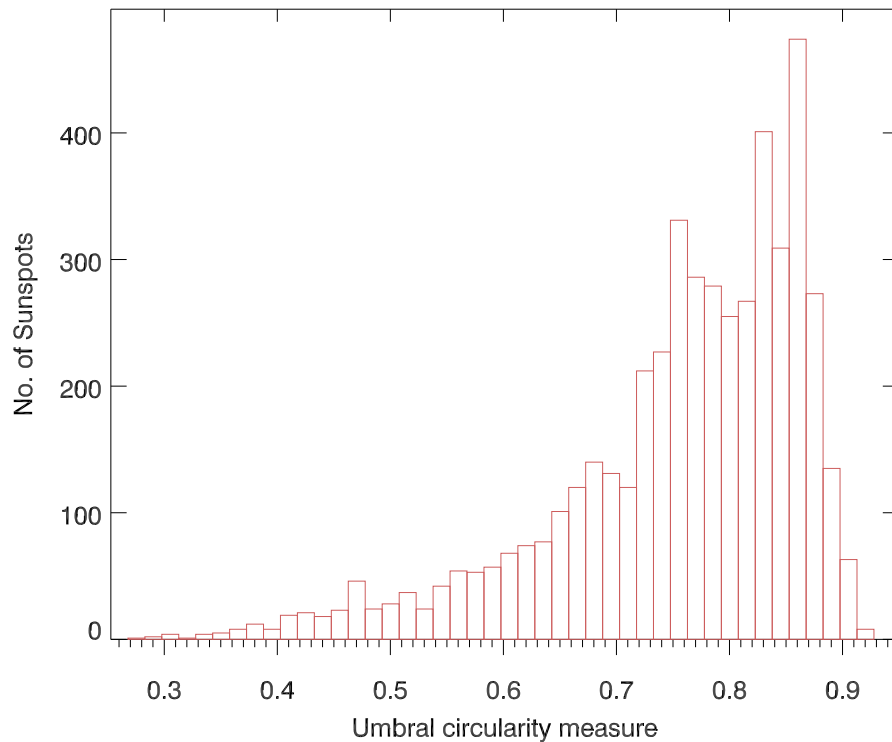


**Figure 3.4:** The histogram of the umbral-circularity measure of regular sunspots with single umbra and close to the disk-center (data set SIII).

We selected two ranges of umbral-circularity measure; 1)  $U_c = [0.0 - 0.7]$  and 2)  $U_c = [0.8 - 1.0]$ , from the data set SIII. Then, generated the area-binned (for details of binning, see Figure [3.1]) plot of umbral-core intensity

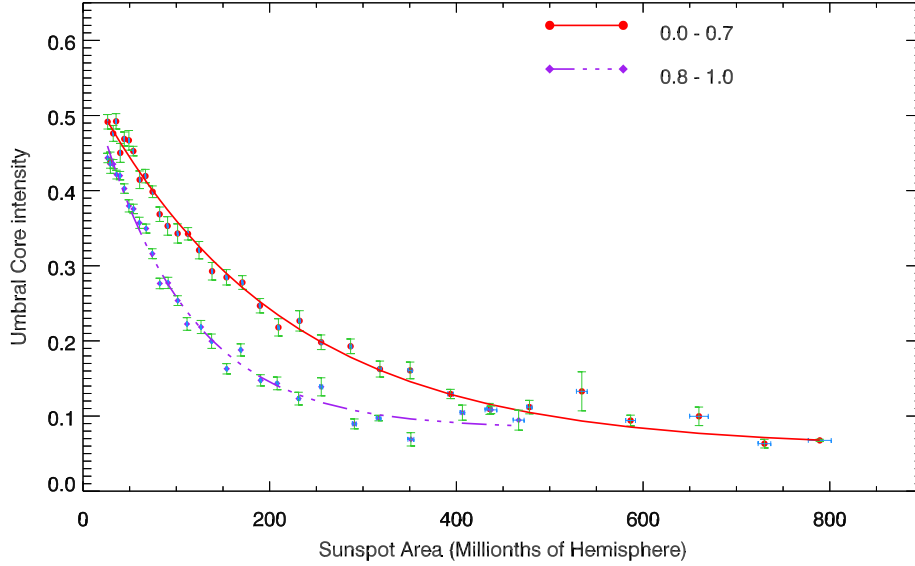


**Figure 3.5:** The variation of umbral-core intensity vs sunspot area (in MSH) for two range of umbral-circularity measure; a)  $U_c = [0.0 - 0.7]$  and b)  $U_c = [0.8 - 1.0]$ . The area is binned into equally-spaced 35 bins in log-scale starting from 5 MSH to 850 MSH. The error-bars represents the standard errors in each bin. The exponential function ( $AB^x + C$ ) fitted for; a) in solid-line and b) in dashed-triple-dot are also plotted. The fit parameters of these functions are listed in Table [3.4].

Circularity range	A	B	C	$\chi^2$
0.0 - 0.7	0.495(0.005)	0.995(0.0001)	0.058(0.002)	1.8415
0.8 - 1.0	0.494(0.006)	0.989(0.0003)	0.083(0.003)	3.7213

**Table 3.4:** Fit-parameters and one-sigma errors (in brackets), and chi-square values for the Exponential ( $AB^x + C$ ) functions of umbral-core intensity vs sunspot area for two range of umbral-circularity measures as shown in Figure [3.5]. The data set used for this plot was SIII (see Section [3.2]).

and sunspot area for these two range of circularity measure separately with corresponding fitted exponential functions as shown in Figure [3.5]. This plot clearly shows that the relation between core-intensity and sunspot area changes with the circularity measure of umbrae. For small to intermediate size sunspots, the compact umbrae with circularity measure in range 0.8 - 1.0 have lower intensity values as compared to that for umbrae having circularity measure in the range 0.0 - 0.7. However, for large sunspots both types of um-

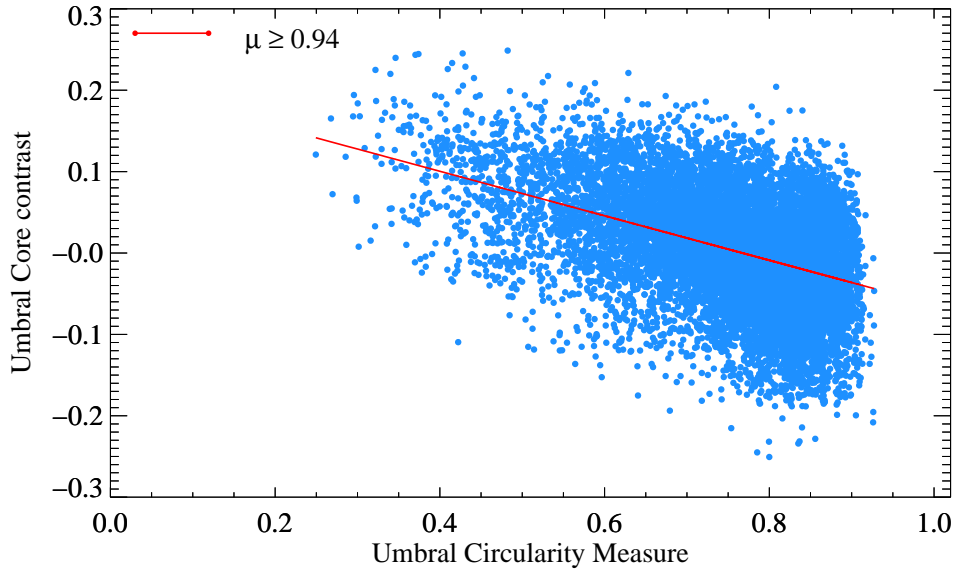


**Figure 3.6:** The variation of umbral-core residual intensity (called as contrast) with umbral-circularity measure for the data set SIII. A straight line fit (red) is also shown. The fit parameters for the straight line is listed in Table [3.5].

A	B	$\chi^2$
Regression coefficient		
0.210(0.004)	-0.273(0.005)	49.3747
-0.44		

**Table 3.5:** Fit-parameters and one-sigma errors (in brackets), and chi-square values for the straight-line ( $A + B(x)$ ) for umbral-core intensity vs circularity measure (Figure [3.6]). The data set used for this plot was SIII (see Section [3.2]).

brae have conjoint intensity values. The Table [3.4] lists all the fit-parameters and one-sigma error of exponential functions for both the range of circularity measure. Here, we restricted this study to regular sunspots with single umbra close to the solar disk-center ( $\mu \geq 0.94$ ) only, and not included sunspots at higher heliocentric angles in order to mitigate intensity dependence on  $\mu$  (if any), which we will study in Section [3.3.9.1].

Next, we derived the dependence of core intensity with the umbral-circularity measure. For this, we have first computed the intensity for the given sunspot area (of data set SIII) using the exponential function obtained

from the binned plot of Figure [3.1(b)]. The computed intensity was subtracted from the measured intensity to obtain the residual intensity to compensate for the area dependency. In Figure [3.6] is plotted the residual umbral-core intensity with the circularity measure. We fitted a straight line to the variation of residual intensity with the circularity. The fit-parameters and one-sigma errors are listed in Table [3.5].

### 3.3.3 Umbral mean intensity and sunspot area

In this section, we studied the umbral-mean intensity variation with the sunspot size. In Figure [3.7] is shown the variation of umbral-mean intensity with sunspot area (in MSH) for regular sunspots with single umbra and close to solar disk-center (data set SIII).

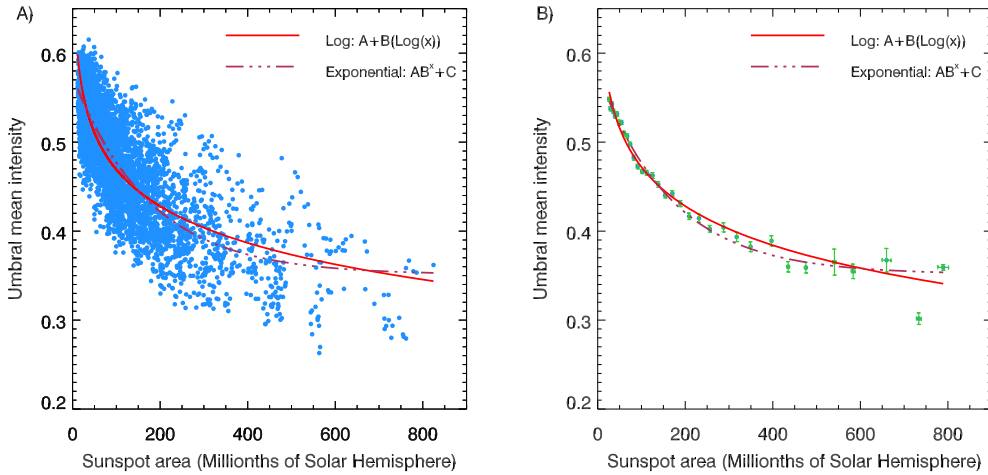


**Figure 3.7:** The variation of umbra-mean intensity with sunspot area (in MSH) for data set SIII. **A**, the scatter plot and **B**, the binned data plot. The area is binned into 35 bins of equal size in logarithmic scale. The exponential (dashed-triple-dot) and log (solid-line) functions are also plotted to the binned data (**B**). The fit-parameters are listed in the Table [3.6].

Figure [3.7(a)] is the scatter plot, where individual dots (blue) represents data-points. While, Figure [3.7(b)] is the area-binned plot. The area was binned into equally-spaced 35 bins in logarithmic scale starting from 5 MSH to 850 MSH. The dots (blue) represents the average of umbral-mean intensity

Fit function	A	B	C	$\chi^2$
<b>For binned-data (SIII)</b>				
Exponential	0.223(0.002)	0.994(0.0002)	0.352(0.003)	5.3973
Log	0.764(0.003)	-0.146(0.001)	-	7.5122

**Table 3.6:** Fit-parameters and one-sigma errors (in brackets), and chi-square values for the Exponential ( $AB^x + C$ ) and Log ( $A + B \log x$ ) functions for umbral-mean intensity vs sunspot area (MSH) (Figure [3.7]). The data set used for this plot was SIII (see Section [3.2]).

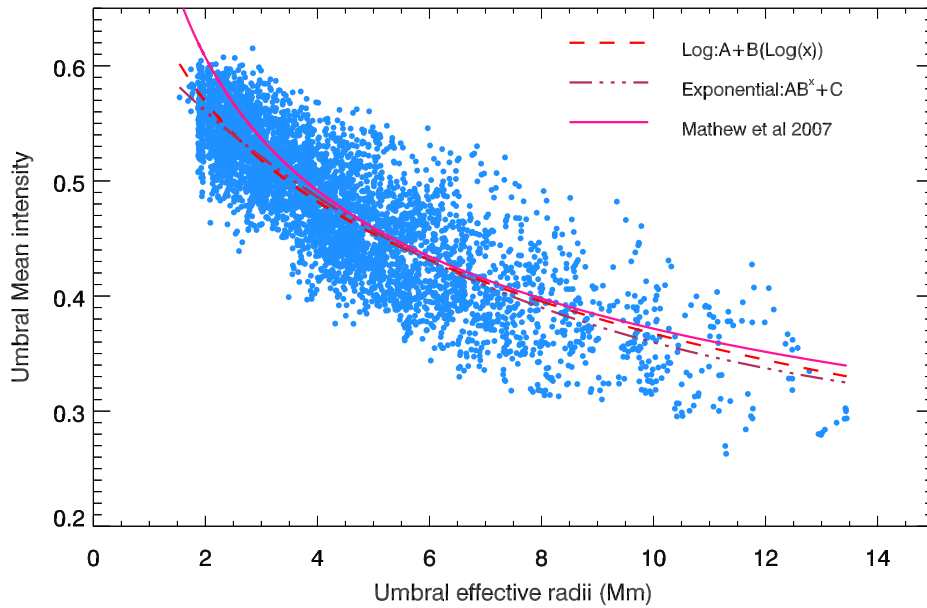


**Figure 3.8:** The variation of umbral-mean intensity with umbral effective radius (in Mm) for data set SIII. The exponential (dashed-triple-dot), log (dashed) fit functions, and the power-law function from Mathew *et al.* (2007) (solid-line) are also plotted. The parameters of all these functions are listed in Table [3.7].

and sunspot area in each bin. The error bars are the standard errors in each bin. An exponential function and a log-function fit for the binned data are also shown. The fit-parameters, their one-sigma errors and chi-square values are listed in the Table [3.6]. The exponential function has better fit to the umbral-mean intensity data and have lower chi-square values as compared to log-function. Here, hyperbolic function and power-law has poor fit in comparison to exponential function, hence not shown. The benefit of an exponential

function is that it will remain positive for large sunspot size, which is an expected physical condition.

Data set	fit function	A	B	C	$\chi^2$
SIII (binned)	exponential ( $AB^x + C$ )	0.388(0.191)	0.861(0.193)	0.273(0.274)	0.0012
	$\log(A + B \log x)$	0.656(0.048)	-0.288(0.076)	-	0.0012
Mathew <i>et al.</i> (2007)	power-Law ( $Ax^B$ )	0.828	-0.305(0.013)	-	0.0002

**Table 3.7:** Fit-parameters and one-sigma errors (in brackets), and chi-square values for the Exponential and Log functions for umbral-mean intensity vs umbral effective radius (Mm) (Figure [3.8]). The data set used for this plot was SIII (see Section [3.2]). Also shown the fit-parameters for the power-law function obtained in Mathew *et al.* (2007).

To compare the present result with previous similar study, we plotted umbral-mean intensity with umbral effective radii in Figure [3.8]. Also plotted the exponential and log fit functions of the present data, along with the power-law function obtained by Mathew *et al.* (2007). The fit-parameters of all these plotted functions are listed in the Table [3.7]. Small discrepancy between present and previous study may be due to different sampling of sunspots.

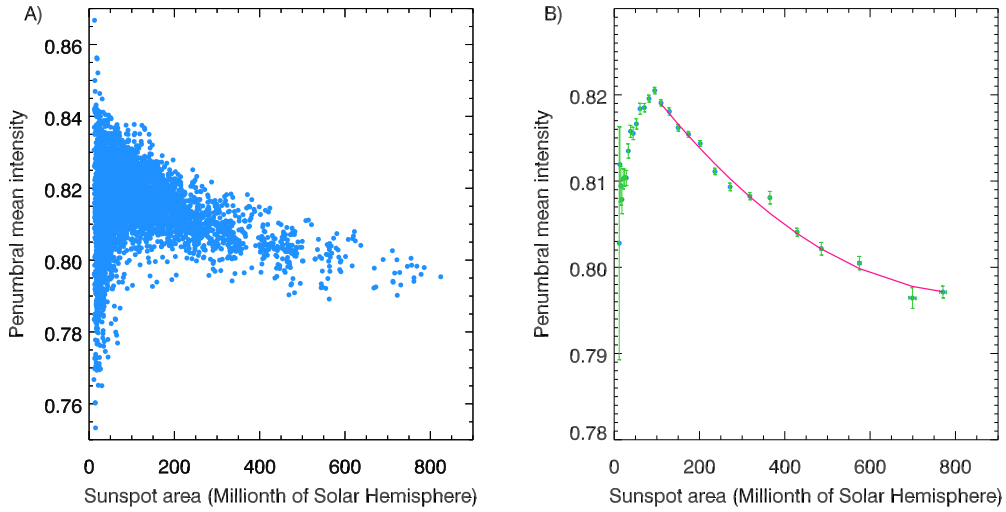
### 3.3.4 Penumbra mean intensity and sunspot area

Figure [3.9] shows the relation between penumbral-mean intensity and sunspot area. It shows a non-linear dependency for sunspots of size greater than  $\sim 100$  MSH. Figure [3.9(b)] shows the plot for binned-data (35 equal-sized bins of area in log-space). We fitted a quadratic function for sunspots  $\geq 100$  MSH. The fit-parameters of the quadratic function are listed in the Table [3.8].

A	B	C	$\chi^2$
0.826(0.001)	$-10^{-4}(0.0000)$	$0.7(0.1)(10^{-9})$	22.9976

**Table 3.8:** Fit-parameters and one-sigma errors (in brackets), and chi-square values for the quadratic fit ( $A + B(x) + C(x^2)$ ) for penumbral-mean intensity vs sunspot area (Figure [3.9]). The data set used for this plot was SIII (see Section [3.2]).

The sunspots below 100 MSH have peculiar downturn. This lowered intensity could possibly be an artifact because of limited resolution to efficiently



**Figure 3.9:** The variation of penumbral-mean intensity with sunspot area (in MSH) using the data set SIII. **A**, the scatter plot and **B**, the binned plot. A quadratic fit ( $A+Bx+Cx^2$ ) (solid-line) for sunspots  $\geq 100MSH$  is plotted in **B**. The fit-parameters are listed in Table [3.8].

distinguish umbra-penumbra boundary for small sunspots.

### 3.3.5 Penumbra-umbra area ratio

In this study, we investigated the dependence of Penumbra-umbra area (PU) ratio on sunspot size for regular sunspots, having single umbra and close to solar disk-center of data set SIII. Figure [3.10] shows the distribution of PU ratio of the sampled sunspots. The Gaussian function fit (with four terms) is also shown and this has the mean value of 3.96, which is close to the generally accepted value of 4 used in models for irradiance reconstruction (Wenzler, Solanki, and Krivova, 2005).

In Figure [3.11(a)] is plotted the PU ratio with the sunspot area (in MSH). We found that the Penumbra to Umbra area ratio has dependency on the total sunspot area and this ratio has smaller value for large sunspots. This dependency is more easily comprehensible in binned-data plot shown in Figure [3.11(b)], where area is binned in 35 equally-spaced bins in logarithmic space starting from 5 MSH to 850 MSH. We obtained a quadratic fit to the

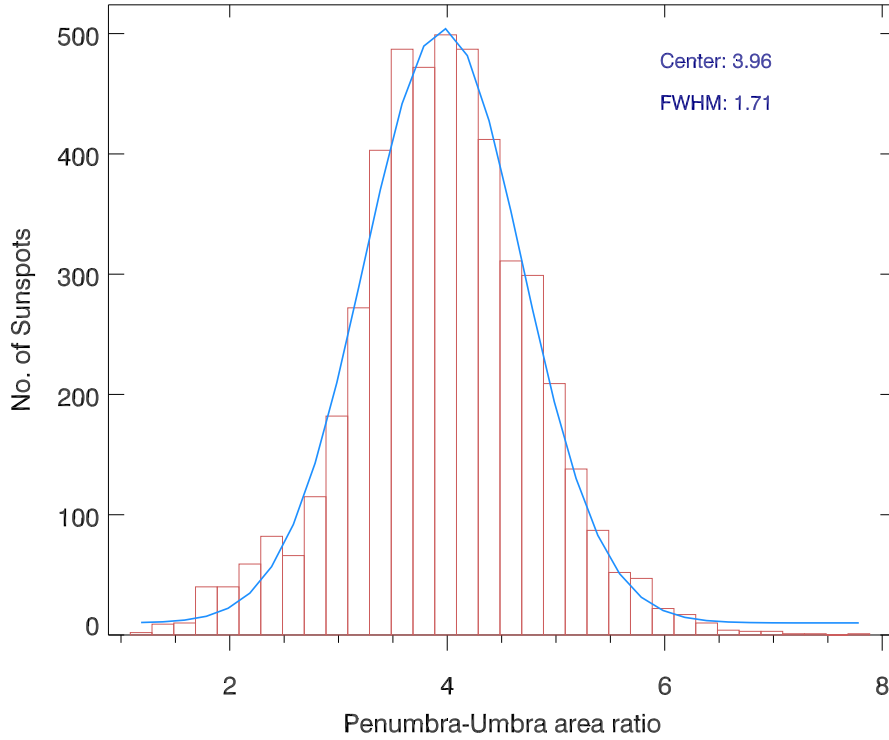


**Figure 3.10:** The distribution of Penumbra-umbra area ratio for the data set SIII. The Gaussian function ( $G(x)$ ) (solid-line) is fitted to the distribution, where  $G(x) = \frac{1}{\sigma\sqrt{2\pi}}e^{-(x-\mu)^2/(2\sigma^2)} + c$ . The mean,  $\mu$  has value 3.96 and the full width at half maximum, FWHM ( $\approx 2.36\sigma$ ) has value 1.71.

PU ratio vs sunspot area variation. The fit-parameters and one-sigma errors are listed in Table [3.9].

A	B	C	$\chi^2$
4.454(0.044)	$-3.0(0.3) \times 10^{-3}$	$3.4(0.7) \times 10^{-8}$	20.3174

**Table 3.9:** Fit-parameters and one-sigma errors (in brackets), and chi-square values for the quadratic fit ( $A + B(x) + C(x^2)$ ) for penumbra-umbra area ratio vs sunspot area (Figure [3.11]). The data set used for this plot was SIII (see Section [3.2]).

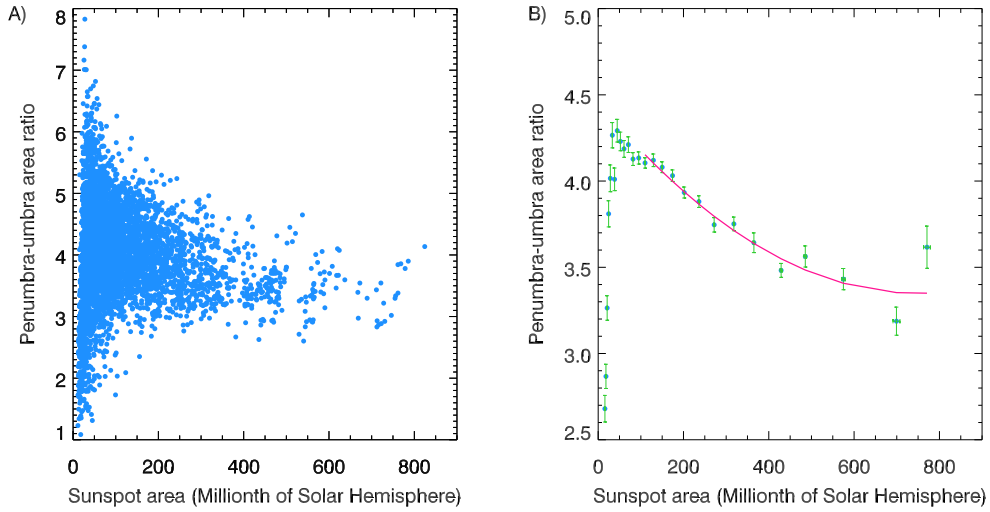


**Figure 3.11:** The variation of Penumbra-umbra area ratio with sunspot area. **A**, the scatter plot; **B**, the binned-data plot (area binned into 35 equally-spaced bins in log-space starting from 5 MSH to 850 MSH). A quadratic fit ( $A + B(x) + C(x^2)$ ) (in solid-line) is fitted to the binned data (**B**). The data set used for this plot was SIII (see Section [3.2]).

### 3.3.6 Sunspot-umbra area ratio

The distribution of sunspot to umbra area ratio (SU) of the data set SIII of sunspots is shown in Figure [3.12]. The mean of a Gaussian function fit to this distribution has the value 4.96 which is close to the literature value of 5 for the sunspot to umbra area ratio. The SU ratio also shows a slow decreasing trend with the sunspot area as shown in Figure [3.13] with a quadratic fit to the binned data and corresponding fit-parameters in Table [3.10].

### 3.3.7 Leading and following sunspots

The leading and the following polarities of an active region shows asymmetry in their morphology, where the leading polarity flux tends to be concentrated into a well-formed sunspot, whereas the following polarity flux tends to appear more fragmented and dispersed (Bray and Loughhead, 1979). To examine whether the umbral intensity values or the penumbra-umbra area ratios have radical difference among the leading and following sunspots, we first

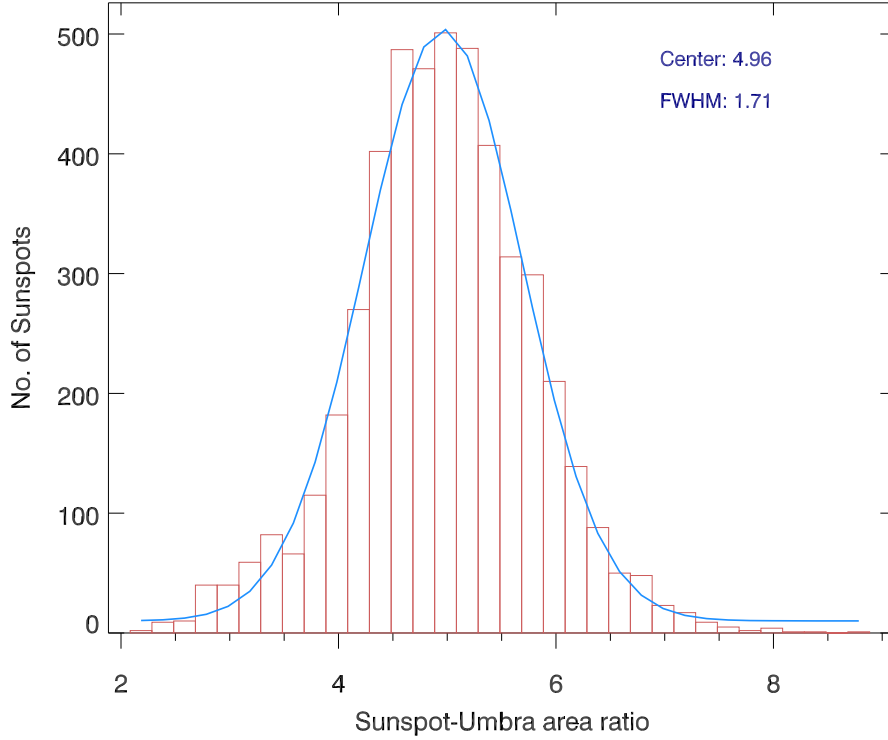


**Figure 3.12:** The distribution of Sunspot-umbra area ratio for the data set SIII. The Gaussian function ( $G(x)$ ) (solid-line) is fitted to the distribution, where ( $G(x) = \frac{1}{\sigma\sqrt{2\pi}}e^{-(x-\mu)^2/(2\sigma^2)} + c$ ). The mean,  $\mu$  has value 4.96 and the full width at half maximum, FWHM ( $\approx 2.36\sigma$ ) has value 1.71.

A	B	C	$\chi^2$
5.456(0.044)	$-3.0(0.3) \times 10^{-3}$	$3.4(0.7) \times 10^{-8}$	20.3462

**Table 3.10:** Fit-parameters and one-sigma errors (in brackets), and chi-square values for the quadratic fit ( $A+B(x)+C(x^2)$ ) for sunspot to umbra area ratio vs sunspot area (Figure [3.13]). The data set used for this plot was SIII (see Section [3.2]).

distinguished the regular sunspots data set into leading and following regions. To achieve this, we matched the analyzed regular sunspots (data set SII) with the Debrecen observatory’s catalog of sunspots derived from MDI, where the group information as well as their leading and preceding sunspots information are listed.

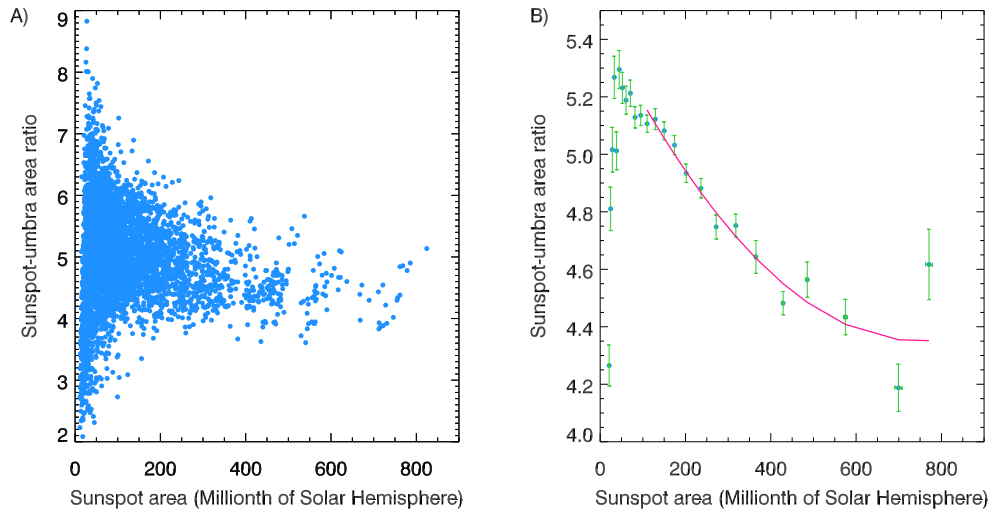


**Figure 3.13:** The variation of sunspot-umbra area ratio with sunspot area. **A**, the scatter plot; **B**, the binned-data plot (area binned into 35 equally-spaced bins in log-space starting from 5 MSH to 850 MSH). A quadratic fit ( $A + BX + Cx^2$ ) (in solid-line) is fitted to the binned data (**B**). The data set used for this plot was SIII (see Section [3.2]).

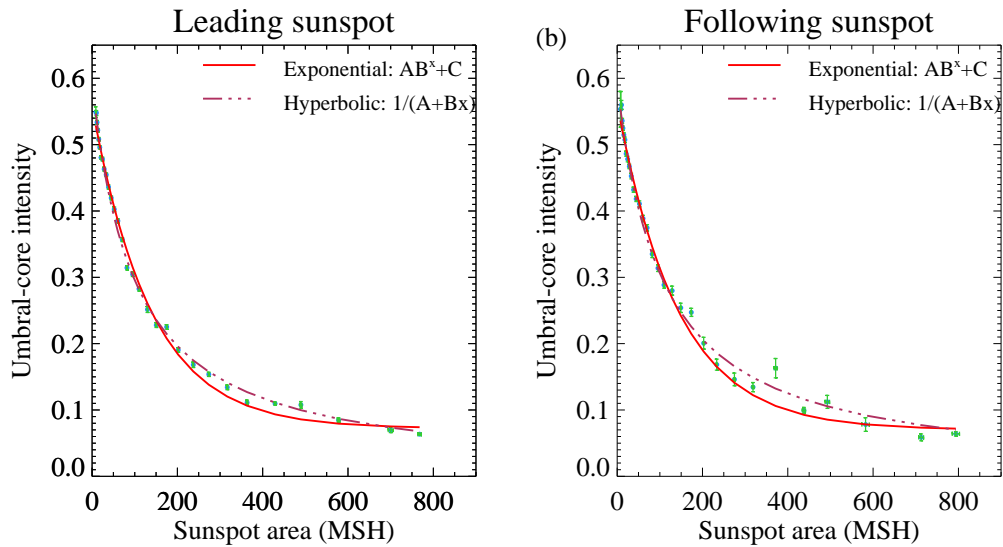


**Figure 3.14:** The variation of umbral-core intensity with sunspot area (in MSH; with area binned into equally-spaced 35 bins in log-scale starting from 5 MSH to 850 MSH) along with the exponential (solid curve) and hyperbolic (triple-dot-dashed) fit functions for (a) Leading sunspots, and (b) following sunspots. The error bars represents the standard errors.

In Figure [3.14] is shown the sunspot area dependence of umbral-core intensity separately for leading sunspots and preceding sunspots, with the

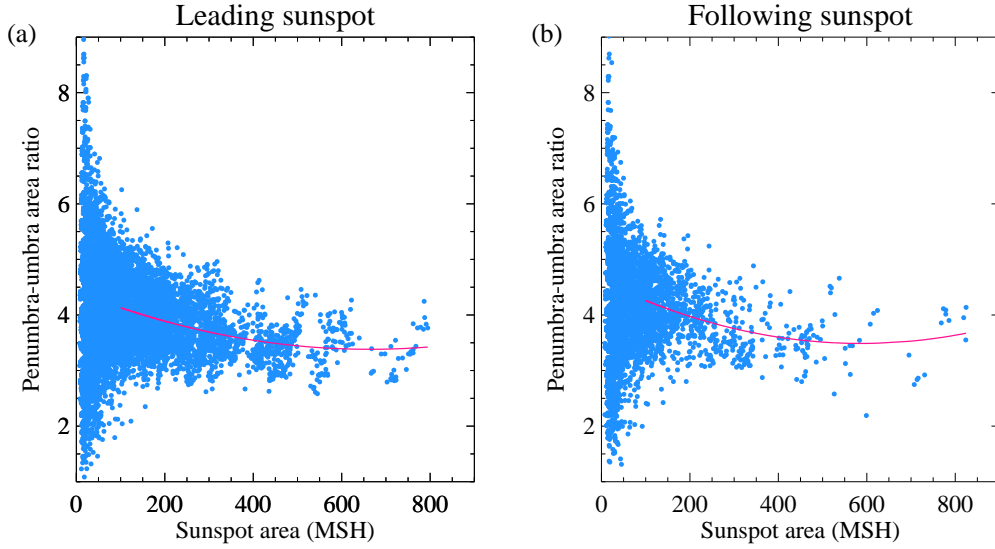


**Figure 3.15:** Variation of PU ratio with the sunspot total area for (a) Leading sunspots and (b) for following sunspots. The solid-curve in both plots are the polynomial fit (of two degree).

Parameter	A	B	C	$\chi^2$
<b>Umbral-core intensity</b>				
Exponential	0.487(0.001)	0.993(0.0001)	0.072(0.001)	14.11
Hyperbolic	1.678(0.005)	0.017(0.0001)	-	6.29
<b>PU ratio</b>				
Quadratic	4.419(0.032)	$-3.0(0.2) \times 10^{-3}$	$(4.0(0.6))10^{-8}$	898.97

**Table 3.11:** Fit-parameters and one-sigma errors (in brackets), and chi-square values for  $(AB^x + C)$  and Hyperbolic  $(1/(A + Bx))$  functions for umbral-core intensity vs sunspot area (MSH) (Figure 3.14) and quadratic-fit  $(A + B(x) + C(x^2))$  of PU ratio vs sunspot area (MSH) (Figure 3.15) for leading sunspots.

obtained exponential and hyperbolic fit functions. The plot and also the obtained fit parameters (listed in Tables 3.11 & 3.12) shows that there is no significant difference in area and umbra-core intensity relation between the leading and following regular sunspots of magnetic bipoles and matches with the results obtained for complete regular sunspot data (Table 3.1). Also, leading and following sunspots have similar ratio of penumbra to umbra area (Figure 3.15) and follows similar decreasing rate with the increasing sunspot size.

Fit function	A	B	C	$\chi^2$
<b>Umbral-core intensity</b>				
Exponential	0.492(0.003)	0.993(0.0001)	0.070(0.003)	5.63
Hyperbolic	1.686(0.007)	0.016(0.0002)	-	3.60
<b>PU ratio</b>				
Quadratic	4.609 (0.056)	$-4.0(0.4) \times 10^{-3}$	$(5.5(1.0))10^{-8}$	262.99

**Table 3.12:** Fit-parameters and one-sigma errors (in brackets), and chi-square values for ( $AB^x + C$ ) and Hyperbolic ( $1/(A + Bx)$ ) functions for umbral-core intensity vs sunspot area (MSH) (Figure 3.14) and quadratic-fit ( $A + B(x) + C(x^2)$ ) of PU ratio vs sunspot area (MSH) (Figure 3.15) for preceding sunspots.

### 3.3.8 Verification of results via thresholding method

In the present study we had extracted sunspots via automated method. In literature most of the sunspot properties had been obtained by extraction of sunspot using thresholding method, that is by choosing a global threshold intensity for the umbra-penumbra and penumbra-photosphere boundaries. While in automated procedure adopted here, does not relate to assign particular values of intensity to these boundaries. So there might be difference in selection of regions from images in thresholding and our automated procedure, which may lead to different range of intensity and area estimations of features of interest.

Parameter	Fit function	A	B	C	$\chi^2$
Umbral-core intensity	exponential	0.444(0.004)	0.994(0.0001)	0.083(0.004)	5.524
	hyperbolic	1.794(0.011)	0.013(0.0002)	-	9.43
Umbral-mean intensity	Exponential	0.203(0.003)	0.995(0.0002)	0.393(0.004)	7.34
	Logarithmic	0.750(0.003)	-0.120(0.001)	-	25.24
Penumbra-mean intensity	Quadratic(scatter plot)	0.853(0.001)	$-10^{-4}(0.0000)$	$1.2(0.1)(10^{-9})$	0.12
	Quadratic (binned plot)	0.854(0.001)	$-10^{-4}(0.0000)$	$(1.2(0.1))(10^{-9})$	53.13
PU ratio	Quadratic	4.480(0.072)	-0.002(0.001)	$(1.9(1.2))10^{-8}$	14.98
TU ratio	Quadratic	5.480(0.072)	-0.002(0.001)	$(1.9(1.2))10^{-8}$	14.98

**Table 3.13:** Fit-parameters and one-sigma errors (in brackets), and chi-square values for the Exponential ( $AB^x + C$ ) and Hyperbolic ( $1/(A + Bx)$ ) functions for umbral-core intensity vs sunspot area (MSH) (Figure [3.1]). The data set used for this plot was SIII (see Section [3.2]).

To check the consistency of results presented in this work, we also derived the sunspots parameters using intensity threshold for identification of

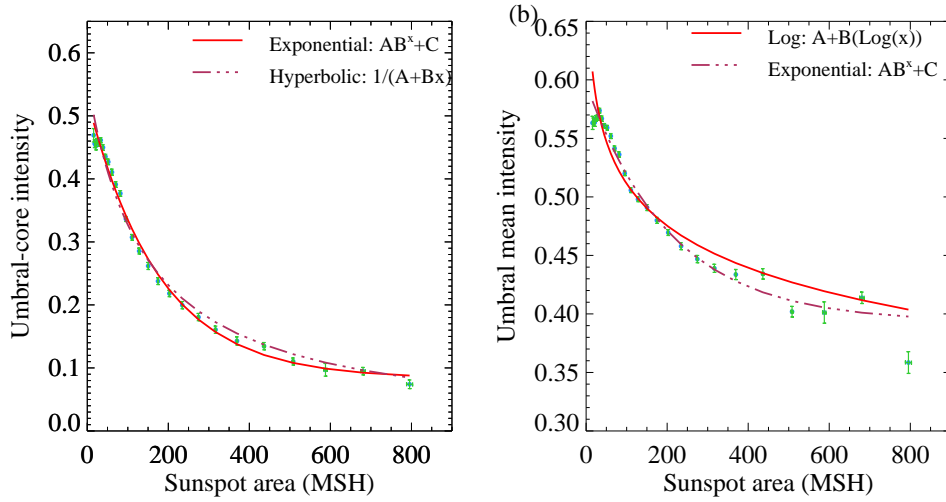


**Figure 3.16:** Variation of (a) umbral-core and (b) umbral-mean intensity with sunspot area (MSH) for sunspots identified using thresholding method. The sunspot area are binned into equally-spaced 35 bins in log-scale starting from 5 MSH to 850 MSH. The error-bars represents the standard errors.

sunspots. We obtained threshold intensities of 0.616 and 0.932 for umbral and penumbra outer boundaries respectively, using the cumulative histogram method described in (Mathew *et al.*, 2007). With this threshold intensity we did re-identification of regular sunspots of data set SII from the continuum images, and calculated the sunspot parameters of each identified region.

In Figures 3.16, 3.17, & 3.18 are plotted the umbral-core and umbral-mean intensity vs sunspot area; penumbra-mean intensity vs area; and PU ratio and TU ratio vs sunspot area respectively for sunspots obtained via thresholding. In Table [3.13] are listed the fit-parameters for all these relations. All the results obtained with thresholding are in agreement with the results obtained in the present study.

### 3.3.9 Temporal and center-to-limb variation

In this section we will investigate the solar-cycle dependencies and center-to-limb variation in the umbral-core intensity and penumbra-umbra area ratio for the sunspots sampled from the complete solar cycle 23 and the

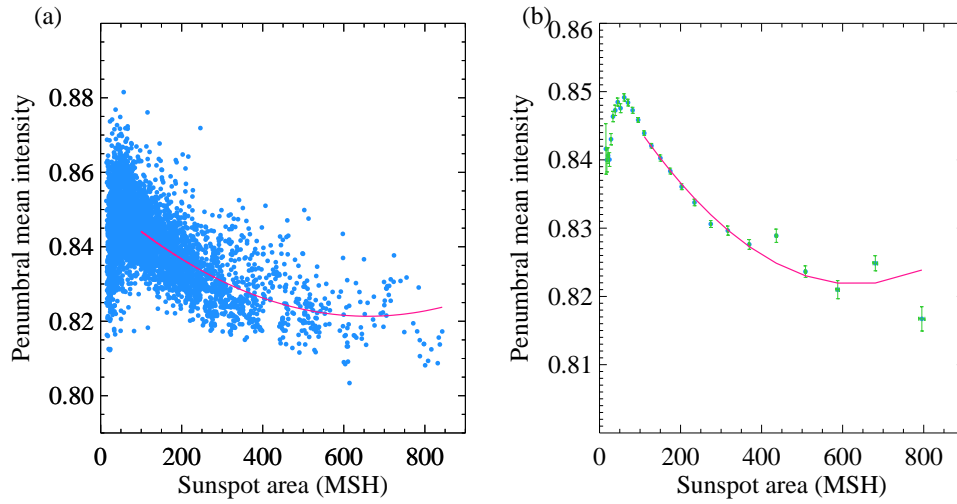


**Figure 3.17:** Variation of penumbral-mean intensity with sunspot area (MSH) in (a) scatter plot and (b) area log-binned plot, for sunspots identified using thresholding method. The error-bars represents the standard errors. The fit parameters of quadratic function (solid curve) are listed in the Table 3.13.

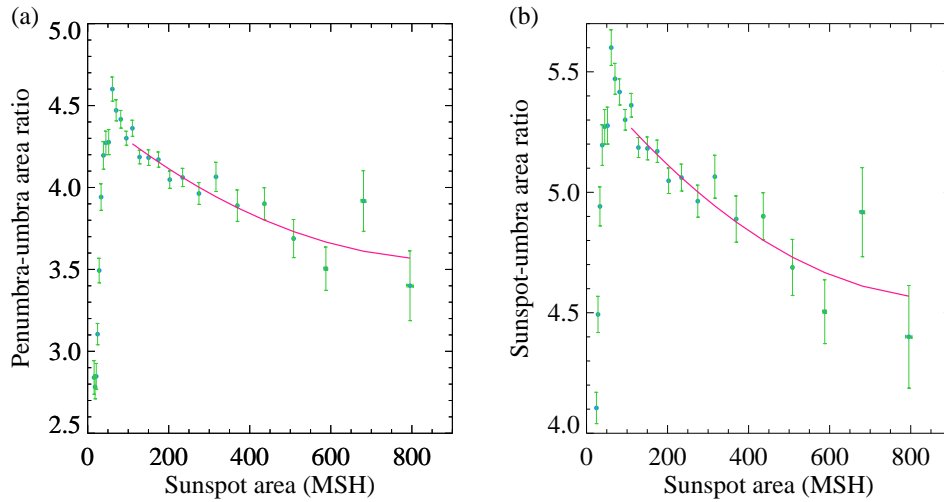


**Figure 3.18:** Variation of (a) PU ratio and (b) TU ratio with sunspot area (MSH) for sunspots identified using thresholding method. The sunspot area are binned into equally-spaced 35 bins in log-scale starting from 5 MSH to 850 MSH. The error-bars represents the standard errors. The fit parameters of quadratic function (solid curve) are listed in the Table 3.13.

rising phase of cycle 24 (May 1996 to April 2011).

### 3.3.9.1 Umbral-core intensity

We have seen in the Section [3.3.1], that the umbral-core intensity decreases with sunspot area. Hence to study the dependency of sunspot brightness on solar-cycle phase, we need to mitigate the fluctuations in intensity due to the variations in sunspots size with the cycle phase. From data set SIII, we segregated three ranges of sunspots size *i.e.*; small (30-55 MSH); intermediate (70-100 MSH), and large (210-300 MSH) sunspots, such that for each size range core-intensity has small variations with spot size. We looked for the temporal variation in umbral-core intensity for each size range of sunspots.

Spot size-range	A	B	$\chi^2$	Slope/ $\sigma$
30-55 MSH	-3.699(4.822)	0.002(0.002)	0.0014	0.771
70-100 MSH	7.815(4.897)	-0.004(0.002)	0.0015	-1.601
210-300 MSH	-5.859(8.413)	0.003(0.004)	0.0045	0.697

**Table 3.14:** Fit-parameters, one-sigma errors (in brackets), chi-square value, and slope to  $1\sigma$  ratio for straight-line fit ( $A + Bx$ ) to core-intensity variation with solar-cycle phases, separately for small, intermediate and large sunspot size ranges shown in Figure [3.19]. The data set used for this plot was SIII (see Section [3.2]).

Spot size-range	A	B	$\chi^2$	Slope/ $\sigma$
30-55 MSH	-0.123(0.122)	0.138(0.126)	0.0001	1.093
70-100 MSH	0.361(0.174)	-0.389(0.179)	0.0002	-2.171
210-300 MSH	-0.124(0.138)	0.134(0.142)	0.0001	0.940

**Table 3.15:** Fit-parameters, one-sigma errors (in brackets), chi-square value, and slope to  $1\sigma$  ratio for straight-line fit ( $A + Bx$ ) to core-intensity variation with heliocentric positions separately for small, intermediate and large sunspot size ranges shown in Figure [3.20]. The data set used for this plot was SIII (see Section [3.2]).

Figures 3.19(a-c) shows the variation of average of measured core-intensity with the cycle phase for small, intermediate and large sunspots respectively. The x-axis was binned into two years period starting from June 1997, and the data for period before June 1997 was also included in the plot as one bin at the start. For each size range plot, a second y-axis on the right shows the sunspot area scale in MSH, and also plotted the average of sunspot

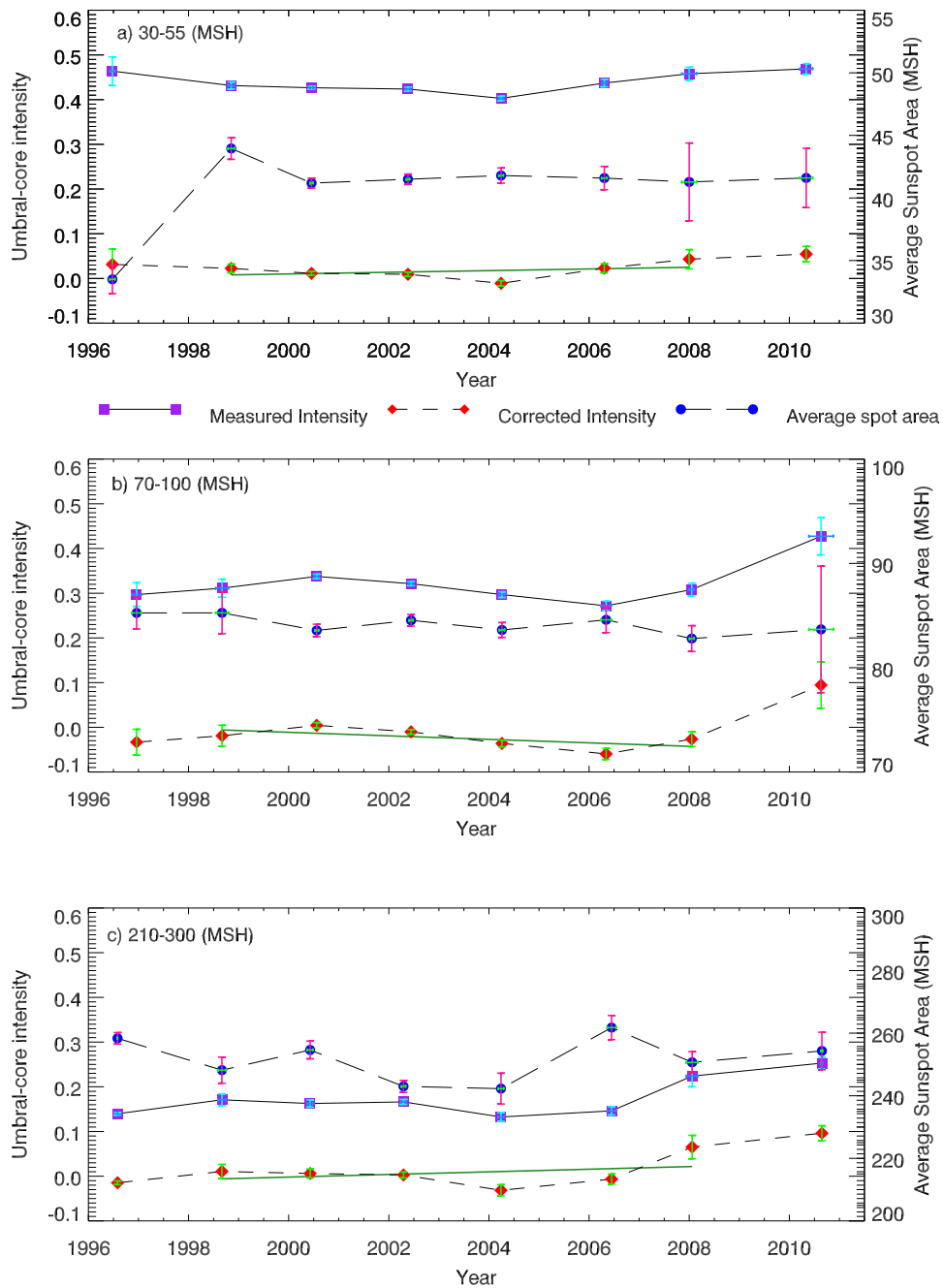


**Figure 3.19:** The variation of umbra-core intensity with solar-cycle phase, for three different sunspot size groups; **a)** 30-55 MSH, **b)** 70-100 MSH, and **c)** 210-300 MSH. The data is binned into 2 years bin starting from June 1997, and also with an additional bin for data between 1996 to June, 1997. The y-axis on right has the sunspot area scale in MSH. Shown in the plot is the average of measured umbral-core intensity (square) and the average sunspot area (circle) in each bin. Also plotted the intensity corrected for the average spot area in each bin (diamonds). A straight-line is fitted (solid-line) to the corrected intensity from period between June 1997 to May 2008. The fit-parameters and one-sigma errors are listed in Table [3.14].

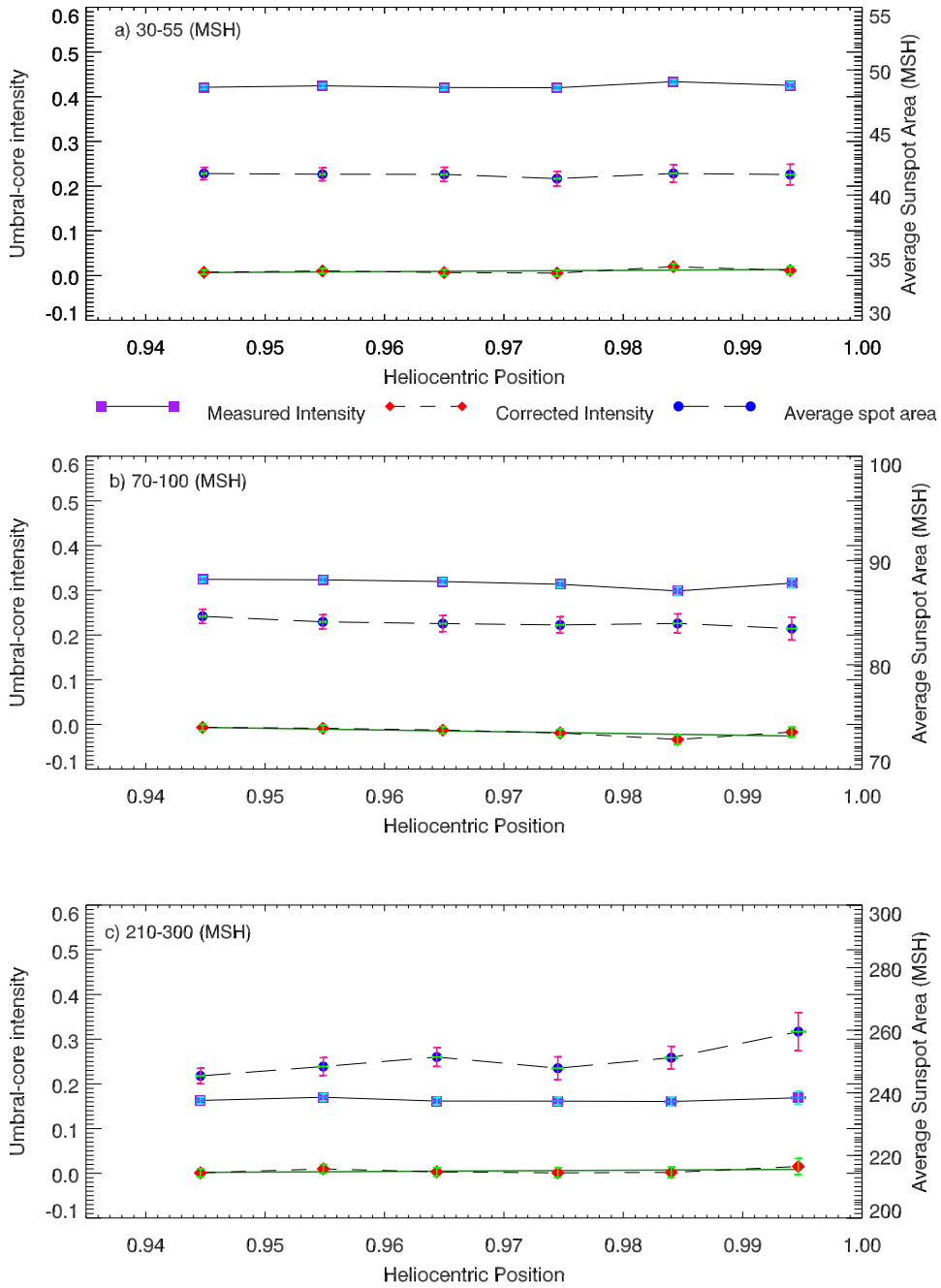


**Figure 3.20:** The variation of umbral-core intensity with heliocentric position, for three different sunspot size groups; **a)** 30-55 MSH, **b)** 70-100 MSH, and **c)** 210-300 MSH. The data is binned into 2 years bin starting from June 1997, and also with an additional bin for data between 1996 to June, 1997. The y-axis on right has the sunspot area scale in MSH. Shown in the plot is the average of measured umbral-core intensity (square) and the average sunspot area (circle) in each bin. Also plotted the intensity corrected for the average spot area in each bin (diamonds). A straight-line is fitted (solid-line) to the corrected intensity from period between June 1997 to May 2008. The fit-parameters and one-sigma errors are listed in Table [3.15].

area for each bin. This was to check the effect of average area on the average of measured core-intensity for a given time period. For each plot, we calculated umbral-core intensities for mean sunspot area values using the exponential function obtained in Fig. [3.1(b)], and then for each bin, this calculated intensity was subtracted from the average of measured umbral-core intensity to obtain the corrected intensity (corrected for sunspot area dependency). We fitted a straight-line to this corrected intensity data within the period of June 1997 to May 2008, that is covering only solar cycle 23 and excluding the contribution from the declining phase of previous cycle 22 and the rising phase of new cycle 24. The fit-parameters of straight-lines of all three plots are listed in Table [3.14]. For all the spot size ranges we did not find any significant variation with solar cycle phase, with any variation being below 2 sigma.

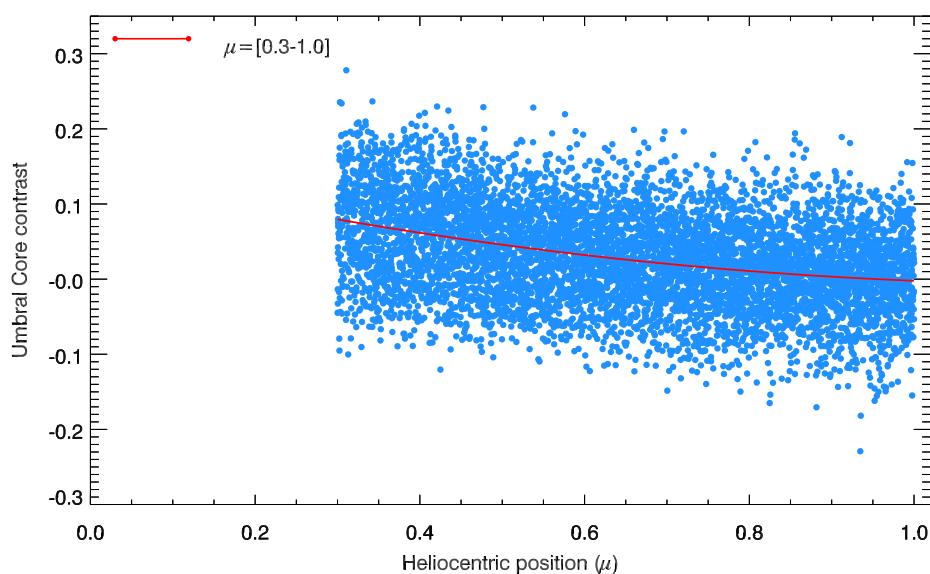


**Figure 3.21:** The variation of residual umbral-core intensity (corrected for spot area and umbral-shape effect) with heliocentric positions,  $\mu$ . The  $\mu$  is in the range 0.3 to 1.0. A quadratic fit (solid-line) to the data is also shown. The fit-parameters and one-sigma errors are listed in Table [3.16]. The data set used for this plot was S1 (see Section [3.2]).

Similarly for the center-to-limb-variation of umbral core intensity in the three sunspot size ranges (shown in Figures [3.20](a-c)), no trend was observed at the 2 sigma level (straight-line fit parameters listed in Table [3.15]).

However, this data set (SIII) covers only  $\mu$  from 0.94 to 1.0. Hence, we re-investigated the dependency of sunspot brightness measurement on  $\mu$  with sunspots from large range of  $\mu$ , *i.e.* from 0.3 to 1.0. We excluded the sunspots with  $\mu$  less than 0.3, since due to pronounced projection-effect and also possibly wilson-effect close to the limb, identification of umbral regions could be erroneous, hence misleading values of umbral-core intensities.

A	B	C	$\chi^2$
0.146(0.004)	-0.252(0.011)	0.104(0.008)	241.4781

**Table 3.16:** Fit-parameters, one-sigma errors (in brackets), chi-square value, and slope to  $1\sigma$  ratio for quadratic fit ( $A+Bx+Cx^2$ ) to residual core-intensity variation with heliocentric position as shown in Figure [3.21]. The data set used for this plot was SIII (see Section [3.2]).

For, this study the suitable data set is SI, having regular sunspots with single umbra, within the [0.3-1.0] heliocentric positions. In Sections 3.3.1 & 3.3.2, we had observed that umbral-core intensity depends on sunspot area, as well as it has small dependency on shape of umbra. Hence, first we removed these two dependencies from the core-intensity to figure-out the variation with  $\mu$ . In Figure [3.6], we obtained the umbral-core intensity residue, that was corrected for the sunspot area variation using the exponential function, and the residue has approximately linear dependency on the umbral-circularity measure (Table [3.5]). Further, we calculated the core-intensity for given circularity indexes using this linear function and then subtracting this from the core-contrast of Fig. [3.6]. Figure [3.21] shows the variation of this new residual core-intensity with heliocentric positions ( $\mu$ ). A quadratic-fit (solid line) fitted to this scatter plot is shown, with parameters listed in Table [3.16]. The contrast decreases by approximately 0.1 from  $\mu = 1$  to  $\mu = 0.3$  on average, irrespective of the absolute contrast.

### Multi-variate analysis

We took another approach to find the variation of umbral-core intensity

on sunspot area, umbral shape, and heliocentric position, they all being taken together into consideration. We did a multivariate analysis, and constructed a function,  $F(x)$ , having combination of an exponential function (to represent area dependency), a quadratic function (for  $\mu$ ), and a linear function (for circularity). That is,

$$F(x) = P_0 + P_1.P_2^{x_1} + P_3x_2 + P_4x_2^2 + P_5x_3 \quad (3.3)$$

where,  $x_1$  is the sunspot area,  $A_s$ ;  $x_2$  is heliocentric position,  $\mu$  in the range [0.3-1.0]; and  $x_3$  is the umbral-circularity measure  $U_c$ . The fit-parameters,  $P_{0-5}$  and the corresponding one-sigma errors for this multivariate function is listed in the Table [3.17]. The fit-parameters for the exponential ( $P_{1-2}$ ) and the linear ( $P_5$ ) functions part of  $F(x)$  are in accordance with that obtained in Figures 3.1 & 3.6. However, the quadratic part for the  $\mu$  dependence, ( $P_{3-4}$ ) have large one-sigma errors.

$P_0$	$P_1$	$P_2$	$P_3$	$P_4$	$P_5$	$\chi^2$
0.431(0.066)	0.528(0.019)	0.994(0.001)	-0.293(0.182)	0.121(0.127)	-0.319(0.038)	228.97

**Table 3.17:** Fit-parameters, one-sigma errors (in brackets), chi-square value, for the multivariate function,  $F(x)$  in Eqn. [3.3] for umbral core intensity versus sunspot area, heliocentric position, and umbral circularity measure.

The intensity values corresponding to exponential, quadratic and the linear part of the function,  $F(x)$  corresponding to the sunspot area ( $A_s$ ), heliocentric position ( $\mu$ ), and umbral-circularity measure ( $U_c$ ) respectively are calculated in the following manner:

$$I_A = P_0 + P_1 * P_2^{A_s} , \quad (3.4)$$

$$I_\mu = P_3\mu + P_4\mu^2 , \quad (3.5)$$

$$I_{uc} = P_5U_c. \quad (3.6)$$

The residual intensity after removal of  $I_A$  and  $I_{uc}$  from measured umbral

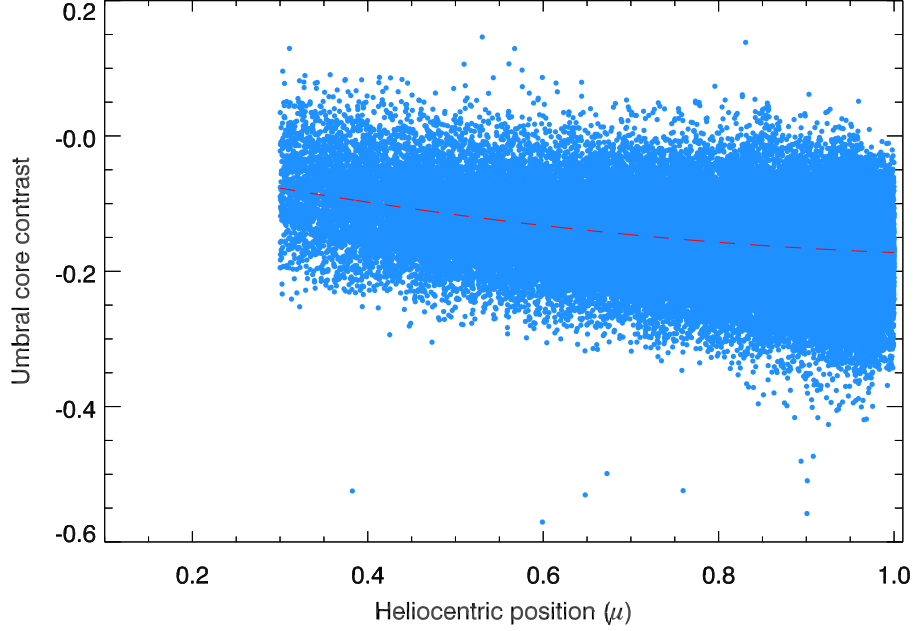


**Figure 3.22:** The variation of residual umbral-core intensity ( $\Delta I_1$ ) with heliocentric position,  $\mu$ . The  $\Delta I_1$  is the residual umbral-core intensity after removal of area and circularity dependency (Eqn [3.7]). The quadratic part derived from fitting of multivariate functional in Eqn [3.3] is plotted (dashed-lines). The data set used for this plot was SI (see Section [3.2]).

core intensity,  $I_u$  using Eqn 3.4 is:

$$\Delta I_1 = I_u - (I_A + I_{uc}) \quad (3.7)$$

We also further checked the dependency of the umbral-core intensity on sunspot area and the circularity measure derived by the multivariate analysis. For this we calculated the intensity,  $I_2$  given by:

$$I_2 = P_0 + P_1 * P_2^{A_s} + P_3 \langle \mu \rangle + P_4 \mu^2 + P_5 \langle U_c \rangle \quad (3.8)$$

where,  $\langle \mu \rangle$  &  $\langle U_c \rangle$  are the mean values of heliocentric position,  $\mu$  and umbral-circularity measure,  $U_c$ . Thus,  $I_2$  depicts the core-intensity variation with sunspot area  $A_s$  of sunspots with all having average value of  $\mu$  and  $U_c$ . Figure

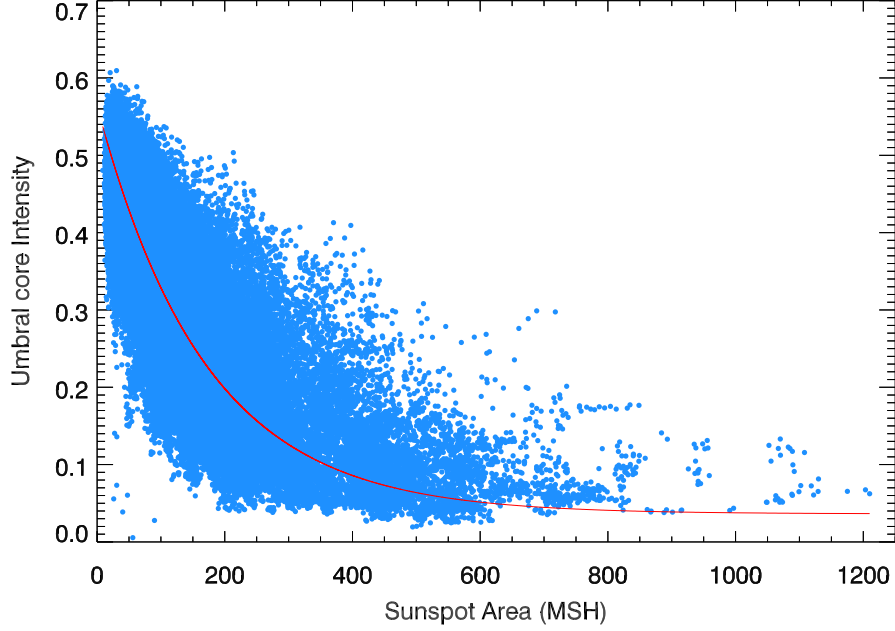


**Figure 3.23:** The variation of umbral-core intensity with sunspot area for sunspots with heliocentric position range of [0.3-1.0] (data set S1). The  $I_2$  (dashed-line) is the umbral-core intensity calculated using the function  $F(x)$  (Eqn [3.7]) for all sunspot areas and using mean value of circularity index and heliocentric position (see Eqn [3.8]).

[3.23] shows the scatter plot of umbral-core intensity with sunspot area of data set S1, while the dashed-line is the variation of  $I_2$  with area. Thus,  $I_2$  represents a good-fit to the core-intensity versus sunspot area and shows asymptotic value of intensity beyond 600 MSH.

Similarly, the residual intensity after removal of sunspot area and heliocentric position dependency is given by:

$$\Delta I_3 = I_u - (I_A + I_\mu) \quad (3.9)$$

Figure [3.24] shows the variation of residual core-intensity,  $\Delta I_3$  with the umbral-circularity measure. The dashed-line is the variation of the intensity calculated from the linear part, *i.e.*  $I_{uc}$  given in Eqn [3.4].

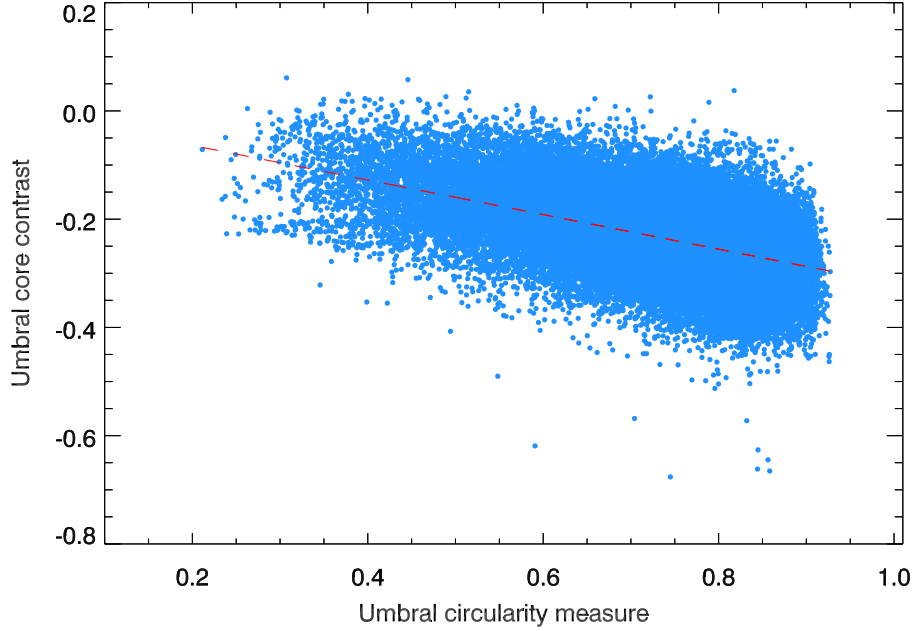


**Figure 3.24:** The variation of umbral-core intensity with umbral-circularity measure for sunspots with heliocentric position range of [0.3-1.0] (data set S1). The  $\Delta I_3$  (dashed-line) is the residual umbral-core after removal of intensity contribution from the sunspot areas and heliocentric position (see Eqn [3.9]).

### 3.3.9.2 Penumbra-umbra area ratio

Similar to investigations in Section [3.3.9.1], we studied solar-cycle variation and center-to-limb variation of Penumbra-umbra area ratio (PU ratio) for small, intermediate, and large size sunspots. In Figure [3.25(a-c)] is shown the variation of average of PU ratio with the solar cycle phase, where time is binned in two years period (see Section [3.3.9.1]).

Spot size-range	A	B	$\chi^2$	Slope/ $\sigma$
30-55 MSH	10.729(45.646)	-0.003(0.022)	0.126	-0.143
70-100 MSH	-75.737(67.876)	0.039(0.033)	0.286	1.177
210-300 MSH	-56.139(33.751)	0.029(0.017)	0.073	1.178

**Table 3.18:** Fit-parameters, one-sigma errors (in brackets), chi-square value, and slope to  $1\sigma$  ratio for straight-line fit ( $A + Bx$ ) of penumbra-umbra area ratio variation with solar-cycle phase separately for small, intermediate and large sunspot size ranges shown in Figure [3.25]. The data set used for this plot was SIII (see Section [3.2]).

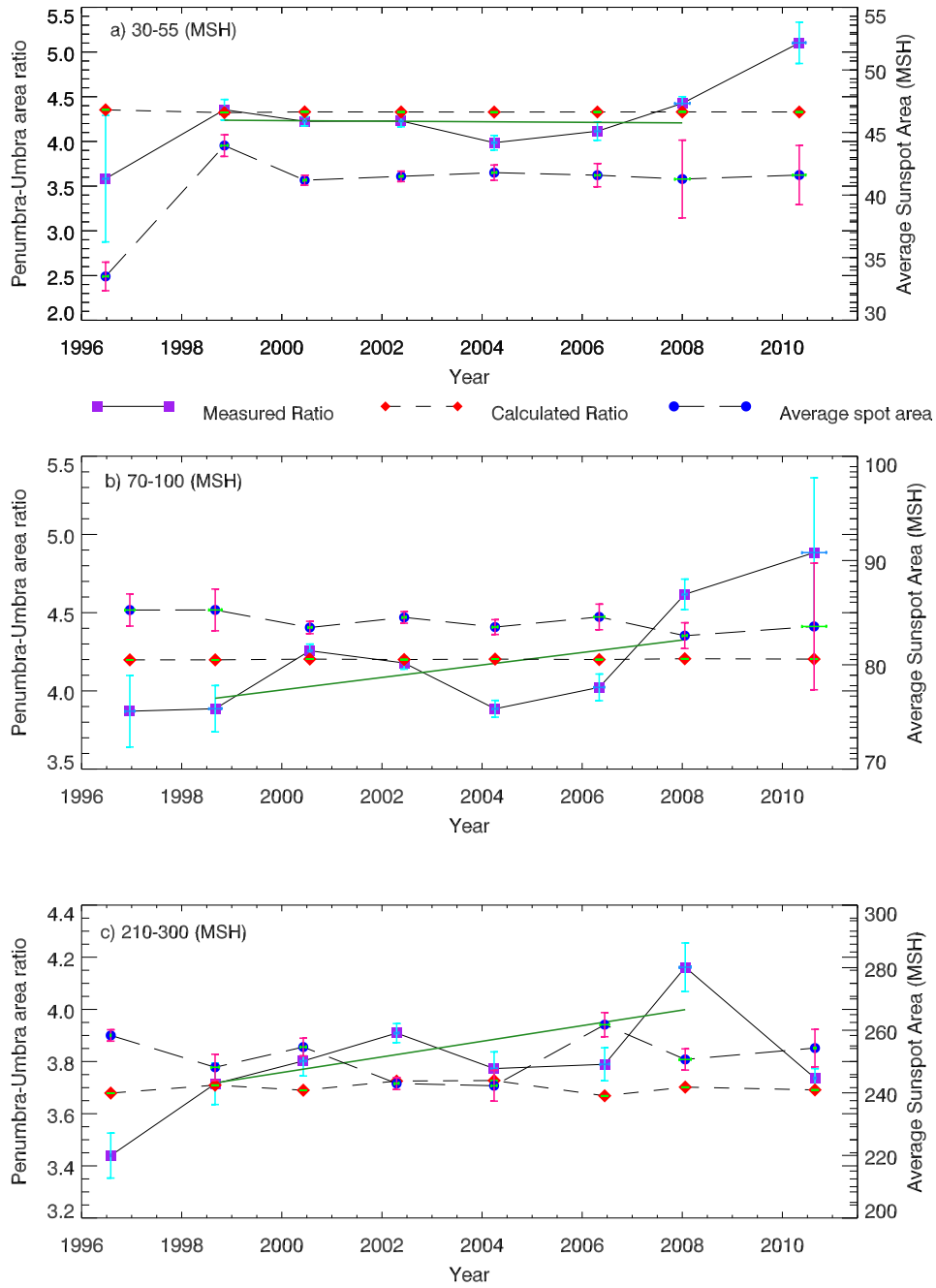


**Figure 3.25:** The variation in penumbra-umbra area (PU) ratio with solar-cycle phase, for three different sunspot size groups; **a)** 30-55 MSH, **b)** 70-100 MSH, and **c)** 210-300 MSH. The data is binned into 2 years bins starting from June 1997, and also with an additional bin for data between 1996 to June, 1997. The y-axis on right has the sunspot area scale in MSH. Shown in the plot is the average of measured PU ratio (square) and the average sunspot area (circle) in each bin. Also plotted the calculated PU ratio for the average spot area in each bin (diamonds) using parameters in Table [3.9]. A straight-line is fitted (solid-line) to the PU ratio from period between June 1997 to May 2008. The fit-parameters and one-sigma errors are listed in Table [3.18].

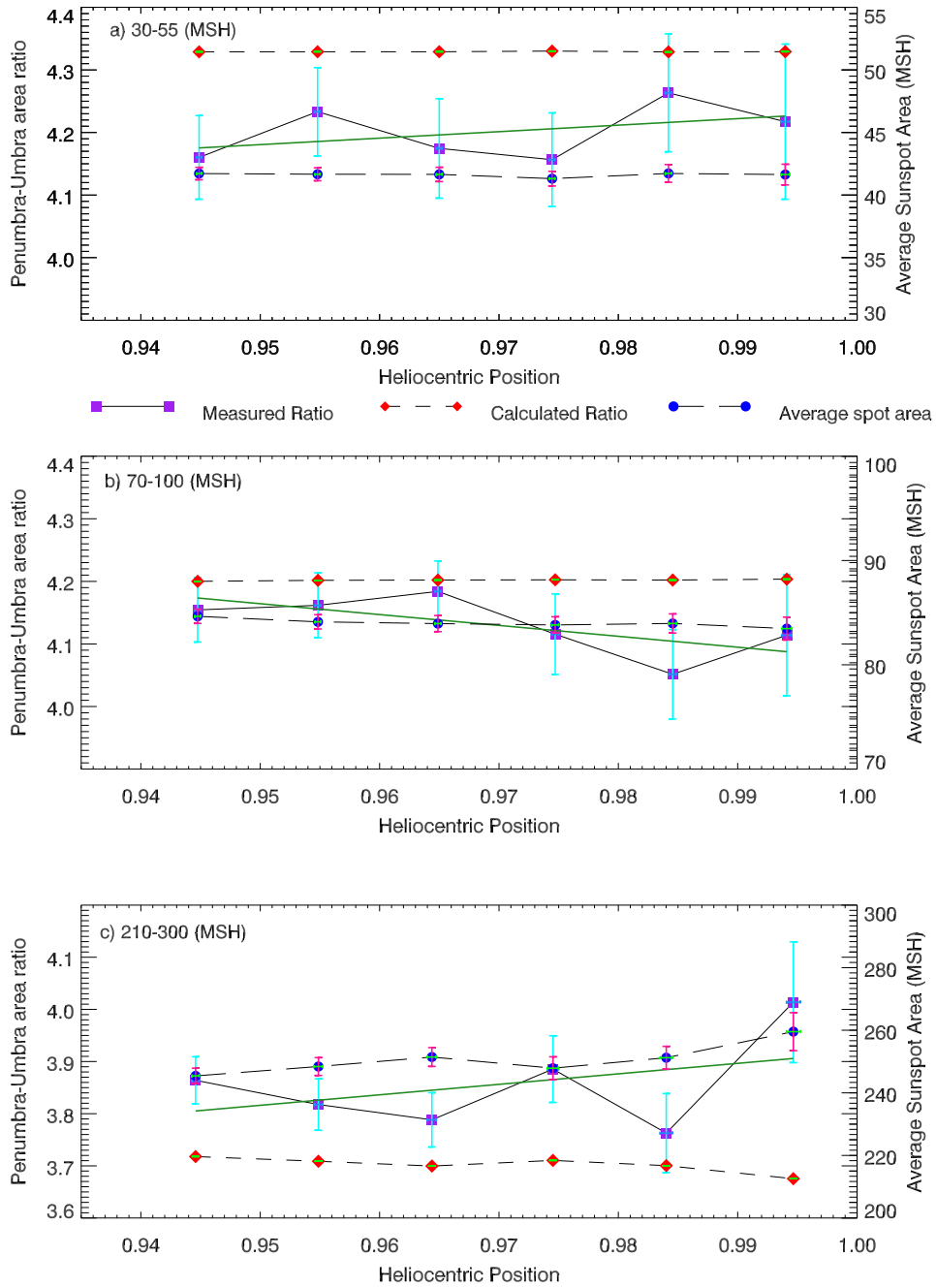


**Figure 3.26:** The variation in penumbra-umbra area (PU) ratio with heliocentric position, for three different sunspot size groups; **a)** 30-55 MSH, **b)** 70-100 MSH, and **c)** 210-300 MSH. The data is binned into 2 years bins starting from June 1997, and also with an additional bin for data between 1996 to June, 1997. The y-axis on right has the sunspot area scale in MSH. Shown in the plot is the average of measured penumbra-umbra area ratio (square) and the average sunspot area (circle) in each bin. Also plotted the calculated PU ratio for the average spot area in each bin (diamonds). A straight-line is fitted (solid-line) to the PU ratio from period between June 1997 to May 2008. The fit-parameters and one-sigma errors are listed in Table [3.19].

For the three sunspot size ranges, we did not find any significant variation in PU ratio over the period of solar cycle 23, with any variation being below 2 sigma. Similarly, PU ratio remains invariant for sunspots observed at different  $\mu$  ranging from 0.94 to 1.0.

Spot size-range	A	B	$\chi^2$	Slope/ $\sigma$
30-55 MSH	3.196(1.039)	1.037(1.071)	0.008	0.968
70-100 MSH	5.816(0.906)	-1.739(0.935)	0.006	-1.861
210-300 MSH	1.906(2.137)	2.010(2.203)	0.034	0.912

**Table 3.19:** Fit-parameters, one-sigma errors (in brackets), chi-square value, and slope to  $1\sigma$  ratio for straight-line fit ( $A + Bx$ ) of variation of penumbra-umbra area ratio with heliocentric position separately for small, intermediate and large sunspot size ranges shown in Figure [3.26]. The data set used for this plot was SIII (see Section [3.2]).

## 3.4 Summary and Discussion

### 3.4.1 Sunspot brightness and size

#### Umbral-core intensity

From the study of regular sunspots close to disk-center for period between 1996-2011, we found the non-linear relation of umbral-core intensity with the sunspot size (or umbral radius) and this is best represented by exponential function and hyperbolic function (Section [3.3.1]). The core brightness has nearly constant value (of about 0.1) past total sunspot area of 600 MSH or past umbral radius of  $\sim 12$  Mm. The two chosen types of function have the advantage that they remains positive for even larger spots than those analyzed in this study. Much larger spots are known to exist on more active Sun-like stars (Berdyugina, 2005; Strassmeier, 2002), even if some of the detected very large starspots are expected to be clusters of smaller spots (Solanki and Unruh, 2004). For example, Strassmeier (1999) observed with Doppler imaging on the active RS CVn binary HD 12545 which, in January 1998, had a spot that extended approximately  $12 \times 20$  solar radii. Hence, the chosen func-

tion can be used to extrapolate the minimum brightness of umbrae to spots detected using, *e.g.*, Doppler-imaging on Sun-like stars.

We had also checked the umbral-core intensity relation for distinct sunspot data set, in order to remove redundancy due to multiple contributions by long-lived sunspots. For this we had tracked the selected regular sunspots, and took their intensity and area parameters at the time when these spots had minimum value of core-intensity during their evolution. The distinct sunspots (also close to disk-center) agrees with the relation obtained with complete sunspot data set that includes multiple observations of same sunspot (Figure [3.2]).

The Mathew *et al.* (2007) studied about 200 regular sunspots close to disk-center obtained from stray-light-corrected MDI images between 1998-2004. They found a power-law relation between umbral-core intensity and umbral radii. Our exponential function fit was obtained from sunspots sampled in large number and that covers complete cycle 23 and it matches closely with their power-law function as shown in Figure [3.3]. During the ongoing work of this thesis, similar study was performed by two groups, Schad (2014) and Kiess, Rezaei, and Schmidt (2014) using higher resolution data (compared to MDI) of Hinode spectro-polarimeter (corrected for stray-light) and SDO/HMI respectively. Both groups obtained non-linear relation for umbral-core intensity and umbral radii, however, Schad (2014) used the logarithmic function representation while, Kiess, Rezaei, and Schmidt (2014) obtained power-law relation. The exponent of Mathew *et al.* (2007) power-law fit compares well with the exponent given by Kiess, Rezaei, and Schmidt (2014) which is around -1, and it is in approximation to the hyperbolic function used in our study. These two recent studies using relatively higher resolution images generally agrees with our results using MDI data; however, small and intermediate size sunspots appear to be cooler in their observations as shown in Figure [3.3]. There could be many possible reasons for this difference in intensity for small sunspots; Hinode and HMI observes at relatively shorter wavelength, hence

higher contrast in comparison to MDI since the umbral intensity contrast decreases with increasing wavelength (Maltby, 1970); the other possibility could be that the high resolution data has been able to observe darker regions within umbrae of small sunspots. Further detailed investigations are required with high resolution images to have proper reasoning of the observed difference.

In this study we found an interesting result of dependence of umbral-core intensity with the shape of umbra. We devised a circularity index, which is a measure of circularity of umbral region corrected for the perspective foreshortening. For regular sunspots with single umbra, the variation of umbral-core intensity to sunspot area changed for different range of circularity measures as shown in Figure [3.5]. The highly circular umbrae had relatively lowered range of core-intensity for all small to intermediate sunspot size range. However, beyond 400 MSH, the core-intensity was observed to be constant irrespective of umbral shape. To derive the core-intensity variation with the umbral-circularity index, we subtracted the area-dependent calculated intensities for respective sunspot area from the measured intensities. The calculated intensity was derived using the exponential function of the core-intensity and sunspot area relation. This area-corrected intensity (of sunspots from  $\mu \geq 0.94$ ) was observed to have linear decrease with the umbral circularity measure; the spots with large circularity measure are more darker as compared to those with small circularity measure or elongated shape.

We segregated the analyzed sunspots as leading and following sunspots, on the basis of their position with their parent sunspot-group. We observed that the leading and following sunspots have similar distribution of umbral intensity with area.

### **Umbral-mean intensity**

For many purposes the mean intensity of an umbra is more useful than the minimum intensity, particularly if sunspot properties are to be used to reconstruct global solar properties, *e.g.*, the solar irradiance, where umbral

and penumbral mean intensities (as a function of wavelength) are employed (Fligge, Solanki, and Unruh, 2000; Unruh, Solanki, and Fligge, 1999). Mean intensities are also a better guide to the properties of the poorly resolved starspots.

In our study we obtained that the umbral-mean intensity varies with the sunspot size similar to core intensity, however at slower rate. This is also best represented by an exponential function as shown in Figure [3.7]. The relation between umbral-mean intensity and umbral size was previously studied by Mathew *et al.* (2007), and they obtained a power-law function which also agrees with the present data set (Figure [3.8]). The umbral-mean intensity was observed to have a constant value of about 0.36 past sunspot area of 600 MSH.

### **Penumbral-mean intensity**

Alike umbral-core or mean intensity, the penumbra was observed to be darker for large sunspots relative to that for small sunspots (Section [3.3.4]). However, for sunspots smaller than 100 MSH, the penumbral-mean intensity shows an opposite trend with sunspot size; for sunspots of size  $< 100MSH$ , the penumbral region is darker for smaller sunspots. This lowered intensity could be an artifact because of limited resolution to efficiently distinguish umbra-penumbra boundary for small sunspots. This downturn observed for small sunspots was also present in Mathew *et al.* (2007) in their sampling of only 160 sunspots from stray-light-corrected SoHO/MDI continuum images. Other difference has been observed with the Mathew *et al.* (2007). The range of penumbral-mean intensity of present data is on lower side as compared to theirs. This might be due to difference in quiet-sun normalization of the two data sets and possibly different stray-light corrections. We had checked the penumbral boundary identification in the present-data using the thresholding method given in their paper, and found no deviation from the penumbral-mean intensity values as presented here with original sunspot data.

### 3.4.2 Solar-cycle and limb variation of sunspot brightness

It has been controversial whether the sunspot intensity and magnetic field strength exhibit a secular trend or solar-cycle variations. In order to derive the temporal variation of core intensity it is necessary to remove the variations of intensity caused by changes in sunspot area with time. Hence, we selected three sunspot size ranges; small, intermediate and large regular sunspots close to disk-center ( $\mu \geq 0.94$ ) to study the temporal variation. For all the three sunspots size groups from complete cycle 23, we did not find significant solar-cycle phase variation within 2 sigma level, which is in agreement with the earlier findings of Mathew *et al.* (2007).

For the sunspots within  $\mu$  of 0.94 to 1.0, we also did not find significant change in umbral-core intensity with  $\mu$  for sunspots of different size. In order to find center-to-limb variation in umbral intensity, we worked-out two different methods described below. For these two analysis, we used sunspots from broader  $\mu$  range, *i.e.*, from 0.3-1.0; we had not analyzed the data below  $\mu = 0.3$ , to avoid the uncertainties in stray-light corrections and in intensity measurement that occur in sunspots close to the limb due to perspective foreshortening.

As discussed earlier, the core intensity has strong non-linear dependence on sunspot size and also slight dependence on umbral shape. For each sunspot, we obtained residual umbral intensity by subtracting from its measured intensity the calculated intensity values for its respective sunspot size and circularity measure using the exponential and linear functions respectively as shown in Figure [3.21]. (These exponential and linear relations were derived using the sunspots close to disk-center, *i.e.*,  $\mu \geq 0.94$ , hence small effect of  $\mu$ .) We found that the core-intensity increases towards the limb, approximately on average an increase of 0.1 from disk-center to the  $\mu=0.3$  (in agreement with Norton and Gilman (2004)). We used a quadratic function for umbral-core

intensity and  $\mu$  relation.

The multivariate analysis was also performed for all regular sunspots obtained between 1996-2011 with  $\mu \geq 0.3$ , which incorporates the dependence of core-intensity on the sunspot area, the umbral-shape (circularity measure), and heliocentric position, taken all together (Section [3.3.9.1]). This study re-confirmed the exponential and linear functional relation of core-intensity with the sunspot area and umbral-circularity measure respectively. The multivariate analysis of this study also obtained the quadratic parameters for  $\mu$  dependence but with high sigma errors.

### 3.4.3 Penumbra-umbra and sunspot-umbra area ratio

It has been believed that the sunspots follows fairly closely a radial similarity rule, for example, the umbral area and the total sunspot area has a constant ratio and this ratio does not depend on sunspot area (Zwaan, 1977). The commonly accepted constant values of total sunspot area to umbra area ratio (SU ratio) is  $\sim 5$  and that of penumbra to umbra area ratio (PU ratio) is  $\sim 4$  (Allen, 1973). From our study, we found that the PU ratio as well as SU ratio decreases slightly with the increasing sunspot area (Sections [3.3.5] & [3.3.6]). However, the mean of the distribution of these two ratios for the given sample of sunspots close to disk-center are in agreement with these constant values listed above. The PU ratio has value on average 4.2 for sunspot smaller than 100 MSH and  $\sim 3.3$  for sunspots of size  $\sim 600$  MSH. Steinegger *et al.* (1990) and Brandt, Schmidt, and Steinegger (1990) found PU ratio of 4.16 and 3.1 for small and large spots, respectively. While Hathaway (2013) reported the average value of PU ratio of 5.5 for sunspot groups. In contrast to our study, this ratio has opposite trend in case of sunspot-groups; they found an increase from 5 to 6 as the group area increases from 100 to 2000 MSH. It appears that the complex sunspot-groups have extended penumbral regions as compared to isolated and regular sunspots. This indicates that the magnetic configuration complexity affects the penumbral region

formation. Rempel and Schlichenmaier (2011); Rezaei, Bello González, and Schlichenmaier (2012); Schlichenmaier *et al.* (2010a,b, and references therein) showed that the penumbral filaments orientation and extension is affected by the nearby emerging small flux regions. The relative sizes of the umbra and penumbra may well also depend on the atmospheric height at which they are measured. Wilson and Cannon (1968); Wilson and McIntosh (1969) have argued that the size of the umbra decreases with height while that of the penumbra increases.

Further we investigated the temporal as well as limb variation of PU ratio. Due to size dependency of PU ratio as observed here, we performed this study for three different sunspot size ranges, and we found no significant solar-cycle and limb variation within 2 sigma level.

### 3.5 Conclusion

We investigated some global properties of sunspots using sunspots parameters that were derived in consistent and efficient manner from SoHO/MDI continuum images which were corrected for limb-darkening, stray-light and foreshortening effects.

We found that the umbral core intensity has non-linear relation with the sunspot area or umbral effective radii, showing that the large sunspots have darker core as compared to small sunspots. The exponential function fits well to this non-linear trend. The umbral-core intensity has slight linear dependence on the umbral shape, the circular umbrae are darker than the elongated ones. The core intensity has small dependence on heliocentric position, it increases slightly towards the limb. In this study, we found no significant solar-cycle variation of umbral-core intensity. The umbral mean intensity versus sunspot area or umbral effective radii is also represented well by an exponential function. The mean penumbral intensity has been observed to reduce by a small amount with increased spot size. The Penumbra to umbra area ratio as well as total sunspot area to umbra area ratio has weak

dependence on sunspot area; large spots have reduced values of these ratios. The core-intensity and PU ratio dependence on area have similar trends for leading and following sunspots.

# Chapter 4

## Study of Differential Rotation of Sun

### 4.1 Introduction

Observations of solar convective surface reveals that it rotates differentially, characterized by faster equatorial regions and a monotonic decrease of angular velocity toward the poles by about 30% (Beck, 2000). Helioseismology has demonstrated that this strong differential rotation imprints the whole convective envelope and then becomes uniform in the radiative interior (Couvdat *et al.*, 2003; Schou, Antia, and *et al.*, 1998; Thompson *et al.*, 2003; Wilson, Burtonclay, and Li, 1997). This implies that the regions inside the sun occupied by differential rotation and convection almost coincide. In the context of mean field hydrodynamics, the differential rotation of the sun is explained by interaction of convection and rotation (Kitchatinov, 2013; Kosovichev, 2011; Miesch *et al.*, 2008). Convective flows in the rotating fluid experiences Coriolis force which has significant effect on convection; and convection also perturbs the rotation making it differential. On the other hand, according to the conventional scenario, twisting by differential rotation converts the poloidal field into toroidal and, in turn, the cyclonic turbulence generates back the poloidal field from toroidal, hence the cyclic solar magnetic activity (Charbonneau,

2010). Thus differential rotation of the convective envelope is a key ingredient of solar dynamo (Parker, 1955). In essence, it is important to understand the interplay of rotation, convective flows and magnetic fields through out the solar convective envelope for a complete description of solar activity dynamics.

The main-sequence stars with masses  $\sim 0.4 - 2.0 M_{\odot}$  ( $M_{\odot}$  is the Solar Mass) are believed to have dynamo mechanism similar to the Sun (Noyes *et al.*, 1984; Thomas and Weiss, 2008) and also exhibits surface differential rotations as derived from studies of starspots (Barnes *et al.*, 2005; Donahue, Saar, and Baliunas, 1996). Pallavicini *et al.* (1981) and several other studies showed that for stars of various spectral types, the magnetic activity increases with the increasing stellar rotation. Though, this relation reaches a saturation limit for magnetic activity at certain spectral-type dependent rotation period (Pizzolato *et al.*, 2003). Stellar rotation studies also suggested that the stellar activity cycle lengths depends on the rotation rates; stars with faster rotation tends to have shorter activity cycles (Noyes, Weiss, and Vaughan, 1984; Oláh, Kolláth, and Strassmeier, 2000; Saar and Brandenburg, 1999). These findings suggests that the stellar rotation has a major impact on the over-all efficiency of the dynamo operations.

The measurement methods of velocity field in the solar atmosphere falls under three categories. The first is the measurement of displacements, using solar features as tracers, for instance by a correlation analysis of series of images or tracking of magnetic features such as sunspots, sunspot-groups, faculae, filaments, coronal holes *etc.* The second is the measurement of Doppler shifts in a spectral line over the solar disk. The third method is the application of helioseismology. Rotation rates deduced from sunspot motions are systematically faster (about 5%) than that deduced from spectroscopic observations at same latitude belt (comparison of rotation rates derived by different methods is given in a review article by Beck, 2000). The difference between the two rates is likely dependent upon the effects of dynamical forces like magnetic buoyancy, Coriolis force, drag, *etc.* on the magnetic structure of the tracer.

Hence, the rotation rates of magnetic features may be carrying information about the dynamics of flux generation and transport in the convective region. Foukal and Jokiipii (1975) conjectured that if the magnetic tracers of rotation are anchored at some depth beneath the surface, then they would reflect the faster rotation rate found there.

The following section provides the recent portrait of internal solar rotation obtained from helioseismology (Section[4.1.1]). Many different kinds of studies had been conducted to understand the possible origin of solar differential rotation, its interactions with magnetic-fields and its role in solar activity cycle. The earlier rotation rate studies using sunspots as tracers and their dependence on various sunspot parameters are discussed in Section [4.1.2]. The long-term and solar cycle related variations observed in rotation parameters are presented in Section [4.1.3]. The observed North-South hemispheric asymmetry found in rotation profiles from previous studies is discussed in Section [4.1.4]. The objectives of the present study and the details of data analysis methods are given in Sections [4.2] & [4.3] respectively, followed by results and discussion in Section [4.4], and conclusions in Section [4.5].

### 4.1.1 Helioseismic records of solar rotation

Helioseismology is the study of solar interior using observations of oscillations on the Sun's surface. It has provided a detailed map of the Sun's structure and internal, large scale flows of solar plasma. The details of methods of helioseimology and its findings are available in reviews by Howe (2009); Miesch (2005); Thompson *et al.* (2003), and references therein. Figure [4.1] shows the rotation frequency variation with the solar radius for various latitudes obtained using the MDI Doppler images from period between 1996-2007 by Antia, Basu, and Chitre (2008). Following are the important inferences drawn about the solar rotation using helioseismological methods.

- (a) In the convection zone the rotation varies principally with latitude and rather little with depth; at low solar latitudes the rotation is fastest,

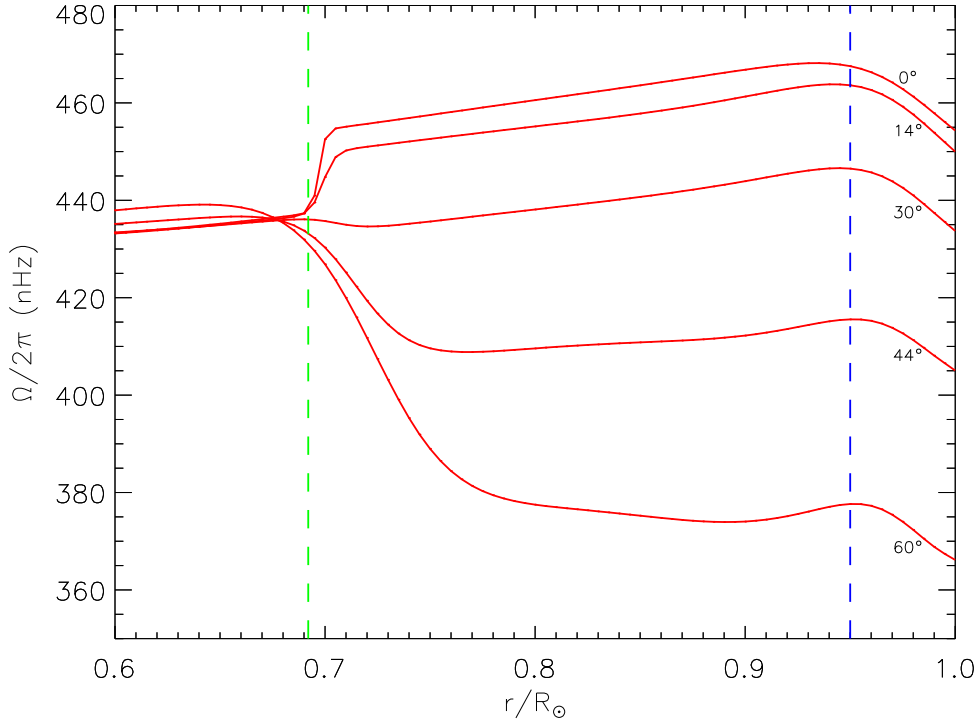


**Figure 4.1:** Radial profiles of rotation frequency for several latitudes from helioseismology using MDI data (1996-2007) from Antia, Basu, and Chitre (2008). The green line (dashed) and blue vertical lines are approx estimated locations of solar tachocline and the near-surface shear line (NSSL).

with a rotation period of about 25 days; while at high latitudes the rotation periods in the convection zone are in excess of 30 days. An angular velocity contrast of about 20% ( $\sim 90$  nHz) between the equator and latitudes of  $\pm 60^\circ$ .

- (b) At low- and mid-latitudes there is a near-surface layer (at  $\sim 0.95R_\odot$ , where  $R_\odot$  is the solar radius) of rotational shear where the rotation rate increases inward by about 2-3%.
- (c) Helioseismology detects the location of the inner boundary of the convection zone at  $\sim 0.713R_\odot$  (Basu and Antia, 1997; Christensen-Dalsgaard, Gough, and Thompson, 1991).
- (d) Near the base of the convection zone the latitudinally differential ro-

tation makes a transition to nearly uniform rotation in the radiative zone. This gives rise to a layer of rotational shear at low and high latitudes, which is called the tachocline (Spiegel and Zahn, 1992). At low latitudes the estimated location of the center of tachocline region is  $\sim 0.692 \pm 0.005R_{\odot}$  with a width of  $\sim 0.04R_{\odot}$ , and it is slightly prolate in shape (Charbonneau *et al.*, 1999).

- (e) The rotation rate of the radiative interior is intermediate between the equatorial and polar regions of the convection zone. The radial angular velocity gradient across the tachocline is positive at low latitudes and negative at high latitudes, crossing zero at a latitude of about  $35^{\circ}$ .
- (f) The torsional oscillations characterized by alternating bands of faster and slower than average zonal rotation moving from high latitudes toward the equator extends throughout the convection zone (Howe *et al.*, 2005, 2006).

### 4.1.2 Rotation rate and sunspot parameters

Several studies suggested that rotation rates are different for different magnetic tracers and depends on their type, evolution, age, size *etc.* For example, plages rotate slower than sunspots, while rotation of plages is comparable to the Doppler rate or even slightly slower (Howard, 1996b). But, there is no clear understanding about mechanism(s) responsible for variations in rotation rates. The solar surface differential rotation has been extensively studied using sunspots or sunspot groups as tracer, and also by classifying sunspots on the basis of their structure (single, bipolar, leader, follower), and characteristics such as, area, age, life span *etc.* (Howard, 1996b; Javaraiah and Gokhale, 2002; Schroeter, 1985; Ward, 1966).

Recurrent sunspots were found to have slowest rotation rate and sunspots in their early stage of development rotate considerably faster (Balthasar and Wöhl, 1980; Ternullo, Zappala, and Zuccarello, 1981). The

rotation rates of sunspot groups has been found to decrease with their age (Balthasar, Schüssler, and Wöhl, 1982; Balthasar, Vázquez, and Wöhl, 1986; Godoli and Mazzucconi, 1979; Ruždjak *et al.*, 2004; Tuominen and Virtanen, 1987; Ward, 1966; Zappala and Zuccarello, 1991; Zuccarello, 1993). Also, Nesme-Ribes, Ferreira, and Mein (1993) found that young spots show a more rigid rotation profile than do older spots, using the data on individual sunspots measured at Meudon observatory for cycles 19 and 21. In contrast, Javaraiah and Gokhale (1997) showed that the decreasing trend of rotation rate with age of sunspots is due to inadequate sampling of sunspots having different life span or area. Sivaraman *et al.* (2003) using Kodaikanal data found that the rotation rates of spot groups increases with their age when the rotation rates are computed after sorting the spot groups life span wise.

Howard, Gilman, and Gilman (1984) found that the large or long-lived sunspot groups rotates slower than the small or short-lived groups (also see Brajša, Ruždjak, and Wöhl, 2006; Hathaway and Wilson, 1990). They also showed that sunspot groups rotate significantly slower than individual sunspots. This implies that the individual flux tubes that form a sunspot group can be influenced by surface plasma rotation, even though they may originate from a deep subsurface flux tube that might be expected to have a uniform rotation rate (Howard, 1996b). Leading and following spots show significantly different rotation rates; for growing sunspots, the leading spots rotates faster than following spots by about 3%, while they rotate slower by 3% in decaying groups (Gilman and Howard, 1985). Also, the rotation rates varies with the polarity separation distance of bipoles; small polarity separation corresponds to slower rotation rate (Howard, 1992).

### 4.1.3 Temporal variation of rotation

The significant example of solar cycle variation of solar rotation is the observed ‘Torsional oscillations’. Labonte and Howard (1982) analyzed the Mt. Wilson Doppler measurements and detected a periodic variation (of about a

solar cycle) of the differential rotations, such that the rotation rates as a function of time could be described as a superposition of an average rotation (at a given latitude) and an oscillating component. They termed this oscillating part as Torsional oscillations; over a solar cycle it appears as bands of faster or slower than average rotation, moving alternatively from high latitudes towards the equator. Snodgrass (1991) found similar torsional oscillations in the magnetic field pattern (also see Howe *et al.*, 2009). However, the connection between the zonal shear flow and activity bands is not understood (Küker, Rüdiger, and Pipin, 1996; Schüssler, 1981; Wilson, 1987).

Several studies showed the dependence of rotation rate on sunspot activity, but different studies have some contradictory conclusions. Most studies had reported a significantly faster rotation rate of spot groups near activity minimum and lesser rates during maximum phase (Arevalo *et al.*, 1982; Balthasar and Wöhl, 1980; Gilman and Howard, 1984; Hathaway and Wilson, 1990; Javaraiah, 2003a; Kambry and Nishikawa, 1990; Lustig, 1983). In contrast, Javaraiah *et al.* (2009) claimed having no periodic variations in solar-equatorial rotation rate from the study of Mt. Wilson Doppler data for period between 1985-2007 in accord with the previous study of Ulrich and Bertello (1996). Also, Lustig (1983) claimed that the solar rotation is less differential at the minimum phase of a cycle and more differential at activity maximum, while opposite trend was noticed by Nesme-Ribes, Ferreira, and Mein (1993). This implies that the temporal variations of solar magnetic fields are intimately related to the temporal variations in differential rotation.

Owing to huge archives of sunspots data for several cycles, that can be utilized to study the long-term variations of differential rotation. Javaraiah (2003a), using Greenwich sunspot group data-set of period 1879-1975 covering cycles 12 to 20 found that the equatorial rotation rate is larger ( $\sim 0.1\%$ ) in the odd-numbered sunspot cycles (ONSCs) than in the even-numbered sunspot cycles (ENSCs). The mean rotation is significantly ( $\sim 10\%$ ) more differential in the ONSCs than in the ENSCs. Javaraiah, Bertello, and Ulrich (2005)

and Suzuki (2012) (also see Zhang, Mursula, and Usoskin, 2013) obtained quasi-periodic variation in B-value of long-term period of eight to nine cycles, similar to higher order cycle of sunspots called as Gleissberg cycle (Hathaway, 2010).

#### 4.1.4 North-South asymmetry of solar rotation

The North-South (NS) asymmetry was revealed in many indices of solar activity, such as the sunspot numbers and areas, magnetic flux, prominences and filaments, coronal mass ejections and also in differential rotation (Badalyan and Obridko, 2011; Badalyan *et al.*, 2005; Nagovitsyn *et al.*, 2010). The NS asymmetry of different solar indices are also observed to have variations with different phases of the solar cycle. Various such studies suggests that the NS asymmetry is a real and systematic phenomenon.

The small differences in the rotation rates of two hemispheres have been observed by various studies (Antonucci, Hoeksema, and Scherrer, 1990; Arevalo *et al.*, 1982; Brajša *et al.*, 1997, 2000; Carbonell, Oliver, and Ballester, 1993; Georgieva *et al.*, 2005; Gigolashvili *et al.*, 2007; Godoli and Mazzucconi, 1979; Hathaway and Wilson, 1990; Howard and Harvey, 1970; Howard, Gilman, and Gilman, 1984; Howard *et al.*, 1983; Javaraiah, 2003a; Javaraiah and Gokhale, 1997; Knaack, Stenflo, and Berdyugina, 2005; Mursula and Hiltula, 2004; Rybak, 1994; Schroeter *et al.*, 1978; Snodgrass, 1983; Verma, 1993; Wöhl *et al.*, 2010). In most of the cases the northern hemisphere has been found to rotate slightly slower than the southern hemisphere. But there is no clear agreement on which hemisphere rotates faster, and on the solar cycle phase variation or secular trend of North-south (NS) asymmetry, and what is the cause of such asymmetry. Helioseismic measurements also reported NS asymmetry in the solar angular velocity (Giles, Duvall, and Kosovichev, 1998; Zaatri *et al.*, 2006, 2009). Javaraiah (2001, 2002, 2003a) showed that the in ENSCs the rotation is more differential in northern hemisphere than in the southern hemisphere and this trend is opposite in the ONSCs. Zhang, Mur-

sula, and Usoskin (2013) obtained a long-term modulation (of about 80-90 years period) of the North-South asymmetry of the solar rotation. Antonucci, Hoeksema, and Scherrer (1990) reported that the NS-asymmetry in the rotation of photospheric magnetic fields was persistent through-out the cycle period of 1976-1986. However, the relation of NS-asymmetry of rotation to solar activity in general and also with the NS-asymmetry of solar activity is not yet clear.

## 4.2 Objectives of the present study

As discussed above, the rotation rates of magnetic tracers not only contains the information of solar angular momentum transport, these rates are also interlinked with the interaction of magnetic fields with convective flows and hence the solar activity dynamics. Thus the study of temporal variation of rotation parameters as well as dependence of these parameters on properties and evolution of magnetic regions may provide vital clue to the understanding of the mechanism of solar cycle.

The sunspot regions extracted from SoHO/MDI continuum images covering the complete solar cycle are best candidates to study the rotation parameters for cycle 23 and compare them with previous cycles, as well as to observe their variation with sunspot parameters and solar cycle phase with better accuracy (see Section [2.4.4] for sunspot parameters).

The previous studies using sunspots as tracers were mostly based on sunspot groups and only few studies took individual sunspots, for instance, individual sunspot data of the Mount Wilson white-light images (Howard, Gilman, and Gilman, 1984) and from Kodaikanal (Sivaraman, Gupta, and Howard, 1993). There are some ambiguities involved in group designation on the basis of proximity to a range of near-by sunspots on solar surface and also in the derivation of area-weighted centroid of the assigned group. Moreover, the area-weighted sunspot group rotation rate is influenced by the largest sunspot within the group (Howard, 1996b).

In this thesis, we undertook the various studies of solar differential rotation using *individual sunspots* as tracers, extracted from MDI continuum images for the period of 1996-2011. Following are the objectives of the present study:

- (a) To derive the latitudinal variation of solar rotation of solar cycle 23 using individual sunspots and compare these profiles with rotation profiles obtained from helioseismic techniques (Section [4.4.1]).
- (b) Study the dependence of rotation parameters on sunspot size (with a more wider range of sunspot area as compared to previous studies) for different latitude bands (Section [4.4.2.1]).
- (c) Study the difference in initial rotation rate of sunspots having different observed life span (Section [4.4.2.2]).
- (d) Study the changes in the mean rotation rate of sunspots with their age for different latitude bands (Section [4.4.2.3]).
- (e) To investigate the solar cycle phase variation in rotation parameters (Section [4.4.3]).
- (f) To look for the North-South hemispheric differences in the solar differential rotation for cycle 23; the solar cycle phase variation in North-South asymmetry of rotation and compare this rotation asymmetry with asymmetry in sunspot activity (Section [4.4.4]).

### 4.3 Observables and data analysis

Sunspots used for the differential rotation study were extracted from the stray-light-corrected continuum images of SoHO/MDI (for details see Section [2.4.3]). The parameters of these extracted sunspots such as, heliographic latitude and longitudes (both Carrington and Stonyhurst); area and time were listed in the FDCT sunspot catalog (Section [2.4.5]). To obtain the longitudinal shifts with time of individual sunspots, available sunspots were

traced for its movement from eastern limb to western limb of solar disk. The details of adopted sunspot tracking procedure is described in Section [2.5]. Following are the features of sunspot parameters used in this study;

- For this study, all the available MDI continuum images for period 1996-2011 were used, which corresponds to on average five images per day.
- The sunspot parameters were obtained from stray-light-corrected images. The sunspot centroid is the inverse-intensity-weighted position, calculated in both Stonyhurst and Carrington Heliographic coordinates. The area of sunspots were corrected for foreshortening.
- The sunspots were traced only for their visibility across east limb to west limb. Every first observation at eastern limb was assigned as a sunspot with new identification code.
- Sunspots with longitudinal shifts of  $\geq \pm 4^\circ \text{ day}^{-1}$  and latitudinal shift of  $\geq \pm 2^\circ \text{ day}^{-1}$  (in Carrington Heliographic coordinates) were excluded during tracking in order to avoid ambiguities due to abnormal sunspot motions (Javaraiah and Gokhale, 1995; Ward, 1965, 1966).
- The sidereal rotation rate,  $\omega$  in degrees/day of a sunspot was computed using the following formula (Javaraiah, 2013, and references therein),

$$\omega = \frac{\Delta L}{\Delta t} + 0.9856, \quad (4.1)$$

where,  $\Delta L$  and  $\Delta t$  are the differences in Stonyhurst Heliographic Longitudes of sunspots centroid position and the observation times of two consecutive images. The value 0.9856 is the correction factor for the Earth's orbital revolution (Graf, 1974). Due to elliptic orbit of the Earth, this correction factor will varies seasonally during a year of observation (Roša *et al.*, 1995). However, this correction is suffice for the present study since we will be studying whole solar cycle's 15 years of data,

or relative difference in rotation rates for the North-south asymmetry studies or yearly variation of rotation rate over a solar cycle period, the seasonal biased introduced in the rotation rates will be averaged out.

- The sunspot data that correspond to Stonyhurst Longitude,  $|L| > 75^\circ$  on any time of observation in its tracing record were excluded in order to mitigate uncertainties in position determination close to limb and hence the anomalous values of  $\omega$ .
- We also applied the filter of  $9^\circ \leq \omega \leq 20^\circ$  in order to remove contribution from anomalous rotation velocities measured.
- The present data-set consists of 2558 distinct sunspots from 1996-2011 which corresponds to 111687 rotation velocities measurements.

To support the interpretations of the present study we also used the rotation radial profiles for various latitudes (shown in Figure [4.1]) which was kindly provided by Prof. H. M. Antia (TIFR, Mumbai); these profiles were obtained from helioseismic measurements using SoHO/MDI Doppler images (Antia, Basu, and Chitre, 2008).

## 4.4 Results and discussion

### 4.4.1 Solar differential rotation using sunspots as tracers

The latitudinal variation of solar rotation, *i.e.*, solar differential rotation from the tracers angular velocities data (Eqn [4.1]) can be determined by using the traditional polynomial expansion,

$$\omega(\phi) = A + B \sin^2 \phi + C \sin^4 \phi, \quad (4.2)$$

where,  $\omega(\phi)$  is the solar sidereal angular velocity at heliographic latitude  $\phi$ , while coefficient A represent rotation rate at the solar equator, and B and C

represents the latitudinal gradient in the rotation rate, B mainly corresponds to gradient in low latitudes and C for higher latitudes.

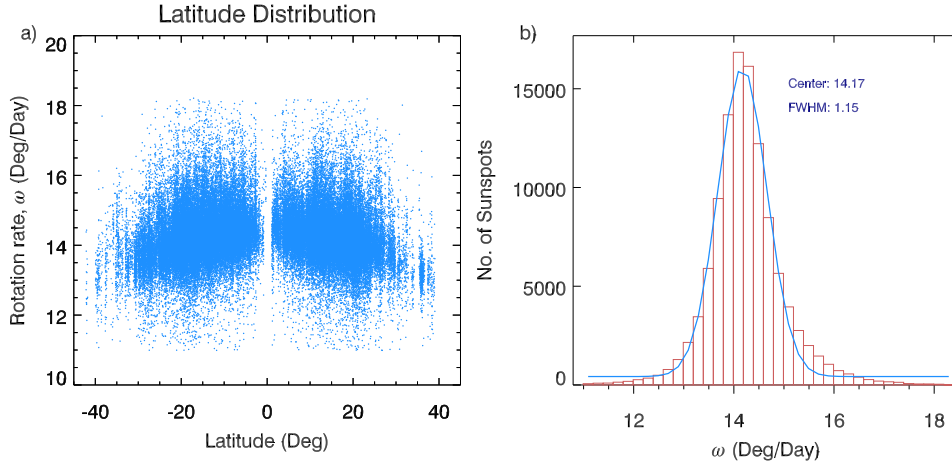


**Figure 4.2:** The latitudinal distribution of solar rotation velocities,  $\omega$  (in deg/day) for solar cycle 23 derived using individual sunspots as tracers extracted from SoHO/MDI continuum images.

In case of sunspot velocity data it is sufficient to use the first two terms of polynomial, *i.e.*

$$\omega(\phi) = A + B \sin^2 \phi, \quad (4.3)$$

since sunspot area observed at low to mid latitude ranges only (Balthasar, Vázquez, and Wöhl, 1986).

Authors	Observed solar features	Period	A	B	N
Present study	Sunspots	1996-2011(cycle 23)	14.49(0.003)	-2.95(0.03)	111567
Suzuki, 2012	Sunspot Groups	1996-2006 (cycle 23)	14.69(0.05)	-3.16(0.20)	10898
Suzuki, 1998	Sunspot Groups	1988-1996 (cycle 22)	14.69(0.05)	-2.16(0.27)	-
Javaraiah, 2013	GPR sunspot groups	1874-1976	14.51(0.004)	-2.64(0.04)	113392
Javaraiah, 2013	SOON sunspot groups	1977-2011	14.45(0.008)	-2.19(1.07)	46882

**Table 4.1:** Fit-parameters and one-sigma errors (in brackets) of rotation coefficients, A and B for the present study of individual sunspots and also from previous studies using sunspot-groups data from various sources.  $N$  is the no. of rotation velocities used for respective studies.

The Figure [4.2] shows the latitudinal distribution of sunspot rotation velocities for the complete observation period (1996-2011) of SoHO/MDI. To obtain the latitudinal profile of sunspot rotation velocities, the latitudes were

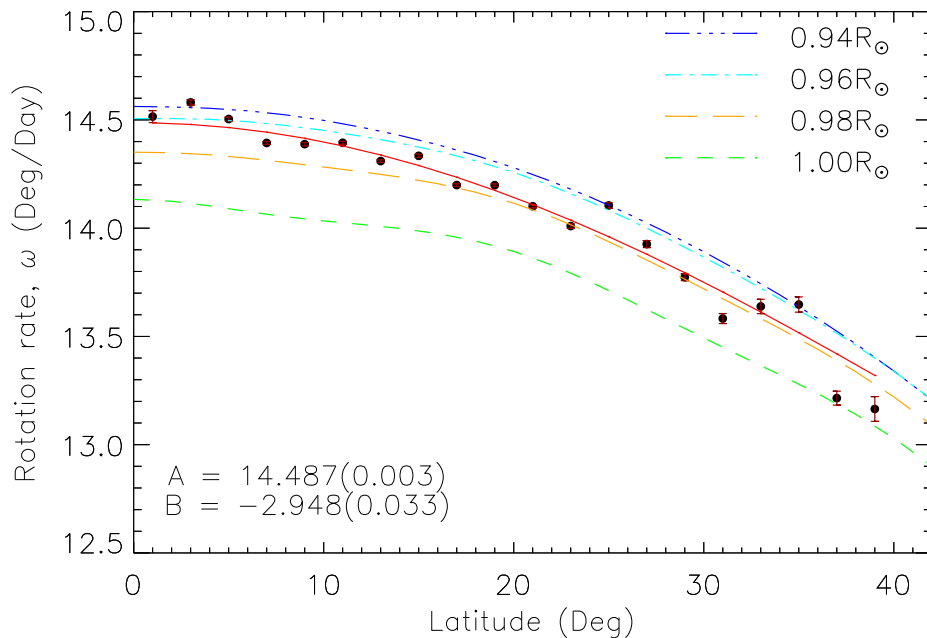


**Figure 4.3:** Latitudinal profile of mean sunspot rotation rate,  $\omega$  (in deg/day) determined by averaging over  $2^\circ$  latitude bins, for solar cycle 23 derived using individual sunspots as tracers extracted from SoHO/MDI continuum images. Also plotted the latitude profiles from helioseismic data for four different depths; at solar surface ( $1R_\odot$ , small-dashed), at  $0.98R_\odot$  (long-dashed),  $0.96R_\odot$  (dash-dotted), and  $0.94R_\odot$  (dash-triple dotted). The error bars represent the standard errors.

binned in  $2^\circ$  (commonly for both hemispheres); the data-set of the average of rotation velocities and the latitudes for each bin was fitted to the polynomial given in Eqn. [4.3]. The derived solar differential rotation using individual sunspots data is shown in Figure [4.3]; the rotation coefficients A and B (with their one sigma errors shown in brackets) are listed in Table [4.1]. The error bars in the plot are the standard errors, *i.e.*,  $1\sigma/\sqrt{n}$ , where  $\sigma$  is the standard deviation and  $n$  is the number of data in a given latitude bin. On average the rotation rate determined from sunspots is higher than that of surface plasma.

Schüssler (1987) and Rhodes *et al.* (1990) suggested that magnetic features such as sunspots, might rotate with velocities corresponding to some characteristic depth in convection zone, which may be called the anchor depth or the coupling depth of the feature. Javaraiah and Gokhale (2002) defined

magnetic ‘anchoring depth’ as the depth of that plasma layer whose rotation is having maximum *influence* on the observed rotation of the tracer. Hence, according to this definition, the two rates can have differences that will depend upon the effects of dynamical forces like magnetic buoyancy, Coriolis force, drag due to the ambient flow, *etc.* D’Silva and Howard (1994). In Figure [4.2], also plotted the latitude profile of solar rotation at four different depths of convection zone;  $1R_{\odot} - 0.94R_{\odot}$  at gaps of  $0.2R_{\odot}$ , deduced from Helioseismic inversion of MDI Doppler data. The rotational profile obtained from individual sunspots data lies between the corresponding profiles at  $0.96R_{\odot} - 0.98R_{\odot}$ . For low latitudes upto about  $20^{\circ}$  the mean rotation velocity decreases in such an order that it descends from profile at  $0.96R_{\odot}$  to profile at depth of  $0.98R_{\odot}$ , while for latitudes beyond  $20^{\circ}$ , the  $\omega$  values lies close to the profile at  $0.98R_{\odot}$ .

In units of  $\mu rad s^{-1}$ , the rotation coefficients of the present study are;  $A = 2.927 \pm 0.001$ ,  $B = -0.596 \pm 0.007$ . The equatorial rotation rate of present study obtained using individual sunspots is close to that obtained from sunspot-group data from the Solar Optical Observing Network (SOON) for cycle 23 (1997-2004) by Javaraiah, Bertello, and Ulrich (2005), which is,  $A = 2.922 \pm 0.004$ ,  $B = -0.509 \pm 0.030$ . However, the B-value of the present study using individual sunspots data has higher value. This is probably due to not sampling minimum activity period of cycle 23 in their study of sunspot-group rotation. Suzuki (2012) studied rotation rates of sunspot-groups for cycle 23, and they obtained an A value larger compared to that of the present study, while B value is similar to ours within  $1\sigma$  errors (see Table [4.1]).

#### 4.4.2 Rotation dependence on sunspot size, age and life-span

In this section, we looked into the dependence of rotation rates on the size of sunspots and the age of sunspot and also if there is significant difference in initial rotation rates of sunspots having longer life span to those which are short-lived.

#### 4.4.2.1 Rotation variation with sunspot area

To derive the dependence of rotation rate on sunspot area, we segregated the sunspot angular velocities (4.1) data into equally-spaced 12 bins of area in log-space starting from 8.5 MSH to 2530 MSH, for all the available cycle period irrespective of sunspots latitudes. For each area bin we calculated the average angular velocity,  $\omega$ . Figure [4.4a] shows the variation of rotation rate,  $\omega$  (in Deg/Day) with sunspot area (in MSH). The data in the x-axis represents the average sunspot area of the corresponding area bin. The error bars represents the standard error. To this we fitted a logarithmic function; the fit-parameters and  $1\sigma$  errors are listed in the Table [4.2]. Figure [4.4b] shows the  $\omega$  dependence on logarithm of sunspot area and to this we fitted a straight line; the obtained fit-parameters and corresponding  $1\sigma$  errors are also listed in the Table [4.2]. These plots clearly shows that the small sunspots on average have large angular velocities as compared to larger sunspots.

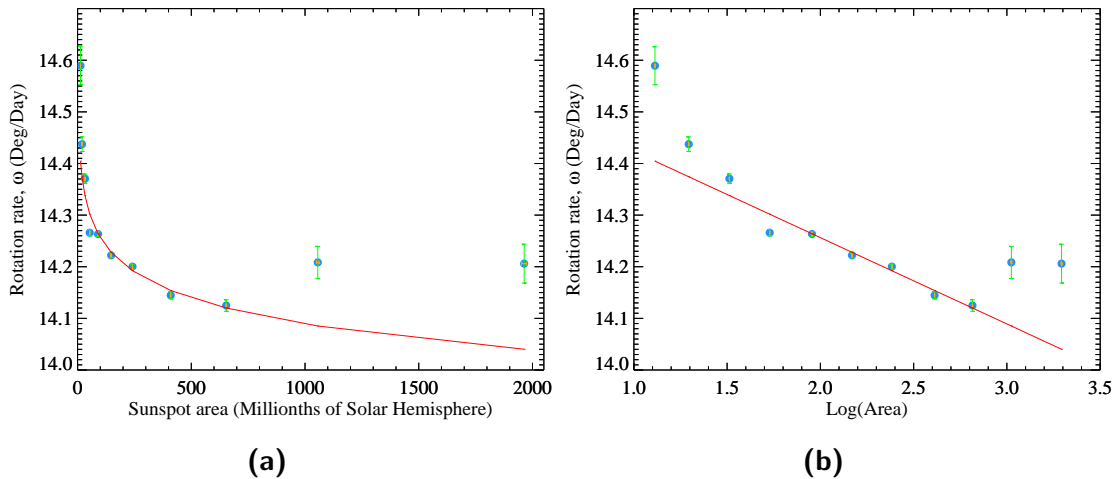


**Figure 4.4:** The dependence of mean rotation rate,  $\omega$  (Deg/Day) with (a) sunspot area (in MSH) and (b) logarithm of sunspot area, for all latitude ranges. The area binned into equally-spaced 12 bins in log-scale starting from 8.5 MSH to 2530 MSH. The error bars are standard errors.

Owing to the differential rotation, the mean rotation depends on latitudes as shown in the previous section; we checked the dependence of mean ro-

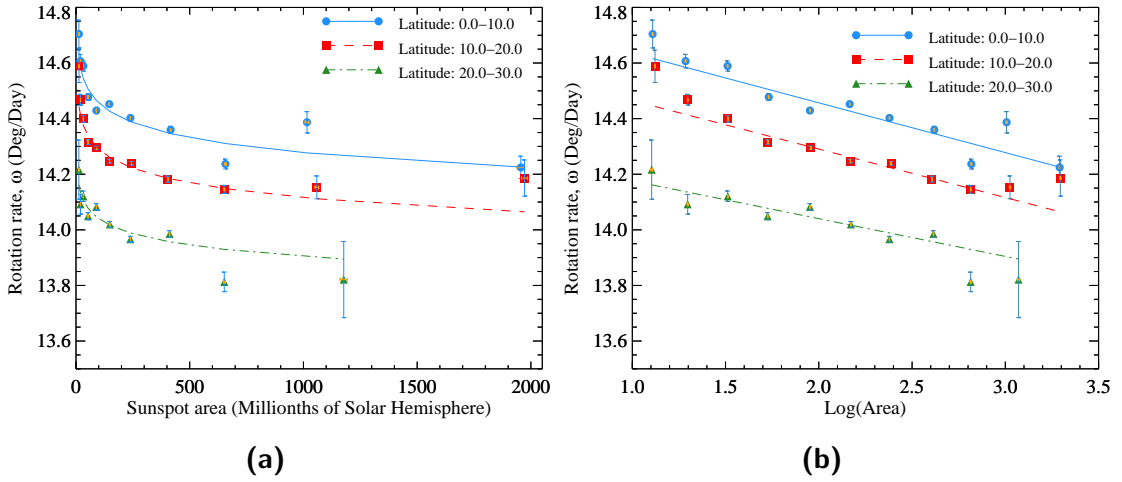


**Figure 4.5:** The dependence of mean rotation rate,  $\omega$  (Deg/Day) with (a) sunspot area (in MSH) and (b) logarithm of sunspot area, for three latitude ranges;  $0^\circ - 10^\circ$  (Blue dot, solid line),  $10^\circ - 20^\circ$  (Red square, dashed), and  $20^\circ - 30^\circ$  (Green triangle, dot-dashed). The area binned into equally-spaced 12 bins in log-scale starting from 8.5 MSH to 2530 MSH. The error bars are standard errors.

tation on sunspot area by binning data in different latitude bins. The Figures [4.5] shows the variation of mean rotation rate with sunspot area separately for three latitude ranges  $0^\circ - 10^\circ$ ,  $10^\circ - 20^\circ$ , and  $20^\circ - 30^\circ$ . In all latitude ranges the mean rotation has similar non-linear (logarithmic) dependence on sunspot area (Fig [4.5a]) as was with data from all latitudes. The straight-line fits in Figure [4.5b] between mean rotation and the logarithm of sunspot area with negative slopes are almost parallel to one another for different latitude ranges; with slope of  $-0.18$  for  $0^\circ - 10^\circ$ ,  $-0.17$  for  $10^\circ - 20^\circ$ ,  $-0.14$  for  $20^\circ - 30^\circ$ , and  $-0.19$  for all latitudes data. This implies that the dependence of rotation rate on sunspot area doesn't varies significantly with their latitude of emergence. The small value of the slope for higher latitude range of  $20^\circ - 30^\circ$  could be resulted due to small ambiguity in measurements of area and centroid position of sunspots (hence their angular velocities) caused by increased foreshortening effects away from the solar-disk.

Further to investigate the dependence of equatorial rotation rate and differential rotation on sunspot size, we derived latitudinal profile of rotation

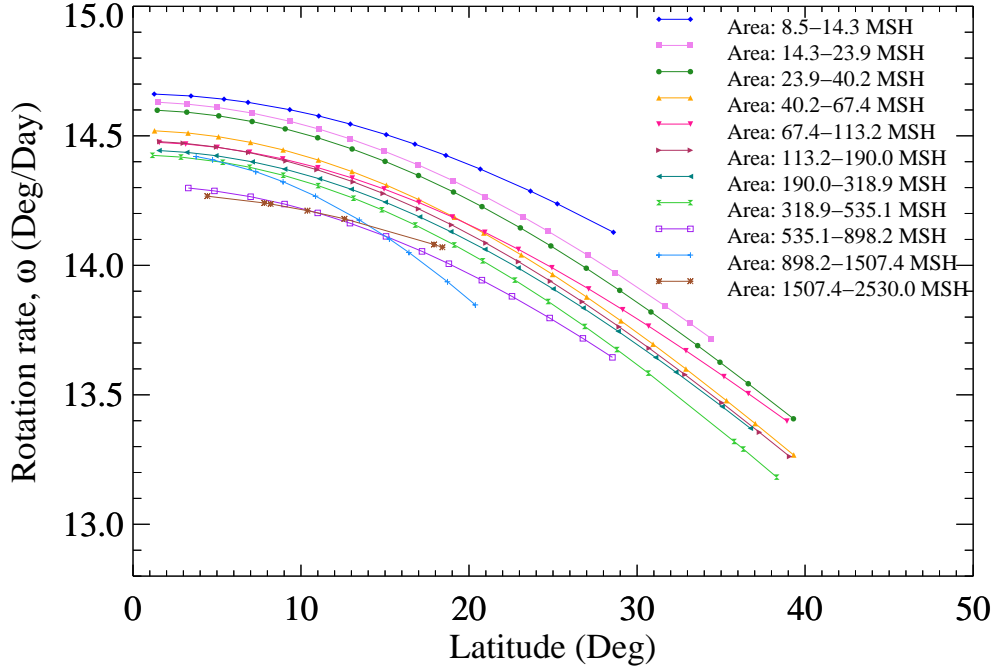


**Figure 4.6:** Latitudinal profile of mean rotation rate,  $\omega$  (Deg/Day) of individual sunspots for different ranges of sunspot area in MSH. The area binned into equally-spaced 12 bins in log-scale starting from 8.5 MSH to 2530 MSH.

as described in Section [4.4.1] for sunspot velocities data segregated in 12 area-bins irrespective of latitude and cycle phase. Figure [4.6] shows the obtained latitudinal profiles for each area range. This plot clearly shows that the equatorial rotation rate has different values for different sunspot sizes; smaller sunspots have the highest equatorial rate. The obtained equatorial rotation coefficients,  $A$  (from plot of Fig. [4.6] for each size range was plotted with the corresponding average value of sunspot area in that area bin in Figure [4.7a]. Clearly, the  $A$  has non-linear dependence on sunspot area, and is best represented by a logarithmic function, its parameters are listed in Table [4.2]. Figure [4.7b] shows the variation of  $A$  with the sunspot area in logarithmic scale, here is shown the straight-line fit function. These plots shows that small sunspots rotates faster than the larger sunspots in agreement with previous study of Howard, Gilman, and Gilman (1984). However, beyond 300 MSH

the equatorial rotation reaches an asymptotic value of about  $14.35^\circ \text{ day}^{-1}$ .

Relation	a	b	$\chi^2$	c	d	$\chi^2$
<b>For all latitudes</b>						
$\omega$ vs Area [4.4]	14.591(0.013)	-0.167(0.006)	14.98	14.591(0.013)	-0.167(0.006)	134.80
A vs Area [4.7]	14.792(0.019)	-0.149(0.009)	6.29	14.792(0.019)	-0.149(0.009)	56.59
B vs Area [4.8]	-2.600(0.193)	-0.192(0.090)	134.80	-2.600(0.193)	-0.192(0.090)	28.78
<b>Latitude band: <math>0^\circ - 10^\circ</math></b>						
$\omega$ vs Area [4.5]	14.815(0.023)	-0.179(0.010)	7.72	14.815(0.023)	-0.179(0.010)	69.48
<b>Latitude band: <math>10^\circ - 20^\circ</math></b>						
$\omega$ vs Area [4.5]	14.639(0.018)	-0.174(0.008)	4.65	14.639(0.018)	-0.174(0.008)	41.87
<b>Latitude band: <math>20^\circ - 30^\circ</math></b>						
$\omega$ vs Area [4.5]	14.312(0.029)	-0.136(0.013)	4.88	14.312(0.029)	-0.136(0.013)	39.07

**Table 4.2:** The fit-parameters, their one-sigma errors in brackets and corresponding chi-squared values for the logarithmic fit-functions ( $a + b(\log x)$ ) and the straight-line fits ( $c + d(x_1)$ ) for mean rotation rate,  $\omega$ , A, and B variation with sunspot area ( $x$ ) or log of sunspot area ( $x_1$ ).

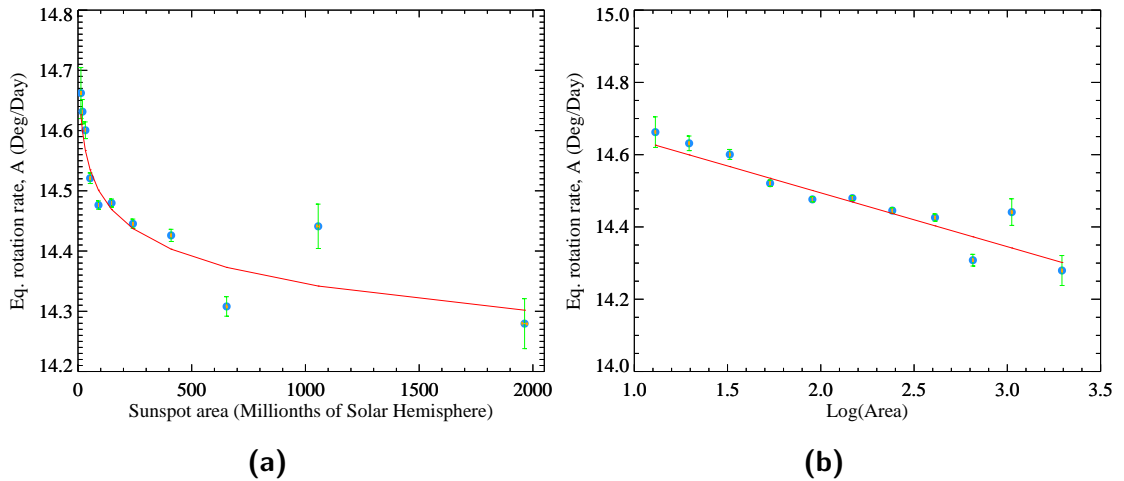


**Figure 4.7:** The dependence of Equatorial rotation rate, A (Deg/Day) with (a) sunspot area (in MSH) and (b) logarithm of sunspot area, for all latitude ranges. The area binned into equally-spaced 12 bins in log-scale starting from 8.5 MSH to 2530 MSH. The error bars are standard errors.

Komm, Howard, and Harvey (1993) speculated that the supergranules which have fastest rotation as compared to magnetic regions and surface plasma, and they reflect the rotation rates of surface layers down to about  $0.05R_\odot$  below surface where solar internal rotation have a local maximum as found from helioseismic studies (see Section [4.1.1]). While, the small magnetic features such as sunspots would be rooted deeper. In this scenario,

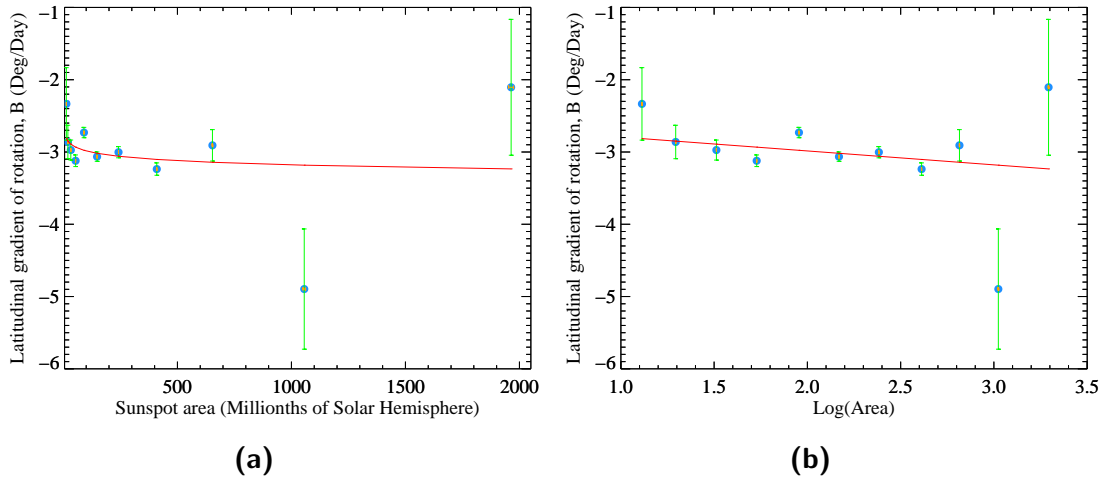


**Figure 4.8:** The dependence of Latitudinal gradient of rotation rate,  $B$  (Deg/Day) with (a) sunspot area (in MSH) and (b) logarithm of sunspot area, for all latitude ranges. The area binned into equally-spaced 12 bins in log-scale starting from 8.5 MSH to 2530 MSH. The error bars are standard errors.

varying rotation rates with the size of sunspots could be mimicked as varying depths of ‘roots’ of their magnetic flux tubes. In contrast, helioseismic measurements of subsurface structure of sunspots suggested that sunspots are rather shallow structures (Basu, Antia, and Bogart, 2004; Couvidat, Birch, and Kosovichev, 2006; Kosovichev, Duvall, and Scherrer, 2000). Schüssler and Rempel (2005) showed in their numerical studies that sunspots get dynamically disconnected from their magnetic roots at depths above 10 Mm (also see reviews by Fan, 2009; Gizon and Birch, 2005).

D’Silva and Howard (1994) explained the observed variation in rotation rate with the size of sunspots in terms of effect of dynamical forces acting on the rising flux tubes. They derived that the magnetohydrodynamic drag force on the rising flux tube increases with the decreasing size of the flux tubes, which suppresses the Coriolis force more efficiently; *i.e.*, the drag on the large flux tubes is less than it is on smaller ones and they emerge faster, giving Coriolis force less time to act and hence large flux get less of a boost in the direction of rotation than the smaller tubes. Also the magnetic buoyancy varies inversely with the strength of magnetic fields of flux tube. Hence, flux

tubes with high magnetic fields due to their large buoyancy, emerge rapidly to the surface and giving no time for the Coriolis force to interact and hence lowered rotation velocity as compared to flux tubes with low field strengths. We had discussed in previous chapter (Section [3.1.3] and references therein) that the magnetic field strength of sunspots are correlated with their area. Thus, the combined interplay of drag force, magnetic buoyancy, and Coriolis force on the rising flux tube appears to be a plausible reason for the varying rates of sunspots of different sizes and also their higher rates as compared to surface plasma.

Similar to the equatorial rotation rate,  $A$ , the differential rotation coefficient,  $B$  also shows slight non-linear dependence with the sunspot area as shown in Figures [4.8]. A logarithmic fit function is shown in Figure [4.8a] for  $B$  versus mean sunspot area. While the plot of  $B$  and logarithm of mean sunspot area give more clear dependence as a linear variation with negative slope, however not much significant within 2 sigma level. The fit parameters of both the fit functions are listed in Table [4.2]. These plots show that larger sunspots have slight rigid rotation as compared to small sunspots. In contrast, Suzuki (1998) studied variations in sunspot-group's rotation parameters for different Zürich classes of sunspots, and found that the groups having larger maximum area reveal more differential rotation than those with small value of their maximum area, which was in agreement with the results obtained by Balthasar and Wöhl (1980), Arevalo *et al.* (1982) and Lustig (1982). But, our present study suggests that the  $B$ -values have insignificant dependence on area, however since the equatorial-rotation rate has strong dependence with the size, their sunspot-group velocities were probably influenced by amalgamation of sunspots of different sizes within a group and hence the latitudinal fit was affected, though this needs further investigations to make a conclusion.

The dependence of solar rotation on sunspot area may have significant effect on observed North-South asymmetry in rotation rate or the variations with the solar activity phase or strength of activity cycle, which we will discuss

in the following Sections [4.4.4] & [4.4.3].

#### 4.4.2.2 Initial rotation rate and life span

For each sunspot from its tracking records we derived its initial rotation and the life-span; the start and end observations of a sunspot are counted within the longitudes  $< 75^\circ$ . Figure [4.9] shows the dependence of initial rotation frequency (in nHz) with the life-span of a sunspot, in different latitude intervals. The error-bars represent the standard errors.

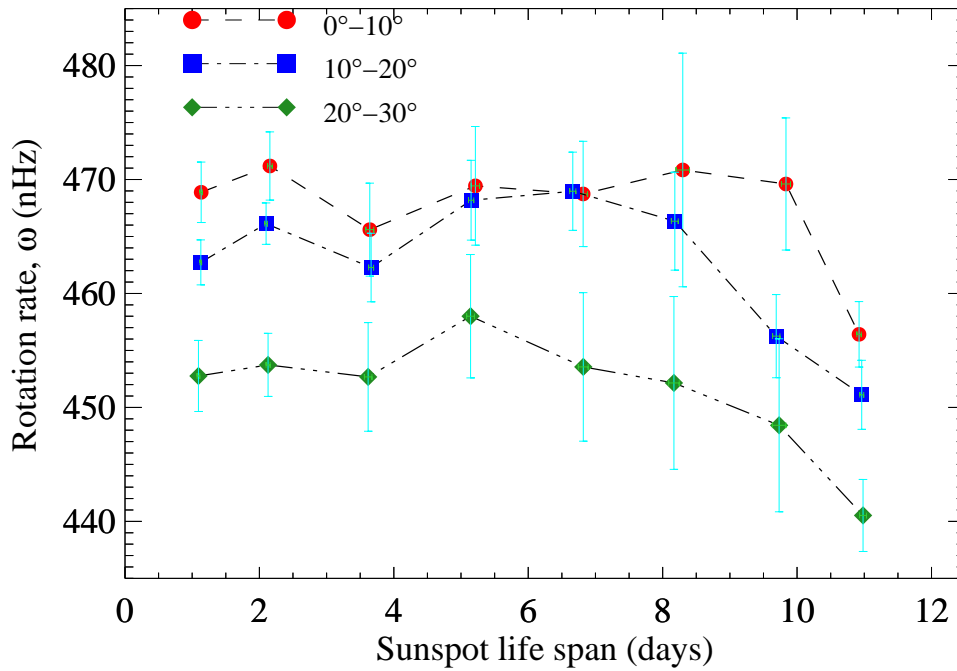


**Figure 4.9:** The initial rotation rate,  $\omega$  (nHz) for sunspots having different life span (in days) for three latitude bands;  $0^\circ - 10^\circ$  (Red dot, dashed),  $10^\circ - 20^\circ$  (Blue square, dot-dashed), and  $20^\circ - 30^\circ$  (Green diamond, triple-dot-dashed). The sunspot's life-span is binned into intervals of 1.5 days starting from 0 upto 12 days. The error-bars represent the standard errors.

The variation of initial rotation frequency with the sunspot's life-span has similar patterns in all three latitude bands and has close resemblance to the results obtained by (Javaraiah and Gokhale, 1997) in a similar study using sunspot-group data. They found similarity between the variation in the initial

rotation rates of sunspot-groups with their lifetimes and the radial variation of the internal rotation rate deduced from helioseismology and suggested that the magnetic structures of sunspot-groups with longer life-spans are initially anchored in successively deeper layers of convection zone (Hiremath, 2002; Sivaraman *et al.*, 2003). Javaraiah (2013) found that the profiles of the mean initial rotation rates of sunspot-groups having life-span shorter than 5 days, 5-8 days and longer than 8 days are closer to the internal rotation at  $> 0.94R_{\odot}$ ,  $0.94R_{\odot} - 0.96R_{\odot}$  and  $0.8R_{\odot}$ , respectively.

#### 4.4.2.3 Rotation variation with age

In this section we studied the dependence of rotation rate on its evolution. During the growth phase, the sunspot increases in area and attains a maximum area, and then quickly decays (Solanki, 2003). Thus, it is expected that the rotation rate will change with the varying area of sunspot, since sunspot rotation velocity has dependence on its area as discussed in previous section. Moreover, changes in the rotational velocities of sunspot groups with age can be connected with the rise of their magnetic flux tubes due to buoyancy with aging.

To study the rotation rate variation with sunspot age, we selected sunspots having life-span of 10-12 Days, estimated from their observations within the  $75^{\circ}$  of longitudes; and we further restricted the sunspot data-set to those having area in the range 300-800 MSH in order to prevent significant rotation rate variation with sunspot area in this study. Since, rotation depends on latitude, we further separated data into three latitude bands:  $0^{\circ} - 10^{\circ}$ ,  $10^{\circ} - 20^{\circ}$ , and  $20^{\circ} - 30^{\circ}$ . For each latitude band we calculated the average of rotation rate for sunspots having different ages, where the sunspot ages were binned in equal intervals of 1.5 Days, starting from 0 to 12 Days. Figure [4.10] shows the plot of variation of rotation rate with sunspot age for three latitude bands where error-bars represents the standard errors. In all three latitude bands, there is a slight increase in rotation rate in about first two-three days;

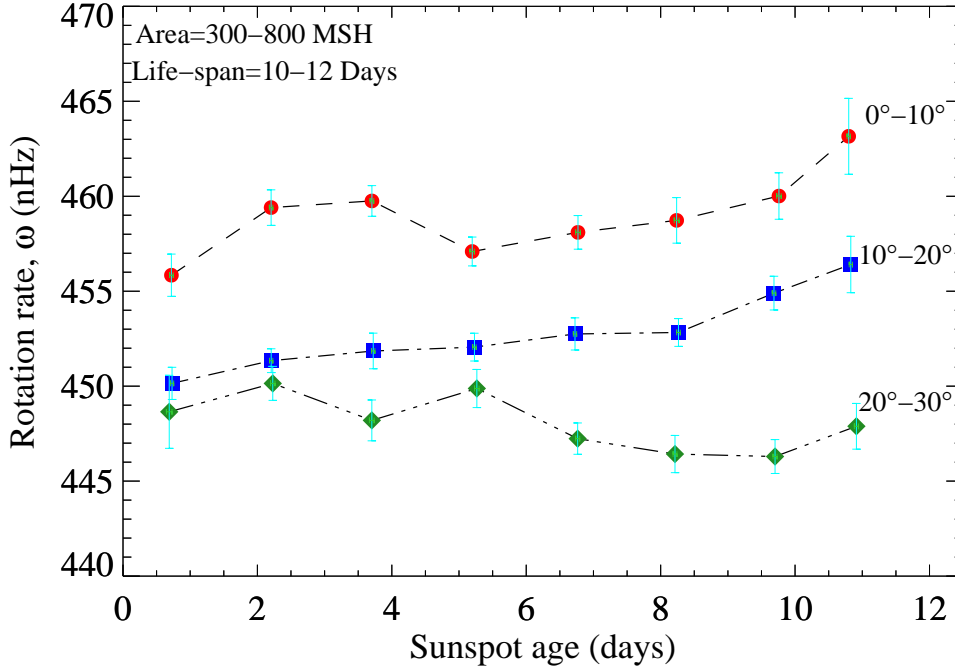


**Figure 4.10:** The variation in mean rotation rate,  $\omega$  (nHz) with sunspot age for sunspot having life span of 10-12 days and area 300-800 MSH for three latitude bands;  $0^\circ - 10^\circ$  (Red dot, dashed),  $10^\circ - 20^\circ$  (Blue square, dot-dashed), and  $20^\circ - 30^\circ$  (Green diamond, triple-dot-dashed). The sunspot age was binned into intervals of 1.5 days starting from 0 upto 12 days. The error-bars corresponds to the standard errors.

and also beyond  $\sim 8$  to 12th day there is again some acceleration in rotation rate. In between periods have no systematic trends. However, the rotation rates for the mid-latitude band appears to be increasing with the age in agreement with the results obtained from the study of Kodaikanal sunspot-data, where sunspots were grouped according to their life-spans by Sivaraman *et al.* (2003).

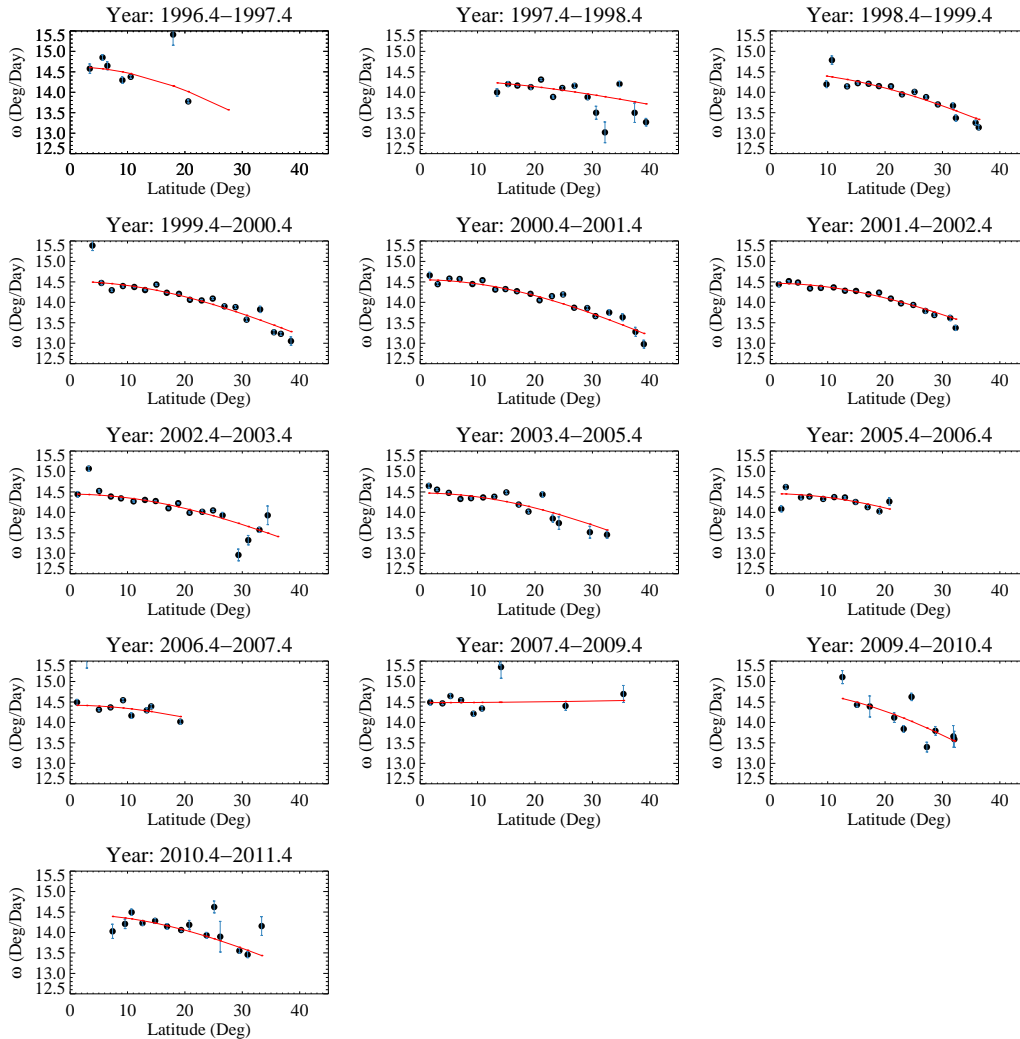
Javaraiah and Gokhale (1997) studied the rotation rate variation with age for sunspot-groups having life-span of 10-12 days, in three latitude bins as considered here, for data during 1874-1939. In agreement to our result, they observed that the rotation is accelerated for the initial period of about three days. However, in contrast to our result, they found deceleration after the 9th day in agreement to results of Gokhale and Hiremath (1984) and Ruždjak

*et al.* (2004). They also compared the variation of rotation rates with age to the radial profiles of solar rotation inferred from helioseismology considering that with increasing age, the effective anchoring of the tracer might rise towards photosphere, due to buoyancy (Schüssler, 1987). Using this comparison they derived that magnetic structures rise across the envelope at the rate of  $\sim 21\text{Mm/day}$ . However, Petrovay (1993) showed that area-weighted positions of sunspot-group leads to fake proper motions in the decaying phase of sunspot-groups and hence ambiguous deduction of rotation velocities. The present velocity data-set of individual sunspot has no such ambiguity in position determination (except for the anomaly due to some sunspots having high inherent proper motions). Only the sufficient sample of sunspots that have been observed to be born close to the eastern-limb and traced during their evolution, can provide insight about the variation of rotation velocities with the aging of sunspots.

### 4.4.3 Solar-cycle phase variation of rotation parameters

To study the solar cycle phase variation of rotation parameters from the present sunspot velocity data-set from period 1996-2011, we binned the data into annual bins, starting from June, 1996 to May, 2011. However, during minimum phase of cycle 23 due to less number of sunspot data, we binned that period in two years bin, *i.e.*, from June, 2007 to May, 2009; and total of 13 bins. For each 13 time period bins, the latitudinal profile of rotation rate was calculated. Figure [4.11] & [4.12] shows the differential rotation profile for different solar cycle periods.

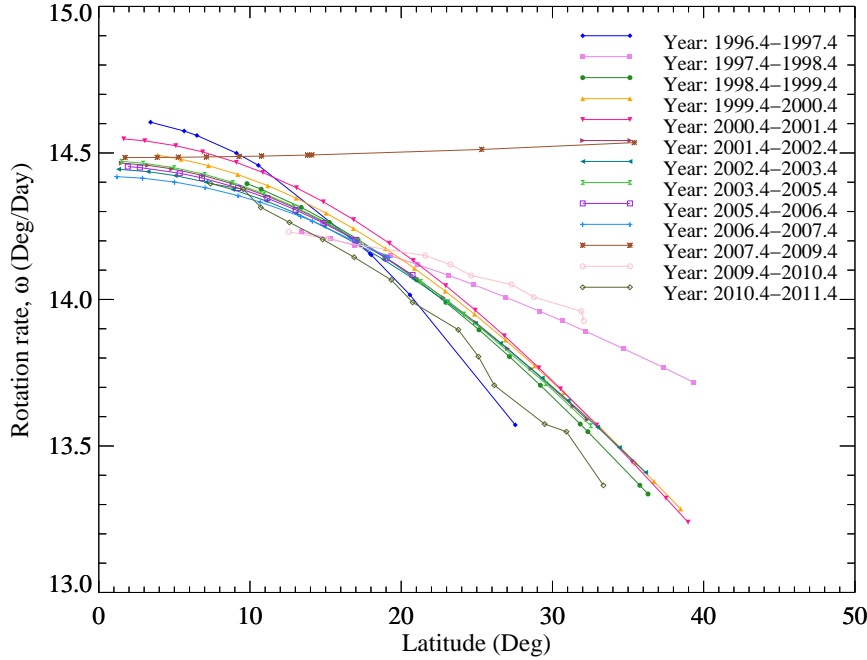
In Figure [4.13], the average value of rotation rate of sunspots from a given yearly bin is plotted. Also plotted the averages of the latitudes of corresponding sunspots observed in a given time period. This plot clearly shows that, at the beginning of a cycle when the mean latitudes of sunspots are at higher latitude then the average sunspot angular velocity has lowest value, and with the progress of cycle, as the mean latitude shifting towards



**Figure 4.11:** The latitudinal profiles of sunspot rotation rate derived annually during 1996–2011, only during minimum of cycle 23 a 2 year bin was taken.

the equator, the mean of sunspot rotation rates increases. At the start of MDI observation near the year 1996 sunspots of new cycle 23 started emerging at higher latitudes, similarly during the minima of cycle 23 around the year 2009 sunspots from cycle 24 showed up at higher latitudes, and hence relatively lower rotation rates as compared to their respective preceding years.

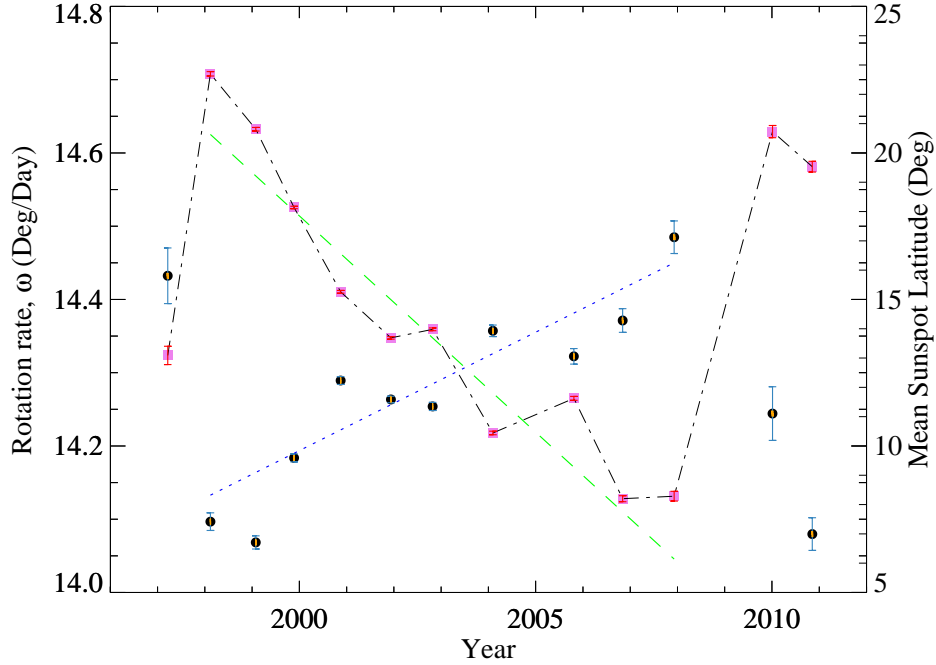
From the latitudinal profiles derived for different yearly bins, we plotted the resultant equatorial-rotation rates,  $A$  and differential rotation coefficients,  $B$ , against the corresponding time-period in Figure [4.14]. As shown in Figure



**Figure 4.12:** The yearly differential rotation profiles for the period 1996 to 2011 covering solar cycle 23 and the minima of cycle 24.

[4.14a], at the beginning of cycle 23, the  $A$ , steeply increased; a similar steep rise was observed at the start of next cycle 24 showing the cyclic modulation of 11 year period; and the maximum at the beginning of cycle 24 is lower than that is for the previous cycles 23. Other than periods close to the minimas, the  $A$ -value fluctuates in small amounts around the global value obtained for the complete cycle period, here it is  $14.49^\circ \text{ day}^{-1}$ .

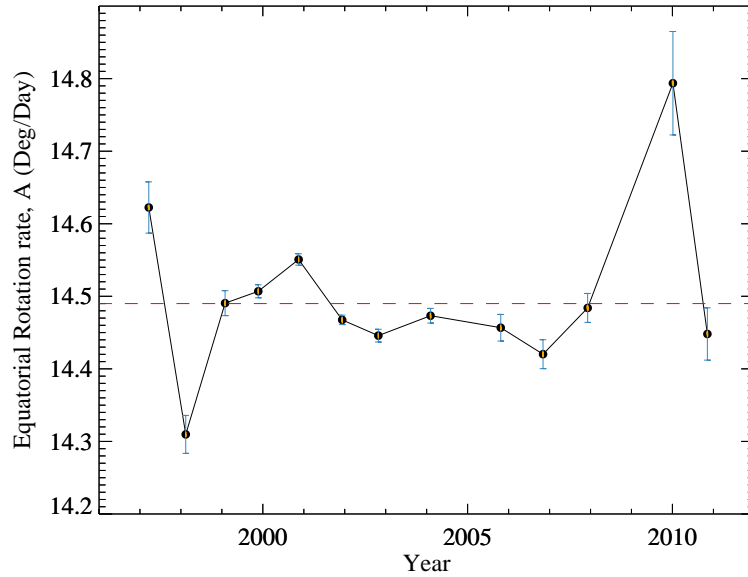
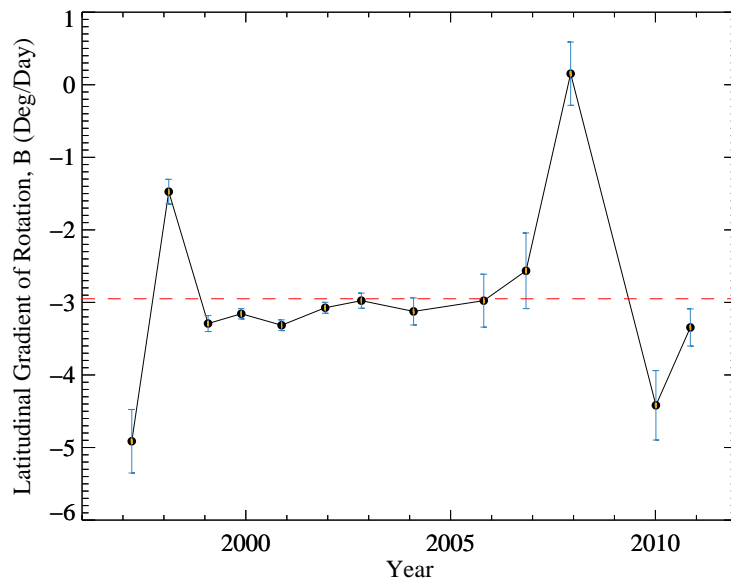
Javaraiah (2013) from the study of sunspot-group data reported that the temporal variation of equatorial-rotation rate obtained from different types of solar data. The pattern of  $A$  reported in their paper for cycle 23 from sunspot-group data matches almost exactly with ours of the same period. However, we had seen in the previous section [4.4.2.1], that the rotation rates of sunspots (or sunspot-groups) depends on their area; small sunspots rotates faster than the large sunspots (or groups). Javaraiah (2012) pointed out that the minimum years of solar cycle contains mainly small sunspots, hence



**Figure 4.13:** The solar cycle phase variation of Mean rotation rate,  $\omega$  (black dots) and mean sunspot latitudes (pink squares, dash-dotted). The period from 1996-2011 is binned into 13 yearly bins, starting from 1996.4 to 2011.4, with a one bin of two year period, (2007.4-2009.4). The error-bars corresponds to the standard errors.

the observed variation in rotation rates with cycle phase could be due to or influenced by the sunspot properties. To mitigate the contributions of sunspot (or magnetic features) properties on observed temporal pattern in  $A$ , we need to look if there are any similar temporal variations seen in the surface plasma rotation rates.

Javaraiah (2013) reported that the equatorial-rotation rates derived from sunspot-group data and the Doppler-velocity data follows similar pattern, which suggests that the temporal variation in the equatorial-rotation is of solar origin. This gives an impression that the sunspot activity and the solar rotation pattern are indeed inter-linked. However, the temporal variation in the equatorial-rotation rates derived from the GONG data at  $1R_{\odot}$  by Antia and Basu (2010) do not shows significant fluctuations around solar minima

(a) Equatorial-rotation rate,  $A$ (b) Differential-rotation coefficient,  $B$ 

**Figure 4.14:** The solar cycle phase variation of (a) Equatorial-rotation rate,  $A$  (Deg/Day), and (b) Differential rotation coefficient,  $B$  (Deg/Day). The period from 1996-2011 is binned into 13 yearly bins, starting from 1996.4 to 2011.4, with a one bin of two year period, (2007.4-2009.4). The error-bars corresponds to the standard errors. The horizontal red small-dashed lines in (a) and (b) are the global values of  $A$  and  $B$  as obtained in Fig 4.3.

as has been observed by sunspot tracer methods. In their study the temporal variation in rotation rates is less than 2 nHZ.

The differential rotation coefficient (B-value) has the same solar-cyclic pattern as that for the equatorial-rotation rate as shown in Figure [4.14b]. The differential rotation appears to be high at the time of the end of a previous cycle 22 and during the rising phase of cycle 24, as can be seen from high negative values for the periods 1996.4-1997.4 and 2009.4-2010.4. While, at the beginning of a cycle 23 and towards its end, the  $B$  has low negative value, *i.e.*, less differential. And in mid-term years of cycle 23, the B-value is nearly constant, close to the global value for the cycle 23 (derived in Section [4.4.1]). Recently, Suzuki (2014, Fig 4) observed a similar variations in the yearly  $B$  values for cycle 23, and the northern and southern hemisphere has similar modulation as that of the global one.

In agreement to our findings, Lustig (1983) from the study of sunspot observations at Kanzelhoehe observatory, found that the solar rotation is less differential at the activity minimum and more differential near the activity maximum. Recently, Suzuki (2014) argued that temporal variations of the NS asymmetry of  $B$  may be the cause of the observed cyclic modulation of the  $B$ . We will examine the modulation of North-south asymmetry in rotation during cycle 23 in the next Section [4.4.4].

Javaraiah (2000) reported that the solar cycle phase variation of  $A$  is significant only in odd cycles, while the corresponding variation in  $B$  is anticorrelated between odd and even cycles. The cycle-to-cycle variation of  $B$  suggests 22 year periodicity (Javaraiah and Gokhale, 2002, and references therein).

#### **4.4.4 North-south asymmetry of rotation for cycle 23**

The latitudinal profile of sunspot velocity data derived for Northern and Southern hemispheres separately is shown in Figure [4.15]; where latitudes in each hemisphere has been binned in  $2^\circ$  intervals. The obtained equatorial-

rotation and differential rotation coefficients with corresponding one-sigma errors are listed in Table [4.3]. The obtained  $B$ -values shows that the Northern Hemisphere has more differential rotation as compared to the Southern hemisphere, and the Northern  $B$  value is slightly higher (on negative scale) than the global value. The Table [4.3] also lists the rotation-parameters obtained from Greenwich (1879-1976) and SOON (1977-2004) sunspot-groups data for the whole-disk, northern and southern hemisphere separately in units of  $\mu\text{rad day}^{-1}$ . For the cycle 23, in agreement with their results from sunspot-group-data for cycle 23; the equatorial-rotation rates of whole-disk, northern and southern hemispheres are almost same within one-sigma level; and the Northern hemisphere has more differential rotation on average over the cycle period as compared to Southern hemisphere (however, the cycle 23 is not completely covered in their data-set).

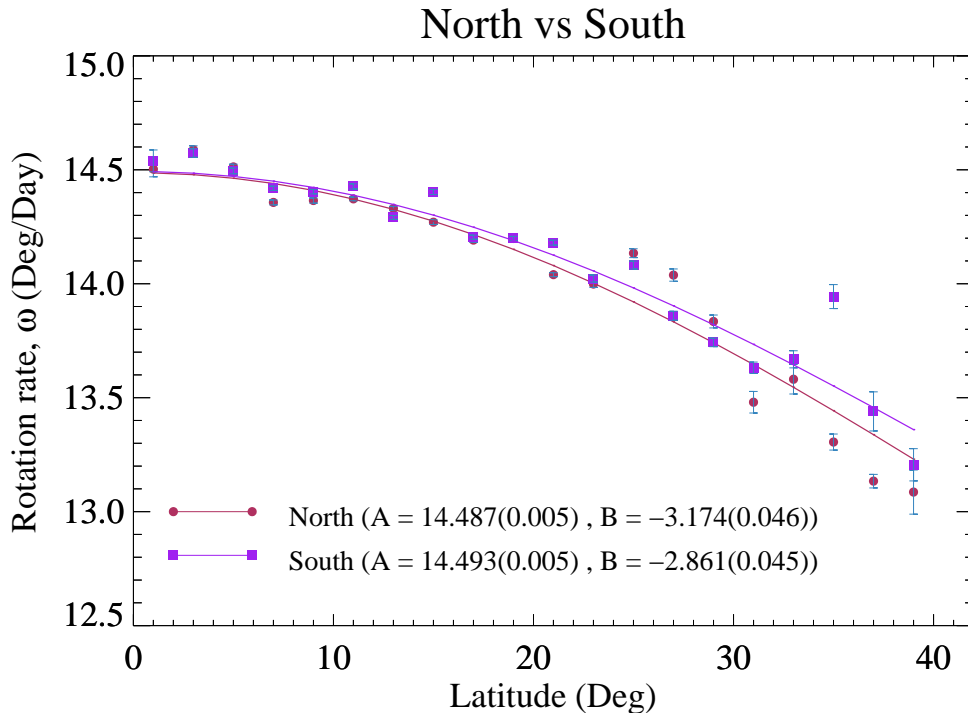


**Figure 4.15:** Latitudinal profile of mean rotation rate,  $\omega$  (in deg/day) separately for Northern (maroon) and Southern (violet) Hemispheres for solar cycle 23 derived using angular velocities of individual sunspots extracted from SoHO/MDI continuum images.

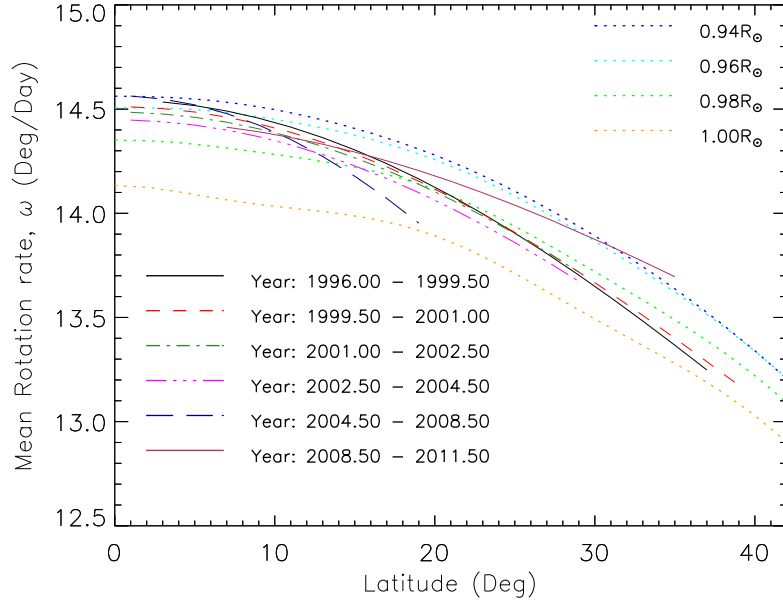
Javaraiah (2003b) reported that in all the ONSCs the A-value is larger in the Southern hemisphere than in the northern hemisphere; and the rotation is generally more differential in southern hemisphere than in northern hemisphere (except for cycle 15). For example, from the studies of sunspot groups by various authors (Howard, Gilman, and Gilman, 1984; Kambry and Nishikawa, 1990; Lustig, 1982, 1983; Nesme-Ribes, Ferreira, and Mein, 1993) for cycle 21, the rotation rate in the northern hemisphere was found to be more rigid than in the south when averaged over the whole cycle. While, in all ENSCs, the A-value in north-south have statistically equivalent magnitude (except cycle 12); and the southern hemisphere has more rigid rotation than northern hemisphere. Hence, according to this odd-even law, the cycle 23 is an exception; it has features similar to that for the ENSCs; the similar exception case of an ONSC was of cycle 15.

To examine whether the observed NS-asymmetry in rotation for a complete cycle period exists at different phases of solar cycle, we obtained sidereal rotation rate dependence on latitudes separately for North and South hemispheres for different periods of cycle as shown in Figures [4.16(a-b)]. The period from 1996 to 2011, which covers the complete cycle 23 and the ascending phase of cycle 24, was divided into 6 variable-sized intervals, *i.e.*, (1996.0-1999.5), (1999.5-2001.0), (2001.0-2002.5), (2002.5-2004.), (2004-2008.5) and (2008.5-2011.5); which approximately (not strictly) resembles the minimum, the rising, the maximum, the declining, and the minimum period of the cycle 23, and the minimum at the start of cycle 24 respectively.

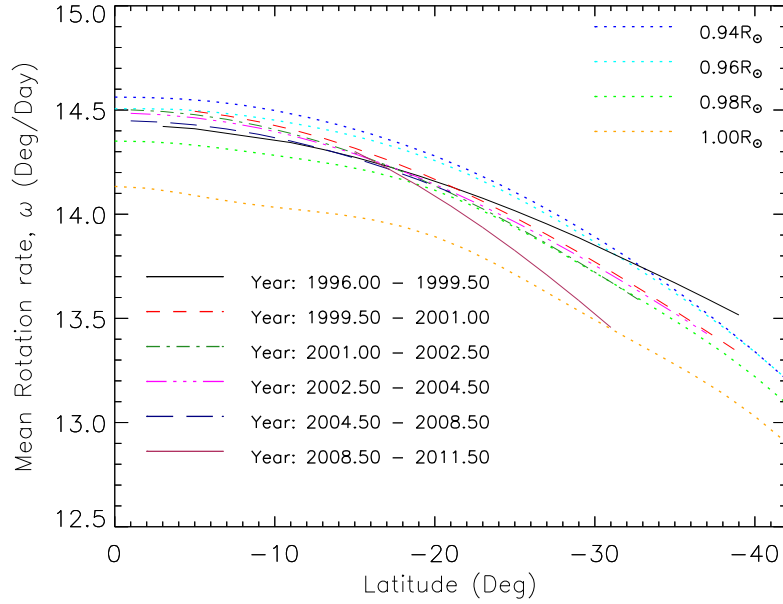
The obtained equatorial-rotation rates (A) and latitudinal gradient of rotation rates (B), for different phases of the cycle for both the Northern and Southern hemispheres as well as for Whole-disk are shown in the Figure [4.17(a)&(b)]. The plots shows that the rotation parameter A as well as the B-value of North and South are anti-correlated.  $r_A$  is the correlation coefficient between the A-values of the North and South hemispheres, and has a significant value of  $-0.741$ . Similarly, the correlation coefficient of B-values

Cycle	Whole disk			Southern Hemisphere			Northern Hemisphere		
	A	B	N	A	B	N	A	B	N
Present Study									
23	2.927(0.001)	-0.596(0.007)	111567	2.928(0.001)	-0.578(0.009)	56954	2.927(0.001)	-0.641(0.009)	54613
Javaraiah, Bertello, and Ulrich, 2005									
12(1879-1889)	2.943(0.003)	-0.540(0.036)	8015	2.935(0.004)	-0.442(0.048)	4530	2.953(0.005)	-0.669(0.056)	3485
13(1890-1901)	2.945(0.003)	-0.502(0.031)	10926	2.941(0.004)	-0.504(0.040)	5914	2.949(0.004)	-0.492(0.048)	5012
14(1902-1912)	2.928(0.003)	-0.458(0.043)	8674	2.933(0.005)	-0.462(0.060)	4432	2.924(0.004)	-0.465(0.063)	4242
15(1913-1922)	2.932(0.003)	-0.537(0.031)	10973	2.937(0.004)	-0.507(0.046)	5133	2.929(0.004)	-0.589(0.043)	5840
16(1923-1933)	2.930(0.003)	-0.493(0.027)	10371	2.929(0.004)	-0.476(0.042)	4841	2.931(0.004)	-0.504(0.036)	5530
17(1934-1943)	2.934(0.002)	-0.594(0.022)	13697	2.938(0.003)	-0.613(0.030)	6879	2.930(0.003)	-0.574(0.033)	6818
18(1944-1953)	2.926(0.002)	-0.520(0.021)	15801	2.927(0.003)	-0.497(0.028)	7915	2.926(0.003)	-0.555(0.032)	7886
19(1954-1964)	2.926(0.002)	-0.541(0.016)	18929	2.930(0.003)	-0.572(0.027)	7921	2.924(0.003)	-0.524(0.020)	11008
20(1965-1975)	2.928(0.002)	-0.479(0.023)	15000	2.929(0.003)	-0.464(0.037)	6718	2.926(0.003)	-0.483(0.030)	8282
21(1976-1986)	2.926(0.003)	-0.420(0.022)	-	2.928(0.004)	-0.454(0.031)	-	2.923(0.004)	-0.382(0.032)	-
22(1987-1996)	2.910(0.003)	-0.416(0.024)	-	2.907(0.004)	-0.428(0.033)	-	2.913(0.004)	-0.406(0.034)	-
23(1997-2004)	2.922(0.004)	-0.509(0.030)	-	2.918(0.005)	-0.477(0.042)	-	2.925(0.005)	-0.535(0.044)	-

**Table 4.3:** Fit-parameters and one-sigma errors (in brackets) of rotation coefficients, A and B (in  $\mu\text{rad day}^{-1}$ ) for the present study of individual sunspots separately for Whole-disk, Northern and Southern hemispheres. N is the no. of rotation velocities used for a given study. Also included the rotation coefficients obtained for different solar cycles using sunspot-groups data given in Javaraiah, Bertello, and Ulrich (2005) and Javaraiah (2003a); Greenwich data on sunspot groups during the period January, 1879 December, 1976, and spot group data from the Solar Optical Observing Network (SOON) during the period January, 1977-August, 2004.



(a) Northern Hemisphere



(b) Southern Hemisphere

**Figure 4.16:** The latitudinal profiles of solar mean rotation,  $\omega$  (Deg/Day) at different phases of Solar activity cycle during 1996-2011 separately for (a) Northern Hemisphere, and (b) Southern Hemisphere. Also, shown in both plots the latitudinal profiles at solar radius of  $0.94R_{\odot}$ ,  $0.96R_{\odot}$ ,  $0.98R_{\odot}$  and,  $1.0R_{\odot}$ .

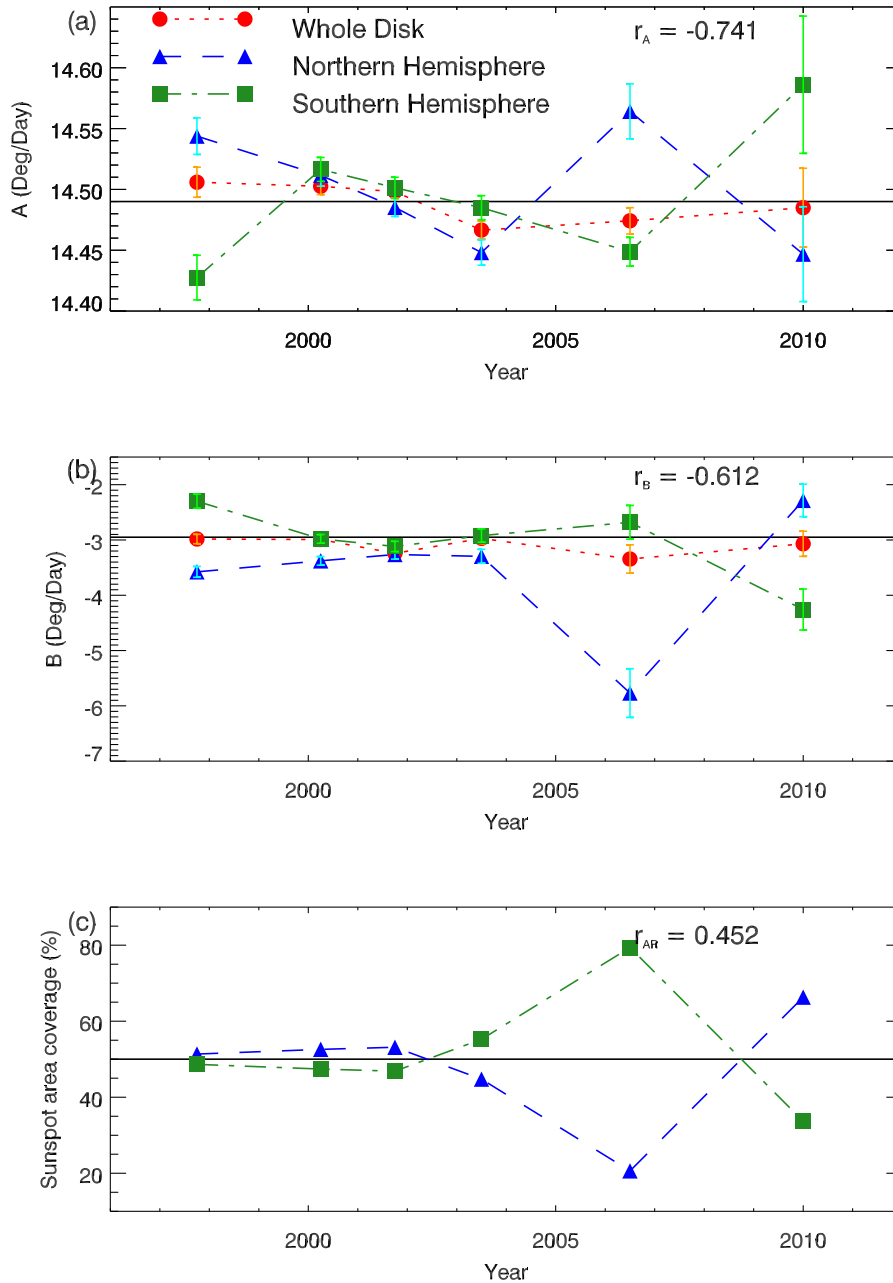


**Figure 4.17:** The variation in (a) equatorial rotation rate,  $A$ , (b) latitudinal gradient of rotation,  $B$  in (Deg/Day), and (c) Percentage of sunspot coverage area with the solar cycle phase for the Whole disk (red dots, dotted), Northern Hemisphere (blue triangle, dashed), and Southern Hemisphere (green Squares, dot-dashed).  $r$ -value in each plots is the correlation coefficient of respective parameters for North and South hemispheres. The solid horizontal line in plots a) & b) represents the global value of  $A$  and  $B$  for the whole cycle respectively.

Hemisphere	1996.5-1999.5	1999.5-2001.5	2001.5-2002.5	2002.5-2004.5	2004.5-2008.5	2008.5-2011.5
<b>Mean sunspot latitude (Deg)</b>						
Whole-disk	20.97	17.05	13.92	13.01	9.88	20.09
Northern	20.54	16.56	13.52	12.49	11.39	19.21
Southern	21.38	17.55	14.42	13.40	9.35	21.48
<b>% of sunspots in latitude <math>\geq 15^\circ</math></b>						
Whole-disk	89.76	59.03	42.77	36.51	13.65	73.68
Northern	89.76	60.05	37.87	31.73	18.34	62.89
Southern	89.75	57.94	48.96	40.03	12.02	90.81

**Table 4.4:** The values of mean sunspot latitude and the percentage of sunspot population at higher latitudes at different phase of solar cycle during 1996-2011 for whole-disk, Northern and Southern hemispheres separately.

of two hemispheres is,  $r_B = -0.612$ . These significant values of correlation coefficients implies that the NS-asymmetry is persistent throughout the cycle. A and B in respective hemispheres has similar pattern of variations with the cycle phase as it was seen in the Section [4.4.3] for whole-disk with annual binning. In Figures [4.17(a-b)], the pattern of equatorial-rotation variation with the solar cycle phase are similar in both hemispheres; the southern hemisphere follows the northern hemisphere in similar fashion, but with a phase-lag of few years. For the southern hemisphere, the equatorial-rotation rate as well as the differential rotation coefficient (in negative scale), starts with a small value (as compared to global values) at the beginning of cycle, then it ascends to a peak value near the sunspot maximum, and then the A (B)-value descends with the cycle and reaches again a minimum value at the cycle minima (lowered minimum value as compared to that at the beginning of cycle); and for the next cycle 24, the A (B)-value in South is higher than the global value of A (B) and even larger than than any Northern value during cycle 23. In the Northern hemisphere, A (B) has peak values at the start and end phase of cycle 23, where the end phase has comparatively higher value; after the maximum phase, the A(B) has the minimum value of the cycle; and for the next cycle 24, A has lowered valued than the global value and northern hemisphere is less differential. Recently, (Suzuki, 2014) undertook such study with long-term series of sunspot data; they examined the long-term modulation of B during cycles 16 to 23 as well as the yearly fluctuations in B in every cycle. They reported that the B-values in sunspot minimum years show large and

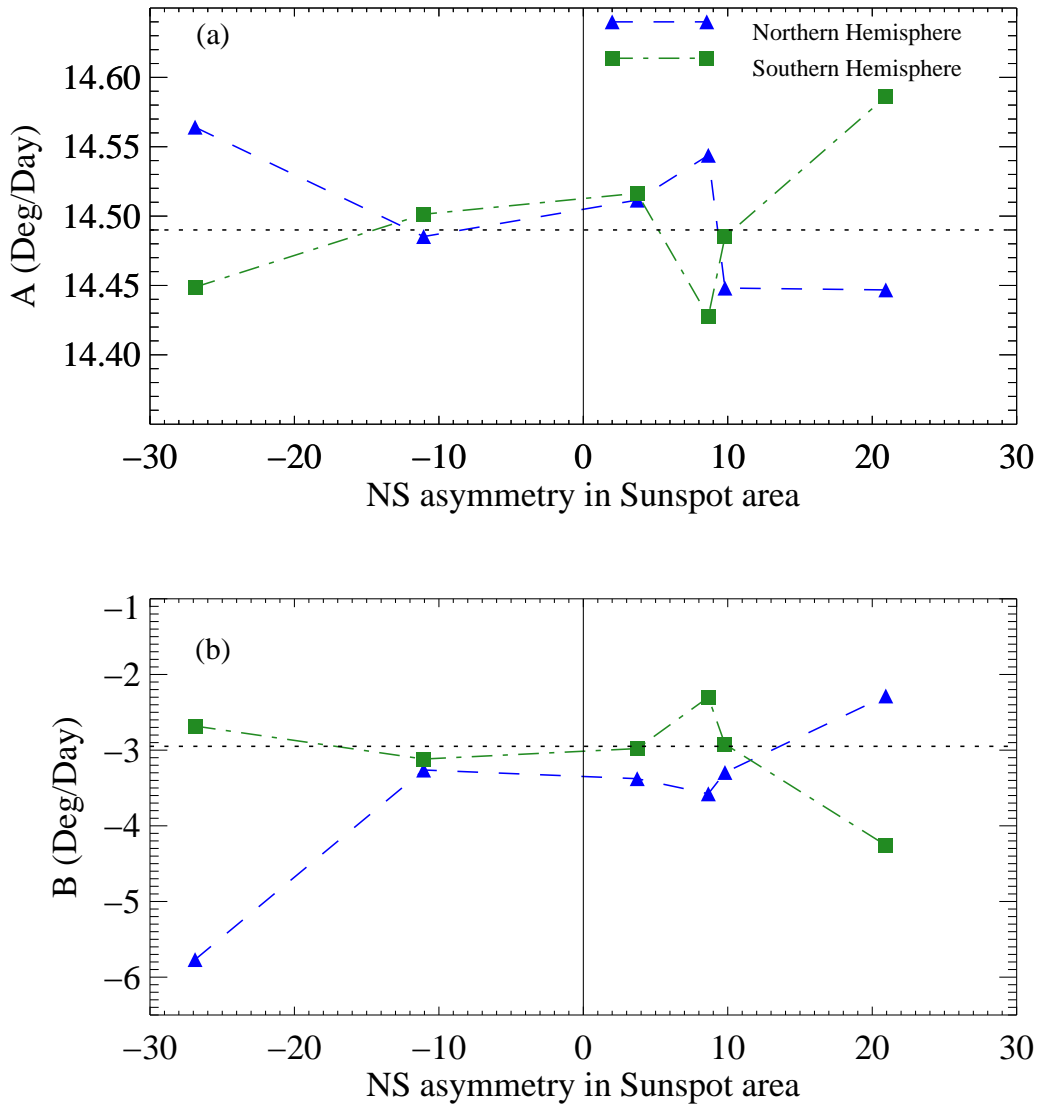


**Figure 4.18:** The variation in (a) Equatorial rotation rate,  $A$  (Deg/Day), (b) Latitudinal gradient of rotation,  $B$  (Deg/Day) with the NS-asymmetry of mean sunspot area, for the Northern Hemisphere (Blue triangle, dashed), and Southern Hemisphere (Green Squares, dot-dashed). The horizontal dotted line represents the global value of (a) Equatorial-rotation rate,  $A$ , and (b) Latitudinal gradient of rotation rate,  $B$  obtained for whole cycle period.

erratic variations, while during maximum years it has small fluctuations.

To understand the possible origin of the North-South asymmetry of rotation we computed the mean latitude at each cycle phase for North and South

hemispheres. As listed in the Table [4.4], the mean sunspot latitudes of North and South hemispheres have similar shifts in latitudes with the cycle phases. We also computed the percentage of population of sunspots observed beyond  $15^\circ$  latitudes in each cycle phase for both the hemispheres. The percent of sunspots observed at higher latitudes are again have similar values in both hemispheres at each cycle phase (Table [4.4]). Hence, the different distribution of sunspots or difference in population of sunspots from higher latitude zones in North and South hemispheres can be eluded from the possible cause of NS-asymmetry of differential rotation.

Hathaway and Wilson (1990) examined sunspot rotation rates from Mount Wilson for the period from 1921-1982, and reported that the southern hemisphere had less area covered by sunspots and had faster rotation rates than the northern hemisphere. Similar observations were also reported by Howard, Gilman, and Gilman (1984) for the time interval of 1970-1984. Hathaway and Wilson (1990), did not find good correlation between changes in latitudinal gradient of rotation with the sunspot area. In order to make comparison with their study, we also calculated the mean sunspot area in each phase of cycle for each hemispheres, and also for the whole solar-disk. Using this, we calculated an index of NS-asymmetry in mean sunspot area,  $a_{NS}$ , as follows,

$$a_{NS} = \frac{(a_N - a_S) * 100}{a}, \quad (4.4)$$

where,  $a_N$ ,  $a_S$ , and  $a$  are the mean sunspot area of Northern and Southern hemispheres, and of whole-disk, respectively at a given phase. Hence, this value has positive value when Northern hemisphere has relatively higher mean than that of southern hemisphere and vice-verse.

Figure [4.18] shows the variation of rotation parameters with the NS-asymmetry index of mean sunspot area (4.4) for both the hemispheres. The first plot clearly shows that when the Northern hemisphere had higher mean sunspot area relative to Southern hemisphere, it had lowered value of equatorial-rotation rate (in agreement with Hathaway and Wilson (1990),

Balthasar, Vázquez, and Wöhl (1986) and Javaraiah and Gokhale (1995). However, within  $\pm 10\%$  difference in mean sunspot area, there is opposite trend, the one with higher mean area has slightly higher value of equatorial-rate. Similar are the observations for the latitudinal gradient, B-value. The hemisphere with small mean sunspot area has more differential rotation; and within  $\pm 10\%$  range of difference in mean area, the hemisphere has slightly high rigid rotation having relatively smaller mean of sunspot area. Hence, the correlation between NS-asymmetry in rotation and the average sunspot area is not conclusive.

Next, we examined the possible difference in sunspot area coverage, we calculated the total sunspot area covered in each cycle phase for whole-disk, northern and southern hemisphere separately; for each hemisphere, we further calculated the percentage of sunspot area coverage with respect to total area covered in whole-disk at a given phase. Figure [4.17(c)] shows the variation of percent of sunspot area-coverage of both hemispheres with the cycle phase. The pattern in the variation of sunspot area coverage in each hemisphere is similar to the patterns of A and B (in negative scale).

To illustrate the above interpretation, we calculated the NS-asymmetry index of sunspot area coverage

$$x_{NS} = \frac{(x_N - x_S) * 100}{x}, \quad (4.5)$$

where,  $x$ ,  $x_N$ , and  $x_S$  are the total area covered by sunspots in the solar-disk, Northern and Southern hemispheres respectively.  $x_{NS}$  is the index of NS-asymmetry in sunspot area coverage. Figure [4.19] shows the variation of  $x_{NS}$ , A-values and B-values of both hemispheres with the cycle phase (6 phases). Here, are listed the observations from the plot:

- (a) At the start (phase 1), there was significant difference in the A(B)-values of two hemispheres.
- (b) Then in the subsequent phase of cycle, the  $x_{NS}$  increases slightly in posi-

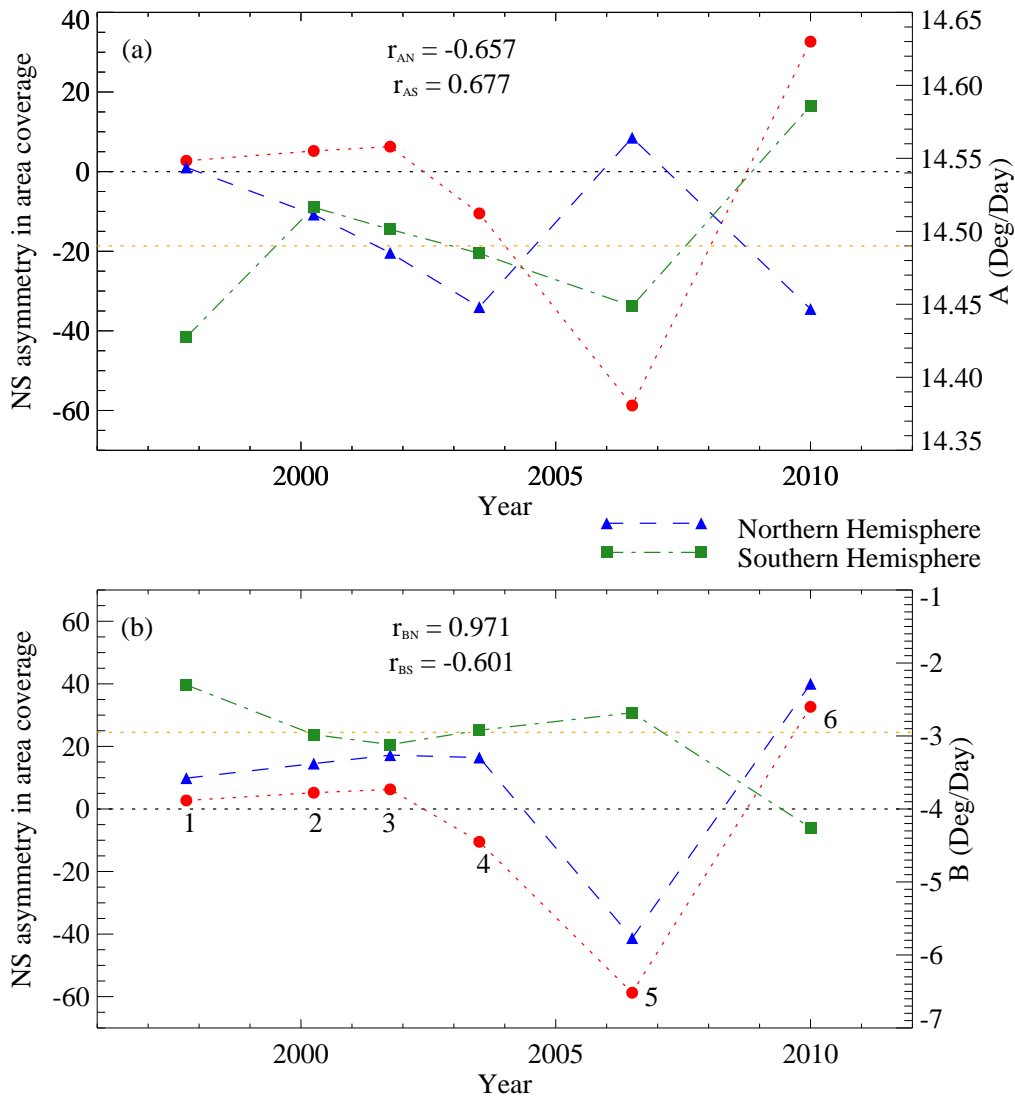


**Figure 4.19:** The variation in NS-asymmetry index of Sunspot area coverage ( $x_{NS}$ , Red dots, dotted) with the cycle phase along with (a) Equatorial rotation rate, A (Deg/Day), (b) Latitudinal gradient of rotation, B (Deg/Day) for the Northern Hemisphere (Blue triangle, dashed), and Southern Hemisphere (Green Squares, dot-dashed). The horizontal dotted line represents the global value of (a) Equatorial-rotation rate, A, and (b) Differential-rotation coefficient, B obtained for whole cycle period.  $r_{AN}$  and  $r_{AS}$  ( $r_{BN}$  and  $r_{BS}$ ) are the correlation coefficients of A(B)-values with the NS-asymmetry index of sunspot area coverage for the Northern and Southern hemispheres respectively.

tive direction (that is Northern hemisphere has higher activity than the Southern hemisphere), during which the A-value of Northern hemisphere decreases and it became more rigid, while that of Southern hemisphere

became faster and more differential.

- (c) At phase 3, there is still slight increment in  $x_{NS}$ , but here Southern hemisphere turned to have lower A-value (however, with slight increase in B-value), while the North continued to have decrease in A, with slight increase in B-value.
- (d) In next phase (4), the southern hemisphere became more active and slower and more rigid; however, Northern hemisphere *continued* to have the decreasing trend.
- (e) When the  $x_{NS}$  had highest negative value (Southern hemisphere being more active) then, the northern hemisphere was faster and more differential than southern hemisphere.
- (f) In the next cycle, the  $x_{NS}$  turns positive, with southern hemisphere having faster and more differential rotation.
- (g) We observed that between phase 2-3, there was slight increment in activity in north, followed by high activity in south between phase 3-4 (with significantly high negative value of  $x_{NS}$ ). It appears that, the South picked slower rotation in earlier period (between phases 2-3 before  $x_{NS}$  turned negative). On the other hand, between phases 3-4, the Northern hemisphere continued to have the decreasing trend in A-value and also continued to have A-value lower than that of Southern hemisphere.

Hemisphere	Correlation with A	Correlation with B
Northern	-0.657	0.971
Southern	-0.713	0.649

**Table 4.5:** The correlation coefficients of A and B-values with the sunspot area coverage percentage for Northern and Southern hemispheres.

The table [4.5] lists the correlation coefficients of rotation parameters, A & B with % of sunspot area-coverage for both the hemispheres. The variation of A & B with the sunspot-area coverage percentage for each hemisphere is

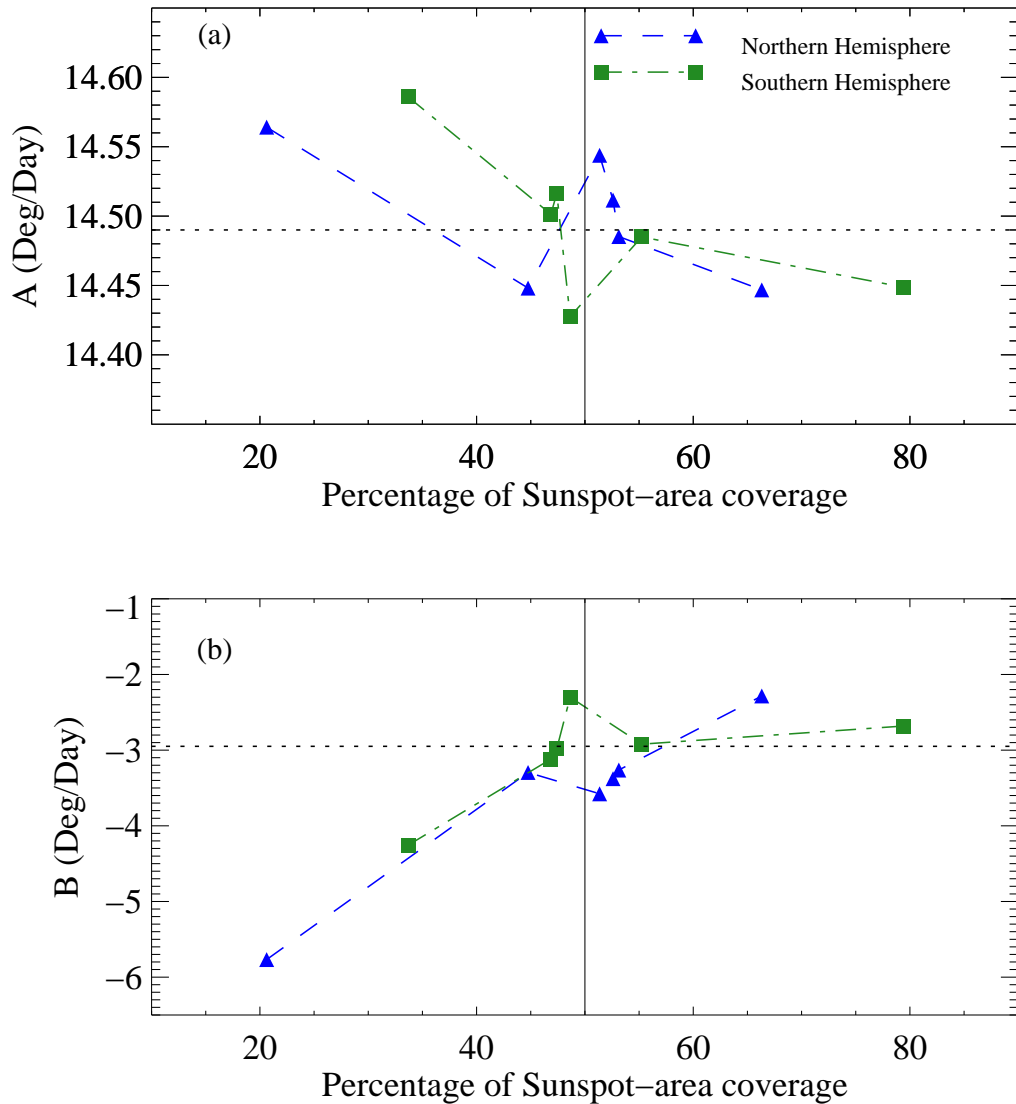


**Figure 4.20:** The variation in (a) Equatorial rotation rate,  $A$  (Deg/Day), (b) Latitudinal gradient of rotation,  $B$  (Deg/Day) with the Percentage of sunspot area coverage for the Northern Hemisphere (Blue triangle, dashed), and Southern Hemisphere (Green Squares, dot-dashed). The horizontal dotted line represents the global value of (a) Equatorial-rotation rate,  $A$ , and (b) Differential-rotation coefficient,  $B$  obtained for whole cycle period.

shown in Figure [4.20]. The significant values of correlation coefficients and the trend in the plot suggests that, for a given hemisphere, when it has relatively larger area coverage of sunspots (as compared to other hemisphere), then it has lowered value of equatorial-rotation rate,  $A$ ; and also it has more rigid

rotation compared to when it has smaller area coverage. This supports the argument that the hemisphere with more activity has slower and more rigid rotation. This is in agreement with several observations for different solar-features; Obridko and Shelting (2001) suggested that for any solar-feature of interest, with the increase of its characteristic size, its differentiability index and equatorial-rotation rate decreases; for more active features, the rotation is more rigid and slow (small A). Obridko and Shelting (2001) reported that the rotation of global magnetic fields is slower and rigid for hemisphere having higher local magnetic fields. Zhang, Mursula, and Usoskin (2013) reported that the long-term NS-asymmetry in solar surface rotation has a clear anti-correlation with the NS-asymmetry of large sunspots ( $> 2000$  MSH). The similar rotation characteristics were also observed for Small Bright Coronal Structures (SBCS) by Zaatari *et al.* (2009). In agreement to present findings for similar time periods, they found that during the first half of declining phase of cycle 23 (about 2001-2004), the northern coronal activity prevailed and rotates more slowly than the southern hemisphere. However, northern hemisphere maintained slow rotation in the next phase between years 2004-2006, even when it becomes less active. We also found in the present study (listed above) that the switching of rotation rates in northern hemisphere lags behind the changes in solar activity, while the southern hemisphere picked change in rotation prior to the sign switch of NS-asymmetry index of activity (Carbonell and Ballester, 1992). The NS-asymmetry in subsurface rotation velocity also shows the anti-correlation with activity at low latitudes, showed by Zaatari *et al.* (2006) using the GONG++ data-set.

The Grand-minimum phenomena may have correlation with the NS-asymmetry in the solar activity and hence the NS-asymmetry of rotation. The most recent Grand-minimum was the Maunder minimum (MM) from years 1645-1715; sunspots were observed during 368 days within the deep MM (1645-1700) (Hoyt and Schatten, 1998); yearly sunspot numbers were below 4 for the deep MM, and below 8 for the cycle 1700-1712 (Kovaltsov,

Usoskin, and Mursula, 2004). Towards the end of the MM (1698-1712), the sunspot number becomes relatively large. However, the NS-asymmetry of activity was unusually high during MM and the sunspots were located only in the Southern hemisphere and were confined to a region near the equator ( $0^\circ - 20^\circ$ ) (Nesme-Ribes, Ferreira, and Mein, 1993; Sokoloff, 2004; Sokoloff and Nesme-Ribes, 1994; Usoskin, Mursula, and Kovaltsov, 2000). Only after the minimum in 1715, a regular cycle commenced with sunspots in both hemispheres. Nesme-Ribes, Ferreira, and Mein (1993) found that during Maunder minimum, the equatorial-rotation rate was reduced by 2% and rotation was more differential as compared to modern times. The physical mechanism for this anti-correlation between NS-asymmetry of activity and rotation can be understood from the recent 3D MHD simulations of interaction between differential rotation and magnetic fields in the solar convection zone by Brun, Miesch, and Toomre (2004). The Maxwell stresses originate from the reaction on the flow by the Lorentz forces Sturrock (1994), hence they are enhanced for higher magnetic activity. These simulations shows that the Maxwell stresses tends to oppose Reynolds stresses and transfer the angular momentum to the poles, thus reducing the latitudinal angular velocity contrast. This implied, that when magnetic-fields are weaker, there is enhanced differential rotation, and faster velocity at low latitudes on average, in agreement with the findings for Maunder minimum.

## 4.5 Conclusion

Using the velocity data of individual sunspots as tracers for the period of solar cycle 23 and the minimum phase of cycle 24 we calculated the differential rotation rate for the whole cycle and its dependence on activity cycle, sunspot properties and the North-South asymmetry in rotation for cycle 23 and dependence of this asymmetry with the activity indices. Following are the key findings of this study:

- (a) For cycle 23, the equatorial-rotation rate,  $A = 14.49 \pm 0.003$  (deg/day) and coefficient of differential rotation,  $B = -2.95 \pm 0.03$  (deg/day).
- (b) The latitudinal profile of differential rotation for cycle 23, was within the ranges of latitudinal profiles for the depths of  $0.96R_{\odot} - 0.98R_{\odot}$ , which may be related to the fact that these depths have significant influence on the rotation rates of sunspots observed on solar surface.
- (c) For solar cycle 23, the Northern hemisphere has more differential rotation than Southern hemisphere. The Northern hemisphere is having a slightly lower value of equatorial-rotation rate, however the difference is insignificant withing one-sigma level. The cycle 23 (alike cycle 15) is an exception to the odd-even cycle rule (Javaraiah, 2003b), which assumes that odd cycle should have more differential rotation in the southern hemisphere. The rotation rate derived from individual sunspots in this study are in agreement with those derived using sunspot-groups data (Javaraiah, Bertello, and Ulrich, 2005).
- (d) The mean rotation rate,  $\omega$  and equatorial-rotation rate,  $A$ , has strong non-linear dependence on sunspot area, represented by a logarithmic function. Small sunspots rotates faster than the larger ones in agreement with Howard, Gilman, and Gilman (1984). The relation between  $\omega$  and sunspot size remains invariant for different latitude bands.
- (e) The latitudinal gradient of rotation rate,  $B$  has small (statistically insignificant) logarithmic dependence on sunspot area, with small sunspots having more differential rotation than the larger sunspots.
- (f) We studied the variation of rotation rates with the age of sunspots. The sunspots selected for this study were having life-span of 10-12 days and area between 300-800 MSH. We did not find consistent deceleration as reported for the sunspot-group study of Ruždjak *et al.* (2004). We find an acceleration in initial (1 – 3 days) and last days (> 8th day) of sunspot from different latitude bands. For mid-latitude band, the rota-

tion rates increase with age in agreement with the findings of Sivaraman *et al.* (2003). The individual sunspots and sunspot-groups studies have disagreements on the changes in rotation rate with evolution, probably due to errors introduced by area-weighted position determinations in case of sunspots-groups (Petrovay, 1993).

- (g) The initial rotation rates dependence on sunspot life-span from this study is in agreement with the results presented by Javaraiah and Gokhale (1997) using sunspot-group data. However, conclusions can not be drawn here due to limited knowledge of true evolution stages of sunspots. We need to have sufficient data of sunspots from their emergence to decay phase, then only we can reliably derive the life-span and age dependence of rotation rates.
- (h) In our study we found that during the minimum of solar cycle, the equatorial-rotation rate and coefficient of differential rotation has erratic changes, with faster and more rigid rotation than the rest of the cycle phases. For years away from the solar minimum, the A and B have small fluctuations around their global value. The solar cycle phase variation in equatorial-rotation rate from sunspots data is in agreement with the solar cycle variation of surface plasma rotation rates, which suggests the solar origin of rotation changes (Javaraiah, 2013).
- (i) The North-South asymmetry in rotation is persistent throughout the solar cycle 23, and also in the minimum of the next cycle.
- (j) The NS asymmetry in rotation has no dependence on the difference in latitudinal distribution of sunspots and the number of sunspots occurring at higher latitudes in North and South hemispheres.
- (k) The hemisphere having larger mean value of sunspot area at a given phase have slower and more rigid rotation as compared to the other hemisphere.
- (l) The total area covered by sunspots in each hemisphere at a given phase

appears to be a better index for the sunspot activity. The hemisphere with relatively smaller sunspot coverage area (*i.e.* lower activity) has faster and more differential in rotation.

- (m) Our study shows that the NS-asymmetry in the percentage of sunspot coverage area radically attained high magnitude with reversed sign during the maximum phase of the cycle 23. However, it appears from the present study that the change in rotation rates in southern hemisphere occurred prior to this change in activity, while the northern hemisphere's changes in rotation followed later in accord with the changes in sunspot activity.

In the present study we have observed only one solar cycle sunspot data, in order to check the exact anti-correlation between the NS asymmetry in rotation and activity index, and the relative solar cycle phase changes in hemispheric rotation profiles we need to perform similar study as suggested in this thesis using long time series of sunspot data covering several solar cycles.

# Chapter 5

## Study of Bipolar Tilt angles

### 5.1 Introduction

The average inclination of bipolar active regions on solar surface is not exactly toroidal, but have some inclination with respect to the east-west direction, statistically, the leading (west-ward) polarity is slightly closer to the equator than the following polarity. The systematic origin of tilt of bipolar active regions on solar surface is a relevant tracer for two crucial components of solar dynamo models; the process of active region flux emergence and the mechanism of generation of poloidal magnetic fields.

Using thin flux tube simulations, D'Silva and Choudhuri (1993), Fan, Fisher, and McClymont (1994), Fisher, Fan, and Howard (1995) and Fisher *et al.* (2000) showed that, during the buoyant rise to the surface, the toroidal flux tubes are acted upon by a variety of forces, notably the Coriolis force and turbulent convective buffeting. Both of these physical processes imprint their signatures in the form of tilt and twist on the rising magnetic fields (also see Fan, 2009; Weber, Fan, and Miesch, 2013). These simulations suggested that the Coriolis force induced by diverging and expanding motions of rising flux loops, imparts a tilt to the summit clockwise (counter-clockwise) in the northern (southern) hemisphere, such that the leading polarity is tilted equatorward relative to the following polarity as viewed from above the surface. Since, the

Coriolis force increases with latitude, the amount of tilt angle of bipoles with respect to the equator, has approximately  $\sin(\text{latitude})$  dependence, which is the well known Joy's Law (introduced in Chapter 1 in Section 1.3.1.2). The tilt-angle distribution observations provides guidance and constrain to the solar dynamo theories. To be consistent with the observed tilt-angle behavior of bipolar active regions, the present  $\alpha - \omega$  dynamo models parameterized the initial field strength near  $4 \times 10^4$  G (Weber, Fan, and Miesch, 2011). Kosovichev and Stenflo (2008) from the study of MDI magnetograms they observed that the tilt angles restores to the mean angle expected from Joy's law at a given latitude band with the evolution of bipolar regions, instead of relaxing towards the east-west direction as expected from the Coriolis force based theory, according to which the relaxation should be towards the direction where the Coriolis force vanishes. This finding was in agreement with the results of Howard (1996c) and Sivaraman *et al.* (2007). Moreover, they did not find the dependence of tilt on the magnetic flux, in contradiction to the Coriolis force effect (Dasi-Espuig *et al.*, 2010; Tian, Liu, and Wang, 2003). There exists other theoretical explanations for the observed bipoles tilt-angles. Babcock (1961) suggested that the bipolar-tilt-angles reflects the orientation of sub-surface magnetic field lines stretched by the differential rotation. Another explanation by Howard (1996c) is that the tilt is created by shearing due to subsurface large-scale flows, differential rotation and meridional flows, after the emergence (also see Brandenburg, 2005).

In the current paradigm of large-scale solar dynamo, the differential rotation largely drives the toroidal field, however, the driver of the poloidal magnetic field in the solar dynamo is much less well known. Tilts of bipolar sunspots constitute a vital ingredient in many models of solar dynamo, contributing to the creation of solar poloidal field through the decay of tilted bipolar active regions (Nandy and Choudhuri, 2001). In the Babcock-Leighton (BL) dynamo model, the poloidal magnetic field results from the systematic tilt of sunspot-groups and bipolar magnetic regions and subsequent redistri-

bution of their magnetic fluxes by near-surface flows (see review on dynamo models by Charbonneau, 2010). Recently, Dasi-Espuig *et al.* (2010) and McClintock and Norton (2013) found anti-correlation between the mean tilt angle (normalized to emergence latitude) of a given cycle and the strength of that cycle.

However, there are no clear consensus about the mechanism of the origin of bipolar-tilt angles; and its contribution to the evolution of large-scale magnetic fields and to polar field reversals. Using large time-series of bioplar data-base, and accompanying technically advanced and consistent statistical studies of evolution of time-latitudinal distribution of tilt-angles with various properties of bipolar regions and with solar activity phases can provide more insight about the origin of inclined bipoles and hence the feedback mechanism between magnetic-fields and convective flows.

Recently, using advanced computational techniques, Stenflo and Kosovichev (2012), Li and Ulrich (2012) and Tlatov *et al.* (2013) extracted bipolar active regions from large solar archives and confirmed the Joy's law. The high resolution magnetograms and continuum images from SoHO/MDI provides reliable and sufficient data to study the bipolar-tilt angles and other related properties. The study of tilt angles of bipolar sunspot-groups obtained from the MDI data-set is not available for the complete solar cycle 23. In this thesis, we identified sunspot-groups and derived the latitudinal and time distributions of bipolar tilt-angles. Also, we studied the size dependence of tilt angles and separation distance of two polarities of a bipole. In the Section [5.2] we provide the details of sunspot-group parameters which were derived relevant to this study, followed by results of various studies undertaken pertaining to magnetic-bipoles tilt-angles and polarity-separation distance, and their dependence on bipole size and solar cycle phase in Section [5.3]. The conclusions drawn from these studies are presented in Section [5.4].

## 5.2 Data and observables

We employed stray-light-corrected full-disk SoHO/MDI continuum images and magnetograms to study the temporal-spatial distribution of sunspot-bipolar tilt-angles during the course of cycle 23 and the minimum phase of cycle 24, spanning from years 1996 to 2011. We extracted sunspot-bipoles on the basis of proximity and analogous magnetic-field strengths of the neighboring opposite polarity sunspots in an automated manner. The details of procedures developed for polarity measurement and sunspot-group identification were presented in the Section [2.6]. The same bipolar regions were may be identified several times in different continuum images but they have been treated as separate regions as they may represent different evolutionary phases.

For each identified sunspot-group we derived the following parameters relevant for the present study:

- (a) **Area of Bipoles:** The area of each sunspot and pores were corrected for the foreshortening (see Section [2.4.4] of Chapter 2 for details of sunspots parameters calculations). For both the negative and positive polarity regions (constituting a number of sunspots and pores) of the group we calculated its total area. And their combined area constitutes the total bipole area.
- (b) **Area-weighted centroid:** We calculated the area-weighted centroid position (in heliographic latitudes and longitudes) of unipolar regions of each sunspot-bipoles. Using the centroid position and total area of both polarity regions, we calculated the area-weighted centroid position of the sunspot-group.
- (c) **Heliocentric position:** The heliocentric position,  $\mu$  of sunspot-group was calculated using its centroid position. In the present study we have utilized sunspot-groups within the longitudes of  $\leq 75^\circ$ , or  $\mu \geq 0.26$ .

With this limit, we had total of 48674 sunspot-groups for the period 1996-2011.

- (d) **Polarity separation distance:** Polarity separation distance is the geodesic distance between latitude and longitudes of two centroid points of opposite polarity regions of a sunspot-group.
- (e) **Tilt-angle of sunspot-bipoles:** The tilt-angle is the angle the axes of bipoles make with respect to the local circle of latitude passing through its middle. The region west-ward is considered the leading side while the east-ward region as the following side. The tilt angle was measured clockwise (counter-clockwise) from the east-west latitude line passing from the center of axis joining the leading and following regions area-weighted centroids, for northern (southern) hemisphere, irrespective of polarities of the leading side of the group. Thus, the tilt-angle has positive value, if the leading side is equator-ward, for both the hemispheres. With the above definition, the tilt-angle values has range of  $[-90^\circ, +90^\circ]$ .

## 5.3 Results and discussion

### 5.3.1 Latitudinal distribution of bipoles and joy's law

Figure [5.1] shows the distribution of tilt-angles of 48674 sunspot-bipoles obtained for the complete period of 1996-2011. To this distribution we fitted a Gaussian function (of four terms), *i.e.*,  $G(x) = \frac{1}{\sigma\sqrt{2\pi}}e^{-(x-\mu)^2/(2\sigma^2)} + c$ , with a positive mean value,  $\mu = 6.53^\circ$  and  $\sigma = 14.97^\circ$ . Hale *et al.* (1919) also found that the tilt angles of sunspot-groups are statistically positive and are in the range  $5^\circ - 10^\circ$ . Sivaraman, Gupta, and Howard (1999) found the peak value of tilt-angle at about  $+6^\circ$  for sunspot-groups data-sets of Kodaikanal Observatory (1906-1987) and Mt. Wilson Observatory (1917-1985). From the study of magnetogram data Howard (1996a) and Stenflo and Kosovichev (2012) found that the most common tilt angle of  $\sim 10^\circ$  for all bipolar regions between  $15^\circ - 20^\circ$  latitude range including the largest active regions down to

regions of  $\sim 10^{20}$  Mx. Howard (1996c) found that the magnetic loops tend to relax at equilibrium tilt-angle of  $\sim 5^\circ - 7^\circ$  on timescales of 4.37 days.

The negative tilt-angle values corresponds to bipoles with poleward leading polarity. The Coriolis forces is expected to impart an equator-ward tilt (according to the definition of tilt used here, the equatorward leading polarity will have positive tilt-angle). However, other phenomena may affect this axis orientation and induce randomness, for example the buffeting of rising magnetic-flux loops by the turbulent convective flows (Longcope, Fisher, and Arendt, 1996; Weber, Fan, and Miesch, 2013). Since, we have used an intricate computer algorithm to identify sunspot-groups, it is also likely that there may be an artifact in some cases of angle estimations caused by false or mis-identification of sunspots belonging to a sunspot-group.

To obtain the latitude variation of tilt-angles, we binned latitudes in  $5^\circ$  bins (with combined Northern and Southern hemispheres) and calculated the mean of tilt angles in each bin. Figure [5.2] shows the plot of mean sunspot tilt-angle (in degrees) with the respective latitude bins. The standard error of means are shown as error bars. For the latitude range of upto  $30^\circ$ , the tilt-angle increases with latitude, as shown with a linear-fit, in agreement with the Joy's Law. The obtained linear-fit between tilt-angle ( $\gamma$ ) and latitude ( $\theta$ ) is:

$$\begin{aligned}\gamma &= (0.38 \pm 0.02)\theta - (2.40 \pm 0.34) , \\ \gamma &= (22.41 \pm 1.23) \sin \theta - (2.49 \pm 0.35)\end{aligned}\tag{5.1}$$

In the plot we also observed the bending of tilt-angles for latitudes  $> 30^\circ$ . This bending was also recently reported by Tlatov *et al.* (2013) for active-region bipoles of area  $> 300$  MSH extracted from MDI magnetograms for period 1996-2011. They also confirmed these findings with the bipoles extracted from Kitt-Peak magnetograms (1975-2003) and HMI data (2010-2012). In contrast, in another recent study by Stenflo and Kosovichev (2012), the bending was absent, though they also obtained bipoles from MDI magnetograms

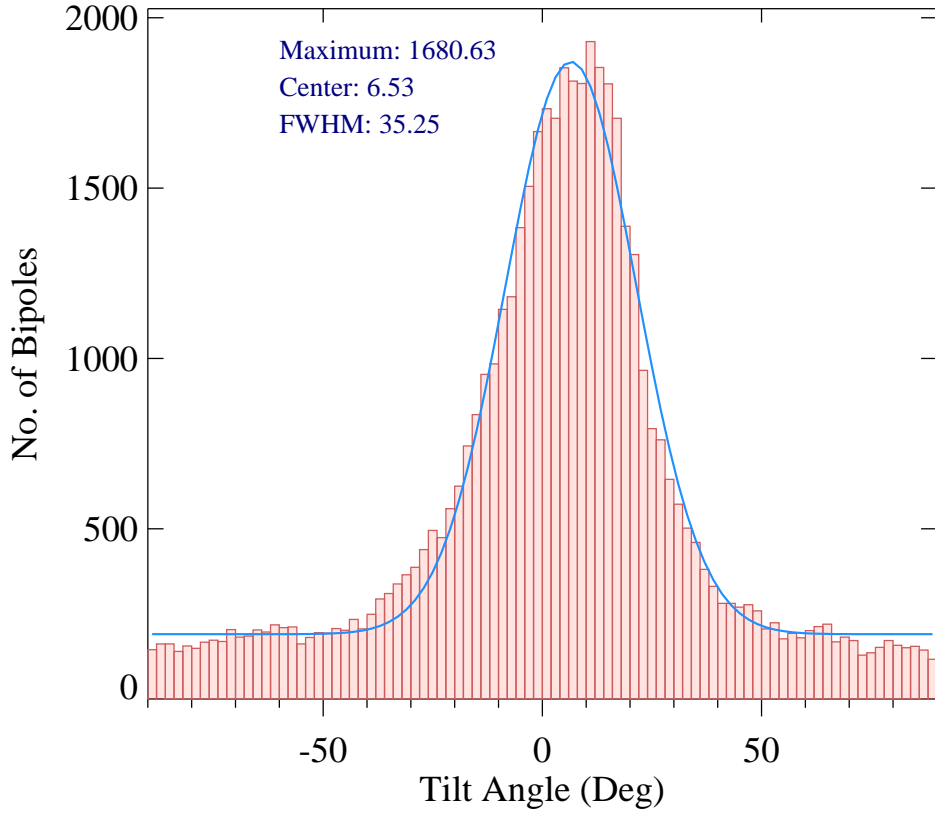


**Figure 5.1:** The distribution of sunspot-bipoles tilt angle (in Deg) for solar cycle 23. The Gaussian function fit with four terms;  $G(x) = \frac{1}{\sigma\sqrt{2\pi}}e^{-(x-\mu)^2/(2\sigma^2)} + c$  is also shown. This has the mean value ( $\mu$ ) of  $6.53^\circ$  and the full width at half maximum, FWHM ( $\approx 2.36\sigma$ ) has value  $35.25^\circ$ .

Authors	Observed solar features	Data	slope1	slope2
Present study	Sunspot-groups	MDI continuum, 1996-2011(cycle 23)	0.38(0.02)	22.41(1.23)
Fisher, Fan, and Howard, 1995	Sunspot Groups	Mt. Wilson data, 1917-1985 (cycles 16-21)	-	15.69(0.66)
Dasi-Espuig <i>et al.</i> , 2010	Sunspot-groups	Mt. Wilson, 1917-1985	0.26(0.05)	-
Dasi-Espuig <i>et al.</i> , 2010	Sunspot-groups	Kodaikanal 1906-1987	0.28(0.06)	-
Stenflo and Kosovichev, 2012	Magnetic bipoles	MDI magnetograms, 1996-2011	-	32.1(0.7)
Tlatov <i>et al.</i> , 2013	Magnetic bipoles	MDI magnetograms, 1996-2011	-	27( $2\sigma=4$ )
Weber, Fan, and Miesch, 2013	$10^{20} - 10^{22}$ Mx	Simulations	0.36(0.02)	22(1)

**Table 5.1:** The value of slopes between tilt-angle ( $\gamma$ ) and latitudes ( $\theta$ ) is listed with their one-sigma errors for the present study of sunspot-groups and from previous studies of sunspot-groups or magnetic bipoles from different data-sets. Slope1 (in deg) corresponds to  $k$ , from the fit,  $\gamma = k\theta + c_1$ , while slope2 (in deg) corresponds to  $\gamma_0$ , from the fit of the form,  $\gamma = \gamma_0 \sin \theta + c_2$ . In the last row is listed the results of Joy's law for simulated magnetic flux-tubes with flux in the range of  $10^{20} - 10^{22}$  Mx.

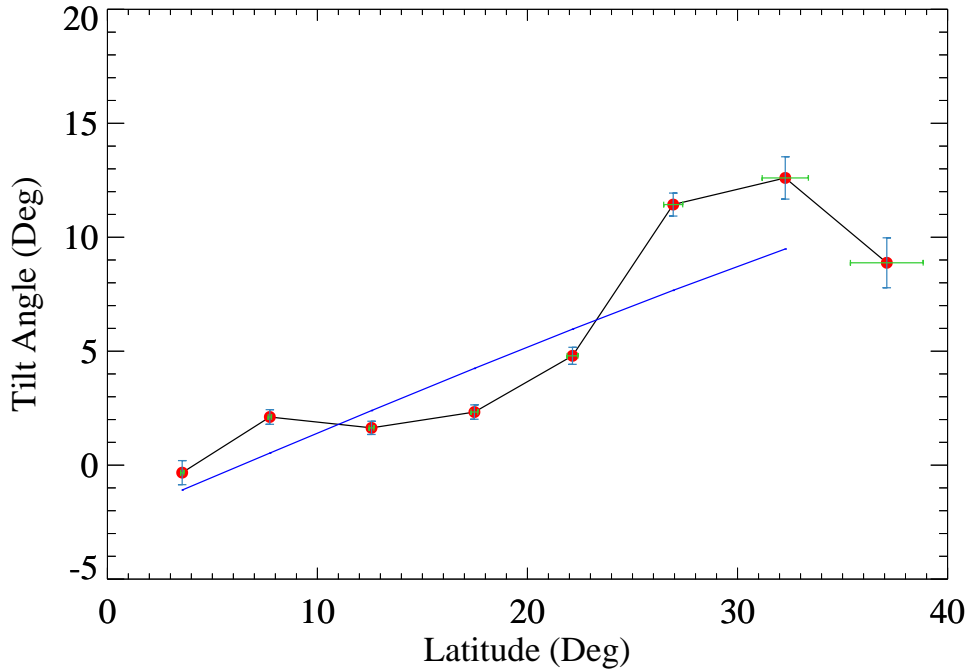


**Figure 5.2:** The sunspot-groups tilt-angle variation with latitude for cycle 23. The slope of the linear-fit (Joy’s Law) is listed in the Table 5.1.

of same period, but using different algorithm and tilt-angle calculations.

According to the Tlatov *et al.* (2013), the regions with area less than 300 MSH corresponds to ephemeral regions, which had different tilt-angle distribution in comparison to large-active regions, however, small bipoles also had slight bending of Joy’s law at latitudes  $30^\circ - 40^\circ$ . The sunspots observed from white-light images corresponds to large-flux regions, hence the present sunspot-groups data may not incorporate small ephemeral regions as can be identified from magnetograms. To compare the obtained Joy’s law, the slope obtained from other previous studies are listed in the Table [5.1] (for further comparisons on Joy’s law, see McClintock and Norton, 2013). The present slope is higher as compared to previous studies based on sunspot-group data, and closer to the values obtained from active regions identified from magnetograms. The different values might be due to varying selection approach employed by various authors. Interestingly, our values  $0.38^\circ$  (or  $22.4^\circ$ ) (Eq

[5.1]) are in agreement with the values  $0.36^\circ$  (or  $22^\circ$ ) obtained from simulated flux-tubes having flux in the range  $10^{20} - 10^{22}$  Mx by Weber, Fan, and Miesch (2013).

### 5.3.2 Bipoles separation distance distribution

For each extracted sunspot-bipole, we measured the polarity separation distance, which is the geodesic distance of the line joining the centroids of two polarities. Figure [5.3] shows the distribution of the polarity separation distance for the present sunspot-group data set from solar-cycle 23. A Gaussian function fit has the mean,  $\mu$  of  $4.14^\circ$ , with  $\sigma = 1.86^\circ$ . In Figure [5.4] is plotted the variation of polarity separation distance with latitudes binned in  $5^\circ$ . According to this plot, the average polarity separation distance increases with latitudes upto about  $22^\circ$ , beyond which the average distance between bipoles decreases. There is again deflection at higher latitudes around  $30^\circ$  similar to mean tilt-angle bending in Figure [5.2].

To the latitudinal variation of average separation distance we fitted a sine function of the form,  $d = P_0 + P_1(\sin(P_2\theta))$ , where  $d$  and  $\theta$  are the average polarity separation distance (in deg) and latitude (in deg). The obtained fit for latitude upto  $35^\circ$  is of the form:

$$d = 4.14(1.19) + 2.10(1.54) \sin(4.97(0.84)\theta), \quad (\chi^2 = 0.161). \quad (5.2)$$

Tian, Liu, and Wang (2003) found that the magnetic flux of bipoles is correlated to the separation distance in agreement with Wang and Sheeley (1989). They also found that the tilt-angle is a function of polarity separation distance, it increases with the distance, while for distance greater than 80 Mm, the tilt-angle decreases with the increasing distance.  $d$  also includes the radii of two unipolar region, hence  $d$  is also a measure of bipole size. According to the Coriolis force based tilt-angle generation, since the speed of the buoyant rise of loop depends on both the amount of flux and magnetic-field strength, the tilt-

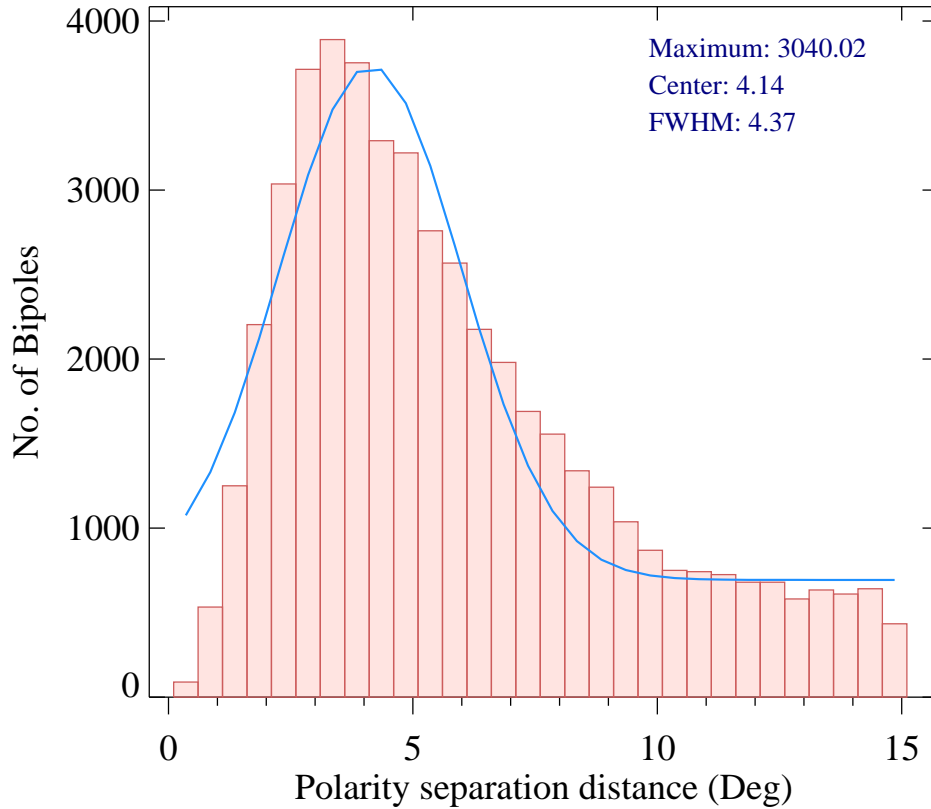


**Figure 5.3:** The distribution of polarity separation distance (in Deg) of sunspot-bipoles from solar cycle 23. The Gaussian function (with four terms), it has the mean value ( $\mu$ ) of  $4.14^\circ$  and the full width at half maximum, FWHM of  $4.37^\circ$ .

angle magnitude should be correlated with these properties of bipoles (Fisher, Fan, and Howard, 1995). However, simulations suggests that the drag-force due to convective motions can overcome magnetic-buoyancy and magnetic-forces for certain range of initial flux, and hence tilt-angle may show different correlations with the flux magnitude in these range (Weber, Fan, and Miesch, 2013). We had undertook the study of dependence of tilt-angle and separation distance on bipole area and obtained results are presented in Section [5.3.4].

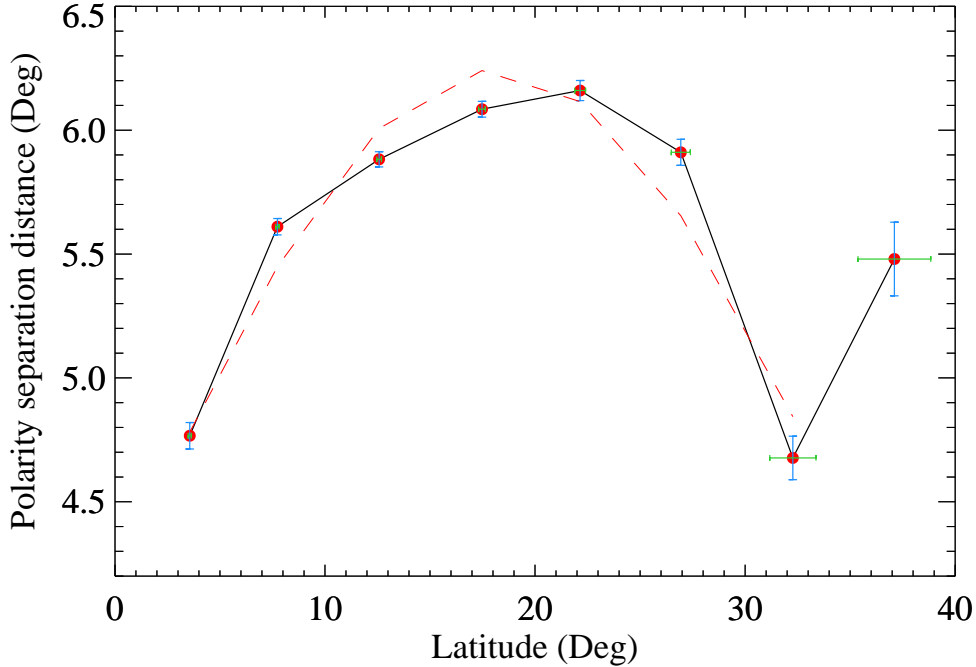


**Figure 5.4:** Latitudinal variation of mean polarity separation distance (in Deg) of sunspot-bipoles. The error bars represent standard errors. The dashed-curve is the sine-fit function (Eq 5.2) upto latitude  $< 35^\circ$ .

### 5.3.3 North-South asymmetry in distribution of bipoles

We investigated the presence and nature of North-South asymmetry in sunspot-group tilt-angles and polarity separation distances. Figure [5.5] shows the tilt-angle distribution for northern and southern hemispheres. The Gaussian fit has different mean ( $\mu$ ) values for different hemispheres;  $\mu_N = 7.40^\circ$  and  $\mu_S = 5.89^\circ$  for northern and southern hemisphere respectively. The northern hemisphere has large positive tilt-angle on average during the course of solar cycle 23 as compared to the southern hemisphere. In contrast, Li and Ulrich (2012) from the study bipoles extracted from magnetograms of Mt. Wilson (1974-2012) and MDI (1996-2010), found that the southern hemisphere has higher positive tilt-angles at all latitude ranges as compared to that in the northern hemisphere. Though they have also utilized the cycle 23 bipoles similar to our study, the discrepancy in results could be due to different hemi-

spheric asymmetry in previous cycles data. McClintock and Norton (2013) also reported that the cycle averaged mean tilt-angles show significant hemispheric asymmetry. They found significant inverse correlation between tilt angle and total sunspot area (a proxy for cycle strength) for the southern hemisphere. Dasi-Espuig *et al.* (2010) from the study of sunspot-groups from various cycles observed that the stronger cycles produces small average tilt-angles. Thus, the asymmetry in sunspot area distribution in two hemispheres is probably the cause of asymmetry in average tilt-angles. A stronger activity leading to smaller tilt angle may cause weaker poloidal seed field for the next-cycle, since Cameron and Schüssler (2012) postulated that the amount of poloidal field around sunspot minimum and the strength of next cycle are correlated.

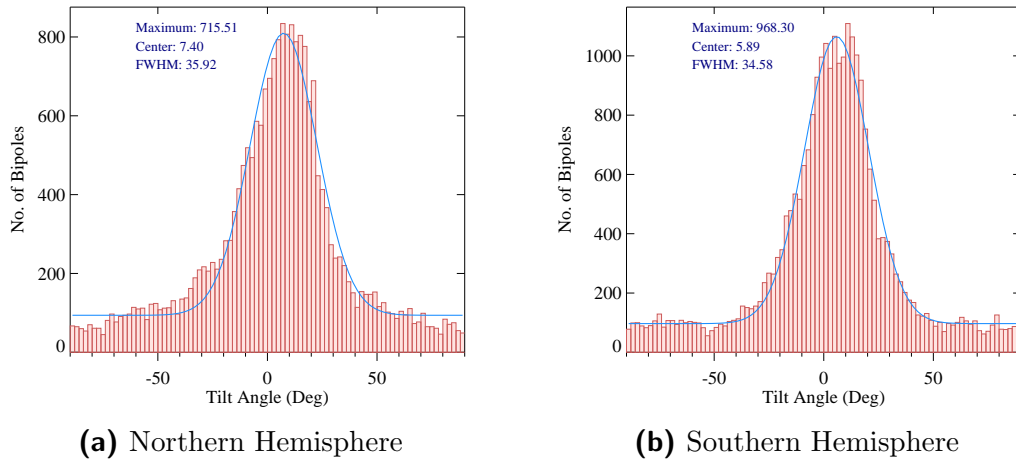


**Figure 5.5:** The distribution of sunspot-bipoles tilt angle (in Deg) for (a) northern, and (b) southern hemispheres respectively. The solid-curve is the fitted Gaussian function (with four terms).

The latitudinal variation of tilt-angle (for  $5^\circ$  latitude bins) is plotted in the Figure [5.6]. The downturn in tilt-angle for latitudes beyond  $30^\circ$  is present in both hemispheres as it was noted for latitudinal distribution of tilt-angle data for whole-disk. For latitudes beyond  $20^\circ$  upto about  $35^\circ$ , the mean tilt-angles in Northern hemisphere are  $\sim 2^\circ - 3^\circ$  higher than it is for southern hemisphere.

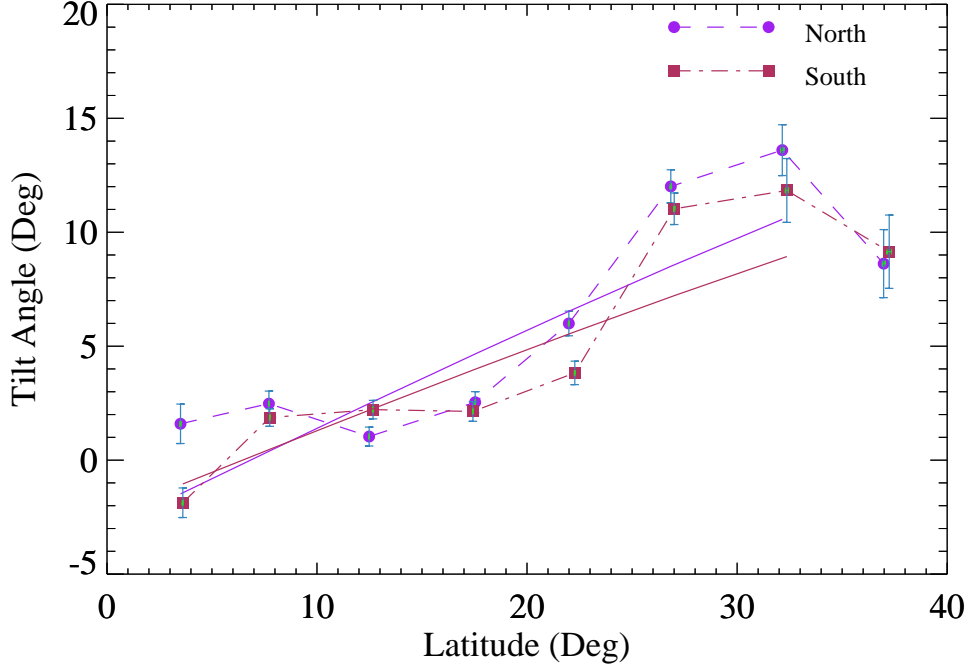


**Figure 5.6:** The sunspot-groups tilt-angle variation with latitude for northern (dot, dashed), and southern (square, dot-dashed) hemispheres of cycle 23. The slope of the linear-fit (Joy's Law) is listed in Equations 5.3 & 5.4. The error bars represents the standard error.

The Joy's law for northern and southern hemispheres are:

$$\begin{aligned}\gamma_N &= (0.43 \pm 0.03)\theta - (2.93 \pm 0.53) , \\ \gamma_N &= (25.57 \pm 1.84) \sin \theta - (3.04 \pm 0.54)\end{aligned}\quad (5.3)$$

$$\begin{aligned}\gamma_S &= (0.36 \pm 0.03)\theta - (2.29 \pm 0.44) , \\ \gamma_S &= (21.12 \pm 1.62) \sin \theta - (2.38 \pm 0.45)\end{aligned}\quad (5.4)$$

The peak values of distribution of polarity separation distance,  $d$  (in degree) for northern and southern hemispheres are equivalent to each other, as shown with Gaussian-function fits in the respective distributions in Figure [5.7]. The latitudinal variation (with  $5^\circ$  latitude bins) of separation distance in northern and southern hemispheres have no identifiable asymmetry (Figure

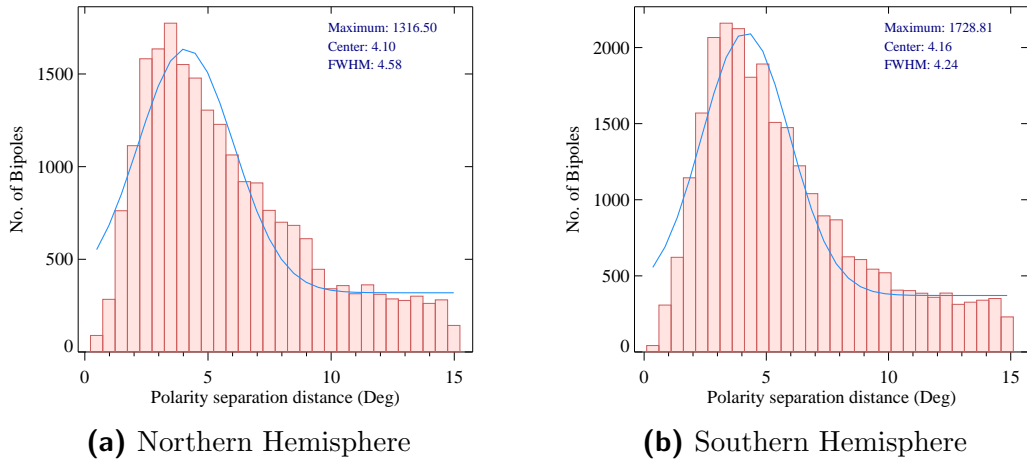


**Figure 5.7:** The distribution of sunspot-bipoles separation distance (in Deg) for (a) northern, and (b) southern hemispheres respectively. The solid-curve is the fitted Gaussian function (with four terms).

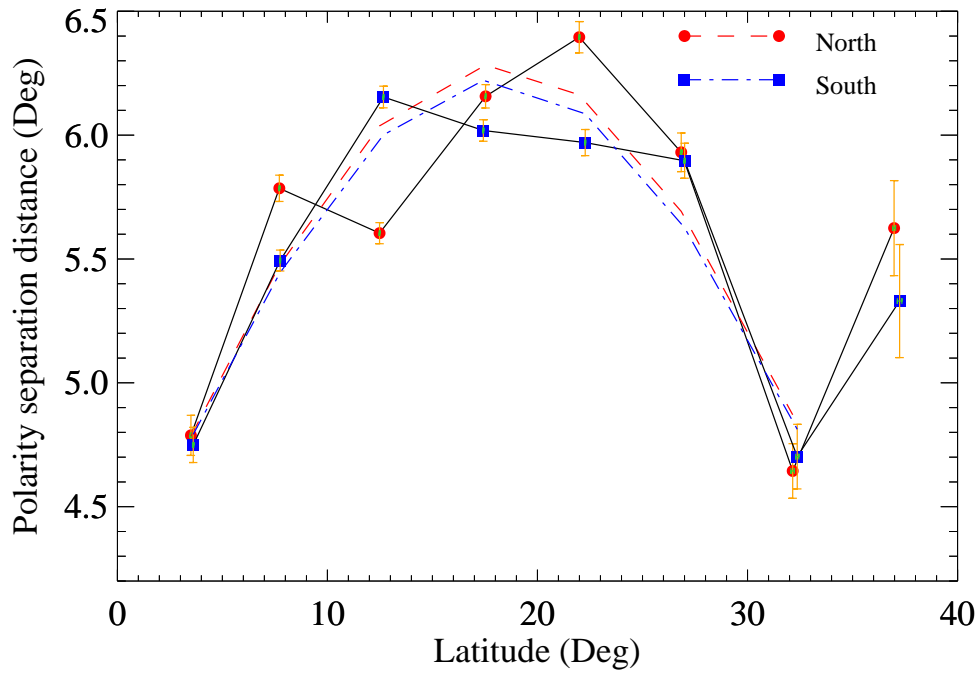


**Figure 5.8:** The sunspot-groups separation distance variation with latitude and sine fit functions for northern (dot, dashed), and southern (square, dot-dashed) hemispheres of cycle 23. The error bars represents the standard error.

[5.8]). The sine fit function of the form in Eq [5.2] between separation distance and latitude for the northern and southern separately are:

$$d_N = 4.14(1.18) + 2.14(1.53) \sin(4.98(0.83)\theta), \quad (\chi^2 = 0.464). \quad (5.5)$$

$$d_N = 4.15(1.19) + 2.07(1.54) \sin(4.98(0.85)\theta), \quad (\chi^2 = 0.168). \quad (5.6)$$

### 5.3.4 Tilt-angle and polarity separation distance dependence on sunspot bipoles area

To figure out the dependence of tilt-angle on the size of bipoles, the sunspot-groups were binned into equally-spaced 19 bins in log-scale starting from 2.5 MSH to 2850 MSH and for each bin we calculated the average tilt-angle. In Figure [5.9] is plotted the variation of average tilt-angle with the average area for each binned sunspot-group data. For sunspot-groups having area less than 1000 MSH, we fitted a logarithmic function to this plot. This non-linear relation between tilt-angle and group area is more clear in logarithmic scale for area as shown in the Figure [5.9b] with a linear fit. The fit-parameters with one-sigma errors and chi-square values are listed in Table [5.2]. The linear-fit has a statistical significance of above  $2\sigma$ . This shows that larger bipoles have relatively small tilt-angles as compared to small bipoles, however the decrease in tilt-angle is infinitesimal; as the fit-parameters coefficients implies, the change in  $\gamma$  for bipole of area 100 MSH to that of 1000 MSH is about  $-0.73^\circ$ . Stenflo and Kosovichev (2012) did not find any dependence of tilt angle with the flux of bipoles. They argued that with this no relation of tilt-angle with bipole size and also considering the results reported by Sivaraman *et al.* (2007) and Kosovichev and Stenflo (2008) *i.e.*, the tilt-angle relax after emergence to an equilibrium angle prescribed by Joy's law independent of bipole size or flux, and not towards the east-west orientations, the Coriolis force theory of tilt-angle generation is untenable. They

further suggested that, in a scenario, where average tilt-angle is independent of bipole size implies that smaller bipoles have significant contributions to the N-S dipole moment, and hence to polar field reversal.

Another form to define region size is the bipolar moment,  $B_m = F \cdot d$ , it is a function of magnetic flux of bipole,  $F$ , and the separation distance,  $d$  between unipolar regions (Stenflo and Kosovichev, 2012). The flux of bipole may be correlated with the size of the bipoles (as discussed in previous Chapter 3). In agreement to our results, Illarionov, Tlatov, and Sokoloff (2015) reported that for large bipoles having area  $> 300$  MSH, the tilt-angle increases moderately with increasing bipolar moment.

Relation	Logarithmic-fit, $A + B(\log(x_1))$			Linear-fit, $C + Dx_2$			
	A	B	$\chi^2$	C	D	$\chi^2$	$D/\sigma$
$\gamma$ vs Area	4.798(0.586)	-0.725(0.290)	4.295	4.798(0.587)	-0.725(0.290)	55.837	-2.499
$d$ vs Area	3.491(0.058)	1.199(0.030)	14.295	3.491(0.060)	1.199(0.030)	185.835	40.644

**Table 5.2:** The fit-parameters with one-sigma errors in brackets and chi-square values for different fit-functions. The logarithmic fit is for variation of tilt-angle ( $\gamma$ ) or polarity separation distance ( $d$ ) with sunspot-group area ( $x_1$ ). The linear fit is for variation of  $\gamma$  or  $d$  with logarithm of sunspot-group area ( $x_2$ ).

We further looked for the area dependence of polarity separation distance. Figure [5.10a] plots the separation distance (in deg) with binned sunspot-group area, also with the logarithm of area as shown in Figure [5.10b]. A logarithmic-function fit and a linear fit for area upto 1000 MSH are also shown in these two plots, the fit-parameters are listed in Table [5.2]. The linear-fit of separation distance and logarithm of bipole area has a positive slope. The bipoles having area  $> 1000$  MSH have a downturn in separation distance. These results implies that the distance between unipolar regions increases with their total area, however, bipoles larger than 1000 MSH tend to have reduced separation distance with increasing size. The logarithmic scale of area also implies that the bipoles size increases faster as compared to the separation distance; it increases by  $1.2^\circ$  between bipoles having area 100 MSH and 1000 MSH. Cameron *et al.* (2010) and recently, Illarionov, Tlatov, and Sokoloff (2015) found that  $d$  is a function of square-root of sunspot-group area

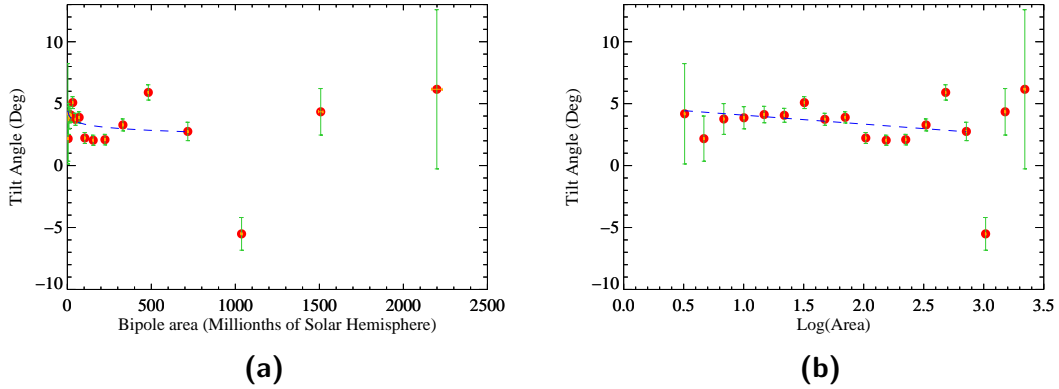


**Figure 5.9:** The variation of tilt-angle (in deg) with (a) sunspot-group area (in MSH), and (b) logarithm of sunspot-group area. In both plots the sunspot-group data was binned into 19 equally-spaced area bins in logarithmic scale starting from 2.5 MSH to 2850 MSH. The solid-curve in (a) is the logarithmic-function fit upto 1000 MSH and the solid-line in (b) is a linear-fit. The fit-parameters are listed in Table 5.2. The error-bars represents the standard errors.

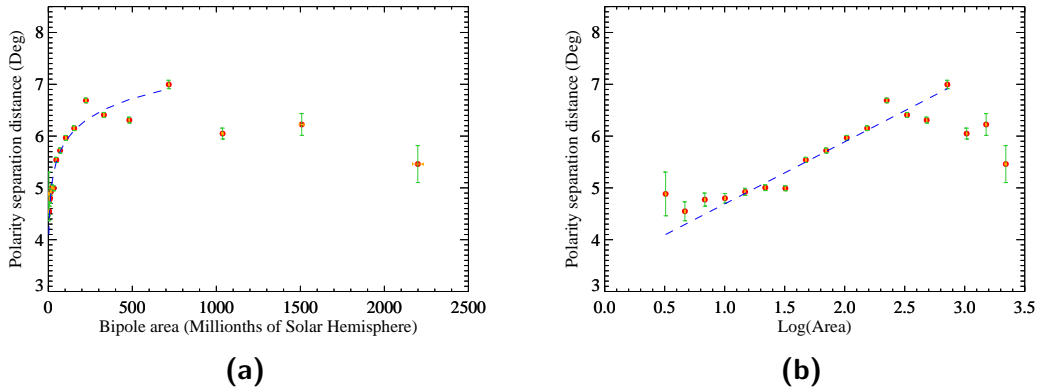


**Figure 5.10:** The variation of polarity separation distance (in deg) with (a) sunspot-group area (in MSH), and (b) logarithm of sunspot-group area. In both plots the sunspot-group data was binned into 19 equally-spaced area bins in logarithmic scale starting from 2.5 MSH to 2850 MSH. The solid-curve in (a) is the logarithmic-function fit upto 1000 MSH and the solid-line in (b) is a linear-fit. The fit-parameters are listed in Table 5.2. The error-bars represents the standard errors.

with a slope smaller than one. Wang and Sheeley (1989) from the study of bipoles of solar cycle 21, found that the bipole region flux,  $F \propto d^{1.3}$ .

### 5.3.5 Solar cycle phase variation of bipoles properties

To study the dependence of tilt-angle magnitude on the phase of cycle, we calculated the median tilt-angle in 2 years bins, starting from year 1997. Figure [5.11] shows the variation of median tilt-angle (red-dots) with the binned period from 1997-2011, separately for northern and southern hemispheres. The tilt-angle has gradual decrease with the cycle progress. A linear-fit (dashed-line) to each the plots is also shown, and fit-parameters are listed in Table [5.3].

The tendency of the tilt-angle to decrease as the solar cycle progresses may reflect the migration of distributions of active regions towards equator and the latitude dependence of tilt-angle (Section [5.3.1]). To check this we also calculated the median latitude for each cycle phase, and its decrements with cycle phase is also shown in the plot, with a dot-dashed line is the corresponding linear fit (fit-parameters are listed in Table [5.3]).

The median tilt-angle decreases at a rate of  $\sim 0.5^\circ \text{ yr}^{-1}$  in northern hemisphere and  $\sim 0.3^\circ \text{ yr}^{-1}$  in southern hemisphere. While, the median latitude decrease at rate of  $\sim 1.6^\circ$  and  $\sim 1.5^\circ \text{ yr}^{-1}$  for northern and southern hemispheres respectively. In accordance to the Joy's law (Eq 5.3 & 5.4), the tilt-angle decreases at rate of  $\sim 0.43^\circ$  and  $0.36^\circ$  per degree of latitude for northern and southern hemispheres respectively; which amounts to tilt-angle decreasing at a rate of roughly  $0.69^\circ \text{ yr}^{-1}$  and  $0.54^\circ \text{ yr}^{-1}$  for respective hemispheres. These rates are higher than the obtained values, which implies that tilt-angle are not decreasing with time following the Joy's law only. In contrast, in a similar study, Li and Ulrich (2012) reported that the decreasing rate of tilt-angle is consistent with decrements expected from Joy's law.

In Figure [5.12a] is shown the variation of mean tilt-angle with the cycle phase (shown with dots and dashed-line). In the periods away from cycle minimum, the tilt-angle remains close to the global mean tilt-angle of  $3.28^\circ$ . Also plotted the mean sunspot area for each cycle phase. We found the correlation coefficient of mean tilt-angle with mean sunspot area of  $-0.64$

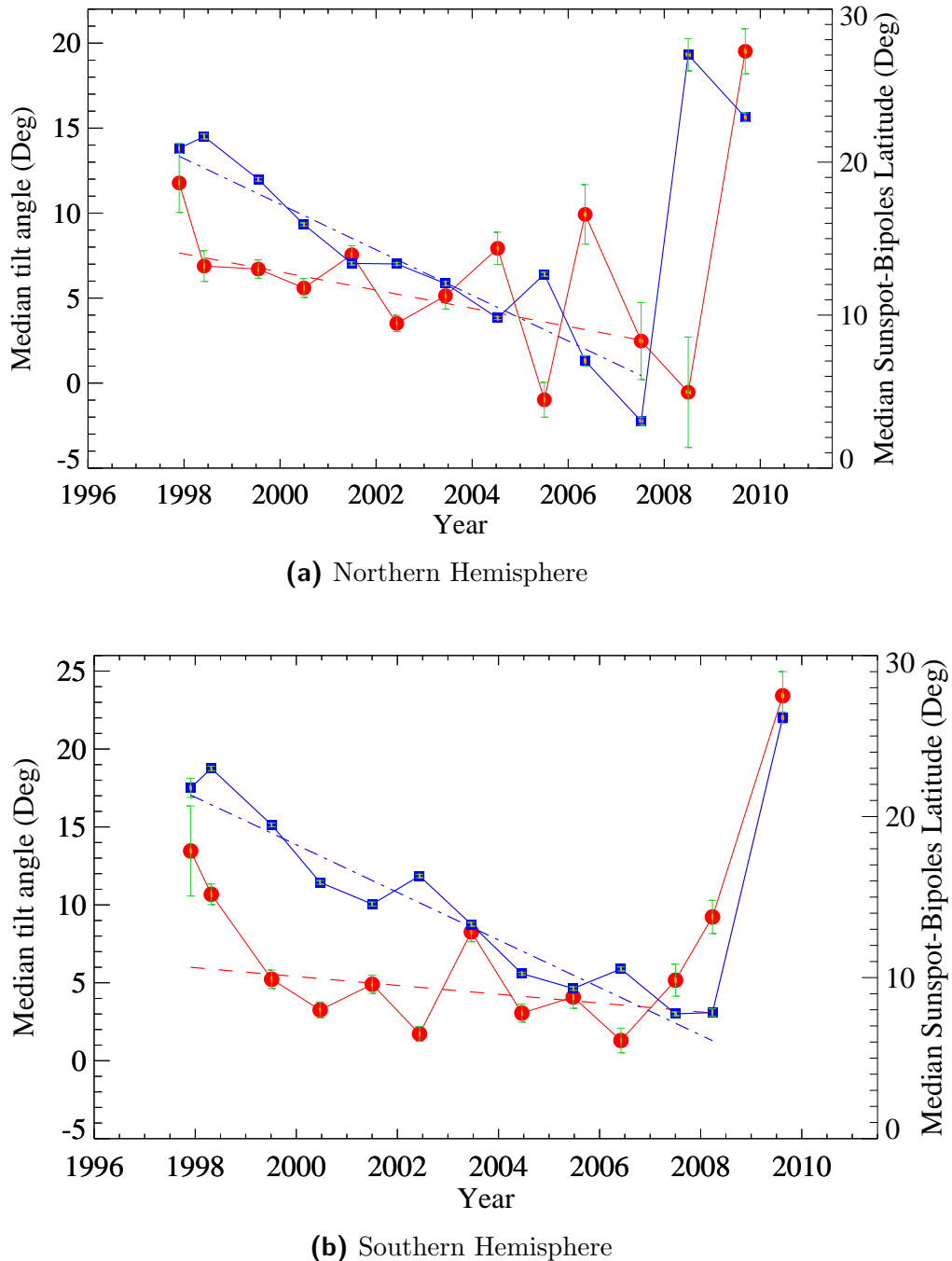


**Figure 5.11:** The variation of median sunspot-groups tilt-angles (dots) and median latitude (squares) with the cycle phase, binned in two years intervals for period 1997-2011 for (a) northern and (b) southern hemisphere. Dashed and dot-dashed lines are linear-fit to tilt-angle and latitude variation with  $t$ , where  $t$  (in years) is the time since the start of cycle 23. The linear-fit is for period upto June 2008. The error bars represent the standard errors. The fit-parameters and  $1\sigma$  errors are listed in Table 5.3.

Relation	Northern hemisphere				Southern hemisphere			
	A	B	$\chi^2$	$B/\sigma$	A	B	$\chi^2$	$B/\sigma$
$\theta$ vs $t$	21.046(0.084)	-1.548(0.017)	1113.31	-90.18	21.336(0.076)	-1.471(0.013)	1557.96	-117.80
$\gamma$ vs $t$	7.657(0.466)	-0.534(0.110)	83.32	-4.83	5.995(0.381)	-0.284(0.072)	200.75	-3.97
$d$ vs $t$	5.884(0.046)	-0.234(0.011)	326.77	-22.27	5.466(0.041)	-0.106(0.008)	135.25	-13.41

**Table 5.3:** The fit-parameters with one-sigma errors in brackets and chi-square values for different fit-functions.  $\theta$ ,  $\gamma$ , and  $d$  are the median latitude (in deg), median tilt-angle (deg), and median polarity separation distance (deg) in 2 year intervals for period 1997-2011, respectively.  $t$  (year) is the time since the start of the cycle. The linear-fit is of the form  $\theta, \gamma, d = A+Bt$ .

and with mean latitude of 0.77. The significant anticorrelation between mean tilt-angle and mean sunspot area may implies that the variations in tilt-angle with cycle phase is not only caused by equatorward migrating active zones (in accord with Joy's law) but also by distribution of sunspots.

In Figure [5.12b] is plotted the mean tilt-angle variation with cycle phase for different latitude zones. Overall, the mean tilt-angle fluctuates by  $\approx \pm 10^\circ$  around the peak-value of  $6.5^\circ$  (Figure 5.1). Around the minimum phase and for latitudes between  $30^\circ - 40^\circ$ , there are large fluctuations. These large fluctuations at higher latitudes and during sunspot minimum could be due to low statistics, hence needs further investigation with more cycle data. For lower latitudes upto  $20^\circ$  for almost whole cycle period (except during minimum), the mean tilt angle in this range has small positive constant values (close to the global mean tilt-angle of  $3.28^\circ$ ), independent of cycle phase in agreement with results of Li and Ulrich (2012).

In the scenario, where polarity separation distance ( $d$ ) depends on bipoles flux or latitude of emergence, then the separation distance would be varying with the phase-of-cycle. To investigate the cyclic variation, in Figure [5.13] is shown the cycle variation of median of separation distance (data are shown with dots) in two-years bins starting from 1997 to 2011, separately for northern and southern hemispheres. The median of separation distance decreases with the cycle progress, as shown with a linear-fit (dashed line), and the obtained fit-parameters are listed in Table [5.3]. The cyclic-variation of median latitude (for two-year binned period) is also shown in the plot

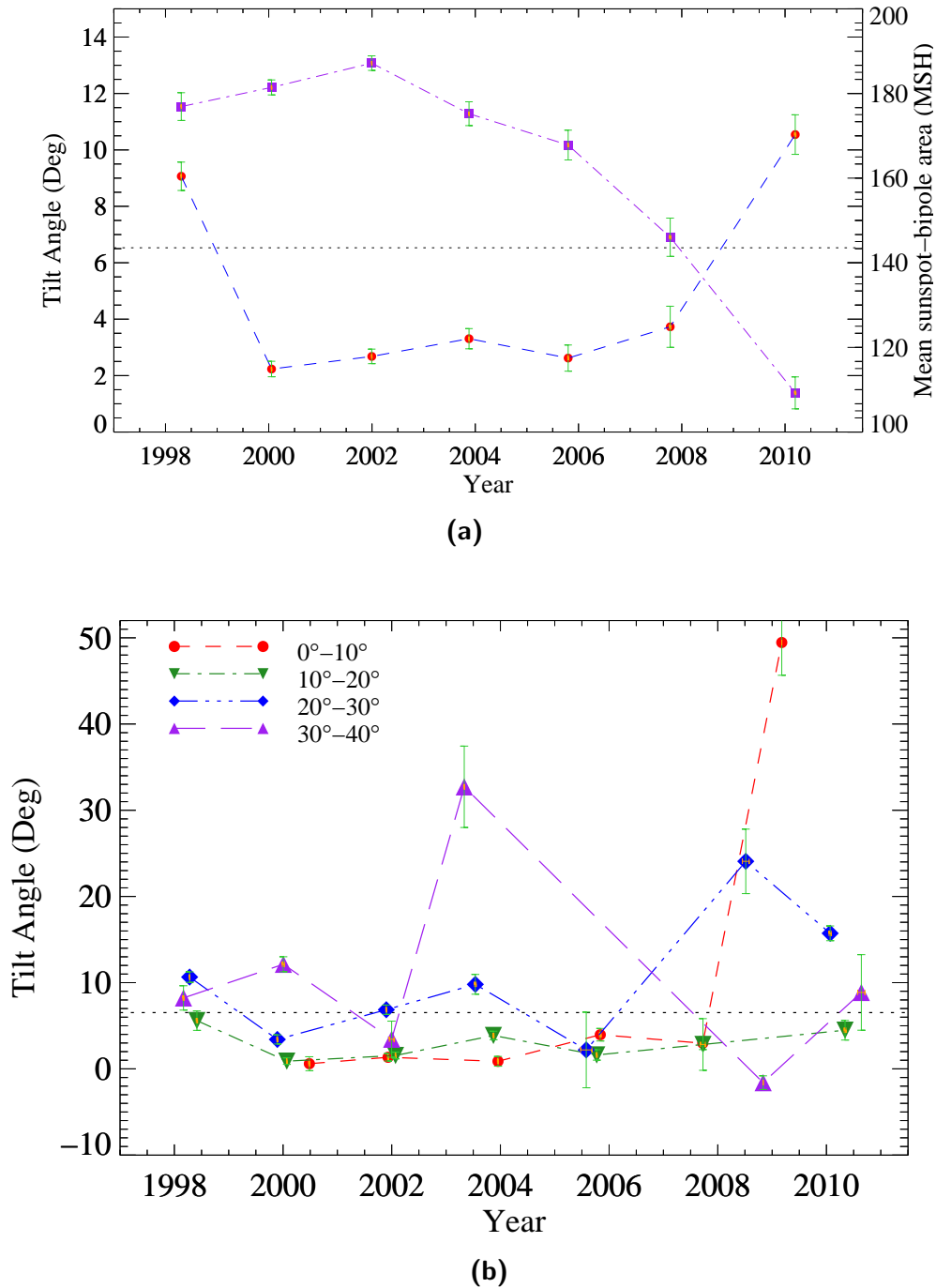


**Figure 5.12:** The solar-cycle phase variation of mean value of tilt angle in two-years bins, starting from 1997 to 2011 for (a) all latitudes (dots), and (b) in different latitude bands. In (a) is also plotted the mean sunspot-group area (square, dot-dashed). The error bars represents the standard errors.

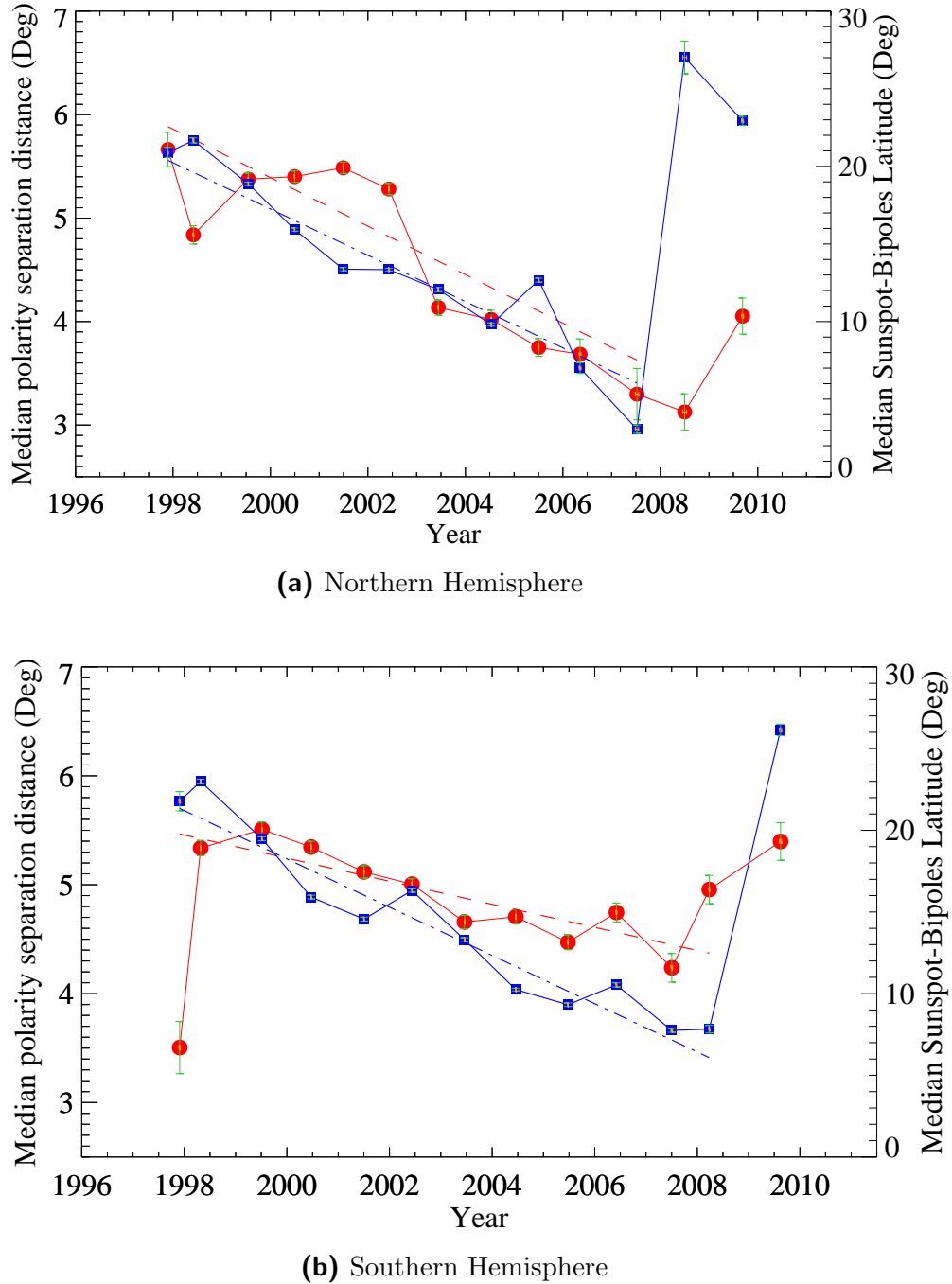
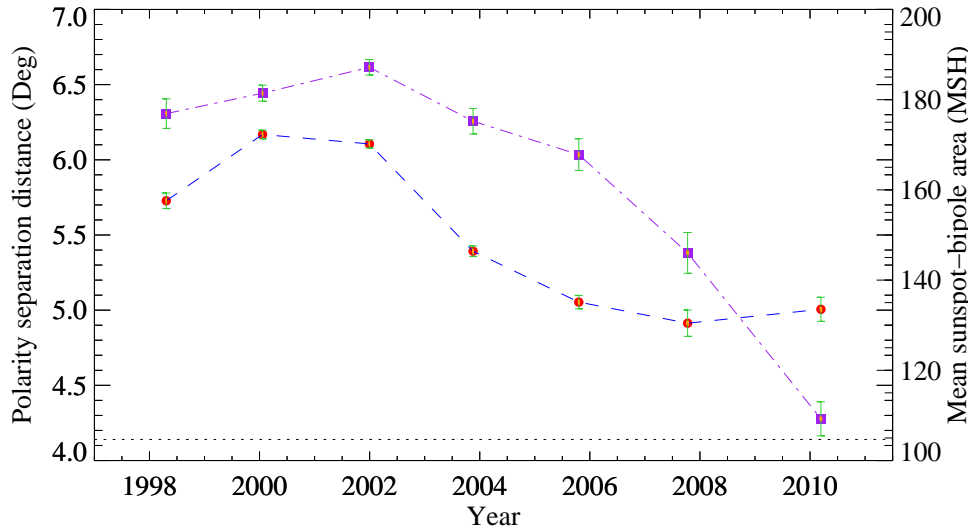
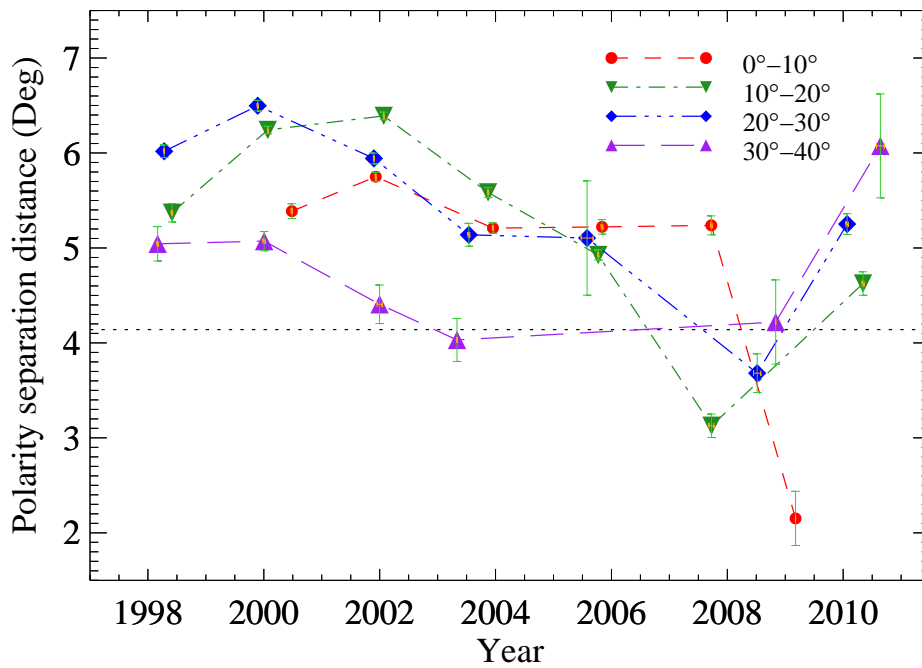


**Figure 5.13:** The variation of median polarity separation distance (dots) and median latitude (squares) with the cycle phase, binned in two years intervals for period 1997-2011 for (a) northern and (b) southern hemisphere. Dashed and dot-dashed lines are linear fit to separation distance and latitude variation with  $t$ , where  $t$  is the time (in years) at zero value for the first x-bin value. The error bars represent the standard errors. The fit-parameters and  $1\sigma$  errors are listed in Table 5.3.



(a)



(b)

**Figure 5.14:** The solar-cycle phase variation of mean value of polarity-separation distance in two-years bins, starting from 1997 to 2011 for (a) all latitudes (dots), and (b) in different latitude bands. In (a) is also plotted the mean sunspot-group area (square, dot-dashed). The error bars represents the standard errors.

(squared-data), with its corresponding linear-fit as dot-dashed line. As listed in Table [5.3], though the rate of decrease of median latitude has similar values in both hemispheres. the polarity separation distance decreases each year relatively faster in northern hemisphere than southern hemisphere. We also noted in previous discussions, that the rate of decrease of median tilt-angle with cycle progression, as well as the peak value of tilt-angle are higher in northern hemisphere in comparison to the values for southern hemisphere. Also in previous chapter (Section 4.4.4) we noted that the northern hemisphere has more differential rotation possibly owing to higher activity than the southern hemisphere. Thus, the NS-asymmetry is reflected in various solar parameters, *i.e.*, the local magnetic-bipoles properties, global differential rotation rate and hemispheric magnetic-flux distribution. A thorough investigation of correlations between these various solar parameters at different phases of cycle across two hemispheres is needed with larger time-series of data-set.

In Figure [5.14a] shows the cyclic variation of average of separation distance (in deg) in two year bins starting from year 1997 to 2011. The plot shows that during the rising phase of cycle 23, the mean separation distance gradually reaches value close to the global mean value of separation distance, *i.e.*,  $5.84^\circ$ , then it gradually decreases with cycle progress and approaches value near the peak value obtained for the polarity separation distance of  $4.14^\circ$  at the end of cycle 23. Also plotted the mean sunspot-group area, which shows a good correlation with mean separation distance, with correlation factor of 0.734, which again supports the dependence of polarity separation distance on bipole size.

We further looked for the cyclic variation of mean polarity separation distance for different latitude bands as shown in Figure [5.14b]. In general all latitude bands shows a slight increase for 2-3 years and reaches maxima close to sunspot maximum, then descends down with cycle progress and reaches peak-*d* (*i.e.*,  $4.14^\circ$ ) value near the end of cycle. The similar pattern of variation

of polarity separation was reported by Wang and Sheeley (1989). However, the variation in mean  $d$  have some phase-difference in different latitude-bands also have different maximum values. At low latitudes, between  $0^\circ - 10^\circ$ , the separation distance remains nearly constant through-out the cycle at value slightly lower than the global mean of  $d$  (*i.e.*,  $5.8^\circ$ ). For higher latitudes ( $> 30^\circ$ ), the mean  $d$  has lowered value as compared to other latitude bands, but it reaches an asymptotic value (close to peak value of  $d$ ) in the declining phase.

Further thorough investigations are required from data of many cycles, to check for the existence of above observed pattern of cyclic-variation of polarity separation distance.

## 5.4 Conclusions

In this chapter, we investigated the latitudinal and bipole-size dependence of tilt-angles and polarity separation distance for sunspot-group data of solar cycle 23 extracted from stray-light-corrected continuum images of SoHO/MDI. We also looked for the solar-cycle variation and North-South asymmetry of these sunspot-group parameters. Following are the key findings of these investigations:

- (a) The sunspot-group tilt-angles,  $\gamma$ , for solar-cycle 23, had most probable value of  $\approx 6.5^\circ$  and mean value of  $\approx 3.8^\circ$ .
- (b) The tilt-angles of sunspot-group data follows the Joy's law, *i.e.*, the tilt-angle increases with latitude at rate of  $0.38^\circ$  per degree of latitude. However, we also observed the bending in tilt-angle at  $\sim 35^\circ$  latitude. This bending was previously reported by Tlatov *et al.* (2013) for magnetic-bipoles of size  $> 300$  MSH. The reasons for this bending at higher latitude and its relation to magnetic-flux is not known.
- (c) The polarity separation distance,  $d$ , of sunspot-groups have the peak value at  $4.14^\circ$ , while the global mean value of  $5.8^\circ$ .

- (d) The separation distance,  $d$ , shows a sinusoidal variation with latitude (Eq 5.2), within the latitude range of  $0^\circ - 35^\circ$ .
- (e) The North-South asymmetry has been observed in bipole tilt-angles. The peak value of tilt-angle and the slope of Joy's law have higher values for northern hemisphere than the values for southern hemisphere.
- (f) Both the tilt-angle and polarity separation distance have non-linear dependence on sunspot-group area, represented by linear-logarithmic functions;  $\gamma = 4.80 - 0.73(\log S)$  and  $d = 3.49 - 1.20(\log S)$ , where  $S$  is the group area.
- (g) The median tilt angle decreases since the start of solar cycle at rate of  $0.28^\circ \text{ yr}^{-1}$  and  $0.53^\circ \text{ yr}^{-1}$  in southern and northern hemispheres, which are lower rates as expected from Joy's law, where median latitude decreases at rate of  $\sim 1.5^\circ \text{ yr}^{-1}$ .
- (h) The variation of mean tilt-angle with cycle phase shows anti-correlation with mean sunspot-group area. At low latitudes  $< 20^\circ$ , the tilt-angle remains nearly constant during the most of the part of the solar cycle. There are wider fluctuations ( $\pm 10^\circ$ ) in tilt-angles for latitudes beyond  $20^\circ$ . These fluctuations are partly due to less number of sunspots at higher latitudes, hence reaffirmation is needed by combining data from other cycles.
- (i) The median polarity separation distance decreases with the cycle progression, and similar to the case of median tilt-angle results, this rate of decrease is relatively higher in northern hemisphere than southern hemisphere.
- (j) The solar cycle variation of mean polarity separation distance shows correlation with mean sunspot-group area. The pattern of variation of mean of separation distance are similar in different latitude bands, but differ in magnitude and are out-of-phase with each other.

# Chapter 6

## Summary, Conclusions and Future prospects

### 6.1 Modules for processing solar images

In this thesis we developed a procedure for estimation of PSF of MDI continuum images and used that to correct  $\sim 50K$  continuum images of MDI for stray-light, which were also corrected for center-to-limb variation. These stray-light corrected images are then flat-fielded by using median-combined master flat images corresponding to each carrington rotation period.

We have also made automated modules for identification (based on level-set method), sunspot parameters cataloging, tracking of identified sunspots from full-disk continuum images. A procedure was developed to computationally extract sunspot bipolar regions from full-disk continuum images and calculating their polarity separation distances and tilt angles.

### 6.2 Statistical studies of sunspot properties

- (a) From the study of sunspot parameters obtained from stray-light-corrected images, we found that the umbral-minimum (core) intensity and umbral mean intensity (normalized to quiet Sun intensity) decreases

with the sunspot size, statistically described as exponential functions and reaches an asymptotic value at about sunspot area of 600 MSH. Though in all sunspot size ranges the intensities have intrinsic scatter, which may be due to varying amount of umbral dots in the resolution element.

It is known from previous studies that the sunspot size is the proxy of its magnetic flux, while umbral-minimum intensity is correlated with maximum field strength (Kiess, Rezaei, and Schmidt, 2014; Norton and Gilman, 2004), thus, these results suggests that larger flux regions are relatively darker (and cooler) than regions having small flux. This possibly implies that the magnitude of deficit caused by sunspot in total solar irradiance (TSI) should be modulated by the distribution of magnetic flux (or sunspot size).

In the general paradigm of active regions formed by the buoyantly rising flux tubes within the convective envelope, the field strength of emerged flux will depend on the initial magnetic flux of rising flux tube, and its interaction with turbulent convection. In other words, the magnetic flux of the rising tube and the interplay of magnetic fields and convective flows, will define the observed sunspot size, intensity and the field-strength. In case of small sunspots observed from MDI, the measured intensities are relatively higher than those from HMI, possibly due to smaller spatial resolution of MDI images.

- (b) In our study, we observed that the umbral-core intensity depends on the compactness of umbra, that is, the core intensity is relatively small for circular umbra as compared to elongated ones.
- (c) We observed that the umbral intensity does not show any variation with the solar cycle phase in contrast to the observed long-term decreasing trend of sunspot magnetic field by Penn and Livingston (2006).
- (d) The umbral intensity is slightly positively correlated with the limb po-

sition in contrast to the results by Norton and Gilman (2004).

- (e) The penumbral mean intensity also decreases with sunspot size, in agreement with the umbral intensity. However, for small sunspots ( $< 100MSH$ ), penumbral-mean intensity is positively correlated with sunspot size. This needs further investigation with the consideration of magnetic-field inclination variation with the size.
- (f) Penumbra-umbra area (also sunspot-umbra area ratio) is anticorrelated with the sunspot size. This implies that the total flux of sunspot designs the structure of sunspot. The variation in the area ratio with evolution of the sunspot and complexity of the active region will provide more understanding of the penumbra formation mechanism.

It would be more fruitful to further study the variation of intensity, field strength, size, penumbra-umbra area ratio, and also the filling factor of umbral-dots, while tracing sample of sunspots, from their growth to decay.

### 6.3 Study of solar differential rotation

Using individual sunspots as tracers, we obtained the differential rotation rate for the solar cycle 23, with equatorial rotation rate, A of  $14.49^\circ \text{ day}^{-1}$ , and the coefficient of differential rotation, B of  $-2.95^\circ \text{ day}^{-1}$ . For solar cycle 23, the Northern hemisphere has more differential rotation than southern hemisphere. Both, the A-value and B-value have dependence on the size of the sunspots, with smaller sunspots having the faster rotation in agreement with the findings of Howard, Gilman, and Gilman (1984). It has been postulated that the rotation variation of sunspots of different size is due to their different anchoring depths, that is, sunspots are rooted deep within the convection zone at different depths and their rotation is influenced by the angular velocity in respective depths. However, helioseismological investigations have suggested that sunspots are shallow features (Couvidat, Birch, and Kosovichev,

2006), hence the anchoring depth reasoning seems inappropriate. D'Silva and Howard (1994) postulated that the varying rotation rate of sunspots of different size is the net-effect of the interplay of convective flow, magnetic fields, and Coriolis force during the buoyant rise of flux tubes in the convection zone.

The rotation rate parameters also shows radical changes during the sunspot-minimum, while in mid-period of the solar cycle, the A and B-values have very small fluctuations around the global mean rates, these are in agreement with the solar-cycle variation observed from the Doppler data, which implies that the changes in differential rotation with cycle phase is real, and not the artifact of sunspot measurements. However, A and B-values have significant variations during the course of solar cycle when calculated for northern and southern hemispheres separately. The A-value of Northern hemisphere is anticorrelated with that of Southern hemisphere, similar is the case for the B-value. We derived a sunspot activity index; fraction of the total area of all sunspots in a hemisphere with respect to the global value of the total area of sunspots at a given solar cycle phase. For a hemisphere, when its total sunspot coverage area was relatively larger, then that hemisphere had slower and rigid rotation, and the other hemisphere having lower sunspot coverage showed opposite behavior. However, the variations in NS-asymmetry in sunspot coverage was out-of-phase with the corresponding variations in the A-value and B-value. We observed a radical change in NS-asymmetry of total sunspot coverage area around the sunspot maximum period, existence of this behavior needs to be confirmed with long time-series of sunspot data.

This observed NS-asymmetry in rotation rates and its correlation with the sunspot activity suggests that the activity causes modulations in differential rotation. Some simulations (Brun, Miesch, and Toomre, 2004) have also indicated that the back-reaction of magnetic fields causing changes in differential rotation; during the minimum activity the rotation is faster and more differential. During the Maunder minimum, the NS-asymmetry in activity was observed for extended duration along with the significant changes in the rota-

tion parameters as compared to present times values (Nesme-Ribes, Ferreira, and Mein, 1993). Recently, Suzuki (2014) suggested that the observed cyclic modulation of B-value is net-effect of temporal variation of NS-asymmetry in B. This indicates that, the NS-asymmetry of solar parameters, sunspots or differential rotation are not only inter-linked but possibly are the progenitors of cycle modulation. However, to look for such possibility, it requires investigation of NS asymmetry with amalgamation of various solar activity indices from various solar cycles.

In the present study we have converted synodic rotation to sidereal using a constant correction factor for the Earth orbital motion, we would in future apply the improved sidereal calculations to this data set which will incorporate the elliptic orbit of the Earth as suggested by recent study of Skokić *et al.* (2014).

The measurement of rotation rate and area, and magnetic flux, during the evolution of sunspot and also a separate study of leading and following sunspots, can provide more insight on the relation between flux and rotation, and the changes in rotation with the aging of sunspots.

## 6.4 Study of sunspot-groups tilt-angles

From the study of tilt-angle of sunspot-groups for the cycle 23, we re-confirmed the Joy's law, that is, the tilt-angle systematically increases with the latitude, we found the slope of  $0.38^\circ$  per degree of latitude. However, tilt angle for latitudes  $> 35^\circ$  does not follow systematic increase in tilt angle as per Joy's law, this behavior has recently been reported by Tlatov *et al.* (2013), however, the reason for such behavior is unknown. In our sample, we found the most probable value of tilt angle of  $6.5^\circ$ , and polarity separation distance has the value  $4.14^\circ$ . The polarity separation distance has sinusoidal dependence with latitude range of  $0^\circ - 35^\circ$ . The tilt angle is found to be decreasing with the sunspot-group area, as represented by a linear logarithmic function. This is in agreement with the Coriolis force theory of generation

of bipolar tilt-angles (D'Silva and Choudhuri, 1993). The magnetic tension force counteracts the Coriolis force, hence for the rising flux tubes with larger flux or strong magnetic field strength will be less affected by Coriolis force, and hence would have smaller tilt. And in the Section 6.2, we noted that that the magnetic flux of the rising flux tube defines the size and structure of sunspots. We also found that the polarity separation distance too decreases with the sunspot size.

The tilt-angle averaged in yearly bins shows solar cycle variation in anti-correlation with the average of sunspot-group area. However, tilt angle in the low latitudes ( $< 20^\circ$ ) remains constant over the course of the solar cycle. The mean polarity separation distance on other hand, varies during the solar cycle in correlation with the mean sunspot-group area. The separation distance, initially increases with the rising phase of solar cycle and then it descends down between the maximum and declining phase of cycle. This pattern was observed to be persistent for all different latitude zones. Similar pattern was observed by Wang and Sheeley (1989).

The NS-asymmetry in the Joy's law was observed, with the Northern hemisphere having the larger slope than the southern hemisphere. Also, the rate of decrease of median tilt angle with the cycle phase was higher in the northern hemisphere.

Again, more detailed investigations from larger bipole data-set of North-South asymmetry of tilt angle can reflect more light on the understanding of cycle modulation.

# Bibliography

- Albregtsen, F., Maltby, P.: 1981, Solar cycle variation of sunspot intensity. *Solar Phys.* **71**, 269. DOI. ADS. 50, 52
- Albregtsen, F., Joras, P.B., Maltby, P.: 1984, Limb-darkening and solar cycle variation of sunspot intensities. *Solar Phys.* **90**, 17. DOI. ADS. 51, 53
- Alfvén, H.: 1943, On the effect of a vertical magnetic field in a conducting atmosphere. *Arkiv for Astronomi* **29**, 1. ADS. 48
- Allen, C.W.: 1973, *Astrophysical quantities*. ADS. 94
- Antalová, A.: 1971, The ratio of penumbral and umbral areas of sun-spots in the 11-year solar activity cycle. *Bulletin of the Astronomical Institutes of Czechoslovakia* **22**, 352. ADS. 54
- Antia, H.M., Basu, S.: 2010, Solar rotation rate during the cycle 24 minimum in activity. *Astrophys. J.* **720**, 494. DOI. ADS. 124
- Antia, H.M., Basu, S., Chitre, S.M.: 2008, Solar rotation rate and its gradients during cycle 23. *Astrophys. J.* **681**, 680. DOI. ADS. 99, 100, 108
- Antonucci, E., Hoeksema, J.T., Scherrer, P.H.: 1990, Rotation of the photospheric magnetic fields - A north-south asymmetry. *Astrophys. J.* **360**, 296. DOI. ADS. 104, 105
- Arevalo, M.J., Gomez, R., Vázquez, M., Balthasar, H., Wöhl, H.: 1982, Differential rotation and meridional motions of sunspots from 1874 to 1902. *Astron. Astrophys.* **111**, 266. ADS. 103, 104, 117
- Aschwanden, M.J.: 2010, Image processing techniques and feature recognition in solar physics. *Solar Phys.* **262**, 235. DOI. ADS. 27
- Babcock, H.W.: 1961, The topology of the Sun's magnetic field and the 22-year cycle. *Astrophys. J.* **133**, 572. DOI. ADS. 9, 145
- Badalyan, O.G., Obridko, V.N.: 2011, North-south asymmetry of the sunspot indices and its quasi-biennial oscillations. **16**, 357. DOI. ADS. 104
- Badalyan, O.G., Obridko, V.N., Rybák, J., Sýkora, J.: 2005, Quasi-biennial oscillations of the north-south asymmetry. *Astronomy Reports* **49**, 659. DOI. ADS. 104

- Balthasar, H., Wöhl, H.: 1980, Differential rotation and meridional motions of sunspots in the years 1940-1968. *Astron. Astrophys.* **92**, 111. ADS. 101, 103, 117
- Balthasar, H., Schüssler, M., Wöhl, H.: 1982, On changes of the rotation velocities of stable, recurrent sunspots and their interpretation with a flux tube model. *Solar Phys.* **76**, 21. DOI. ADS. 102
- Balthasar, H., Vázquez, M., Wöhl, H.: 1986, Differential rotation of sunspot groups in the period from 1874 through 1976 and changes of the rotation velocity within the solar cycle. *Astron. Astrophys.* **155**, 87. ADS. 102, 109, 135
- Barnes, J.R., Collier Cameron, A., Donati, J.-F., James, D.J., Marsden, S.C., Petit, P.: 2005, The dependence of differential rotation on temperature and rotation. *Mon. Not. Roy. Astron. Soc.* **357**, L1. DOI. ADS. 98
- Basu, S., Antia, H.M.: 1997, Seismic measurement of the depth of the solar convection zone. *Mon. Not. Roy. Astron. Soc.* **287**, 189. ADS. 100
- Basu, S., Antia, H.M., Bogart, R.S.: 2004, Ring-diagram analysis of the structure of solar active regions. *Astrophys. J.* **610**, 1157. DOI. ADS. 116
- Beck, J.G.: 2000, A comparison of differential rotation measurements. *Solar Phys.* **191**, 47. DOI. ADS. 3, 11, 97, 98
- Beck, J.G., Chapman, G.A.: 1993, A study of the contrast of sunspots from photometric images. *Solar Phys.* **146**, 49. DOI. ADS. 28, 29
- Beck, J.G., Duvall, T.L., Scherrer, P.H.: 1998, Long-lived giant cells detected at the surface of the Sun. *Nature* **394**, 653. DOI. ADS. 3
- Berdyugina, S.V.: 2005, Starspots: A key to the stellar dynamo. *Living Reviews in Solar Physics* **2**, 8. DOI. ADS. 89
- Berry, R., Burnell, J.: 2005, *The handbook of astronomical image processing*. ADS. 20
- Biermann, L.: 1941, Der gegenwärtige Stand der Theorie konvektiver Sonnenmodelle. *Vierteljahresschrift der Astronomischen Gesellschaft* **76**, 194. ADS. 47
- Blake, A., Isard, M.: 1998, *Active contours: The application of techniques from graphics, vision, control theory and statistics to visual tracking of shapes in motion*, 1st edn. Springer, New York. ISBN 3540762175. 30
- Borrero, J.M., Ichimoto, K.: 2011, Magnetic structure of sunspots. *Living Reviews in Solar Physics* **8**, 4. DOI. ADS. 46, 49
- Brajša, R., Ruždjak, D., Wöhl, H.: 2006, Temporal variations of the solar rotation determined by sunspot groups. *Solar Phys.* **237**, 365. DOI. ADS. 102

- Brajša, R., Ruždjak, V., Vršnak, B., Pohjolainen, S., Urpo, S., Schroll, A., Wöhl, H.: 1997, On the possible changes of the solar differential rotation during the activity cycle determined using microwave low-brightness regions and H $\alpha$ -filaments as tracers. *Solar Phys.* **171**, 1. DOI. ADS. 104
- Brajša, R., Ruždjak, V., Vršnak, B., Wöhl, H., Pohjolainen, S., Upro, S.: 2000, Statistical weights and selective height corrections in the determination of the solar rotation velocity. *Solar Phys.* **196**, 279. DOI. ADS. 104
- Brandenburg, A.: 2005, The case for a distributed solar dynamo shaped by near-surface shear. *Astrophys. J.* **625**, 539. DOI. ADS. 145
- Brandt, P.N., Schmidt, W., Steinegger, M.: 1990, On the umbra-penumbra area ratio of sunspots. *Solar Phys.* **129**, 191. DOI. ADS. 28, 53, 94
- Brants, J.J., Zwaan, C.: 1982, The structure of sunspots. IV - Magnetic field strengths in small sunspots and pores. *Solar Phys.* **80**, 251. DOI. ADS. 50
- Bray, R.J., Loughhead, R.E.: 1979, *Sunspots.*, Dover Publications, New York. ISBN 9780486637310. ADS. 47, 50, 71
- Brun, A.S., Miesch, M.S., Toomre, J.: 2004, Global-scale turbulent convection and magnetic dynamo action in the solar envelope. *Astrophys. J.* **614**, 1073. DOI. ADS. 140, 173
- Bushby, P.J.: 2006, Zonal flows and grand minima in a solar dynamo model. *Mon. Not. Roy. Astron. Soc.* **371**, 772. DOI. ADS. 10
- Cameron, R.H., Schüssler, M.: 2012, Are the strengths of solar cycles determined by converging flows towards the activity belts? *Astron. Astrophys.* **548**, A57. DOI. ADS. 155
- Cameron, R.H., Jiang, J., Schmitt, D., Schüssler, M.: 2010, Surface flux transport modeling for solar cycles 15-21: Effects of cycle-dependent tilt angles of sunspot groups. *Astrophys. J.* **719**, 264. DOI. ADS. 159
- Carbonell, M., Ballester, J.L.: 1992, The periodic behaviour of solar activity - The near 155-day periodicity in sunspot areas. *Astron. Astrophys.* **255**, 350. ADS. 139
- Carbonell, M., Oliver, R., Ballester, J.L.: 1993, On the asymmetry of solar activity. *Astron. Astrophys.* **274**, 497. ADS. 104
- Chandrasekhar, S.: 1952, Xlvi. on the inhibition of convection by a magnetic field. *Philosophical Magazine Series 7* **43**(340), 501. DOI. 47
- Chandrasekhar, S.: 1981, *Hydrodynamic and hydromagnetic stability*, Dover Publications, N.Y. ISBN 9780486640716. 47, 53
- Charbonneau, P.: 2010, Dynamo models of the solar cycle. *Living Reviews in Solar Physics* **7**, 3. DOI. ADS. 7, 8, 46, 97, 146

- Charbonneau, P., Christensen-Dalsgaard, J., Henning, R., Larsen, R.M., Schou, J., Thompson, M.J., Tomczyk, S.: 1999, Helioseismic constraints on the structure of the solar tachocline. *Astrophys. J.* **527**, 445. DOI. ADS. 101
- Cheung, M.C.M., Schüssler, M., Moreno-Insertis, F.: 2007, Magnetic flux emergence in granular convection: radiative MHD simulations and observational signatures. *Astron. Astrophys.* **467**, 703. DOI. ADS. 11
- Chitre, S.M.: 1963, The structure of sunspots. *Mon. Not. Roy. Astron. Soc.* **126**, 431. ADS. 48
- Chitre, S.M., Shaviv, G.: 1967, A model of the sunspot umbra. *Solar Phys.* **2**, 150. DOI. ADS. 48
- Choudhuri, A.R.: 1992, The cluster model of sunspots. In: Thomas, J.H., Weiss, N.O. (eds.) *Sunspots: Theory and observations, NATO Advanced Science Institutes (ASI) Series C* **375**, 243. ADS. 48
- Christensen-Dalsgaard, J., Gough, D.O., Thompson, M.J.: 1991, The depth of the solar convection zone. *Astrophys. J.* **378**, 413. DOI. ADS. 100
- Colak, T., Qahwaji, R.: 2008, Automated McIntosh-based classification of sunspot groups using MDI images. *Solar Phys.* **248**, 277. DOI. ADS. 28, 30
- Collados, M., Martínez Pillet, V., Ruiz Cobo, B., del Toro Iniesta, J.C., Vázquez, M.: 1994, Observed differences between large and small sunspots. *Astron. Astrophys.* **291**, 622. ADS. 50, 61
- Couvidat, S., Birch, A.C., Kosovichev, A.G.: 2006, Three-dimensional inversion of sound speed below a sunspot in the Born approximation. *Astrophys. J.* **640**, 516. DOI. ADS. 116, 172
- Couvidat, S., García, R.A., Turck-Chièze, S., Corbard, T., Henney, C.J., Jiménez-Reyes, S.: 2003, The rotation of the deep solar layers. *Astrophys. J.* **597**, L77. DOI. ADS. 97
- Cowling, T.G.: 1946, The growth and decay of the sunspot magnetic field. *Mon. Not. Roy. Astron. Soc.* **106**, 218. ADS. 48
- Cowling, T.G.: 1953, *Solar electrodynamics, The Sun*, ed. Gerard P. Kuiper, The University of Chicago Press, Chicago, 532. ISBN 9789998357303. ADS. 47
- Cowling, T.G.: 1976, On the thermal structure of sunspots. *Mon. Not. Roy. Astron. Soc.* **177**, 409. ADS. 48
- Cowling, T.G., Lindsay, R.B.: 1957, Magnetohydrodynamics. *Physics Today* **10**, 40. DOI. ADS. 48
- Criscuoli, S., Ermolli, I., Uitenbroek, H., Giorgi, F.: 2013, Effects of unresolved magnetic field on Fe I 617.3 and 630.2 nm line shapes. *Astrophys. J.* **763**, 144. DOI. ADS. 56

- Curto, J.J., Blanca, M., Martínez, E.: 2008, Automatic sunspots detection on full-disk solar images using mathematical morphology. *Solar Phys.* **250**, 411. DOI. ADS. 28, 29, 30
- Danielson, R.E.: 1961, The structure of sunspot penumbras. II. Theoretical. *Astrophys. J.* **134**, 289. DOI. ADS. 47, 53
- Danielson, R.E.: 1964, The structure of sunspot umbras. I. Observations. *Astrophys. J.* **139**, 45. DOI. ADS. 47
- Dasi-Espuig, M., Solanki, S.K., Krivova, N.A., Cameron, R., Peñuela, T.: 2010, Sunspot group tilt angles and the strength of the solar cycle. *Astron. Astrophys.* **518**, A7. DOI. ADS. 145, 146, 150, 155
- de Toma, G., Chapman, G.A., Cookson, A.M., Preminger, D.: 2013, Temporal stability of sunspot umbral intensities: 1986-2012. *Astrophys. J.* **771**, L22. DOI. ADS. 51
- de Wijn, A.G., Stenflo, J.O., Solanki, S.K., Tsuneta, S.: 2009, Small-scale solar magnetic fields. *Space Sci. Rev.* **144**, 275. DOI. ADS. 5
- DeForest, C.E., Martens, P.C.H., Wills-Davey, M.J.: 2009, Solar coronal structure and stray light in TRACE. *Astrophys. J.* **690**, 1264. DOI. ADS. 19, 20
- Deinzer, W.: 1965, On the magneto-hydrostatic theory of sunspots. *Astrophys. J.* **141**, 548. DOI. ADS. 47
- Dikpati, M., Charbonneau, P.: 1999, A Babcock-Leighton flux transport dynamo with solar-like differential rotation. *Astrophys. J.* **518**, 508. DOI. ADS. 9
- Dikpati, M., Gilman, P.A.: 2009, Flux-transport solar dynamos. *Space Sci. Rev.* **144**, 67. DOI. ADS. 9
- Dikpati, M., de Toma, G., Gilman, P.A., Arge, C.N., White, O.R.: 2004, Diagnostics of polar field reversal in Solar cycle 23 using a flux transport dynamo model. *Astrophys. J.* **601**, 1136. DOI. ADS. 9
- Djafer, D., Irbah, A., Meftah, M.: 2012, Identification of sunspots on full-disk solar images using wavelet analysis. *Solar Phys.* **281**, 863. DOI. ADS. 28
- Domingo, V., Fleck, B., Poland, A.I.: 1995, The SoHO mission: an overview. *Solar Phys.* **162**, 1. DOI. ADS. 15
- Donahue, R.A., Saar, S.H., Baliunas, S.L.: 1996, A relationship between mean rotation period in lower main-sequence stars and its observed range. *Astrophys. J.* **466**, 384. DOI. ADS. 98
- D'Silva, S., Choudhuri, A.R.: 1993, A theoretical model for tilts of bipolar magnetic regions. *Astron. Astrophys.* **272**, 621. ADS. 144, 175

- D'Silva, S., Howard, R.F.: 1994, Sunspot rotation and the field strengths of subsurface flux tubes. *Solar Phys.* **151**, 213. DOI. ADS. 111, 116, 173
- Fan, Y.: 2009, Magnetic fields in the solar convection zone. *Living Reviews in Solar Physics* **6**, 4. DOI. ADS. 46, 116, 144
- Fan, Y., Fisher, G.H., Deluca, E.E.: 1993, The origin of morphological asymmetries in bipolar active regions. *Astrophys. J.* **405**, 390. DOI. ADS. 6
- Fan, Y., Fisher, G.H., McClymont, A.N.: 1994, Dynamics of emerging active region flux loops. *Astrophys. J.* **436**, 907. DOI. ADS. 144
- Feng, S., Xu, Z., Wang, F., Deng, H., Yang, Y., Ji, K.: 2014, Automated detection of low-contrast solar features using the phase-congruency algorithm. *Solar Phys.* **289**, 3985. DOI. ADS. 28
- Fisher, G.H., Fan, Y., Howard, R.F.: 1995, Comparisons between theory and observation of active region tilts. *Astrophys. J.* **438**, 463. DOI. ADS. 144, 150, 153
- Fisher, G.H., Fan, Y., Longcope, D.W., Linton, M.G., Pevtsov, A.A.: 2000, The solar dynamo and emerging flux. *Solar Phys.* **192**, 119. DOI. ADS. 144
- Fleck, B., Domingo, V., Poland, A.: 2011, *The SoHO mission*, 1995 edn. Springer, Netherlands. ISBN 9789401065696. ADS. 15
- Fligge, M., Solanki, S.K., Unruh, Y.C.: 2000, Modelling irradiance variations from the surface distribution of the solar magnetic field. *Astron. Astrophys.* **353**, 380. ADS. 92
- Fonte, C.C., Fernandes, J.: 2009, Application of fuzzy sets to the determination of sunspot areas. *Solar Phys.* **260**, 21. DOI. ADS. 28, 30
- Foukal, P., Jokipii, J.R.: 1975, On the rotation of gas and magnetic fields at the solar photosphere. *Astrophys. J.* **199**, L71. DOI. ADS. 99
- Foukal, P., Lean, J.: 1990, An empirical model of total solar irradiance variation between 1874 and 1988. *Science* **247**, 556. DOI. ADS. 53
- Foukal, P.V.: 2004, *Solar astrophysics*. ADS. 19
- Georgieva, K., Kirov, B., Javaraiah, J., Krasteva, R.: 2005, Solar rotation and solar wind magnetosphere coupling. *Planet. Space Sci.* **53**, 197. DOI. ADS. 104
- Gigolashvili, M.S., Japaridze, D.R., Mdzinarishvili, T.G., Chargeishvili, B.B., Kukhianidze, V.J.: 2007, Investigation of the NS asymmetry of the differential rotation of H $\alpha$  filaments and large-scale magnetic elements. *Advances in Space Research* **40**, 976. DOI. ADS. 104
- Giles, P.M., Duvall, T.L. Jr., Kosovichev, A.G.: 1998, Solar rotation and large-scale flows determined by time-distance helioseismology MDI. In: Deubner, F.-L., Christensen-Dalsgaard, J., Kurtz, D. (eds.) *New Eyes to See Inside the Sun and Stars, IAU Symposium* **185**, 149. ADS. 104

- Gilman, P.A., Howard, R.: 1984, Variations in solar rotation with the sunspot cycle. *Astrophys. J.* **283**, 385. DOI. ADS. 103
- Gilman, P.A., Howard, R.: 1985, Rotation rates of leader and follower sunspots. *Astrophys. J.* **295**, 233. DOI. ADS. 102
- Gizon, L., Birch, A.C.: 2005, Local helioseismology. *Living Reviews in Solar Physics* **2**, 6. DOI. ADS. 116
- Godoli, G., Mazzucconi, F.: 1979, On the rotation rates of sunspot groups. *Solar Phys.* **64**, 247. DOI. ADS. 102, 104
- Goel, S., Mathew, S.: 2012, Technique for automatic detection of sunspots from full-disk continuum images. In: *39th COSPAR Scientific Assembly, COSPAR Meeting* **39**, 633. ADS. 12
- Goel, S., Mathew, S.K.: 2014, Automated detection, characterization, and tracking of sunspots from SoHO/MDI continuum images. *Solar Phys.* **289**, 1413. DOI. ADS. 12, 25, 28, 40
- Gokhale, M.H., Hiremath, K.M.: 1984, Variations in the rotational velocity of sunspot groups during their lifetimes. *Bulletin of the Astronomical Society of India* **12**, 398. ADS. 120
- Gonzalez, R.C., Woods, R.E.: 2008, *Digital image processing*, Prentice Hall, Upper Saddle River, NJ, USA. ISBN 978-0131687288. 29
- Gough, D.O., Tayler, R.J.: 1966, The influence of a magnetic field on Schwarzschild's criterion for convective instability in an ideally conducting fluid. *Mon. Not. Roy. Astron. Soc.* **133**, 85. ADS. 47
- Graf, W.: 1974, Yearly variation in the synodic rotation period of the Sun. *Solar Phys.* **37**, 257. DOI. ADS. 107
- Grossmann-Doerth, U., Schmidt, W.: 1981, The brightness distribution in sunspot penumbrae. *Astron. Astrophys.* **95**, 366. ADS. 28
- Györi, L.: 1998, Automation of area measurement of sunspots. *Solar Phys.* **180**, 109. DOI. ADS. 29
- Hale, G.E., Ellerman, F., Nicholson, S.B., Joy, A.H.: 1919, The magnetic polarity of sunspots. *Astrophys. J.* **49**, 153. DOI. ADS. 6, 7, 148
- Harvey, K.L., Zwaan, C.: 1993, Properties and emergence of bipolar active regions. *Solar Phys.* **148**, 85. DOI. ADS. 4
- Hathaway, D.H.: 2010, The solar cycle. *Living Reviews in Solar Physics* **7**, 1. DOI. ADS. 5, 8, 46, 104
- Hathaway, D.H.: 2011, The Sun's shallow meridional circulation. *ArXiv e-prints*. ADS. 3

- Hathaway, D.H.: 2013, A curious history of sunspot penumbrae. *Solar Phys.* **286**, 347. DOI. ADS. 54, 94
- Hathaway, D.H., Wilson, R.M.: 1990, Solar rotation and the sunspot cycle. *Astrophys. J.* **357**, 271. DOI. ADS. 102, 103, 104, 134
- Heinemann, T., Nordlund, Å., Scharmer, G.B., Spruit, H.C.: 2007, MHD simulations of penumbra fine structure. *Astrophys. J.* **669**, 1390. DOI. ADS. 48, 53
- Higgins, P.A., Gallagher, P.T., *et al*: 2011, Solar magnetic feature detection and tracking for space weather monitoring. *Advances in Space Research* **47**(12), 2105. DOI. 40
- Hiremath, K.M.: 2002, Change of rotation rates of sunspot groups during their lifetimes: Clues to the sites of origin of different flux tubes. *Astron. Astrophys.* **386**, 674. DOI. ADS. 119
- Hirzberger, J., Vázquez, M., Bonet, J.A., Hanslmeier, A., Sobotka, M.: 1997, Time series of solar granulation images. I. Differences between small and large granules in quiet regions. *Astrophys. J.* **480**, 406. ADS. 2
- Hirzberger, J., Bonet, J.A., Vázquez, M., Hanslmeier, A.: 1999, Time series of solar granulation images. II. Evolution of individual granules. *Astrophys. J.* **515**, 441. DOI. ADS. 2
- Howard, R., Harvey, J.: 1970, Spectroscopic determinations of solar rotation. *Solar Phys.* **12**, 23. DOI. ADS. 104
- Howard, R., Gilman, P.I., Gilman, P.A.: 1984, Rotation of the sun measured from Mount Wilson white-light images. *Astrophys. J.* **283**, 373. DOI. ADS. 102, 104, 105, 114, 128, 134, 141, 172
- Howard, R.F.: 1992, The rotation of active regions with differing magnetic polarity separations. *Solar Phys.* **142**, 233. DOI. ADS. 102
- Howard, R.F.: 1996a, Axial tilt angles of active regions. *Solar Phys.* **169**, 293. DOI. ADS. 148
- Howard, R.F.: 1996b, Solar active regions as diagnostics of subsurface conditions. *Ann. Rev. Astron. Astrophys.* **34**, 75. DOI. ADS. 101, 102, 105
- Howard, R.F.: 1996c, Tilt-angle variations of active regions. *Solar Phys.* **167**, 95. DOI. ADS. 145, 149
- Howard, R.F., Harvey, J.W., Forgach, S.: 1990, Solar surface velocity fields determined from small magnetic features. *Solar Phys.* **130**, 295. DOI. ADS. 40
- Howard, R., Boyden, J.E., Bruning, D.H., Clark, M.K., Crist, H.W., Labonte, B.J.: 1983, The Mount Wilson magnetograph. *Solar Phys.* **87**, 195. DOI. ADS. 104

- Howe, R.: 2009, Solar interior rotation and its variation. *Living Reviews in Solar Physics* **6**, 1. DOI. ADS. 3, 99
- Howe, R., Christensen-Dalsgaard, J., Hill, F., Komm, R., Schou, J., Thompson, M.J.: 2005, Solar convection-zone dynamics, 1995-2004. *Astrophys. J.* **634**, 1405. DOI. ADS. 101
- Howe, R., Rempel, M., Christensen-Dalsgaard, J., Hill, F., Komm, R., Larsen, R.M., Schou, J., Thompson, M.J.: 2006, Solar convection zone dynamics: How sensitive are inversions to subtle dynamo features? *Astrophys. J.* **649**, 1155. DOI. ADS. 101
- Howe, R., Christensen-Dalsgaard, J., Hill, F., Komm, R., Schou, J., Thompson, M.J.: 2009, A note on the torsional oscillation at solar minimum. *Astrophys. J.* **701**, L87. DOI. ADS. 103
- Hoyle, F.: 1949, *Some recent researches in solar physics*, 1st edn. Cambridge University Press, Cambridge. ADS. 47
- Hoyt, D.V., Schatten, K.H.: 1997, *The role of the sun in climate change*, 1st edn. Oxford University Press, Oxford. ISBN 9780195094145. ADS. 53
- Hoyt, D.V., Schatten, K.H.: 1998, Group sunspot numbers: A new solar activity reconstruction. *Solar Phys.* **181**, 491. DOI. ADS. 139
- Illarionov, E., Tlatov, A., Sokoloff, D.: 2015, The properties of the tilts of bipolar solar regions. *Solar Phys.* **290**, 351. DOI. ADS. 159
- Jahn, K.: 1992, Magnetohydrostatic equilibrium in sunspot models. In: Thomas, J.H., Weiss, N.O. (eds.) *Sunspots: Theory and observations, NATO Advanced Science Institutes (ASI) Series C* **375**, 139. ADS. 46, 48
- Jahn, K.: 1997, Physical models of sunspots. In: Schmieder, B., del Toro Iniesta, J.C., Vazquez, M. (eds.) *1st Advances in Solar Physics Euroconference. Advances in Physics of Sunspots, Astronomical Society of the Pacific Conference Series* **118**, 122. ADS. 48
- Jahn, K., Schmidt, H.U.: 1994, Thick penumbra in a magnetostatic sunspot model. *Astron. Astrophys.* **290**, 295. ADS. 48, 49
- Javaraiah, J.: 2000, 22-year periodicity in the solar differential rotation. *Journal of Astrophysics and Astronomy* **21**, 167. DOI. ADS. 126
- Javaraiah, J.: 2001, Study of Sun's rotation and solar activity. PhD thesis, Indian Institute of Astrophysics Bangalore-560 034, India. ADS. 104
- Javaraiah, J.: 2002, Short-term periodicities in the north-south asymmetry of the Sun's surface rotation. *Bulletin of the Astronomical Society of India* **30**, 587. ADS. 104
- Javaraiah, J.: 2003a, Long-term variations in the solar differential rotation. *Solar Phys.* **212**, 23. DOI. ADS. 103, 104, 129

- Javaraiah, J.: 2003b, Long-term variations in the solar differential rotation. *Solar Phys.* **212**, 23. DOI. ADS. 127, 141
- Javaraiah, J.: 2012, The G-O rule and waldmeier effect in the variations of the numbers of large and small sunspot groups. *Solar Phys.* **281**, 827. DOI. ADS. 123
- Javaraiah, J.: 2013, A comparison of solar cycle variations in the equatorial rotation rates of the Sun's subsurface, surface, corona, and sunspot groups. *Solar Phys.* **287**, 197. DOI. ADS. 11, 107, 109, 119, 123, 124, 142
- Javaraiah, J., Gokhale, M.H.: 1995, Periodicities in the solar differential rotation, surface magnetic field and planetary configurations. *Solar Phys.* **158**, 173. DOI. ADS. 107, 135
- Javaraiah, J., Gokhale, M.H.: 1997, Estimation of the depths of initial anchoring and the rising-rates of sunspot magnetic structures from rotation frequencies of sunspot groups. *Astron. Astrophys.* **327**, 795. ADS. 102, 104, 118, 120, 142
- Javaraiah, J., Gokhale, M.K.: 2002, *The Sun's rotation*, Nova Science Pub Inc, N.Y. ISBN 9781590332504. ADS. 101, 110, 126
- Javaraiah, J., Bertello, L., Ulrich, R.K.: 2005, Long-term variations in solar differential rotation and sunspot activity. *Solar Phys.* **232**, 25. DOI. ADS. 103, 111, 129, 141
- Javaraiah, J., Ulrich, R.K., Bertello, L., Boyden, J.E.: 2009, Search for short-term periodicities in the Sun's surface rotation: A revisit. *Solar Phys.* **257**, 61. DOI. ADS. 103
- Jensen, E., Nordø, J., Ringnes, T.S.: 1955, Variations in the structure of sunspots in relation to the sunspot cycle. *Astrophysica Norvegica* **5**, 167. ADS. 53, 54
- Jensen, E., Nordø, J., Ringnes, T.S.: 1956, Variations in the relative size of penumbra and umbra of sunspots in the Years 1878-1954. *Annales d'Astrophysique* **19**, 165. ADS. 53
- Jones, C.A., Thompson, M.J., Tobias, S.M.: 2010, The solar dynamo. *Space Sci. Rev.* **152**, 591. DOI. ADS. 8
- Jones, H.P., Chapman, G.A., Harvey, K.L., *et al*: 2008, A comparison of feature classification methods for modeling solar irradiance variation. *Solar Phys.* **248**, 323. DOI. ADS. 29
- Kambry, M.A., Nishikawa, J.: 1990, Solar differential rotation derived from sunspot observations. *Solar Phys.* **126**, 89. DOI. ADS. 103, 128
- Kass, M., Witkin, A., Terzopoulos, D.: 1988, Snakes: Active contour models. *Int. J. Comput. Vis.* **1**, 321. DOI. 30

- Kiess, C., Rezaei, R., Schmidt, W.: 2014, Properties of sunspot umbrae observed in cycle 24. *Astron. Astrophys.* **565**, A52. DOI. ADS. 60, 62, 90, 171
- Kitchatinov, L.L.: 2013, Theory of differential rotation and meridional circulation. In: Kosovichev, A.G., de Gouveia Dal Pino, E., Yan, Y. (eds.) *IAU Symposium, IAU Symposium* **294**, 399. DOI. ADS. 97
- Knaack, R., Stenflo, J.O., Berdyugina, S.V.: 2005, Evolution and rotation of large-scale photospheric magnetic fields of the Sun during cycles 21-23. Periodicities, north-south asymmetries and r-mode signatures. *Astron. Astrophys.* **438**, 1067. DOI. ADS. 104
- Komm, R.W., Howard, R.F., Harvey, J.W.: 1993, Torsional oscillation patterns in photospheric magnetic features. *Solar Phys.* **143**, 19. DOI. ADS. 115
- Kopp, G., Rabin, D.: 1992, A relation between magnetic field strength and temperature in sunspots. *Solar Phys.* **141**, 253. DOI. ADS. 50
- Kosovichev, A.G.: 2011, Advances in global and local helioseismology: An introductory review. In: Rozelot, J.-P., Neiner, C. (eds.) *Lecture Notes in Physics, Berlin Springer Verlag, Lecture Notes in Physics, Berlin Springer Verlag* **832**, 3. DOI. ADS. 97
- Kosovichev, A.G., Stenflo, J.O.: 2008, Tilt of emerging bipolar magnetic regions on the sun. *Astrophys. J.* **688**, L115. DOI. ADS. 145, 158
- Kosovichev, A.G., Duvall, T.L.. Jr., Scherrer, P.H.: 2000, Time-distance inversion methods and results. *Solar Phys.* **192**, 159. DOI. ADS. 116
- Kovaltsov, G.A., Usoskin, I.G., Mursula, K.: 2004, An upper limit on sunspot activity during the maunder minimum. *Solar Phys.* **224**, 95. DOI. ADS. 139
- Krivova, N.A., Balmaceda, L., Solanki, S.K.: 2007, Reconstruction of solar total irradiance since 1700 from the surface magnetic flux. *Astron. Astrophys.* **467**, 335. DOI. ADS. 53
- Küker, M., Rüdiger, G., Pipin, V.V.: 1996, Solar torsional oscillations due to the magnetic quenching of the Reynolds stress. *Astron. Astrophys.* **312**, 615. ADS. 103
- Labonte, B.J., Howard, R.: 1982, Torsional waves on the sun and the activity cycle. *Solar Phys.* **75**, 161. DOI. ADS. 102
- Leighton, R.B.: 1969, A magneto-kinematic model of the solar cycle. *Astrophys. J.* **156**, 1. DOI. ADS. 9
- Leighton, R.B., Noyes, R.W., Simon, G.W.: 1962, Velocity fields in the solar atmosphere. I. Preliminary report. *Astrophys. J.* **135**, 474. DOI. ADS. 3
- Leka, K.D., Skumanich, A.: 1998, The evolution of pores and the development of penumbrae. *Astrophys. J.* **507**, 454. DOI. ADS. 53

- Leonard, T., Choudhary, D.P.: 2008, Intensity and magnetic field distribution of sunspots. *Solar Phys.* **252**, 33. DOI. ADS. 50, 61
- Li, J., Ulrich, R.K.: 2012, Long-term measurements of sunspot magnetic tilt angles. *Astrophys. J.* **758**, 115. DOI. ADS. 146, 154, 161, 163
- Livingston, W.: 2002, Sunspots observed to physically weaken in 2000-2001. *Solar Phys.* **207**, 41. DOI. ADS. 50
- Livingston, W., Penn, M.J., Svalgaard, L.: 2012, Decreasing sunspot magnetic fields explain unique 10.7 cm radio flux. *Astrophys. J.* **757**, L8. DOI. ADS. 51
- Longcope, D.W., Fisher, G.H., Arendt, S.: 1996, The evolution and fragmentation of rising magnetic flux tubes. *Astrophys. J.* **464**, 999. DOI. ADS. 149
- Lustig, G.: 1982, The sun's rotation derived from sunspots 1970-1979. *Astron. Astrophys.* **106**, 151. ADS. 117, 128
- Lustig, G.: 1983, Solar rotation 1947-1981 - Determined from sunspot data. *Astron. Astrophys.* **125**, 355. ADS. 103, 126, 128
- Lydon, T.J., Sofia, S.: 1995, A method for incorporating the effects of large-scale magnetic fields in the study of stellar structure and Variability. *Astrophys. J. Sup. Ser.* **101**, 357. DOI. ADS. 47
- Maltby, P.: 1970, On the continuum intensity of the umbra of large sunspots. *Solar Phys.* **13**, 312. DOI. ADS. 91
- Maltby, P., Avrett, E.H., Carlsson, M., Kjeldseth-Moe, O., Kurucz, R.L., Loeser, R.: 1986, A new sunspot umbral model and its variation with the solar cycle. *Astrophys. J.* **306**, 284. DOI. ADS. 52
- Martens, P.C.H., Attrill, *et al*: 2012, Computer vision for the solar dynamics observatory (SDO). *Solar Phys.* **275**, 79. DOI. ADS. 27
- Martínez Pillet, V.: 1992, Stray-light effects on the solar intensity distribution. *Solar Phys.* **140**, 207. DOI. ADS. 21
- Martínez Pillet, V.: 1997, Polarimetric measurements of sunspots. In: Schmieder, B., del Toro Iniesta, J.C., Vázquez, M. (eds.) *1st Advances in Solar Physics Euroconference. Advances in Physics of Sunspots, Astronomical Society of the Pacific Conference Series* **118**, 212. ADS. 53
- Martínez Pillet, V., Vázquez, M.: 1993, The continuum intensity-magnetic field relation in sunspot umbrae. *Astron. Astrophys.* **270**, 494. ADS. 50
- Mathew, S.K., Zakharov, V., Solanki, S.K.: 2009, Stray light correction and contrast analysis of Hinode broad-band images. *Astron. Astrophys.* **501**, L19. DOI. ADS. 20

- Mathew, S.K., Lagg, A., Solanki, S.K., Collados, M., Borrero, J.M., Berdyugina, S., Krupp, N., Woch, J., Frutiger, C.: 2003, Three dimensional structure of a regular sunspot from the inversion of IR stokes profiles. *Astron. Astrophys.* **410**, 695. DOI. ADS. 47
- Mathew, S.K., Martínez Pillet, V., Solanki, S.K., Krivova, N.A.: 2007, Properties of sunspots in cycle 23. I. Dependence of brightness on sunspot size and cycle phase. *Astron. Astrophys.* **465**, 291. DOI. ADS. 20, 21, 23, 29, 51, 52, 56, 57, 60, 62, 67, 68, 76, 90, 92, 93
- Maunder, E.W.: 1903, Spoerer's law of zones. *The Observatory* **26**, 329. ADS. 5
- McClintock, B.H., Norton, A.A.: 2013, Recovering Joy's law as a function of solar cycle, hemisphere, and longitude. *Solar Phys.* **287**, 215. DOI. ADS. 146, 151, 155
- McIntosh, P.S.: 1990, The classification of sunspot groups. *Solar Phys.* **125**, 251. DOI. ADS. 30
- Meunier, N.: 2003, Statistical properties of magnetic structures: Their dependence on scale and solar activity. *Astron. Astrophys.* **405**, 1107. DOI. ADS. 4
- Miesch, M.S.: 2005, Large-scale dynamics of the convection zone and tachocline. *Living Reviews in Solar Physics* **2**, 1. DOI. ADS. 99
- Miesch, M.S., Brun, A.S., De Rosa, M.L., Toomre, J.: 2008, Structure and evolution of giant cells in global models of solar convection. *Astrophys. J.* **673**, 557. DOI. ADS. 97
- Miesch, M.S., Featherstone, N.A., Rempel, M., Trampedach, R.: 2012, On the amplitude of convective velocities in the deep solar interior. *Astrophys. J.* **757**, 128. DOI. ADS. 8
- Moradi, H., Baldner, C., *et al*: 2010, Modeling the subsurface structure of sunspots. *Solar Phys.* **267**, 1. DOI. ADS. 49
- Muller, R.: 1992, Fine structure of umbrae and penumbrae. In: Thomas, J.H., Weiss, N.O. (eds.) *Sunspots: Theory and observations*, NATO Advanced Science Institutes (ASI) Series C **375**, 175. ADS. 47
- Mursula, K., Hiltula, T.: 2004, Systematically asymmetric heliospheric magnetic field: Evidence for a quadrupole mode and non-axisymmetry with polarity flip-flops. *Solar Phys.* **224**, 133. DOI. ADS. 104
- Nagovitsyn, Y.A., Pevtsov, A.A., Livingston, W.C.: 2012, On a possible explanation of the long-term decrease in sunspot field strength. *Astrophys. J.* **758**, L20. DOI. ADS. 51
- Nagovitsyn, Y.A., Ivanov, V.G., Miletsky, E.V., Nagovitsyna, E.Y.: 2010, The Maunder minimum: North-south asymmetry in sunspot formation, mean sunspot latitudes, and the butterfly diagram. *Astronomy Reports* **54**, 476. DOI. ADS. 104

- Nandy, D., Choudhuri, A.R.: 2001, Toward a mean field formulation of the Babcock-Leighton type solar dynamo. I.  $\alpha$ -coefficient versus Durney's double-ring approach. *Astrophys. J.* **551**, 576. DOI. ADS. 145
- Nandy, D., Choudhuri, A.R.: 2002, Explaining the latitudinal distribution of sunspots with deep meridional flow. *Science* **296**, 1671. DOI. ADS. 9
- Nandy, D., Muñoz-Jaramillo, A., Martens, P.C.H.: 2011, The unusual minimum of sunspot cycle 23 caused by meridional plasma flow variations. *Nature* **471**, 80. DOI. ADS. 9
- Neckel, H., Labs, D.: 1994, Solar limb darkening 1986-1990 ( $\lambda$  303 to 1099nm). *Solar Phys.* **153**, 91. DOI. ADS. 21
- Nesme-Ribes, E., Ferreira, E.N., Mein, P.: 1993, Solar dynamics over solar cycle 21 using sunspots as tracers. I. Sunspot rotation. *Astron. Astrophys.* **274**, 563. ADS. 102, 103, 128, 140, 174
- Nordlund, Å., Stein, R.F., Asplund, M.: 2009, Solar surface convection. *Living Reviews in Solar Physics* **6**, 2. DOI. ADS. 2
- Norton, A.A., Gilman, P.A.: 2004, Magnetic field-minimum intensity correlation in sunspots: A tool for solar dynamo diagnostics. *Astrophys. J.* **603**, 348. DOI. ADS. 50, 52, 93, 171, 172
- November, L.J., Toomre, J., Gebbie, K.B., Simon, G.W.: 1981, The detection of mesogranulation on the sun. *Astrophys. J.* **245**, L123. DOI. ADS. 2
- Noyes, R.W., Weiss, N.O., Vaughan, A.H.: 1984, The relation between stellar rotation rate and activity cycle periods. *Astrophys. J.* **287**, 769. DOI. ADS. 98
- Noyes, R.W., Hartmann, L.W., Baliunas, S.L., Duncan, D.K., Vaughan, A.H.: 1984, Rotation, convection, and magnetic activity in lower main-sequence stars. *Astrophys. J.* **279**, 763. DOI. ADS. 98
- Obridko, V.N., Shelting, B.D.: 2001, Rotation characteristics of large-scale solar magnetic fields. *Solar Phys.* **201**, 1. DOI. ADS. 139
- Oláh, K., Kolláth, Z., Strassmeier, K.G.: 2000, Multiperiodic light variations of active stars. *Astron. Astrophys.* **356**, 643. ADS. 98
- Osher, S., Fedkiw, R.P.: 2001, Level set methods: An overview and some recent results. *Journal of Computational Physics* **169**(2), 463. DOI. 31
- Osher, S., Fedkiw, R.P.: 2003, *Level set methods and dynamic implicit surfaces*, Applied mathematical science, Springer, New York, N.Y. ISBN 0-387-95482-1. 31
- Osher, S., Sethian, J.A.: 1988, Fronts propagating with curvature-dependent speed: Algorithms based on hamilton-jacobi formulations. *J. Comput. Phys.* **79**, 12. DOI. ADS. 31

- Ossendrijver, M.: 2003, The solar dynamo. *Astron. Astrophys. Rev.* **11**, 287. DOI. ADS. 8, 46
- Pallavicini, R., Golub, L., Rosner, R., Vaiana, G.S., Ayres, T., Linsky, J.L.: 1981, Relations among stellar X-ray emission observed from Einstein, stellar rotation and bolometric luminosity. *Astrophys. J.* **248**, 279. DOI. ADS. 98
- Parker, E.N.: 1955, Hydromagnetic dynamo models. *Astrophys. J.* **122**, 293. DOI. ADS. 9, 98
- Parker, E.N.: 1975, The nature of the sunspot phenomenon. IV: The intrinsic instability of the magnetic configuration. *Solar Phys.* **40**, 291. DOI. ADS. 49
- Parker, E.N.: 1979a, Sunspots and the physics of magnetic flux tubes. I - The general nature of the sunspot. II - Aerodynamic drag. *Astrophys. J.* **230**, 905. DOI. ADS. 49
- Parker, E.N.: 1979b, Sunspots and the physics of magnetic flux tubes. IX - Umbral dots and longitudinal overstability. *Astrophys. J.* **234**, 333. DOI. ADS. 49
- Parker, E.N.: 1993, A solar dynamo surface wave at the interface between convection and nonuniform rotation. *Astrophys. J.* **408**, 707. DOI. ADS. 9
- Parnell, C.E., DeForest, C.E., Hagenaar, H.J., Johnston, B.A., Lamb, D.A., Welsch, B.T.: 2009, A power-law distribution of solar magnetic fields over more than five decades in flux. *Astrophys. J.* **698**, 75. DOI. ADS. 4
- Passos, D., Charbonneau, P., Beaudoin, P.: 2012, An exploration of non-kinematic effects in flux transport dynamos. *Solar Phys.* **279**, 1. DOI. ADS. 10
- Penn, M.J., Livingston, W.: 2006, Temporal changes in sunspot umbral magnetic fields and temperatures. *Astrophys. J.* **649**, L45. DOI. ADS. 51, 171
- Penn, M.J., Livingston, W.: 2011, Long-term evolution of sunspot magnetic fields. In: Prasad Choudhary, D., Strassmeier, K.G. (eds.) *IAU Symposium, IAU Symposium* **273**, 126. DOI. ADS. 51
- Penn, M.J., MacDonald, R.K.D.: 2007, Solar cycle changes in sunspot umbral intensity. *Astrophys. J.* **662**, L123. DOI. ADS. 52, 53
- Petrovay, K.: 1993, Area-weighting of sunspot group positions and proper motion artifacts. In: Zirin, H., Ai, G., Wang, H. (eds.) *IAU Colloq. 141: The Magnetic and Velocity Fields of Solar Active Regions, Astronomical Society of the Pacific Conference Series* **46**, 123. ADS. 121, 142
- Pettauer, T., Brandt, P.N.: 1997, On novel methods to determine areas of sunspots from photoheliograms. *Solar Phys.* **175**, 197. DOI. ADS. 29

- Pevtsov, A.A., Nagovitsyn, Y.A., Tlatov, A.G., Rybak, A.L.: 2011, Long-term trends in sunspot magnetic fields. *Astrophys. J.* **742**, L36. DOI. ADS. 52
- Pevtsov, A.A., Bertello, L., Tlatov, A.G., Kilcik, A., Nagovitsyn, Y.A., Cliver, E.W.: 2014, Cyclic and long-term variation of sunspot magnetic fields. *Solar Phys.* **289**, 593. DOI. ADS. 50, 52
- Pierce, A.K., Slaughter, C.D.: 1977, Solar limb darkening. I -  $\lambda\lambda$  of 3033-7297. *Solar Phys.* **51**, 25. DOI. ADS. 23
- Pizzolato, N., Maggio, A., Micela, G., Sciortino, S., Ventura, P.: 2003, The stellar activity-rotation relationship revisited: Dependence of saturated and non-saturated X-ray emission regimes on stellar mass for late-type dwarfs. *Astron. Astrophys.* **397**, 147. DOI. ADS. 98
- Poduval, B., DeForest, C.E., Schmelz, J.T., Pathak, S.: 2013, Point-spread functions for the extreme-ultraviolet channels of SDO/AIA telescopes. *Astrophys. J.* **765**, 144. DOI. ADS. 20
- Potts, H.E., Diver, D.A.: 2008, Post-hoc derivation of SoHO Michelson Doppler Imager flat fields. *Astron. Astrophys.* **492**, 863. DOI. ADS. 25
- Preminger, D.G., Walton, S.R., Chapman, G.A.: 2001, Solar feature identification using contrasts and contiguity. *Solar Phys.* **202**, 53. DOI. ADS. 29
- Rast, M.P.: 2003, The scales of granulation, mesogranulation, and supergranulation. *Astrophys. J.* **597**, 1200. DOI. ADS. 2
- Rempel, M.: 2006, Transport of toroidal magnetic field by the meridional flow at the base of the solar convection zone. *Astrophys. J.* **637**, 1135. DOI. ADS. 10
- Rempel, M.: 2010, 3d numerical mhd modeling of sunspots with radiation transport. In: *The Physics of Sun and Star Spots, Proceedings of the International Astronomical Union* **6**, 8. DOI. 48
- Rempel, M., Schlichenmaier, R.: 2011, Sunspot modeling: From simplified models to radiative MHD simulations. *Living Reviews in Solar Physics* **8**, 3. DOI. ADS. 11, 46, 48, 49, 95
- Rempel, M., Schüssler, M., Knölker, M.: 2009, Radiative magnetohydrodynamic simulation of sunspot structure. *Astrophys. J.* **691**, 640. DOI. ADS. 48
- Rempel, M., Schüssler, M., Cameron, R.H., Knölker, M.: 2009, Penumbral structure and outflows in simulated sunspots. *Science* **325**. DOI. ADS. 11, 48
- Rezaei, R., Beck, C., Schmidt, W.: 2012, Variation in sunspot properties between 1999 and 2011 as observed with the Tenerife Infrared Polarimeter. *Astron. Astrophys.* **541**, A60. DOI. ADS. 50, 51

- Rezaei, R., Bello González, N., Schlichenmaier, R.: 2012, The formation of sunspot penumbra. Magnetic field properties. *Astron. Astrophys.* **537**, A19. DOI. ADS. 95
- Rhodes, E.J. Jr., Cacciani, A., Korzennik, S., Tomczyk, S., Ulrich, R.K., Woodard, M.F.: 1990, Depth and latitude dependence of the solar internal angular velocity. *Astrophys. J.* **351**, 687. DOI. ADS. 110
- Ringnes, T.S.: 1961, Secular variations of short-lived sunspots. *Nature* **192**, 151. DOI. ADS. 50
- Ringnes, T.S.: 1964, Secular variations of long-lived sunspots. *Astrophysica Norvegica* **8**, 303. ADS. 54
- Rossbach, M., Schröter, E.H.: 1970, On the dependence of sunspot minimum intensity on area. *Solar Phys.* **12**, 95. DOI. ADS. 50
- Roša, D., Brajša, R., Vršnak, B., Wöhl, H.: 1995, The relation between the synodic and sidereal rotation period of the Sun. *Solar Phys.* **159**, 393. DOI. ADS. 107
- Ruždjak, D., Ruždjak, V., Brajša, R., Wöhl, H.: 2004, Deceleration of the rotational velocities of sunspot groups during their evolution. *Solar Phys.* **221**, 225. DOI. ADS. 102, 120, 141
- Rybak, J.: 1994, Rotational characteristics of the green solar corona: 1964-1989. *Solar Phys.* **152**, 161. DOI. ADS. 104
- Saar, S.H., Brandenburg, A.: 1999, Time evolution of the magnetic activity cycle period. II. Results for an expanded stellar sample. *Astrophys. J.* **524**, 295. DOI. ADS. 98
- Sánchez Almeida, J., Martínez González, M.: 2011, The magnetic fields of the quiet sun. In: Kuhn, J.R., Harrington, D.M., Lin, H., Berdyugina, S.V., Trujillo-Bueno, J., Keil, S.L., Rimmele, T. (eds.) *Solar Polarization 6, Astronomical Society of the Pacific Conference Series* **437**, 451. ADS. 4
- Schad, T.A.: 2014, On the collective magnetic field strength and vector structure of dark umbral cores measured by the Hinode spectropolarimeter. *Solar Phys.* **289**, 1477. DOI. ADS. 60, 62, 90
- Schad, T.A., Penn, M.J.: 2010, Structural invariance of sunspot umbrae over the solar cycle: 1993 - 2004. *Solar Phys.* **262**, 19. DOI. ADS. 50, 51, 52
- Scharmer, G.B., Gudiksen, B.V., Kiselman, D., Löfdahl, M.G., Rouppe van der Voort, L.H.M.: 2002, Dark cores in sunspot penumbral filaments. *Nature* **420**, 151. ADS. 47
- Scherrer, P.H., Bogart, R.S., Bush, R.I., Hoeksema, J.T., Kosovichev, A.G., Schou, J., Rosenberg, W., Springer, L., Tarbell, T.D., Title, A., Wolfson, C.J., Zayer, I., MDI Engineering Team: 1995, The Solar Oscillations Investigation - Michelson Doppler Imager. *Solar Phys.* **162**, 129. DOI. ADS. 12, 14, 16

- Schlichenmaier, R., Rezaei, R., Bello González, N., Waldmann, T.A.: 2010a, The formation of a sunspot penumbra. *Astron. Astrophys.* **512**, L1. DOI. ADS. 95
- Schlichenmaier, R., Bello González, N., Rezaei, R., Waldmann, T.A.: 2010b, The role of emerging bipoles in the formation of a sunspot penumbra. *Astronomische Nachrichten* **331**, 563. DOI. ADS. 95
- Schou, J., Antia, H.M., *et al.*: 1998, Helioseismic studies of differential rotation in the solar envelope by the solar oscillations investigation using the Michelson Doppler Imager. *Astrophys. J.* **505**, 390. DOI. ADS. 97
- Schrijver, C.J., Zwaan, C.: 2008, *Solar and stellar magnetic activity*, Reissue edn. Cambridge University Press, Cambridge. ISBN 9780521739863. ADS. 4
- Schroeter, E.H.: 1985, The solar differential rotation - Present status of observations. *Solar Phys.* **100**, 141. DOI. ADS. 101
- Schroeter, E.H., Woehl, H., Soltau, D., Vazquez, M.: 1978, An attempt to compare the differential rotation of the Ca/plus/-network with that of the photospheric plasma. *Solar Phys.* **60**, 181. DOI. ADS. 104
- Schüssler, M.: 1981, The solar torsional oscillation and dynamo models of the solar cycle. *Astron. Astrophys.* **94**, L17. ADS. 103
- Schüssler, M.: 1987, Magnetic fields and the rotation of the solar convection zone. In: Durney, B.R., Sofia, S. (eds.) *The Internal Solar Angular Velocity, Astrophysics and Space Science Library* **137**, 303. ADS. 110, 121
- Schüssler, M., Rempel, M.: 2005, The dynamical disconnection of sunspots from their magnetic roots. *Astron. Astrophys.* **441**, 337. DOI. ADS. 116
- Schüssler, M., Vögler, A.: 2006, Magnetoconvection in a sunspot umbra. *Astrophys. J.* **641**, L73. DOI. ADS. 48
- Sethian, J.A.: 1999, *Level set methods and fast marching methods: evolving interfaces in computational geometry, fluid mechanics, computer vision, and materials science* **3**, Cambridge University Press, Cambridge, UK. ISBN 0-521-64557-3. 31
- Sivaraman, K.R., Gupta, S.S., Howard, R.F.: 1993, Measurement of Kodaikanal white-light images. I - A comparison of 35 years of Kodaikanal and Mount Wilson sunspot data. *Solar Phys.* **146**, 27. DOI. ADS. 105
- Sivaraman, K.R., Gupta, S.S., Howard, R.F.: 1999, Measurement of Kodaikanal white-light images - IV. Axial tilt angles of sunspot groups. *Solar Phys.* **189**, 69. DOI. ADS. 148
- Sivaraman, K.R., Sivaraman, H., Gupta, S.S., Howard, R.F.: 2003, Measurement of Kodaikanal white-light images - VI. Variation of rotation rate with age of sunspot groups. *Solar Phys.* **214**, 65. DOI. ADS. 102, 119, 120, 142

- Sivaraman, K.R., Gokhale, M.H., Sivaraman, H., Gupta, S.S., Howard, R.F.: 2007, Measurement of Kodaikanal white-light Images: Relaxation of tilts of spot groups as indicator of subsurface dynamics of parent flux loops. *Astrophys. J.* **657**, 592. DOI. ADS. 145, 158
- Skokić, I., Brajša, R., Roša, D., Hržina, D., Wöhl, H.: 2014, Validity of the relations between the synodic and sidereal rotation velocities of the Sun. *Solar Phys.* **289**, 1471. DOI. ADS. 174
- Smart, W.M., Green, E.b.R.M.: 1977, *Textbook on spherical astronomy*. ADS. 36
- Snodgrass, H.B.: 1983, Magnetic rotation of the solar photosphere. *Astrophys. J.* **270**, 288. DOI. ADS. 104
- Snodgrass, H.B.: 1991, A torsional oscillation in the rotation of the solar magnetic field. *Astrophys. J.* **383**, L85. DOI. ADS. 103
- Sobotka, M.: 1997, Sunspots seen at high spatial resolution. In: Schmieder, B., del Toro Iniesta, J.C., Vazquez, M. (eds.) *1st Advances in Solar Physics Euroconference. Advances in Physics of Sunspots, Astronomical Society of the Pacific Conference Series* **118**, 155. ADS. 47
- Sokoloff, D.: 2004, The Maunder minimum and the solar dynamo. *Solar Phys.* **224**, 145. DOI. ADS. 140
- Sokoloff, D., Nesme-Ribes, E.: 1994, The Maunder minimum: A mixed-parity dynamo model? *Astron. Astrophys.* **288**, 293. ADS. 140
- Solanki, S.K.: 1997, Empirical modelling and thermal structure of sunspots. In: Schmieder, B., del Toro Iniesta, J.C., Vazquez, M. (eds.) *1st Advances in Solar Physics Euroconference. Advances in Physics of Sunspots, Astronomical Society of the Pacific Conference Series* **118**, 178. ADS. 48, 50
- Solanki, S.K.: 2003, Sunspots: An overview. *Astron. Astrophys. Rev.* **11**, 153. DOI. ADS. 46, 47, 49, 119
- Solanki, S.K., Unruh, Y.C.: 2004, Spot sizes on Sun-like stars. *Mon. Not. Roy. Astron. Soc.* **348**, 307. DOI. ADS. 89
- Solanki, S.K., Inhester, B., Schüssler, M.: 2006, The solar magnetic field. *Reports on Progress in Physics* **69**, 563. DOI. ADS. 4
- Solanki, S.K., Finsterle, W., Rüedi, I., Livingston, W.: 1999, Expansion of solar magnetic flux tubes large and small. *Astron. Astrophys.* **347**, L27. ADS. 48
- Spiegel, E.A., Zahn, J.-P.: 1992, The solar tachocline. *Astron. Astrophys.* **265**, 106. ADS. 101
- Spruit, H.C.: 1981a, A cluster model for sunspots. In: Cram, L.E., Thomas, J.H. (eds.) *The Physics of Sunspots*, 98. ADS. 49

- Spruit, H.C.: 1981b, Magnetohydrodynamics of sunspots. *Space Sci. Rev.* **28**, 435. DOI. ADS. 48
- Starck, J.L., Pantin, E., Murtagh, F.: 2002, Deconvolution in astronomy: A review. *Pub. Astron. Soc. Pac.* **114**, 1051. DOI. ADS. 20
- Steenbeck, M., Krause, F., Rädler, K.-H.: 1966, Berechnung der mittleren LORENTZ-Feldstärke für  $\mathbf{b} \times \mathbf{B}$  ein elektrisch leitendes Medium in turbulenter, durch CORIOLIS-Kräfte beeinflusster Bewegung. *Zeitschrift Naturforschung Teil A* **21**, 369. ADS. 9
- Stein, R.F.: 2012, Solar surface magneto-convection. *Living Reviews in Solar Physics* **9**, 4. DOI. ADS. 11, 49
- Steinegger, M., Brandt, P.N., Schmidt, W., Pap, J.: 1990, Sunspot photometry and the total solar irradiance deficit measured in 1980 by ACRIM. *Astrophys. Spa. Sci.* **170**, 127. DOI. ADS. 29, 94
- Steinegger, M., Vázquez, M., Bonet, J.A., Brandt, P.N.: 1996, On the energy balance of solar active regions. *Astrophys. J.* **461**, 478. DOI. ADS. 26, 29, 56
- Steinhilber, F., Abreu, J.A., Beer, J., Brunner, I., Christl, M., Fischer, H., Heikkilä, U., Kubik, P.W., Mann, M., McCracken, K.G., Miller, H., Miyahara, H., Oerter, H., Wilhelms, F.: 2012, 9,400 years of cosmic radiation and solar activity from ice cores and tree rings. *Proceedings of the National Academy of Science* **109**, 5967. DOI. ADS. 8
- Stenflo, J.O., Kosovichev, A.G.: 2012, Bipolar magnetic regions on the Sun: Global analysis of the SOHO/MDI data set. *Astrophys. J.* **745**, 129. DOI. ADS. 146, 148, 149, 150, 158, 159
- Strassmeier, K.G.: 1999, Doppler imaging of stellar surface structure. XI. The super starspots on the K0 giant HD 12545: larger than the entire Sun. *Astron. Astrophys.* **347**, 225. ADS. 89
- Strassmeier, K.G.: 2002, Doppler images of starspots. *Astronomische Nachrichten* **323**, 309. DOI. ADS. 89
- Sturrock, P.A.: 1994, *Plasma physics, An introduction to the theory of astrophysical, geophysical and laboratory plasmas.* ADS. 140
- Suzuki, M.: 1998, The rotation of sunspots during activity cycle 22. *Solar Phys.* **178**, 259. DOI. ADS. 109, 117
- Suzuki, M.: 2012, Solar rotation rate during solar activity cycle 23. *Solar Phys.* **278**, 257. DOI. ADS. 104, 109, 111
- Suzuki, M.: 2014, On the long-term modulation of solar differential rotation. *Solar Phys.* **289**, 4021. DOI. ADS. 126, 132, 174
- Tandberg-Hanssen, E.: 1956, A study of the penumbra-umbra ratio of sunspot pairs. *Astrophysica Norvegica* **5**, 207. ADS. 54

- Ternullo, M., Zappala, R.A., Zuccarello, F.: 1981, The age dependence of photospheric tracer rotation. *Solar Phys.* **74**, 111. DOI. ADS. 101
- Thomas, J.H., Weiss, N.O.: 2008, *Sunspots and starspots*, 1st edn. Cambridge University Press, Cambridge. ISBN 9780521860031. ADS. 46, 49, 98
- Thompson, M.J., Christensen-Dalsgaard, J., Miesch, M.S., Toomre, J.: 2003, The internal rotation of the Sun. *Ann. Rev. Astron. Astrophys.* **41**, 599. DOI. ADS. 97, 99
- Thompson, W.B.: 1951, Thermal convection in a magnetic field. *Philosophical Magazine Series 7* **42**(335), 1417. DOI. 47
- Thompson, W.T.: 2006, Coordinate systems for solar image data. *Astron. Astrophys.* **449**, 791. DOI. ADS. 36
- Tian, L., Liu, Y., Wang, H.: 2003, Latitude and magnetic flux dependence of the tilt angle of bipolar regions. *Solar Phys.* **215**, 281. DOI. ADS. 145, 152
- Tlatov, A., Illarionov, E., Sokoloff, D., Pipin, V.: 2013, A new dynamo pattern revealed by the tilt angle of bipolar sunspot groups. *Mon. Not. Roy. Astron. Soc.* **432**, 2975. DOI. ADS. 146, 149, 150, 151, 168, 174
- Tuominen, I., Virtanen, H.: 1987, Solar rotation variations from sunspot group statistics. In: Durney, B.R., Sofia, S. (eds.) *The Internal Solar Angular Velocity, Astrophysics and Space Science Library* **137**, 83. ADS. 102
- Turmon, M., Pap, J.M., Mukhtar, S.: 2002, Statistical pattern recognition for labeling solar active regions: Application to SOHO/MDI imagery. *Astrophys. J.* **568**, 396. DOI. ADS. 30
- Ulrich, R.K., Bertello, L.: 1996, Solar rotation measurements at Mount Wilson over the period 1990–1995. *Astrophys. J.* **465**, L65. DOI. ADS. 103
- Unruh, Y.C., Solanki, S.K., Fligge, M.: 1999, The spectral dependence of facular contrast and solar irradiance variations. *Astron. Astrophys.* **345**, 635. ADS. 92
- Usoskin, I.G., Mursula, K., Kovaltsov, G.A.: 2000, Cyclic behaviour of sunspot activity during the Maunder minimum. *Astron. Astrophys.* **354**, L33. ADS. 140
- Vaquero, J.M., Gordillo, A., Gallego, M.C., Sanchez-Bajo, F., Garcia, J.A.: 2005, The umbra-penumbra area ratio of sunspots from the de la Rue data. *The Observatory* **125**, 152. ADS. 53
- Verbeeck, C., Higgins, P.A., *et al.*: 2013, A multi-wavelength analysis of active regions and sunspots by comparison of automatic detection algorithms. *Solar Phys.* **283**, 67. DOI. ADS. 27
- Verma, V.K.: 1993, On the north-south asymmetry of solar activity cycles. *Astrophys. J.* **403**, 797. DOI. ADS. 104

- Waldmeier, M.: 1939, Über die Struktur der Sonnenflecken. *Astronomische Mitteilungen der Eidgenössischen Sternwarte Zurich* **14**, 439. ADS. 53
- Wang, Y.-M., Sheeley, N.R. Jr.: 1989, Average properties of bipolar magnetic regions during sunspot cycle 21. *Solar Phys.* **124**, 81. DOI. ADS. 152, 160, 168, 175
- Ward, F.: 1965, The general circulation of the solar atmosphere and the maintenance of the equatorial acceleration. *Astrophys. J.* **141**, 534. DOI. ADS. 107
- Ward, F.: 1966, Determination of the solar-rotation rate from the motion of identifiable features. *Astrophys. J.* **145**, 416. DOI. ADS. 101, 102, 107
- Watson, F.T., Fletcher, L., Marshall, S.: 2011, Evolution of sunspot properties during solar cycle 23. *Astron. Astrophys.* **533**, A14. DOI. ADS. 28, 52
- Watson, F., Fletcher, L., Dalla, S., Marshall, S.: 2009, Modelling the longitudinal asymmetry in sunspot emergence: The role of the Wilson depression. *Solar Phys.* **260**, 5. DOI. ADS. 29, 30
- Weber, M.A., Fan, Y., Miesch, M.S.: 2011, The rise of active region flux tubes in the turbulent solar convective envelope. *Astrophys. J.* **741**, 11. DOI. ADS. 145
- Weber, M.A., Fan, Y., Miesch, M.S.: 2013, Comparing simulations of rising flux tubes through the solar convection zone with observations of solar active regions: Constraining the dynamo field strength. *Solar Phys.* **287**, 239. DOI. ADS. 144, 149, 150, 152, 153
- Wedemeyer-Böhm, S.: 2008, Point spread functions for the solar optical telescope onboard Hinode. *Astron. Astrophys.* **487**, 399. DOI. ADS. 20
- Wedemeyer-Böhm, S., Rouppe van der Voort, L.: 2009, On the continuum intensity distribution of the solar photosphere. *Astron. Astrophys.* **503**, 225. DOI. ADS. 20
- Weiss, N.O.: 1964, Magnetic flux tubes and convection in the Sun. *Mon. Not. Roy. Astron. Soc.* **128**, 225. ADS. 47
- Wenzler, T., Solanki, S.K., Krivova, N.A.: 2005, Can surface magnetic fields reproduce solar irradiance variations in cycles 22 and 23? *Astron. Astrophys.* **432**, 1057. DOI. ADS. 53, 69
- Wenzler, T., Solanki, S.K., Krivova, N.A., Fröhlich, C.: 2006, Reconstruction of solar irradiance variations in cycles 21-23 based on surface magnetic fields. *Astron. Astrophys.* **460**, 583. DOI. ADS. 53
- Wesolowski, M.J., Walton, S.R., Chapman, G.A.: 2008, The behavior of sunspot contrast during cycle 23. *Solar Phys.* **248**, 141. DOI. ADS. 51
- Wilson, P.R.: 1987, Solar rotation and the giant cells. *Solar Phys.* **110**, 59. DOI. ADS. 103

- Wilson, P.R., Cannon, C.J.: 1968, The structure of a sunspot. III: Observations of the Wilson effect. *Solar Phys.* **4**, 3. DOI. ADS. 95
- Wilson, P.R., McIntosh, P.S.: 1969, Structure of a sunspot. V: What is the Wilson effect? *Solar Phys.* **10**, 370. DOI. ADS. 95
- Wilson, P.R., Burtonclay, D., Li, Y.: 1997, The rotational structure of the region below the solar convection zone. *Astrophys. J.* **489**, 395. ADS. 97
- Wöhl, H., Brajša, R., Hanslmeier, A., Gissot, S.F.: 2010, A precise measurement of the solar differential rotation by tracing small bright coronal structures in SOHO-EIT images. Results and comparisons for the period 1998-2006. *Astron. Astrophys.* **520**, A29. DOI. ADS. 104
- Yeo, K.L., Feller, A., Solanki, S.K., Couvidat, S., Danilovic, S., Krivova, N.A.: 2014, Point spread function of SDO/HMI and the effects of stray light correction on the apparent properties of solar surface phenomena. *Astron. Astrophys.* **561**, A22. DOI. ADS. 20
- Zaatri, A., Komm, R., González Hernández, I., Howe, R., Corbard, T.: 2006, North south asymmetry of zonal and meridional flows determined from ring diagram analysis of Gong ++ data. *Solar Phys.* **236**, 227. DOI. ADS. 104, 139
- Zaatri, A., Wöhl, H., Roth, M., Corbard, T., Brajša, R.: 2009, Comparison of the sidereal angular velocity of subphotospheric layers and small bright coronal structures during the declining phase of solar cycle 23. *Astron. Astrophys.* **504**, 589. DOI. ADS. 104, 139
- Zappala, R.A., Zuccarello, F.: 1991, Angular velocities of sunspot-groups and solar photospheric rotation. *Astron. Astrophys.* **242**, 480. ADS. 102
- Zhang, K., Zhang, L., Song, H., Zhou, W.: 2010, Active contours with selective local or global segmentation: A new formulation and level set method. *Image Vis. Comput.* **28**, 668. DOI. 32
- Zhang, L., Mursula, K., Usoskin, I.: 2013, Consistent long-term variation in the hemispheric asymmetry of solar rotation. *Astron. Astrophys.* **552**, A84. DOI. ADS. 104, 139
- Zhao, J., Bogart, R.S., Kosovichev, A.G., Duvall, T.L. Jr., Hartlep, T.: 2013, Detection of equatorward meridional flow and evidence of double-cell meridional circulation inside the Sun. *Astrophys. J.* **774**, L29. DOI. ADS. 3
- Zharkov, S., Zharkova, V.V., Ipson, S.S.: 2005, Statistical properties of sunspots in 1996-2004: I. Detection, north south asymmetry and area distribution. *Solar Phys.* **228**, 377. DOI. ADS. 26, 28, 29, 56
- Zharkov, S., Zharkova, V., Ipson, S., Benkhalil, A.: 2005, Technique for automated recognition of sunspots on full-disk solar images. *EURASIP J. Appl. Signal Process.* **15**, 2573. DOI. 28, 29

- Zharkova, V.V., Aboudarham, *et al.*: 2005, Solar feature catalogues in Egso. *Solar Phys.* **228**, 361. DOI. ADS. 28
- Zuccarello, F.: 1993, Influence of the lifetime parameter on the rotation rate of sunspots. *Astron. Astrophys.* **272**, 587. ADS. 102
- Zwaan, C.: 1965, The influence of scattered light on line intensity measurements. In: Lust, R. (ed.) *Stellar and Solar Magnetic Fields, IAU Symposium* **22**, 277. ADS. 50
- Zwaan, C.: 1977, Magnetic structures in photosphere of sun and stars. *Società Astronomica Italiana, Memorie* **48**, 525. ADS. 94
- Zwaan, C., Brants, J.J.: 1981, Magnetic field strengths in umbrae and pores. In: Cram, L.E., Thomas, J.H. (eds.) *The Physics of Sunspots*, 210. ADS. 49

## List of Publications

- (a) **Goel, Suruchi**, Solanki, S., Krivova, N. and Mathew, S. K. (2015). Statistical properties of sunspots from solar cycle 23. (*manuscript in preparation*)
- (b) **Goel, Suruchi**, Javaraiah, J. and Mathew, S. K.(2015). Study of solar differential rotation rate using sunspots as tracers. (*manuscript in preparation*)
- (c) **Goel, Suruchi** and Mathew, Shibu (2014). Automated detection, characterization and tracking of sunspots from SoHO/MDI continuum images. *Sol. Phys.* 289, 1413-1431.
- (d) **Goel, Suruchi** and Mathew, Shibu (2012). Technique for automatic detection of sunspots from full-disk continuum images. 39th *COSPAR Scientific Assembly*, 39.

### Other article

- (a) **Goel, S.**, Mahajan, R.R., and Murty, S.V.S. (2009) Meteorites archives of solar system history. *ICPS-Virat Surya (The Indian Planetary Society)* Vol-Jan-Apr, 27-30.

# Automated Detection, Characterization, and Tracking of Sunspots from SoHO/MDI Continuum Images

Suruchi Goel · Shibu K. Mathew

Received: 19 March 2013 / Accepted: 13 August 2013 / Published online: 25 September 2013  
© Springer Science+Business Media Dordrecht 2013

**Abstract** We describe a procedure for automated detection of sunspots from SoHO/MDI full-disk continuum images. The MDI Level-1.8 continuum images were first corrected for the limb darkening and stray light, and then were flat-fielded. Sunspots were extracted using a newly developed automated sunspot detection procedure, which is based on the level set, namely the selective binary and Gaussian function regularized level set (SBGFRLS) method (Zhang *et al.*, *Image Vis. Comput.* **28**, 668, 2010). In this method we initialize a two-dimensional level-set function and evolve it using a signed pressure force (SPF) function. For sunspot detection, the level-set function was defined twice, first for umbra and then for penumbra extraction. Using this procedure, along with the characterization of detected sunspots we have also generated tracking reports of all sunspots in a fully unsupervised manner.

**Keywords** Automated detection · Point spread function · Stray light · Sunspots · Tracking

## 1. Introduction

The *Michelson Doppler Imager* (MDI; Scherrer *et al.*, 1995) on SoHO provided the continuum images around the NiI 6768 Å mid-photospheric absorption line since May 1996 to April 2011. The observed images cover the entire solar cycle 23 and enable us to investigate the long-term variations of sunspot properties (like area, intensity value of umbra and penumbra, *etc.*) in great detail. Such a study is very useful for solar irradiance modeling, as well as to understand the formation and decay processes of sunspots. It is therefore essential to identify the sunspots and extract their associated properties from available great wealth of solar image-data archives, which needs a robust and reliable automated detection technique.

---

S. Goel (✉) · S.K. Mathew  
Udaipur Solar Observatory, Physical Research Laboratory, Devali, Badi Road, Udaipur, Rajasthan  
313001, India  
e-mail: [suruchigoel20@gmail.com](mailto:suruchigoel20@gmail.com)

S.K. Mathew  
e-mail: [shibu@prl.res.in](mailto:shibu@prl.res.in)

There are several methods available in the literature for sunspot detection from solar images (see reviews by Jones *et al.*, 2008; Aschwanden, 2010; Verbeeck *et al.*, 2013). These methods involve different image processing techniques, for example intensity threshold, edge detection, morphological operations, region growing, fuzzy clustering, *etc.*; however, most of them are not fully automatic (unsupervised).

We have developed a new automated and robust sunspot extraction procedure which is based on the level-set formulation of active contour method, which is fast and simple to implement. This automated detection procedure allows us to generate a catalog with a list of sunspots properties and also track each sunspot in a fully unsupervised manner.

In Section 2, we present a brief review of some of the existing sunspot detection methods. The details of the pre-processing steps applied to continuum images are introduced in Section 3. In Section 4, we give an introduction to the active contour and level-set methods. In Section 5.1, we explain our automated detection procedure. The generated sunspots catalog and tracking results are presented in Sections 5.2 and 5.3. In Section 6, we present comparison of sunspot properties obtained using the technique with the available standard catalogs. In Section 7, we summarize our results and conclude.

## 2. Review of Sunspot Detection Methods

In white-light images sunspots are darker objects than the photosphere. Within the sunspots, we have a darker core called umbra surrounded by relatively brighter region called penumbra. Here the essential image-segmentation problem is to identify dark sunspots from brighter background (photosphere).

For sunspot detection, initial attempts were to set threshold intensities for umbra–penumbra and penumbra–photosphere boundaries. To derive the threshold intensities different approaches were adopted. For example, Grossmann-Doerth and Schmidt (1981), Steinegger *et al.* (1990), and Brandt, Schmidt, and Steinegger (1990) derived these threshold intensities from the brightness distribution of several sunspots. Beck and Chapman (1993) sampled intensity profiles across the sunspots from continuum images and set the threshold intensities corresponding to the point of maximum slope. Pettauer and Brandt (1997) and Steinegger *et al.* (1996) derived the threshold intensity from intersections of linear fits to the intensity cumulative histogram. The threshold method is easy to draw the boundaries (contour) around umbra and penumbra, but it is not true that each sunspot will have the same intensity value at boundaries, which can then affect the derived area values.

Another method is to apply edge-detection to extract objects from background. Pre-minger, Walton, and Chapman (2001) added the gradient information with the threshold intensity. But in the gradient map, sunspots boundaries do not have uniform intensity; also there is non-zero contribution from other features on solar image. Even setting a threshold to the gradient/edge map will not give connected boundaries, and it still further requires more computational effort (Győri, 1998; Zharkov *et al.*, 2005). For example, Zharkov *et al.* (2005) adopted morphological operations to get the connected sunspot regions from edge-based candidate sunspots. Then each candidate sunspot was thresholded based on the size of the sunspot for umbra and penumbra boundaries.

Curto, Blanca, and Martínez (2008) and Watson *et al.* (2009) used morphological tools to detect sunspots. Curto, Blanca, and Martínez (2008) used a top-hat transformation which detects darker (valley) regions smaller than the structure element used. The population of sunspots was checked for stabilization in two iteration loops; one for the size of structure element of closing operation and the other for threshold intensity. Then, to group candidate

sunspot regions, a region-growing procedure was applied. Watson *et al.* (2009) also adopted a detection procedure based on morphological operations but with a different approach. They first applied the morphological erosion to the inverted solar image which results in removal of peaks due to sunspots from the image. Then further, this inverted and eroded image was dilated with the same structure element as was used for erosion to get back to the original intensity levels. The resulted image was then subtracted from the original solar image, which gives candidate sunspot regions to which intensity threshold was applied.

Other computationally extensive methods are also available. For example, Turmon, Pap, and Mukhtar (2002) developed a statistical Bayesian technique for active region and sunspot detection and labeling. Colak and Qahwaji (2008) applied intensity threshold and region-growing techniques for sunspot region detection and used an artificial neural network for their classification. Fonte and Fernandes (2009) applied fuzzy set theory for the determination of umbra and penumbra boundaries.

Our procedure is a generalized approach, called level-set image segmentation. The procedure takes advantage of both the image gradient as well as region-based image statistics to detect sunspots (described in Sections 4 and 5) which is computationally fast and simple to implement.

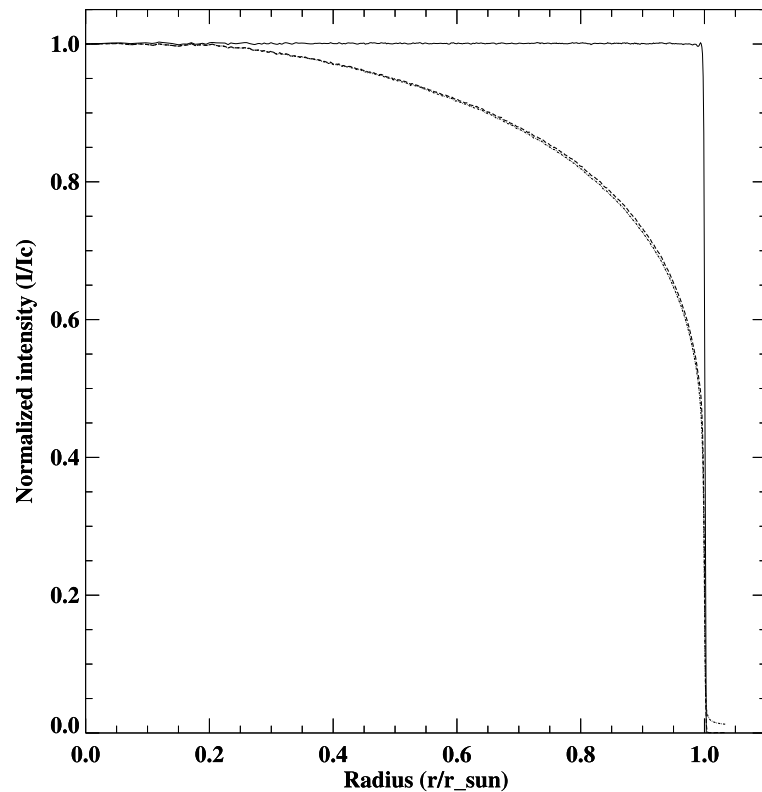
### 3. Pre-processing of SoHO/MDI Continuum Images

Although MDI continuum images are free from atmospheric seeing, they are contaminated from instrumental scattered light. This instrumental scattered-light contamination has increased with the aging of the instrument (Mathew *et al.*, 2007). Also it is observed that over the period of operation of MDI, the degradation in the instrument increased (Potts and Diver, 2008), which thus affects the changes in uniformity in the flat-field images. To attain precise sunspot detection we have done pre-processing to the Level-1.8 MDI full-disk continuum images. The pre-processing includes stray-light correction, limb-darkening removal, and flat fielding.

#### 3.1. Stray-Light and Limb-Darkening Removal

To correct the MDI continuum images for the stray light, we have modeled the change in the point spread function (PSF) of the instrument for each year. For estimating the PSF, we make use of the residual intensity outside the solar limb as described in Martínez Pillet (1992) and in the Appendix of Mathew *et al.* (2007). From full-disk continuum images, we first generated radial profiles by taking median intensity in each annular ring from disk center to regions beyond solar limb. These radial profiles were fitted both for center-to-limb variation (CLV) coefficients and PSF parameters. The CLV was fitted by a fifth order polynomial of  $\cos \theta$  ( $\theta$  is the angular distance from the Sun center), for which initial coefficients were taken from Pierce and Slaughter (1977). On the other hand, PSF parameters include weights and widths of three Gaussian functions and one Lorentzian function (with fixed width of 40 arcsec). The CLV and PSF parameters were fitted to intensity radial profiles for selected images from June month for every year. During these periods we get better off-limb profiles, as the full-disk image size covering the CCD plane is minimum. From these fitted parameters we calculated average CLV and PSF parameters for each year. All the images from May 1996 to April 2011 were deconvolved using the model PSF obtained by using the interpolated PSF parameters. These restored images were then corrected for center-to-limb variation using the average CLV coefficients derived for each year. Figure 1 shows the in-

**Figure 1** Normalized intensity radial profiles of (a) observed MDI Lev-1.8 continuum image (dot-dashed); (b) PSF corrected image (dashed) (c) PSF, CLV-removed and flat-field corrected image (solid line).



tensity profiles (normalized with respect to disk center intensity,  $I_c$ ) for an MDI Level 1.8 image. The dot-dashed line is the observed radial profile, whereas the dashed line is the profile of the scattered-light-corrected image, where the off-limb residual intensity is removed. The flat radial profile in solid line is for the scattered-light-corrected, CLV-removed, and flat-fielded image.

### 3.2. Flat Fielding

In later years of MDI operation, the non-uniformity in detector sensitivity due to the degradation of the instrument has increased considerably in the continuum images (Potts and Diver, 2008). In the flat-field-correction procedure, we have utilized all available continuum images and generated a master flat-field image for each Carrington rotation period. The flat-field correction has the following three steps:

- i) Firstly, all the images were masked for active regions, (*i.e.* umbra–penumbra and facular regions) to avoid their contribution to the flat-field image. This was done by intensity thresholding, where thresholds were chosen statistically from histograms. But as the instrument aged, the non-uniformity in the image increased, which results in reduction in intensity at some locations on the CCD plane to almost the normal penumbral intensity values. Hence, to avoid removal of large portions of images during masking, we chose a lower threshold. In order to mask the left-out penumbral regions completely, we further dilated the masked regions obtained from thresholding.
- ii) For each Carrington rotation (CR), the corresponding set of masked continuum images were then median combined *i.e.* master flats were generated by taking median intensity at each pixel. The master flats were then median filtered to remove small scale structures and normalized with the median intensity value.
- iii) All the continuum images were then normalized with their respective (Carrington rotation number) master flat image.

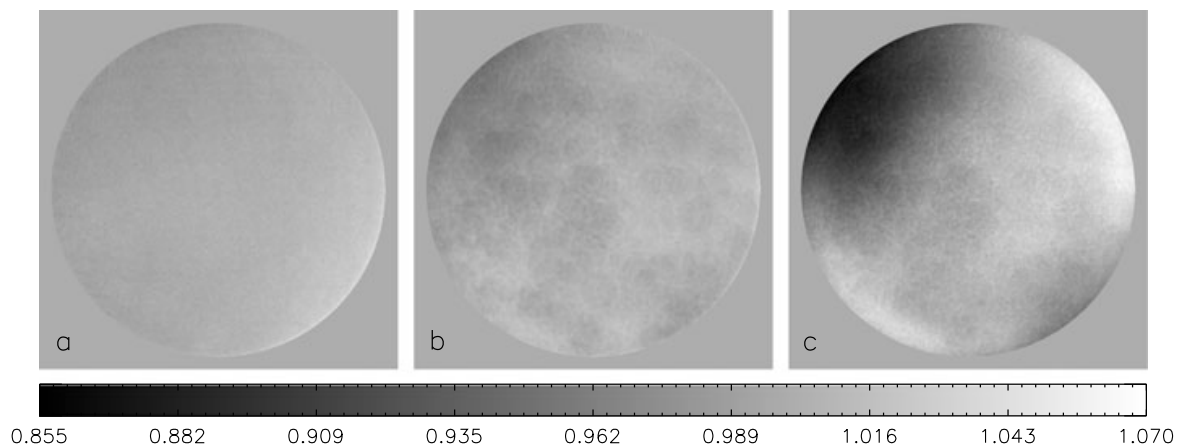


**Figure 2** Flat-field images for Carrington rotation No. (a) 1910 (year 1996), (b) 2004 (year 2003), and (c) 2080 (year 2009). The change in uniformity due to the instrument is clearly visible in these images.

Figure 2 shows the master flat-field images for three different Carrington rotations during the operation period of the MDI. At the start of operation in 1996 the flat field was nearly uniform, but it started developing small scale structures over the period. By the year 2008, some portions of the image have the intensity values similar to penumbral region intensities (Figure 2(c)).

#### 4. Active Contours and Level Set

Image segmentation is defined as partitioning an image into non-overlapping regions based on the intensity or texture. The active contour methods provide an effective way for segmentation, in which the boundary of an object is detected by an evolving curve.

Segmentation using active contour model (snakes) was first introduced by Kass, Witkin, and Terzopoulos (1988). The classical approach is based on deforming an initial contour towards the boundary of the object to be detected. The deformation (the expansion or contraction along the curve) is obtained by minimizing an energy functional, designed so that its local minimum is obtained at the boundary of the object. The energy functional is composed of two components; the internal energy and the external energy. The internal force, defined within the curve, regulates the smoothness of the curve during the deformation process. The external force, which is an image-driven force (for example, local gradient), attracts the curve towards the object boundary.

There are two kinds of active contour models according to the force for evolving the contours: edge-based and region-based. Edge-based active contours use an edge detector, usually based on the image gradient, to find the boundaries of sub-regions and to attract the contours to the desired feature boundaries. Region-based active contours use the statistical information of image intensity inside and outside the evolving curve. With active contour models, the resulting segmentation avoids yielding broken boundaries even in the presence of noise and non-ideal edges. However, there is the possibility of getting caught in local minima, influenced by the initial curve.

The level-set theory, a formulation to implement active contours was first proposed by Osher and Sethian (1988). In the level-set formulation, the curve  $C$  is a level set of a function  $\phi$  defined in higher dimensions (image plane) [Equation (1)].  $C$  coincides with the set of points  $\phi = \text{constant}$ , which is usually set to zero, meaning that  $C$  is the 'zero' level-set of  $\phi$ . At any given time, the level-set function simultaneously defines an edge contour

and a segmentation of the image. The edge contour is taken to be the zero-level set  $(x, y)$  such that  $\phi(x, y) = 0$ , and the segmentation is given by the two regions  $\phi > 0$  and  $\phi < 0$  [Equation (2)]. The level-set function will be evolved according to some partial differential equation [Equation (3)], and hopefully will reach a steady state, which gives a useful segmentation of the image. In this approach the evolution of contours is equivalent to the evolution of the level-set function.

In the level-set formulation of active contours, the fronts, denoted by  $C$ , are represented by the zero-level set

$$C(t) = \{\phi(x, y) | \phi(t, x, y) = 0\} \quad (1)$$

of a level-set function  $\phi(t, x, y)$ , where  $(x, y)$  are coordinates in the image plane and  $t$  is an artificial time such that

$$\begin{aligned} \text{Inside}(C(t)) &= \{\phi(t, x, y) < 0\}, \\ \text{Outside}(C(t)) &= \{\phi(t, x, y) > 0\}. \end{aligned} \quad (2)$$

The evolution equation of the level-set function (LSF)  $\phi$  can be written in the following general form:

$$\frac{\partial \phi}{\partial t} + F|\nabla \phi| = 0 \quad (3)$$

which is called the level-set equation. The function  $F$  is called the speed function. For image segmentation, the function  $F$  depends on the image data and the LSF  $\phi$ . Figure 3 shows an example of level-set segmentation results at different stages, for extraction of boundaries of features in an image. In Figure 3, the second row shows the evolution of LSF while the first row shows the corresponding zero-level-set curve over the image. The zero-level-set curve corresponds to the zero-valued connected boundaries of the LSF; outside and inside this curve the LSF has opposite signs. Figure 3(d) shows the initialized LSF (surface), with the corresponding zero-level-set curve being a square [Figure 3(a)]. Using an evolution equation (the SBFRLS method described in Section 5.1) the LSF has been evolved to the boundaries of the features in the image [Figure 3(c)].

This approach presents several advantages over the traditional parametric active contours. First, the contours represented by the LSF may break or merge naturally during the evolution, and the topological changes are thus automatically handled. Second, the LSF always remains a function on a fixed grid, which allows efficient numerical schemes.

## 5. Automated Detection, Characterization, and Tracking of Sunspots

### 5.1. Level-Set Detection

A novel region-based level set is used in this paper named as selective binary and Gaussian filtering regularized level set (SBGFRLS) method (Zhang *et al.*, 2010). It utilizes the statistical information inside and outside the contour to construct a region-based signed pressure force (SPF) function, which can efficiently stop the contours at weak or blurred edges. Also the exterior and interior boundaries can be automatically detected with the initial contour being anywhere in the image. We construct the SPF function for a given image,  $I$ , as follows:

$$\text{SPF}(I(x)) = \frac{I(x) - \frac{c_1+c_2}{2}}{\max(|I(x) - \frac{c_1+c_2}{2}|)} \quad (4)$$

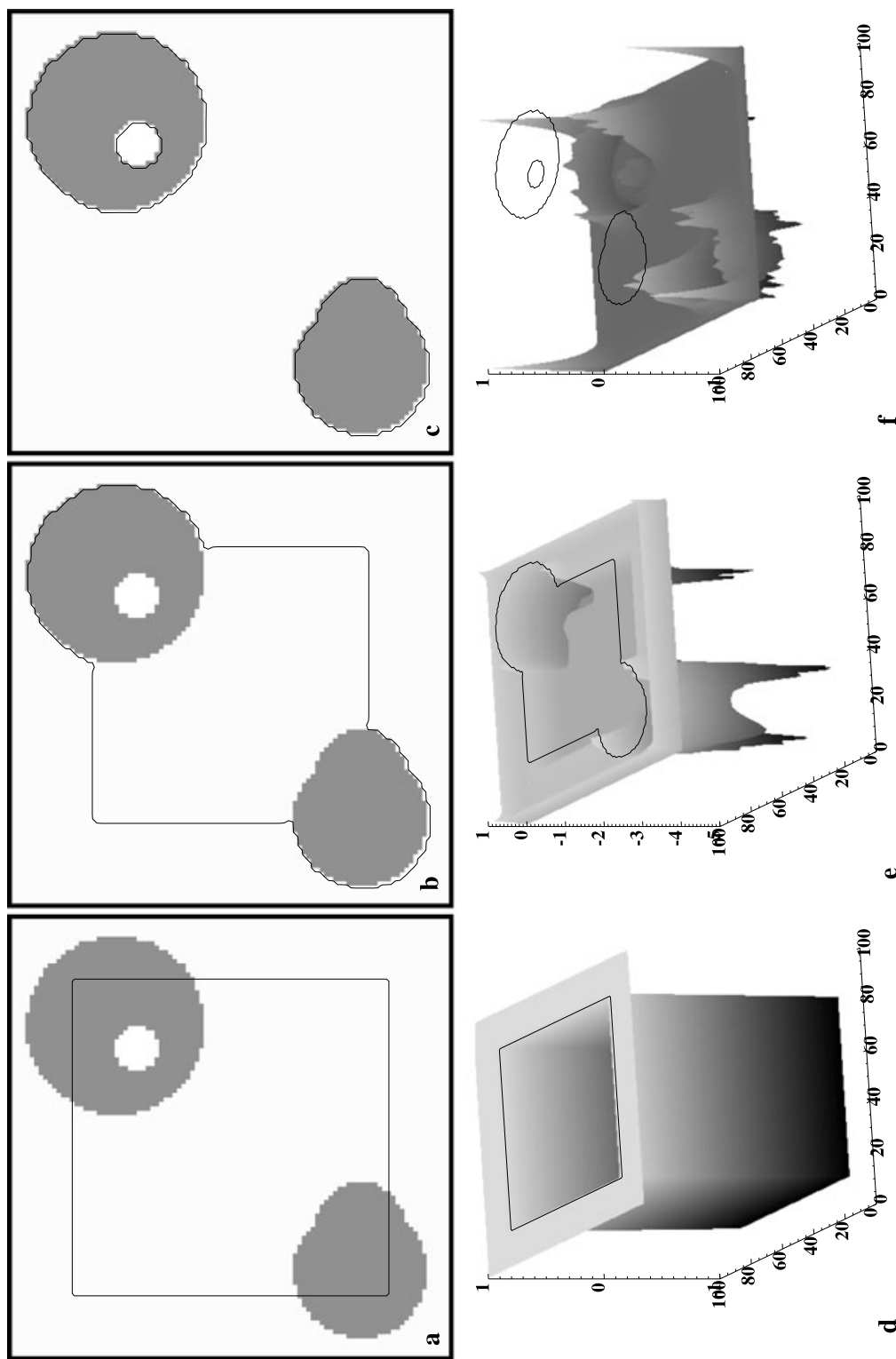


**Figure 3** Illustration of level-set image segmentation. (a, d) The initial level set function (LSF), (b, e) LSF at iteration 13, and (c, f) LSF at the 50th iteration.

where  $c_1$  and  $c_2$  are the average intensities inside and outside the contour, respectively. The SPF function has opposite signs around the object boundary, so the contour can shrink when it is outside the object or expand when inside the object. The following is the procedure for the level-set image segmentation:

- i) Initialize the LSF such that the desired region has a negative value while the outside region has a positive value.
- ii) Compute  $c_1(\phi)$ ,  $c_2(\phi)$ , and SPF.
- iii) Evolve the LSF according to

$$\frac{\partial \phi}{\partial t} + \text{SPF}(I(x)) \cdot \alpha |\nabla \phi| = 0. \quad (5)$$

- iv) Regularize the LSF by convolving with a Gaussian function;

$$\phi^* = \phi * G_\sigma. \quad (6)$$

- v) Check whether the evolution of the LSF has converged using the length of the zero-level curve.

Here, there are two parameters that should be chosen critically. First the standard deviation  $\sigma$  of the Gaussian filter  $G_\sigma$ , which decides the regularization strength, since we utilize the Gaussian filter to smooth the LSF  $\phi$  (step (iv)). Second, the  $\alpha$ -parameter in the evolution equation, since it controls the image-data-driven force inside and outside the contour. Apart from these two critical parameters, another important step is the initialization of an optimal LSF. For this, our strategy is to statistically choose an optimal threshold intensity value ( $T$ ), and define the level-set image from the original image ( $I$ ) as

$$\phi(x, y) \propto I(x, y) - T \quad (7)$$

such that the level-set image has negative values for the region of interest.

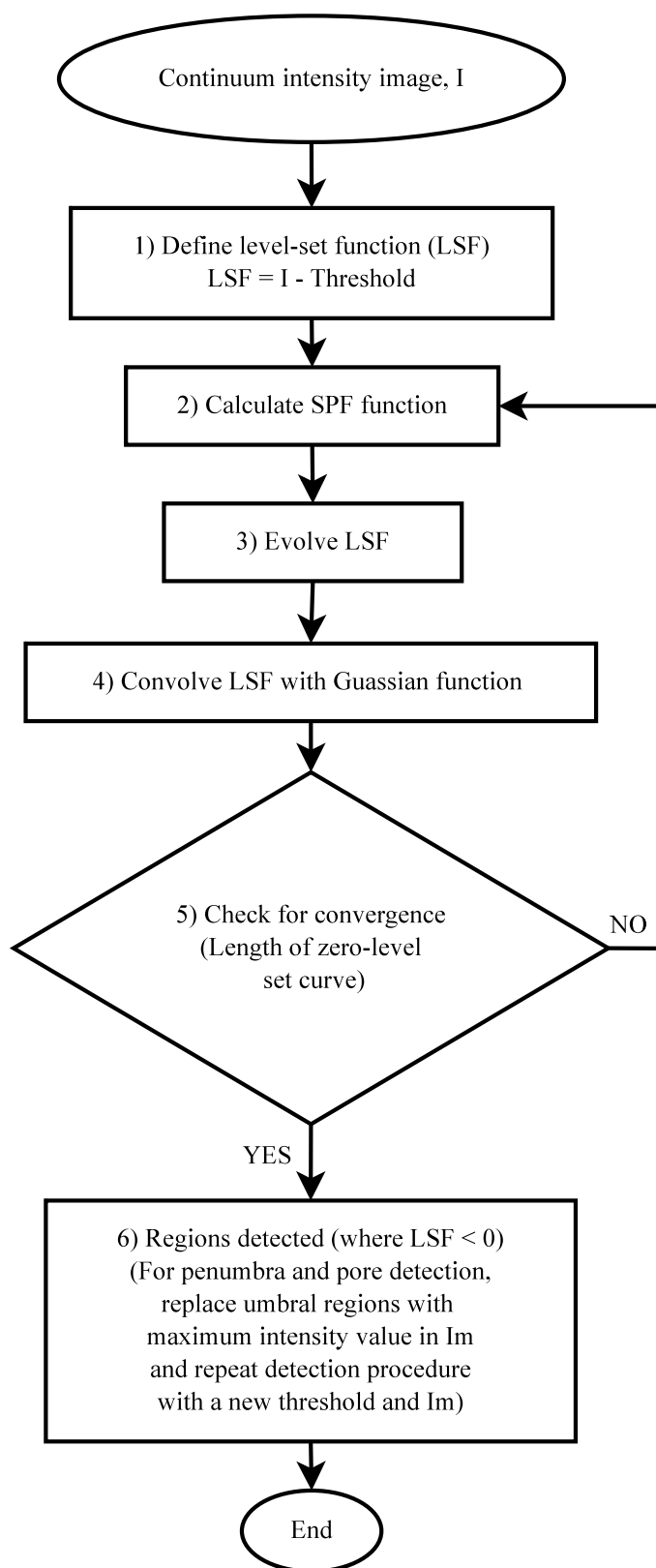
The above procedure can extract regions only from bi-level images, hence the above steps were run in two levels, first for the umbra and then for the penumbra detection. Once umbral regions are detected those pixels were replaced with the maximum intensity value of the image and again all above steps were repeated with a new LSF and other parameter settings for the penumbra detection [Figure 4]. From this detection procedure we have separate region information available for each umbra and penumbra. Figure 5 shows an example of the detection method applied to a full-disk continuum image. The observed image is shown in Figure 5(a), whereas Figure 5(b) shows all the detected sunspots and pores. In Figures 5(c) and 5(d) a zoomed region from the image is shown for clarity.

## 5.2. Sunspot Catalog

Each extracted sunspot and pore obtained from the above detection method (Section 5.1) can be characterized by its position and area on a solar image. With the wealth of solar full-disk continuum images available from MDI, we have generated a sunspot catalog for the complete solar cycle 23. We have termed it the ‘feature detection, characterization, and tracking’ (FDCT) catalog.

The FDCT catalog<sup>1</sup> provides a number of different parameters of sunspots like centroid position, area (projection-corrected), intensity values of umbra and penumbra, *etc.* These

<sup>1</sup><http://www.prl.res.in/~suruchig/FDCT.html>.

**Figure 4** Flowchart of sunspot detection algorithm.

parameters of sunspots are useful for various studies; for example, solar irradiance modeling and for understanding of formation and decay processes of sunspots.

Table 1 shows an example of the above-mentioned catalog, *i.e.* a part of it produced for the continuum image of Figure 6. Total 25 sunspots and pores were identified in the image

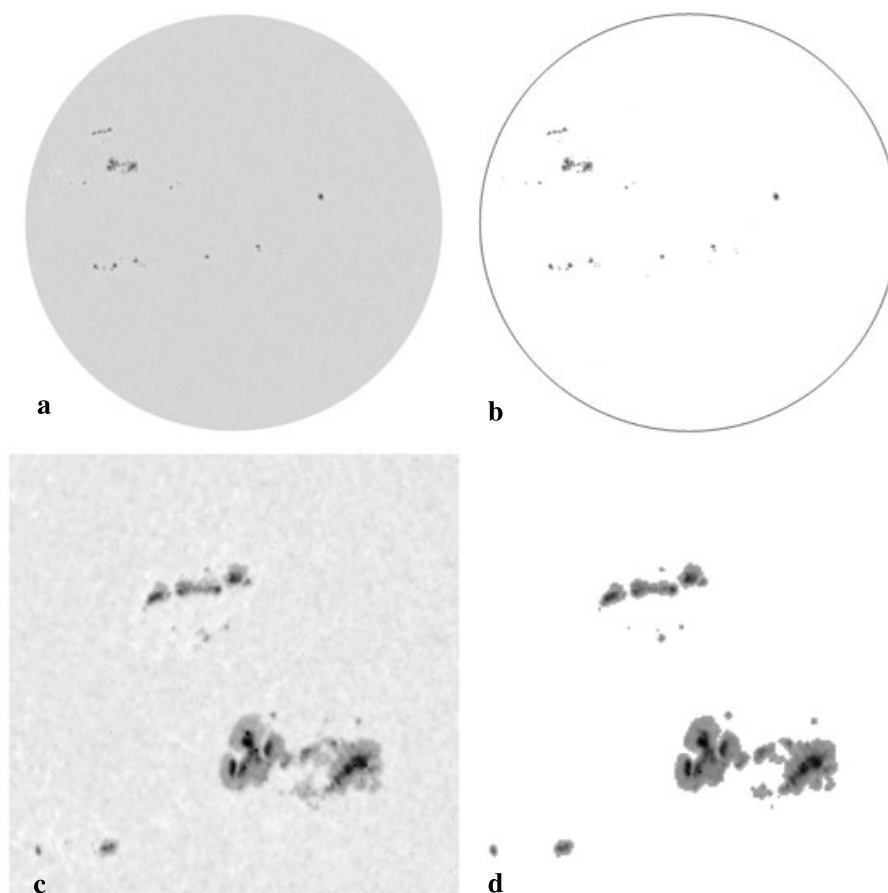


**Figure 5** (a) MDI full-disk continuum image of 21 July 2003. (b) Detected sunspots and pores. Panel (c) gives the zoomed view of a portion of solar disk and the corresponding detected sunspot regions are shown in (d).

(umbrae are listed separately from No. 26 to 33). The details of each column are given below.

Column 1 gives the serial number of the detected region, whereas columns 2 and 3 are the labels and sub-labels for each object. The sub-label ‘0’ corresponds to a pore while ‘-1’ corresponds to a full sunspot. The positive values in the sub-label field represents the detected umbrae. For a given sunspot, the corresponding umbrae (single or multiple) of the sunspot can be identified with the same label values (column 2). In case of a sunspot with multiple umbrae, the umbral objects will have the same label values and increasing counts of sub-label.

For each detected sunspot, pore, and umbral region, the other important parameters which are listed in the table are: geometric area (effective number of pixels covered) (column 4); center of gravity (CG) position in the latitude and longitude in degrees (columns 5 and 6), CG of pixel position (columns 7 and 8); intensity value at CG (column 9); average, minimum, and maximum intensity (columns 10, 11 and 12); projection-corrected area in millionths of hemisphere (column 13); heliocentric angle range in degrees (columns 14 and 15); image coordinates of region’s bounding box (columns 16–19).

### 5.3. Tracking of Sunspots

The automated detection of sunspots and the associated catalog can be used for sunspot tracking. This was done by following the centroid (center of gravity, CG) of each detected sunspot across consecutive images.

**Table 1** The list of properties of detected sunspots and pores of the image shown in Figure 6 (18 June 2002, 22:23:32 UT). 'lb': Label; 'slb': Sub-label; 'GAr': Geometric area; 'CGB', 'CGX', 'CGY', and 'CGL': Center of gravity (CG) position in heliographic latitude (deg), heliographic longitude (deg), image X position, Y position, and intensity at CG position, respectively; 'AvI', 'MnI', and 'MxI': Average, minimum, and maximum intensity of the region (full sunspot, umbra, pore); 'Area': Projection-corrected area (millionth of solar hemisphere, mH); 'H1' and 'H2': Heliocentric angle range of region; 'X1', 'X2', 'Y1', and 'Y2': The region's bounding box image coordinates (top left and bottom right).

No.	lb	slb	GAr	CGB	CGL	CGX	CGY	CGI	AvI	MnI	MxI	Area	H1	H2	X1	X2	Y1	Y2
1	1	-1	237.26	353.85	-17.04	379.22	668.91	0.20	0.70	0.17	0.91	181.30	0.90	0.91	370	388	660	678
2	2	-1	165.89	320.11	-50.78	147.71	609.78	0.14	0.69	0.12	0.91	184.65	0.61	0.64	141	154	601	619
3	3	-1	139.51	82.63	71.75	934.39	326.46	0.20	0.69	0.18	0.93	353.25	0.25	0.30	928	940	315	338
4	4	-1	22.66	353.91	-16.98	374.79	614.34	0.50	0.75	0.50	0.93	16.74	0.93	0.94	372	377	611	617
5	5	-1	20.03	43.56	32.67	763.00	377.55	0.77	0.79	0.67	0.90	17.18	0.80	0.81	760	766	374	381
6	6	-1	11.30	353.27	-17.62	370.02	617.84	0.67	0.80	0.63	0.91	8.39	0.93	0.93	368	372	616	620
7	7	-1	9.94	35.00	24.11	707.13	443.29	0.67	0.81	0.65	0.92	7.61	0.90	0.90	705	709	442	445
8	8	-1	7.84	38.43	27.54	725.22	363.70	0.42	0.83	0.70	0.92	6.43	0.84	0.84	723	728	361	366
9	9	0	32.46	294.06	-76.83	49.65	431.27	0.75	0.80	0.67	0.92	101.92	0.20	0.25	47	53	424	438
10	10	0	22.66	293.90	-76.99	52.13	415.59	0.76	0.80	0.67	0.89	72.38	0.20	0.23	50	54	412	421
11	11	0	9.28	38.11	27.22	723.60	368.60	0.67	0.81	0.67	0.92	7.57	0.84	0.85	722	725	366	371
12	12	0	6.87	309.98	-60.91	102.61	617.45	0.73	0.80	0.73	0.88	9.95	0.47	0.48	101	104	616	620
13	13	0	4.94	13.89	3.00	535.39	657.19	0.72	0.83	0.72	0.90	3.59	0.95	0.95	534	537	656	659
14	14	0	2.68	40.14	29.25	740.06	383.97	0.85	0.85	0.83	0.87	2.21	0.84	0.84	739	741	383	385
15	15	0	2.00	9.96	-0.93	504.12	648.20	0.78	0.83	0.78	0.87	1.44	0.96	0.96	503	505	647	649
16	16	0	0.99	40.54	29.65	742.80	383.49	0.85	0.84	0.84	0.85	0.82	0.83	0.83	742	743	383	384
17	17	0	0.95	33.58	22.69	696.43	446.34	0.86	0.86	0.85	0.86	0.72	0.91	0.91	696	697	446	447
18	18	0	0.83	351.55	-19.34	378.14	765.97	0.88	0.70	0.70	0.70	0.72	0.80	0.80	377	379	765	767
19	19	0	0.76	33.27	22.38	694.12	448.24	0.82	0.82	0.82	0.82	0.57	0.92	0.92	694	695	448	449
20	20	0	0.64	348.32	-22.57	338.78	672.98	0.82	0.82	0.82	0.82	0.51	0.87	0.87	338	339	673	673

Table 1 (Continued.)

No.	lb	slb	GAr	CGB	CGL	CGX	CGY	CGI	AvI	MnI	MxI	Area	H1	H2	X1	X2	Y1	Y2
21	21	0	0.52	339.73	-31.16	264.99	427.91	0.72	0.72	0.72	0.72	0.43	0.84	0.84	265	265	427	428
22	22	0	0.31	352.16	-18.73	367.02	673.20	0.83	0.83	0.83	0.83	0.24	0.89	0.89	367	367	673	674
23	23	0	0.02	317.84	-53.05	227.99	181.01	0.96	0.84	0.84	0.84	0.03	0.42	0.42	228	228	181	181
24	24	0	0.02	42.51	31.62	754.99	371.97	0.85	0.85	0.85	0.85	0.01	0.81	0.81	755	755	372	372
25	25	0	0.01	36.35	25.46	717.98	543.00	0.94	0.85	0.85	0.85	0.01	0.90	0.90	718	718	543	543
26	1	1	65.20	353.84	-17.05	379.12	668.70	0.20	0.47	0.17	0.69	49.81	0.90	0.91	373	385	665	674
27	2	1	49.52	320.19	-50.70	148.17	610.09	0.12	0.46	0.12	0.70	55.01	0.61	0.63	144	152	606	615
28	3	1	43.17	82.59	71.70	934.28	326.47	0.20	0.48	0.18	0.70	108.69	0.26	0.29	931	938	320	333
29	4	1	6.12	353.93	-16.96	374.97	614.72	0.50	0.57	0.50	0.65	4.52	0.93	0.94	374	376	613	616
30	5	1	3.53	43.72	32.83	763.93	376.53	0.55	0.59	0.53	0.67	3.04	0.80	0.80	763	765	376	378
31	6	1	0.19	353.28	-17.61	370.11	617.97	0.67	0.63	0.63	0.63	0.14	0.93	0.93	370	370	618	618
32	7	1	0.02	34.99	24.10	707.06	443.95	0.67	0.65	0.65	0.65	0.02	0.90	0.90	707	707	444	444
33	8	1	8.01	38.52	27.63	725.88	363.56	0.42	0.53	0.42	0.62	6.58	0.84	0.84	724	728	362	365

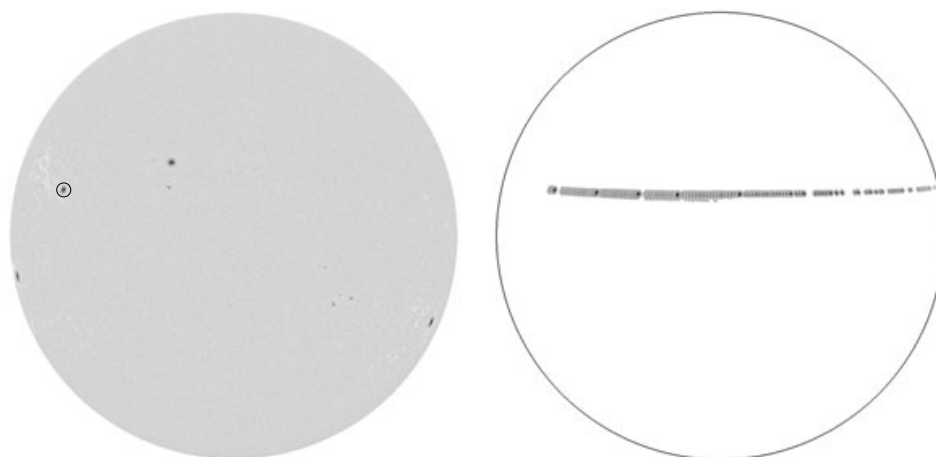
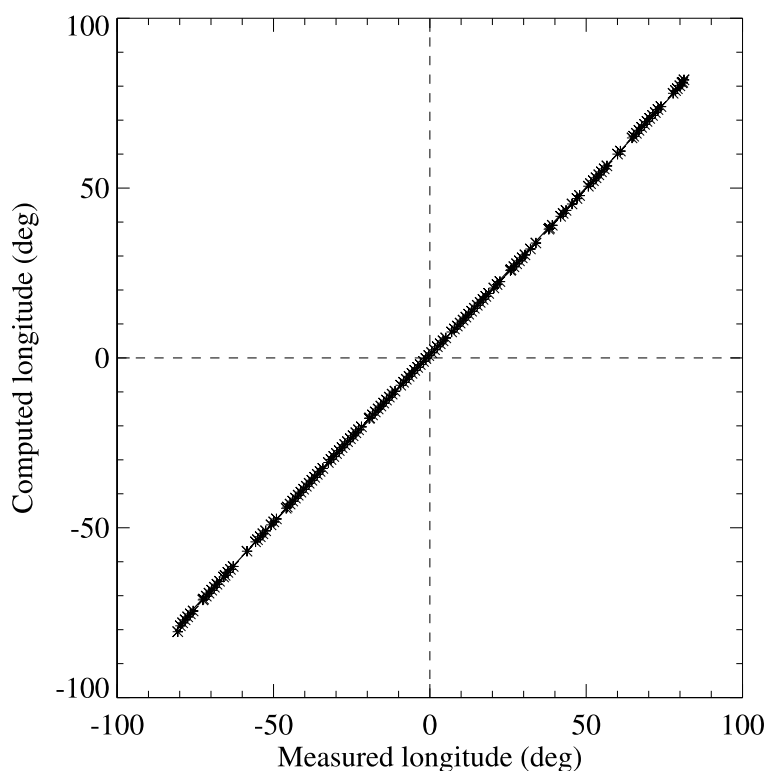


**Figure 6** Tracking of a selected sunspot: From detected sunspots of all images over a period (total 146 images), the selected sunspot (in circle in the left image) has been identified using the tracking algorithm and all the tracked sunspot regions are plotted over the solar disk (right).

**Figure 7** Longitude positions obtained from the tracking of a selected sunspot ( $x$ -axis) are compared with the longitude positions expected from the differential rotation ( $y$ -axis).



In this algorithm, the drift of position of a sunspot region due to differential rotation was compared using the next available images (Higgins *et al.*, 2011). We show an example of tracking in Figures 6 and 7. Figure 6 shows the selected sunspot (encircled in the left image) tracked in the subsequent images obtained on several consecutive days. The stored tracking information of the longitude of the sunspot is used for producing Figure 7. Here, we plot the longitude values obtained using our automated tracking program (asterisk) of the sunspot and the computed longitude using the differential rotation  $\Omega = A + B \sin^2 \theta + C \sin^4 \theta$  ( $\theta$  means the latitude) with coefficients  $A = 2.6662$ ,  $B = -0.3441$ , and  $C = -0.5037$  ( $\mu\text{rad s}^{-1}$ ). For the computation we have taken the initial observed longitude from the first detection of the sunspot. Since the tracking information is

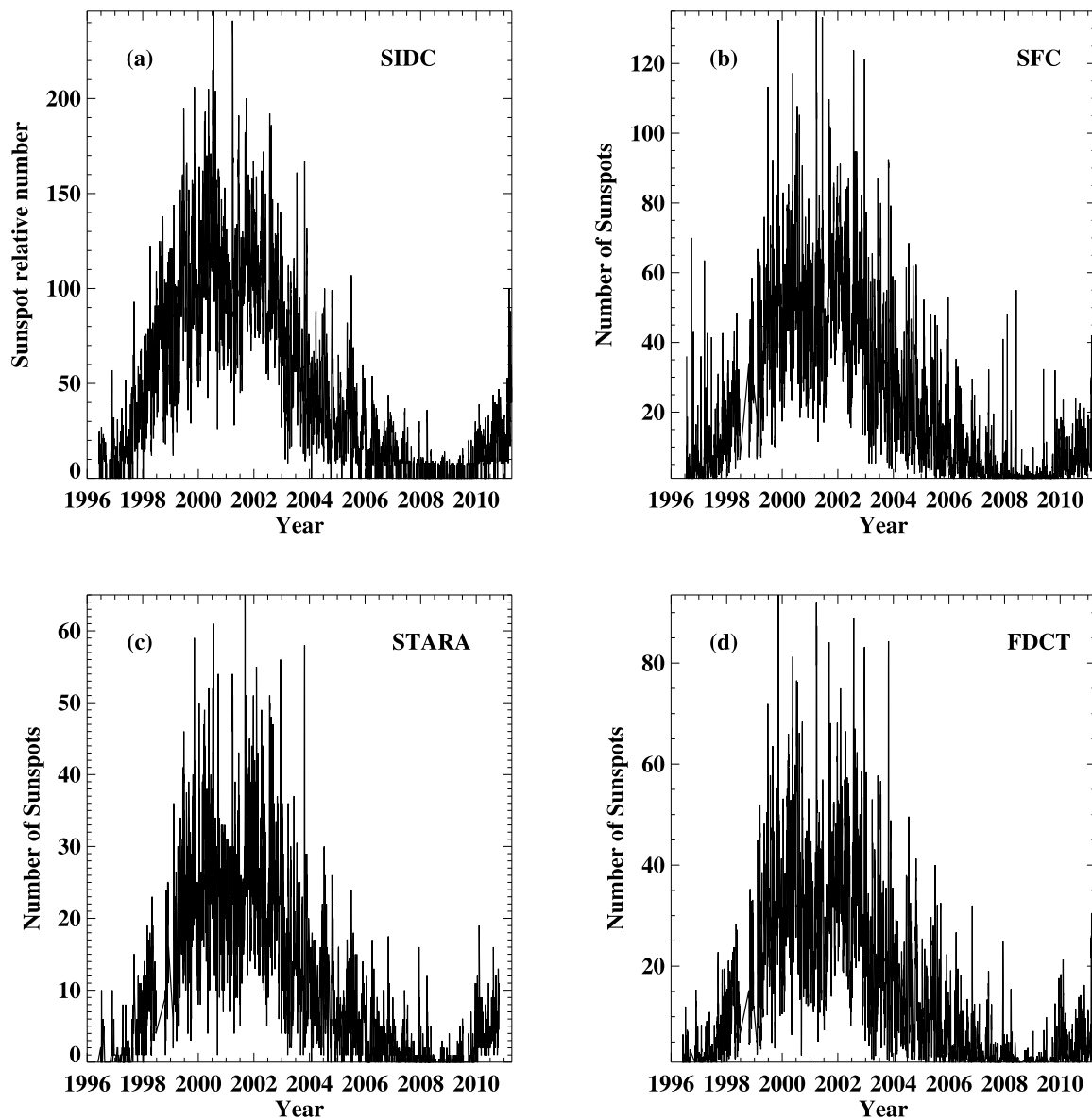


**Figure 8** Comparison of daily average of sunspot counts from SIDC, SFC, STARA, and FDCT for the MDI period (June 1996 to April 2011).

available for most of the observed sunspots in the MDI continuum images, with the large amount of sunspot data and precise tracking we believe that we will be able to refine the differential rotation rates. We plan to pursue such a study at a later stage.

## 6. Verification

In order to verify the results obtained with the FDCT method, we have compared daily averages of sunspot counts and area with some of the available standard sunspot catalogs. Figure 8 shows a comparison between daily average sunspot counts from our FDCT method with the international daily sunspots numbers from SIDC<sup>2</sup> (for MDI data period from June 1996 to 11 April 2011). The comparison is also extended with the catalogs from two sources;

<sup>2</sup><http://www.sidc.be/sunspot-data/>.

Solar Feature Catalogues (SFC;<sup>3</sup> Zharkova *et al.*, 2005; Zharkov, Zharkova, and Ipson, 2005) and STARA<sup>4</sup> (Watson, Fletcher, and Marshall, 2011), which were also generated from the MDI data using the automated detection techniques. It is to be noted that, from June to October 1998, the contact with SOHO spacecraft was lost and no data were recorded for this period; hence there are gaps in Figures 8b–8d around 1998.

The trend of sunspot counts for solar cycle 23 from all catalogs is similar. However, the daily counts differ in each dataset. The SIDC dataset has higher daily counts as compared to all three datasets since other three catalogs presents only raw detection counts while SIDC provides the sunspot relative numbers which are weighted for sunspot groups. Although all were obtained from MDI continuum images, the daily counts in SFC, STARA, and FDCT differ from each other. The SFC has higher counts than the other two sets (STARA and FDCT) because the technique used there tends to detect very small pores. Also, for the SFC data presented here, we have used raw detection counts available from the online catalog, which may not have been processed with refined processes as described in Zharkov *et al.* (2005). Since STARA has higher threshold for the size of sunspot candidates and also in the catalog small sunspots were rejected for removal of bad pixels, and hence lower counts.

In case of FDCT as compared to SFC, a significant difference occurs because of detection of very small pores, and demarcation of nearby sunspot regions. Moreover, we have made refinements after automated detection and listing of sunspots in the catalog. The major refinement in our sunspot list is because of dead-pixels in the SoHO/MDI CCD images. We have found that there was one dead-pixel region in 1999, and by the year 2010, it increased to about 30 dead-pixel regions. By 2010, most of the sunspot detection results corresponds to dead-pixel regions, hence adding a count offset of about 30 during this period. For removal of such false detection, we identified the dead-pixel regions for each year, and then rejected sunspots overlapping with the dead-pixel position. This may also lead to rejection of genuine sunspot(s), but in the next available images, the sunspot could be counted as it passes the dead-pixel region. Also, for daily counts we have further rejected sunspots having geometric area less than 0.72 (see Table 1) in order to remove still left-out false detections corresponding to dead-pixels. Such dead-pixel sunspots can easily be identified on the butterfly diagram. Since these false sunspots remain fixed in the image plane, hence the corresponding latitude follows the sinusoidal pattern in the butterfly diagram. Apart from this, in the catalog, we have not listed sunspots which were touching the solar limb, though they were identified in the automated detection. The detailed comparison of the daily counts for all four catalogs for the period of one month (May 2002) is presented in Figure 10(a). One can see that the FDCT counts lie between the STARA and SFC counts.

Similarly, the daily average value of total area covered by sunspots (projection-corrected) in millionths of solar hemisphere is compared in Figure 9. For this, we have used the USAF/NOAA<sup>5</sup> sunspot data, along with the SFC and STARA catalogs. Here, also the trends are nearly alike. The plots for SFC and FDCT have almost identical trend, but the absolute values differ. The lower value in FDCT could be due to the fact that we did not count the total integral number of pixels within the region boundary for identified sunspot. Instead we

<sup>3</sup><http://ftp.bass2000.obspm.fr/pub/helio/mdiss/>.

<sup>4</sup><http://www.nso.edu/staff/fwatson/STARA>.

<sup>5</sup><http://solarscience.msfc.nasa.gov/greenwch.shtml>.

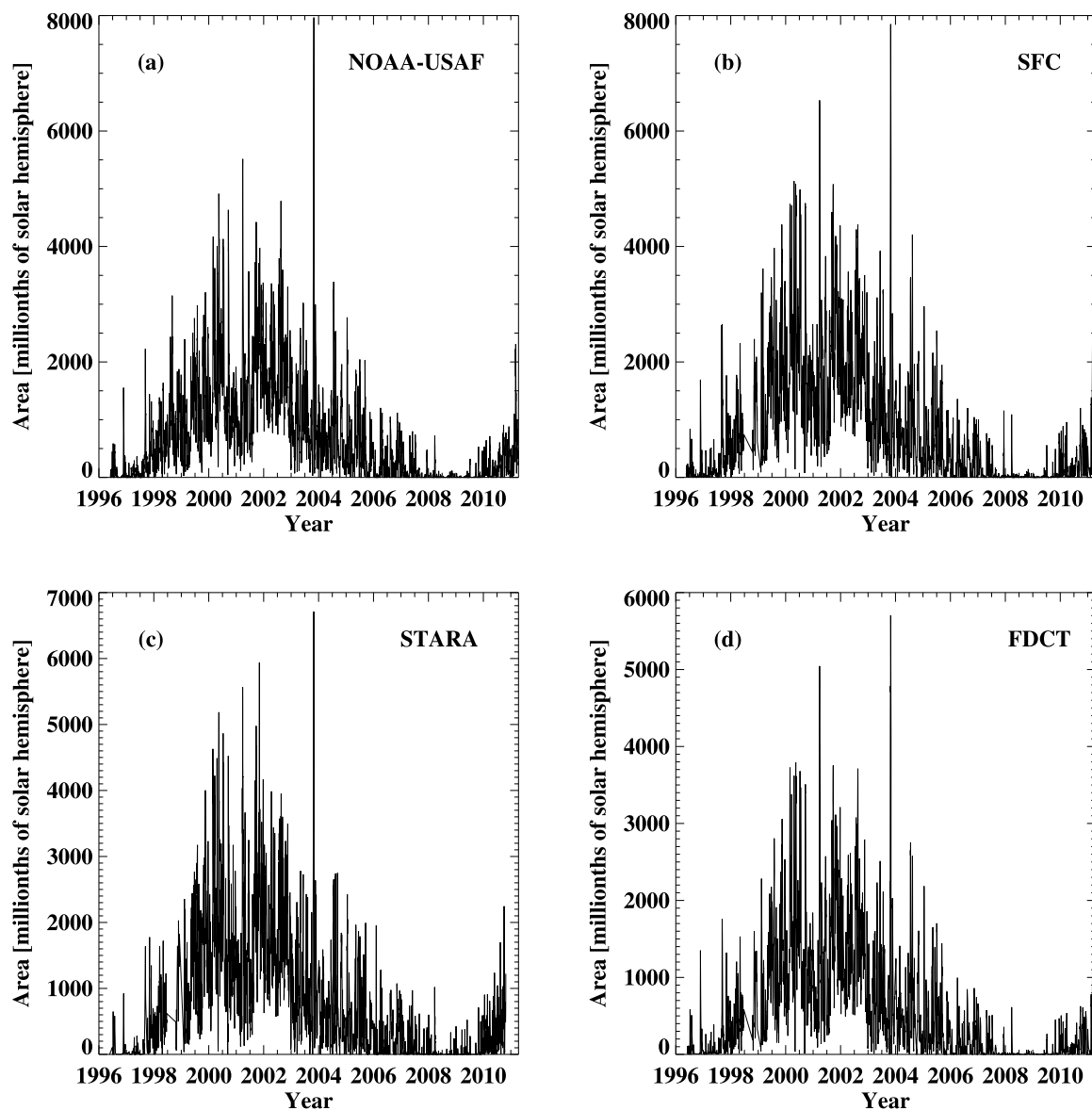


**Figure 9** Comparison of daily average of projection-corrected sunspot area (in millionths of solar hemisphere) from NOAA/USAF, SFC, STARA, and FDCT for the MDI period (June 1996 to April 2011).

considered the fractional contribution of each pixel lying within and on the region boundary, and then corrected for the projection effect. Figure 10(b) presents the comparison of the daily average area from the four catalogs for May 2002.

The FDCT catalog also lists the centroid position in heliographic coordinates of each detected sunspot. After removal of sunspots overlapping with dead-pixels, we have generated the butterfly diagram shown in Figure 11.

## 7. Conclusion

We have developed a new automated sunspots detection procedure based on the level-set method, which is fast and simple to implement. Using this we generated the sunspot catalog (FDCT catalog) for the complete solar cycle 23, which presents various properties of detected sunspots like area, intensity, and position. Using the position information of extracted

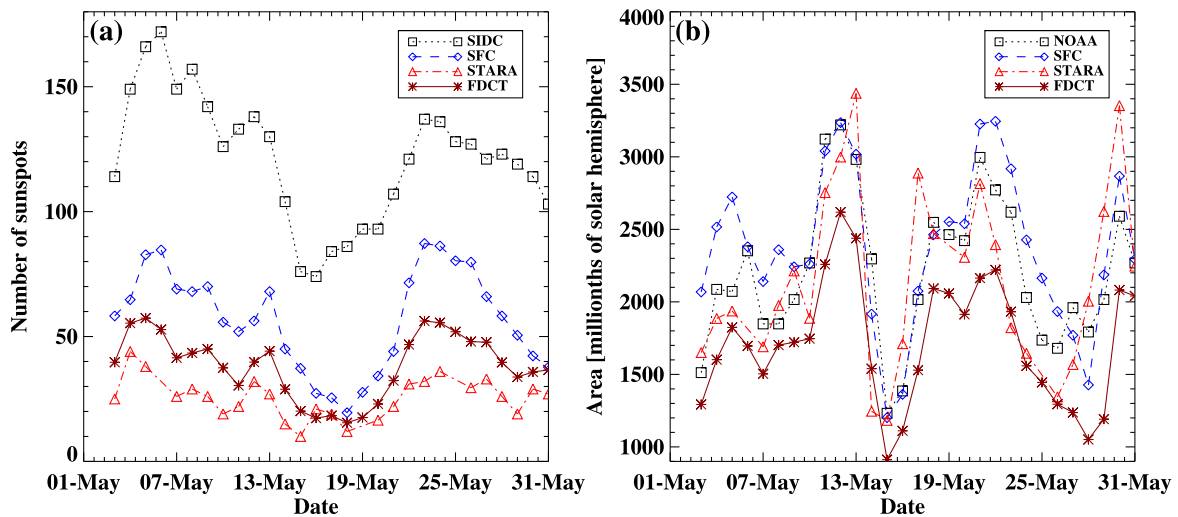
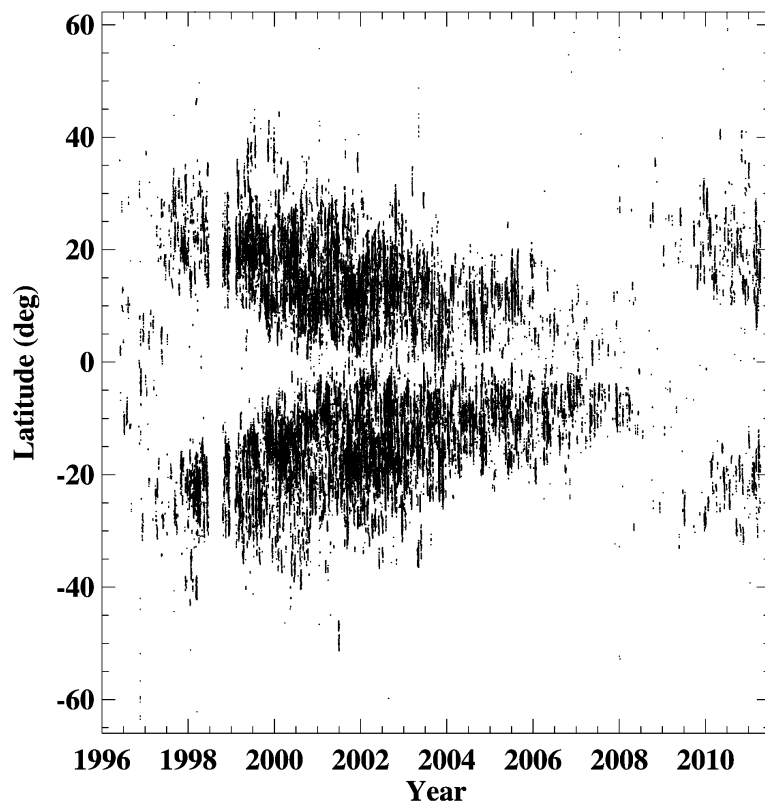


**Figure 10** Comparison of average detection results for May 2002. (a) Daily average sunspot counts from SIDC, SFC, STARA, and FDCT; (b) Daily average of projection-corrected total sunspot area (in millionths of solar hemisphere) from NOAA/USAF, SFC, STARA, and FDCT.

**Figure 11** The latitude distribution for all sunspots from FDCT catalog for period from June 1996 to April 2011.



sunspots from the catalog we have been able to track each sunspot in a fully unsupervised manner and save their tracking reports for future reference.

**Acknowledgements** We would like to thank Dr. Kaihua Zhang for providing the SFGFRLS demo code. SoHO is a project of international cooperation between ESA and NASA. The daily sunspot numbers were obtained from the Solar Influences Data Analysis Center (SIDC) at the Royal Observatory of Belgium. The sunspot area data were obtained from the catalog prepared by the Marshall Space Flight Center using the Royal Greenwich Observatory and USAF/NOAA Sunspot Data.

## References

- Aschwanden, M.J.: 2010, Image processing techniques and feature recognition in solar physics. *Solar Phys.* **262**, 235–275. doi:[10.1007/s11207-009-9474-y](https://doi.org/10.1007/s11207-009-9474-y).
- Beck, J.G., Chapman, G.A.: 1993, A study of the contrast of sunspots from photometric images. *Solar Phys.* **146**, 49–60. doi:[10.1007/BF00662169](https://doi.org/10.1007/BF00662169).
- Brandt, P.N., Schmidt, W., Steinegger, M.: 1990, On the umbra–penumbra area ratio of sunspots. *Solar Phys.* **129**, 191–194. doi:[10.1007/BF00154373](https://doi.org/10.1007/BF00154373).
- Colak, T., Qahwaji, R.: 2008, Automated McIntosh-based classification of sunspot groups using MDI images. *Solar Phys.* **248**, 277–296. doi:[10.1007/s11207-007-9094-3](https://doi.org/10.1007/s11207-007-9094-3).
- Curto, J.J., Blanca, M., Martínez, E.: 2008, Automatic sunspots detection on full-disk solar images using mathematical morphology. *Solar Phys.* **250**, 411–429. doi:[10.1007/s11207-008-9224-6](https://doi.org/10.1007/s11207-008-9224-6).
- Fonte, C.C., Fernandes, J.: 2009, Application of fuzzy sets to the determination of sunspot areas. *Solar Phys.* **260**, 21–41. doi:[10.1007/s11207-009-9436-4](https://doi.org/10.1007/s11207-009-9436-4).
- Grossmann-Doerth, U., Schmidt, W.: 1981, The brightness distribution in sunspot penumbrae. *Astron. Astrophys.* **95**, 366–372.
- Györi, L.: 1998, Automation of area measurement of sunspots. *Solar Phys.* **180**, 109–130. doi:[10.1023/A:1005081621268](https://doi.org/10.1023/A:1005081621268).
- Higgins, P.A., Gallagher, P.T., McAteer, R.T.J., Bloomfield, D.S.: 2011, Solar magnetic feature detection and tracking for space weather monitoring. *Adv. Space Res.* **47**, 2105–2117. doi:[10.1016/j.asr.2010.06.024](https://doi.org/10.1016/j.asr.2010.06.024).
- Jones, H.P., Chapman, G.A., Harvey, K.L., Pap, J.M., Preminger, D.G., Turmon, M.J., Walton, S.R.: 2008, A comparison of feature classification methods for modeling solar irradiance variation. *Solar Phys.* **248**, 323–337. doi:[10.1007/s11207-007-9069-4](https://doi.org/10.1007/s11207-007-9069-4).
- Kass, M., Witkin, A., Terzopoulos, D.: 1988, Snakes: Active contour models. *Int. J. Comput. Vis.* **1**, 321–331. doi:[10.1007/BF00133570](https://doi.org/10.1007/BF00133570).
- Martínez Pillet, V.: 1992, Stray-light effects on the solar intensity distribution. *Solar Phys.* **140**, 207–237. doi:[10.1007/BF00146310](https://doi.org/10.1007/BF00146310).
- Mathew, S.K., Martínez Pillet, V., Solanki, S.K., Krivova, N.A.: 2007, Properties of sunspots in cycle 23. I. Dependence of brightness on sunspot size and cycle phase. *Astron. Astrophys.* **465**, 291–304. doi:[10.1051/0004-6361:20066356](https://doi.org/10.1051/0004-6361:20066356).
- Osher, S., Sethian, J.A.: 1988, Fronts propagating with curvature-dependent speed: Algorithms based on Hamilton–Jacobi formulations. *J. Comput. Phys.* **79**, 12–49. doi:[10.1016/0021-9991\(88\)90002-2](https://doi.org/10.1016/0021-9991(88)90002-2).
- Pettauer, T., Brandt, P.N.: 1997, On novel methods to determine areas of sunspots from photoheliograms. *Solar Phys.* **175**, 197–203. doi:[10.1023/A:1004903201224](https://doi.org/10.1023/A:1004903201224).
- Pierce, A.K., Slaughter, C.D.: 1977, Solar limb darkening. I –  $\lambda\lambda$  of 3033–7297. *Solar Phys.* **51**, 25–41. doi:[10.1007/BF00240442](https://doi.org/10.1007/BF00240442).
- Potts, H.E., Diver, D.A.: 2008, Post-hoc derivation of SOHO Michelson Doppler Imager flat fields. *Astron. Astrophys.* **492**, 863–871. doi:[10.1051/0004-6361:200810606](https://doi.org/10.1051/0004-6361:200810606).
- Preminger, D.G., Walton, S.R., Chapman, G.A.: 2001, Solar feature identification using contrasts and contiguity. *Solar Phys.* **202**, 53–62. doi:[10.1023/A:1011896413891](https://doi.org/10.1023/A:1011896413891).
- Scherrer, P.H., Bogart, R.S., Bush, R.I., Hoeksema, J.T., Kosovichev, A.G., Schou, J., *et al.*: 1995, The Solar Oscillations Investigation – Michelson Doppler Imager. *Solar Phys.* **162**, 129–188. doi:[10.1007/BF00733429](https://doi.org/10.1007/BF00733429).
- Steinegger, M., Brandt, P.N., Schmidt, W., Pap, J.: 1990, Sunspot photometry and the total solar irradiance deficit measured in 1980 by ACRIM. *Astrophys. Space Sci.* **170**, 127–133. doi:[10.1007/BF00652658](https://doi.org/10.1007/BF00652658).
- Steinegger, M., Vazquez, M., Bonet, J.A., Brandt, P.N.: 1996, On the energy balance of solar active regions. *Astrophys. J.* **461**, 478–498. doi:[10.1086/177075](https://doi.org/10.1086/177075).
- Turmon, M., Pap, J.M., Mukhtar, S.: 2002, Statistical pattern recognition for labeling solar active regions: Application to SOHO/MDI imagery. *Astrophys. J.* **568**, 396–407. doi:[10.1086/338681](https://doi.org/10.1086/338681).
- Verbeeck, C., Higgins, P.A., Colak, T., Watson, F.T., Delouille, V., Mampaey, B., Qahwaji, R.: 2013, A multi-wavelength analysis of active regions and sunspots by comparison of automatic detection algorithms. *Solar Phys.* **283**, 67–95. doi:[10.1007/s11207-011-9859-6](https://doi.org/10.1007/s11207-011-9859-6).
- Watson, F.T., Fletcher, L., Marshall, S.: 2011, Evolution of sunspot properties during solar cycle 23. *Astron. Astrophys.* **533**, A14. doi:[10.1051/0004-6361/201116655](https://doi.org/10.1051/0004-6361/201116655).
- Watson, F., Fletcher, L., Dalla, S., Marshall, S.: 2009, Modelling the longitudinal asymmetry in sunspot emergence: The role of the Wilson depression. *Solar Phys.* **260**, 5–19. doi:[10.1007/s11207-009-9420-z](https://doi.org/10.1007/s11207-009-9420-z).
- Zhang, K., Zhang, L., Song, H., Zhou, W.: 2010, Active contours with selective local or global segmentation: A new formulation and level set method. *Image Vis. Comput.* **28**, 668–676. doi:[10.1016/j.imavis.2009.10.009](https://doi.org/10.1016/j.imavis.2009.10.009).

- Zharkov, S., Zharkova, V.V., Ipson, S.S.: 2005, Statistical properties of sunspots in 1996–2004: I. Detection, North South asymmetry and area distribution. *Solar Phys.* **228**, 377–397. doi:[10.1007/s11207-005-5005-7](https://doi.org/10.1007/s11207-005-5005-7).
- Zharkov, S., Zharkova, V., Ipson, S., Benkhalil, A.: 2005, Technique for automated recognition of sunspots on full-disk solar images. *EURASIP J. Appl. Signal Process.* **15**, 2573–2584. doi:[10.1155/ASP.2005.2573](https://doi.org/10.1155/ASP.2005.2573).
- Zharkova, V.V., Abouadarham, J., Zharkov, S., Ipson, S.S., Benkhalil, A.K., Fuller, N.: 2005, Solar feature catalogues in Egso. *Solar Phys.* **228**, 361–375. doi:[10.1007/s11207-005-5623-0](https://doi.org/10.1007/s11207-005-5623-0).